Reconfigurable Micromechanical Filters

By

Jalal Naghsh Nilchi

A dissertation submitted in partial satisfaction of the

requirements for the degree of

Doctor of Philosophy

in

Engineering – Electrical Engineering and Computer Sciences

in the

Graduate Division

of the

University of California, Berkeley

Committee in Charge:

Professor Clark T.-C. Nguyen, Chair
Professor Elad Alon
Professor Liwei Lin

Fall 2017

Abstract

Reconfigurable Micromechanical Filters

By

Jalal Naghsh Nilchi

Doctor of Philosophy in Engineering – Electrical Engineering and Computer Sciences

University of California, Berkeley

Professor Clark T.-C. Nguyen, Chair

Power consumption, form factor and more importantly cost, are major challenges for today's wireless communication systems that hinder realization of the Internet of the Things and beyond, e.g., the Trillion Sensor vision. This dissertation explores micromechanical methods that enable RF channel-selection to simplify receiver architectures and considerably reduce their power consumption.

In particular, strong interfering signals picked up by the antenna impose strict requirements on system nonlinearity and dynamic range, which translate to higher power consumption in the RF front-end and the baseband circuitry. Removal of these unwanted signals relaxes dynamic range requirements and reduces power consumption. Rejection of all interferers, if possible, could potentially lift any nonlinearity requirements on the receiver and considerably reduce power consumption. This work first investigates the requirements for RF channel selection, then demonstrates that capacitive-gap transduced micromechanical resonators possess the high quality factor and strong electromechanical coupling needed for successful demonstration of channel selection at RF.

This dissertation specifically focuses on clamped-clamped beam (CC-beam) micromechanical resonators as building blocks for channel-select filters. Here, a small-signal equivalent model developed for a general parallel-plate capacitive transducer and then refined for CC-beam resonators predicts very strong electromechanical coupling. Experimental measurements on the fabricated CC-beam resonators confirm these predictions and demonstrate coupling strengths greater than 10%. CC-beam resonators with such a strong coupling and equipped with inherent high quality factor enabled by capacitive transducers are a suitable choice for realization of narrow-bandwidth filters at HF, as confirmed by experimental results.

The filter design procedure presented in this dissertation and refinements to narrow mechanical coupling beam modeling pave the way for better understanding of mechanical circuits and comprehensive study of filter transfer function. This dissertation illustrates the importance of

coupling beam design for the optimum filter realization. The refinements to coupling beam formulation also expands our understanding of extensional- and flexural-mode beams, and demonstrate the creation and manipulation of system poles by coupling beam design.

Taking advantage of different theories presented and developed here, the 3rd- and 4th-order micromechanical filters of this work exploit bridging between non-adjacent resonators to insert and control transfer function loss poles that sharpen passband-to-stopband roll-off. Measurement of these filters demonstrates very sharp roll-offs, as evidenced by 20dB shape factors as small as 1.84 for filters with narrow bandwidths of 0.1% to 0.3%, centered at 8MHz. The high-Q CC-beam resonators constituting the filters enable insertion loss of only 1dB in a properly terminated filter.

RF channel selection eliminates unwanted signals sufficiently to relax the nonlinearity requirements on the following stages. Consequently, the micromechanical filter becomes a significant contributor to the nonlinear performance of the overall system. This work investigates different nonlinear phenomena in capacitive-gap transducers and predicts nonlinear performance sufficient for today's wireless system requirements. Experimental measurements on bridged filters confirms these expectations. Specifically, a 4th-order bridged filter has a third-order intercept point (IIP3) of +31.8dBm, which translates to an ample dynamic range of 88dB.

To fully harness the strong electromechanical coupling and high quality factor offered by CC-beam resonators, this dissertation demonstrates a 7th-order bridged micromechanical filter with very sharp passband-to-stopband roll-off, marked by a 20dB shape factor of 1.45, the best shape factor reported so far for any on-chip channel-select filter. This high-order filter with +31.4dBm of IIP3 for 200kHz tone spacing offers the essential framework for the realization of channel selection and the receiver performance enhancement it promises.

Finally, this work addresses concerns on the electromechanical coupling strength of capacitive resonators at higher frequencies. The specialized fabrication processes herein to (1) deposit low-stress polysilicon layers, (2) etch the polysilicon structure with sufficiently smooth sidewalls, and (3) deposit a conformal and uniform thin oxide layer, enable capacitive-gap transducers with gap spacings as small as 13.2nm. Such a small gap spacing delivers strong electromechanical coupling greater than 1.6% in a 60-MHz wine-glass disk resonator.

Dedicated to my dear parents,

and beloved brothers, Jalil and Amirhossein.

None of this would have been possible without their unconditional love and support.

Table of Contents

Acknowledgement

Chapter 1 INTRODUCTION

Wireless communication is an indispensable feature of the modern life which has revolutionized different aspects of our lives by the provision of fast and reliable connection everywhere at any time [1]. This revolution has broadened the expectations of the societies and right now, every one of us expect to have easy access to fast and stable connection: to check the live traffic to our destinations, to unlock the front door for our forgetful roommates, to inspect the soil dampness and water the garden, etc [2]. Such a connected world, with trillions of sensors to collect useful information and massive wireless networks to provide data to people, has been a game changer and not only has made our life easier, but also has enabled new products and services and accelerated technological innovations [2].

Implementation of such a massive connected world, and the Autonomous Swarms [3] and the TerraSwarms of the future [2], demands for reliable wireless communication, since the application of wired networks in this scale is impractical and unachievable. Application of wireless networks provides us with undisputed advantages and conveniences, like mobility and roaming, immense increase in the number of the users and accessibility, far-reaching coverage even over hard-to-reach area, and flexibility [1]. However, the adaptation of wireless networks at such a substantial scale requires addressing of its challenges, namely: shared spectrum and power consumption.

i) The wireless spectrum is a very limited resource that should be shared between many different networks and users [4]. This limitation asks for tight regulation and ongoing inspections to enforce the regulations and make sure different networks and various standards do not interfere with each other and degrade the overall system performance [1]. The demand for higher data rate and more autonomous networks around us makes the frequency spectrum even more crowded, with different bands adjacent to each other, or even coexist on the same frequency range.

The performance of wireless networks in such a congested and busy frequency spectrum (*c.f.* Figure 1.1) heavily depends on the level of filtering offered in the transceiver. The RF filter in the receiver path eliminates some of the strong interfering signals, while the transmitter antenna prevents your transceiver to broadcast strong interferers in adjacent bands/channels (c.f. Figure 1.2). However, this traditional method of static spectrum allocation to different users cannot keep up with the number of users with growing bandwidth request. There are numerous efforts to address this problem: application of different spread spectrum coding techniques such as code-division multiple access CDMA [5], efficient exploitation of available spectrum by cognitive radios [4] [6] or carrier aggregation [7].

ii) Realization of a connected world by implementation of trillions of sensors raises questions on the power consumption of such a massive network. On the other hand,

1

there is no feasible engineering way to power up these networks through wire connections, and hence, the autonomous networks can only rely on batteries or energy harvesting methods as their energy sources. Therefore, there have been substantial efforts to decrease the power consumption of each wireless node [8], improve the battery capacity per weight and volume [9], and increase the available power of different energy harvesting methods [10].

The power consumption breakdown of commercially-available sensor nodes [11] [12], shown in Figure 1.3, reveals that wireless transceivers consume considerable portion of battery energy and hence, this work tries to reduce the receiver power consumption by the application of channel-select filters in the receiver front-ends.

1.1 CONVENTIONAL WIRELESS TRANSCEIVER ARCHITECTURES

A wireless transceiver should transmit and receive signals over the specified frequency band, avoiding strong broadcast outside the allocated bands and rejecting the incoming interferers. As shown in Figure 1.2, a frequency-division duplexing FDD system [13] [14] achieve these purposes by separate frond-end filters in receive and transmit paths. The transmit filter shapes the power amplifier output signal and prevent transmission in other frequencies, while the receive filter improves the receiver chain performance by rejecting the interfering signals. Since numerous factors, such as distance to the base station, surrounding objects, weather, etc., affect the incoming signal power, the receiver dynamic range is not predetermined and the transceiver should be able to detect the desired signal in different condition, with orders of magnitude difference in the incoming signal power [1]. As a result, communication standards define the worst-case scenario in which the transceivers should successfully perceive the incoming signals; for example, 3G GSM standard [15] asks for the receivers to detect signals in vicinity of interferers with 100dB difference in power, i.e. 10 orders of magnitude difference in the power level. On the other hand, the minimum detectable signal requirement set by the communication standards imposes more restrictions on the receiver noise figure. Hence, the receiver filter design is more challenging and comprises of various optimizations and tradeoffs to achieve the requirements.
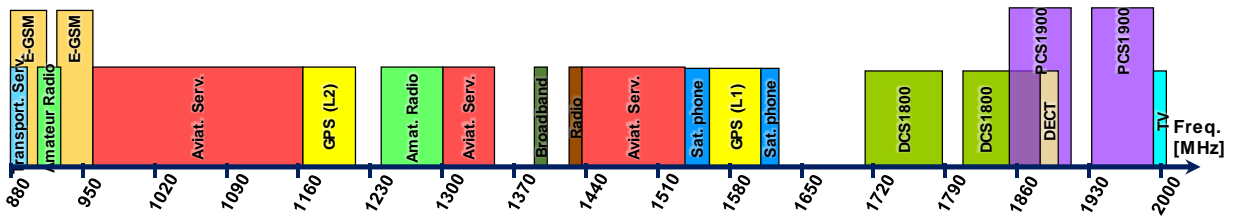
Figure 1.1: A simple version of frequency allocation illustrates the crowded wireless spectrum.

2

1.1.1 THE SUPERHETERODYNE RECEIVER ARCHITECTURE

The superheterodyne receiver architecture [16] was the most popular receiver architecture due to its distinctive advantages. A superheterodyne receiver, like the one shown in Figure 1.4, down converts the input RF signal to the intermediate frequency (IF) range, where highly-selective filters are conveniently implementable. The IF channel-select filters relax the dynamic range requirements on the baseband circuitry by efficiently rejecting the adjacent channels and any interfering signals. Since the implementation of these channel-select filters has been only feasible at lower frequencies, it is imperative for the receiver to mix down the high-frequency input signals and then perform the channel selection.
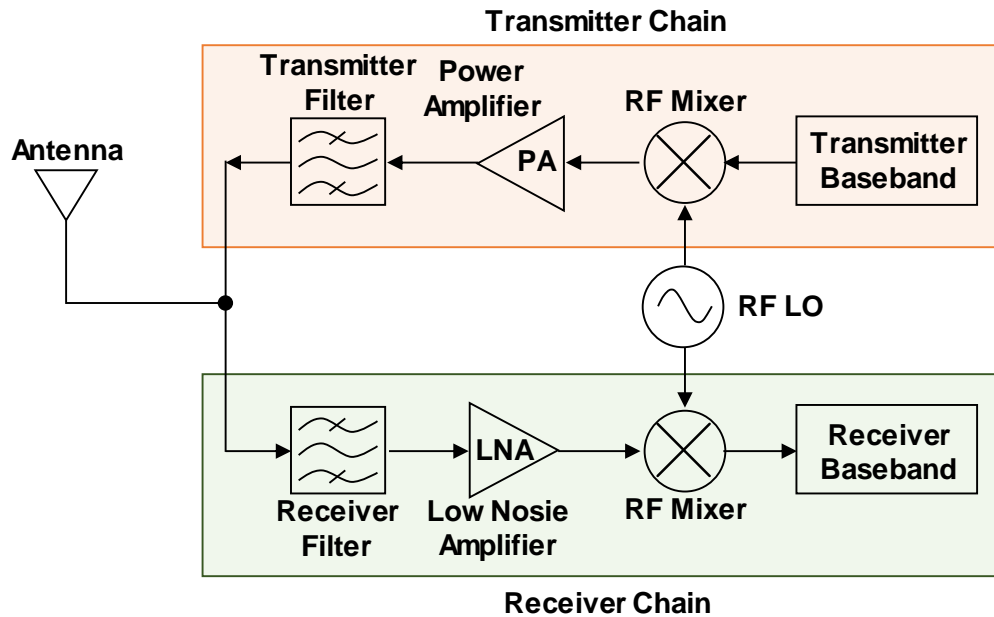
Figure 1.2: Simplified schematic of a conventional FDD transceiver that identifies the transmitter and receiver chains.
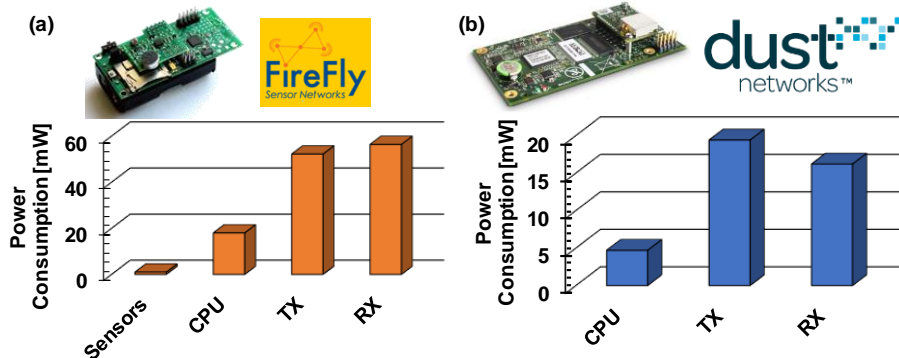
Figure 1.3: the power consumption breakdown of commercially-available wireless sensor nodes illustrates the importance and necessity of power reduction in the transceiver.

3

Figure 1.4 describes a widely-used superheterodyne receiver. The RF band-select filter at the antenna port attenuates RF signals out of the designated receiver frequency band, usually from other communication standards. The band-select filter also limits the thermal noise power at the receiver input. To enhance the noise performance of the receiver chain and to amplify the input signal power, the following low-noise amplifier (LNA) stage provides signal amplification with minimum added noise. The overall noise figure of a cascaded system like the superheterodyne receiver of Figure 1.4 greatly depends on the gain and noise performances of the first few stages, as given in equation 1.1 [17]. While the filter and LNA noise figures affect the system noise figure directly, the LNA gain scales down the effect of the following stage noise figure. Therefore, a receiver with small noise figure asks for large LNA gain and as small as possible values for the RF filter and LNA noise figures. (Equation 1.1 assumes the filter stages have power gain very close to unity, i.e. very small insertion loss. Also, the noise figures and power gains should be in linear scale.)

$$F = F_{RF} + \frac{F_{LNA} - 1}{G_{RF}} + \frac{F_{IR} - 1}{G_{RF} \cdot G_{LNA}} + \frac{F_{Mixer} - 1}{G_{RF} \cdot G_{LNA} \cdot G_{IR}} + \frac{F_{IF} - 1}{G_{RF} \cdot G_{LNA} \cdot G_{IR} \cdot G_{Mixer}} + \cdots$$

$$F \cong F_{RF} + (F_{LNA} - 1) + \frac{F_{IR} - 1}{G_{LNA}} + \frac{F_{Mixer} - 1}{G_{LNA}} + \frac{F_{IF} - 1}{G_{LNA} \cdot G_{Mixer}} + \cdots \qquad (1.1)$$

Equation 1.1 emphasizes on the importance of RF filters with very small insertion loss and also gives the reason why channel selection has not been possible at RF. For a passive component, i.e. a device with power gain smaller than unity, like the RF band-select filter, the noise figure is equal to the insertion loss and therefore, the RF filter insertion loss directly affects the system noise figure. On the other hand, the quality factor of the constituent components in the filters relative to the filter percent bandwidth determines the filter insertion loss, as explained in details in Chapter
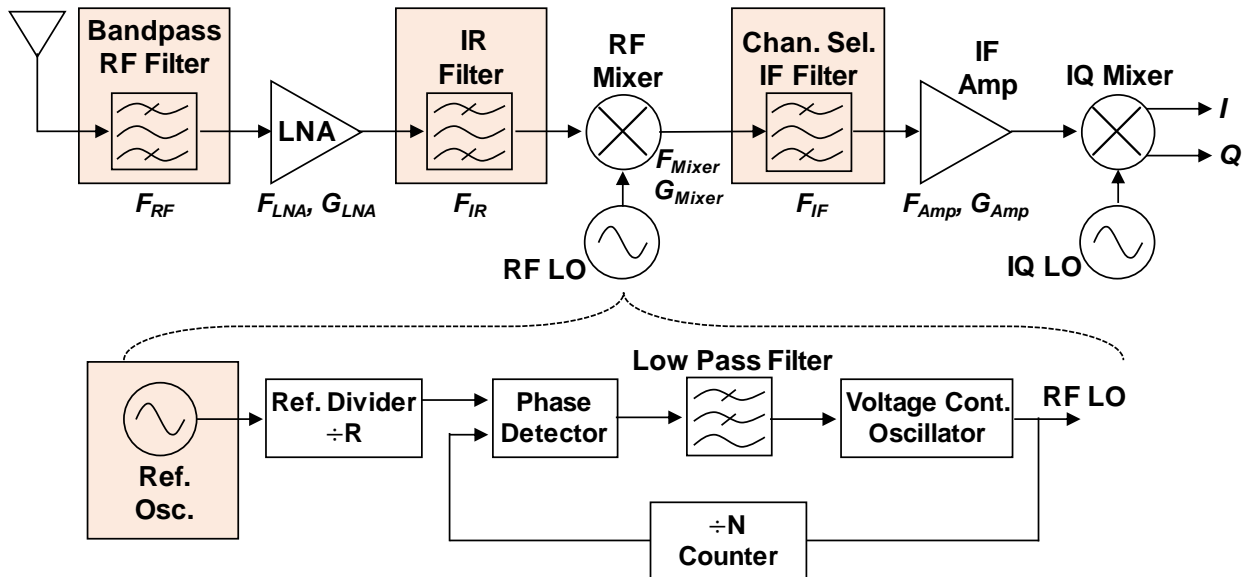
Figure 1.4: Schematic description of a conventional superheterodyne receiver with highlighted off-chip components. The interface to many off-chip components imposes further bottlenecks on the receiver design.

3. This criterion means that the channel-select filter realization at the receiver front-ends entails resonators with quality factor as high as 30,000, while the current resonator technologies such as FBAR [18] and SAW [19], fall short of such high Q requirements. Recent efforts on the capacitive transducers [20] have been able to demonstrate resonators with high quality factors at GHz frequencies, sufficient for the realization of channel selection at these frequencies.

The following mixer converts down the filtered RF input signal to IF frequencies using a local oscillator (LO) signal [17]. A voltage controlled oscillator (VCO) within the feedback loop of a phase-locked loop (PLL) generates the LO signal referenced to an exceptionally-stable oscillator. Quartz crystal oscillators are the prevailing choice for the reference oscillators, since they can provide a reference signal robust against aging and temperature changes. The PLL block can translate the fixed reference signal to any required frequency and provide flexible and wide tuning range for the LO frequency.

The LO frequency can be either higher or lower than the RF input frequency, as in equation 1.2, since the mixer is only responsive to the difference between the RF and LO frequencies and not the absolute values. This implies that for either choice of LO frequency, there will be an image frequency in the input spectrum that the mixer translates it exactly to the output IF frequency, which will degrade the desired signal. The common approach to prevent the image problem is to implement another filter at image frequency f_{Image} of equation 1.3, between the LNA and the mixer. Equation 1.3 suggests that the image channels are only $2f_{IF}$ away from the desired frequency f_{RF}, which imposes tradeoffs between the choice of IF frequency and filter realization. Lower IF frequency means that channel-select filters have larger percent bandwidth and low-Q resonators have sufficient for the successful realization. However, this choice places the image frequency much closer the desired RF and toughens the realization of image reject (IR) filter, since the IR filter should provide sufficient attenuation at frequencies very close to the RF filter passband. This again emphasizes on the importance of frequency-selectivity performance and roll-off of RF filters. Optimum choice of IF frequency compromises between the IR and IF filters performance to ensure sufficient attenuation at image frequencies, while the IF filter insertion loss is in an acceptable range.

$$f_{LO} = f_{RF} \mp f_{IF} \qquad (1.2)$$
$$f_{Image} = f_{RF} \mp 2 \times f_{IF} \qquad (1.3)$$

The IF filter relaxes the dynamic range requirements of the baseband circuitry by rejecting any channel other than the desired one. Therefore, the IF filters should have small bandwidth and offer fast roll-off to provide sufficient attenuation at adjacent channels. On the other hand, since the communication system chooses different channels for different users over time, the heterodyne receivers should be capable of perceiving any channel in the band. A fixed LO system requires different IF filters for different channels, which increases the system footprint. Alternatively, to fix the IF frequency and use only one IF filter, the local oscillator should offer a wide tuning range.

The PLL implementation of the LO in Figure 1.4 grants the required tuning range, but at the expense of considerable power consumption. The baseband circuitry can easily process the IF signal after channel selection and demodulate and recover the transmitted data.

In conclusion, the heterodyne receiver of Figure 1.4 utilizes several off-chip frequency-selective components to offer a robust connection: (1) band-select filters at the receiver front-end, (2) stable reference oscillators for LO generation, (3) image reject filters, (4) IF filters. This level of frequency selection grants a reliable connection even in the presence of strong interfering signals, although at the cost of system complexity and cost, especially since these components are all off-chip.

Possible channel selection at the front-end could considerably reduce the system complexity and cost, since there would be no need for IR or IF filters and a fixed LO would be sufficient to translate the RF input signal to IF.

1.1.2   THE DIRECT-CONVERSION RECEIVER ARCHITECTURE

The introduction of intermediate frequency IF in the heterodyne architecture accomplished a robust receiver, but by using too many off-chip components that increases the design complexity and the assembly time and downgrades the yield, which all translates to the increase in cost. Direct-conversion receivers [21], like the one shown in Figure 1.5, try to solve these obstacles by down converting the RF input directly to the baseband and hence, remove the need for image rejection and IF filters. Elimination of these filters removes the design constraints on the LNA and the mixer due to the interface to off-chip components and relaxes the design requirements considerably.

The band-select filter at the receiver front-end of Figure 1.5 is the only off-chip component to block the interfering signals. The LNA provides considerable power gain with minimum added noise, to improve the receiver chain noise figure, as explained in the previous section. The IQ mixer then directly down converts the RF input signal to the baseband by, and the low pass (LP) filters clean out the mixer output above the baseband frequency. On-chip *RC* filters are capable of the LP filter realization, since the LP filters are at very low frequencies and not required to have very sharp response.

The direct-conversion architecture of Figure 1.5 with the minimum number of off-chip components is well-suited for the multi-mode transceiver systems of today's wireless system [22]. However, the direct conversion to the baseband imposes major design challenges due to more sensitivity to: (1) DC offset, (2) mismatch between I and Q, (3) LO leakage and (4) the flicker noise. The recent advances in RFIC technology and signal processing were the key to address these issues and make the direct-conversion one of the most common receiver architecture design used today.

6

In conclusion, the direct-conversion architecture reduces the wireless transceiver footprints by eliminating off-chips IR and IF filters and eases off the IC design constraints by discarding the interface requirements to off-chip components after the LNA. However, the elimination of these frequency-selective components increases the dynamic range requirements on the baseband circuitry, which translates to higher power consumption.

1.2 RF CHANNEL-SELECTING RECEIVERS

As mentioned in the previous sections, higher level of frequency selection in the heterodyne architecture relaxes the dynamic range requirements and reduces the power consumption, but at the expenses of more off-chip components. On the other hand, the simplicity of direct-conversion architecture makes it a suitable choice for the current multi-mode wireless systems, but sets higher requirements on the dynamic range. Realization of channel selection at RF can break this tradeoff and offer the necessary frequency selection without the need for several off-chip filters [23].

The receiver antenna picks up a very colorful spectrum and the receiver chain should be able to detect and demodulate the desired RF signal among these other unwanted signals, as shown in Figure 1.6. The desired RF signal is usually much weaker than the other interferers, since the base station is often far from the receiver, while other wireless systems close by might create the interfering signals. The difference between the power level of the desired signal and the strongest interferer roughly determines the system dynamic range and as the required dynamic range increases, so does the receiver power consumption. In other words, the strongest unwanted signal determines the system dynamic range and required system linearity, which directly translates to
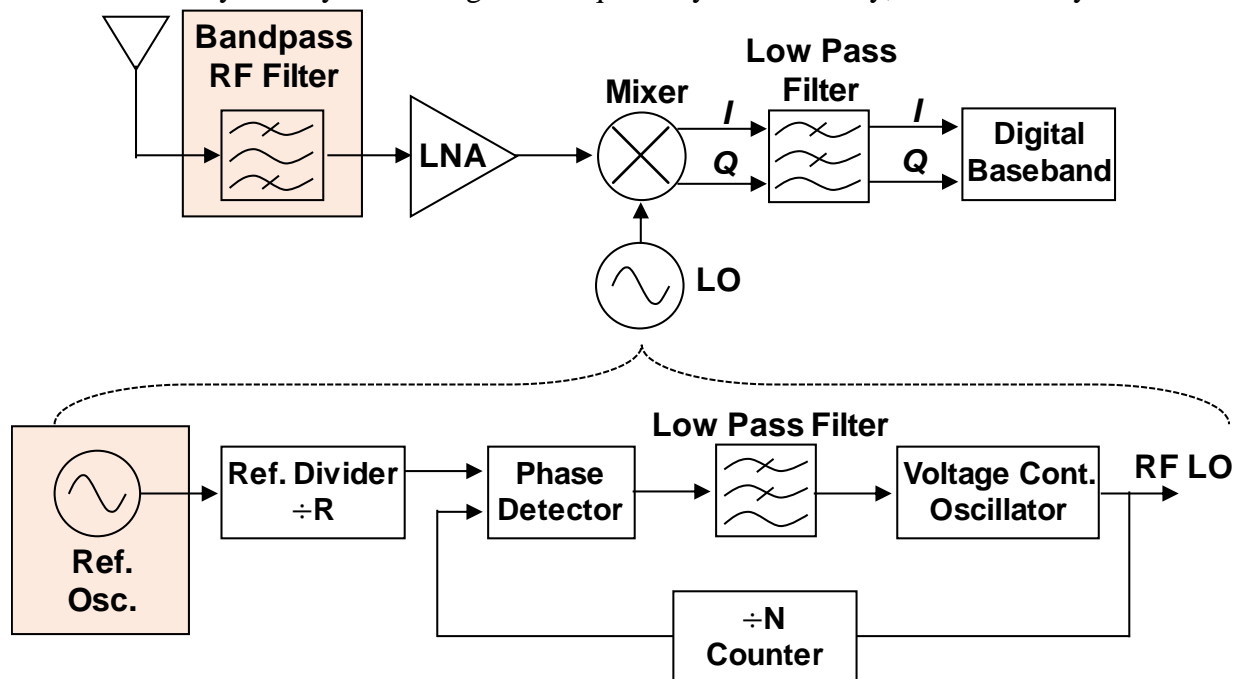
Figure 1.5: Schematic description of a conventional direct-conversion receiver diagram. The highlighted elements indicate off-chip components that pose a bottleneck for miniaturization.

the system power consumption. Therefore, elimination of strong interfering signals lowers the dynamic range requirements and power consumptions. While the conventional band-select architecture of Figure 1.6 helps the power consumption reduction, the proposed RF channel-selection receiver of Figure 1.6 offers the ultimate power reduction by rejecting all unwanted signals and removing the burden of the dynamic range from the following stages.

Realization of channel selection at RF cleans out the input RF signal and hence, the receiver chain does not have to deal with any interfering signal. This considerably reduce the requirements on the linearity of the following integrated circuits and enables significant power reduction. The proposed channel-select architecture of Figure 1.6 employs the abundance of high-Q micromechanical circuits to realize RF channel selection [23] and stable LO synthesizer [24], as shown in Figure 1.7. This architecture takes advantages of low-cost surface and bulk micromachine processes [25] to realize the filter bank at the RF front-end, without the drawbacks of conventional bulky filters.

1.3 BASICS OF THE MICROMECHANICAL FILTER DESIGN

Figure 1.8 presents the frequency response of a typical bandpass filters and highlights the important filter specifications [26]. Group delay, defined as the derivative of the phase response, is a measure of time delay for different frequency component of the incoming signal and it should be flat for an ideal filter. The group delay is inversely proportional to the filter bandwidth and its fluctuations depend on the filter type and order [27]. A bandpass filter should provide sufficient rejection outside the determined frequency range, i.e. large stopband rejection, with minimum
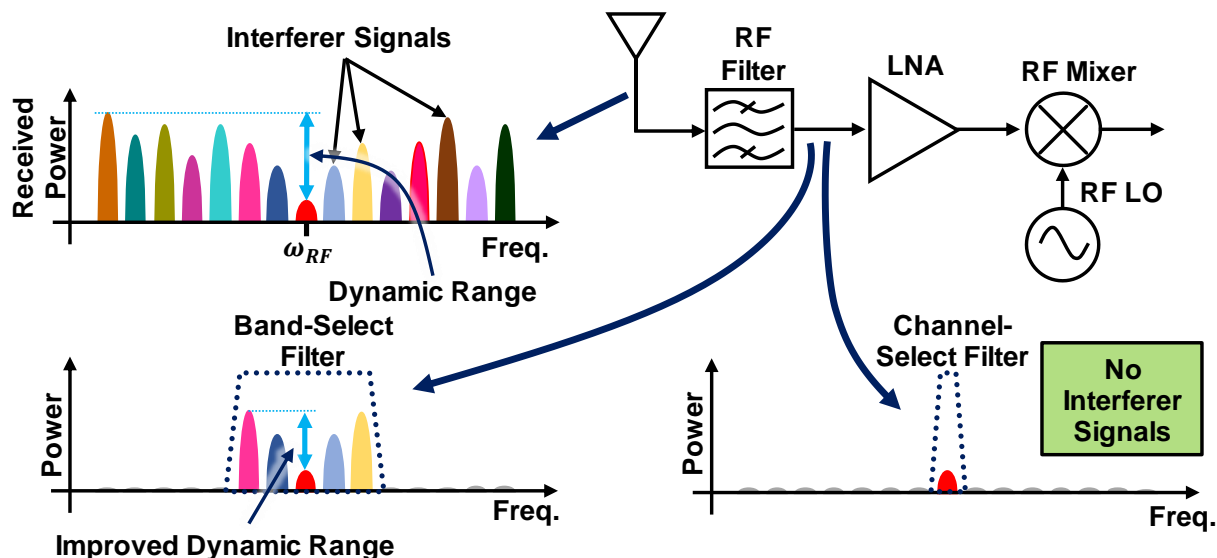
Figure 1.6: The antenna picks up a very colorful spectrum and strong interferers poses very high requirements on the receiver dynamic range. A conventional band-select filter reduced the dynamic range requirements, while the proposed channel-select filter relaxes the dynamic range requirements by rejecting all unwanted signals.

8

attenuation over the passband, i.e. small insertion loss. Different attenuation and group delay over the passband distort the transmitted symbol and introduce error during the demodulation [13] and hence, the in-band ripple and group delay should be as small as possible. Fast passband-to-stopband roll-off ensures sufficient rejection at adjacent channels and enables efficient spectrum utilization.

Micromechanical resonators, either capacitive or piezoelectric, are the only choice capable of providing high quality factor required by channel selection. There are different topologies to harness this high-Q for channel-select filter realization [28] [29]. This work employs mechanically-coupled cascaded capacitive resonators, as shown in Figure 1.9, to form a mechanical circuit and achieve the desired frequency selection. The constituent high-Q capacitive resonators of Figure 1.9 provide the fundamental resonating elements at the filter center frequency that effectively reject out-of-band signals. The mechanical design of coupling beams makes the essential filter bandwidth by distributing resonator center frequencies over the passband (*c.f.* Chapter 3). The termination resistors R_Q at the filter input and output load the quality factor of the resonators in order to flatten the jagged passband and minimize the in-band ripple [26]. The filter performance heavily depends on the constituent resonator characterizations and hence, the following sections briefly describes the basic resonator requirements to meet the design goals described earlier.
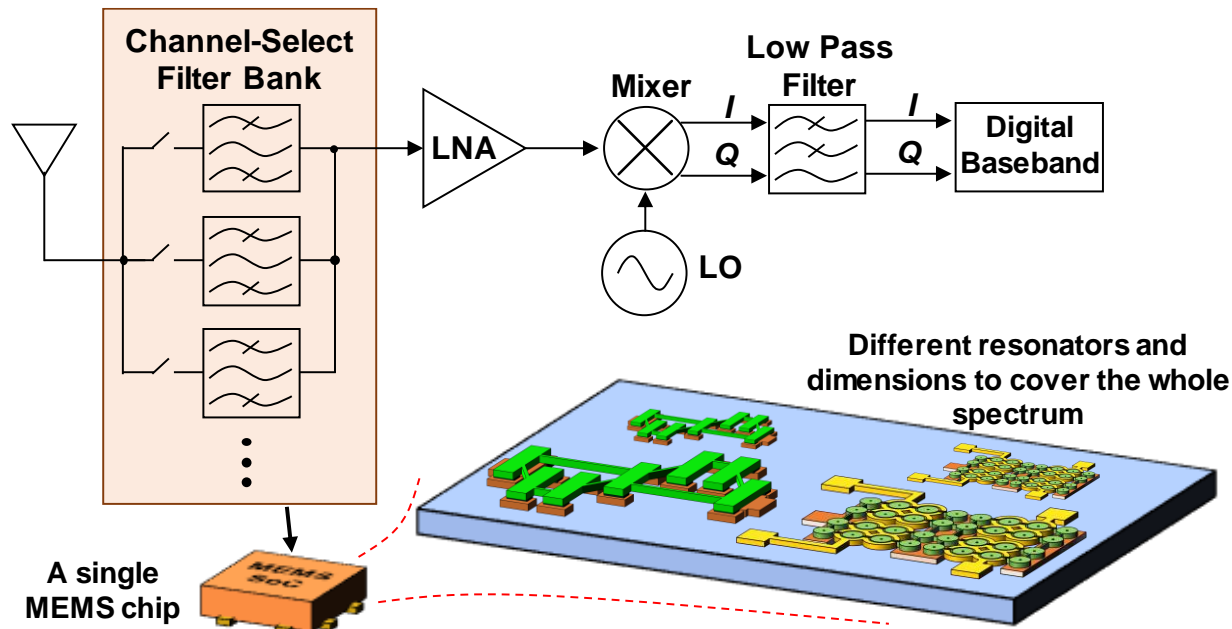
Figure 1.7: The proposed channel-select filter bank offers the advantages of channel-selection at RF, interfacing to only one single MEMS chip. Sine CAD design determines the frequency characteristics of the capacitive resonators, a simple micromachining process is sufficient for realization of channel-select filters at different frequencies.

1.3.1   RESONATOR QUALITY FACTOR

The filter insertion loss is primarily determined by the quality factor ratio between the unloaded resonator Q_o and the filter Q_f, as given by the equation 1.4, explained in more details in Chapter 3. Here, the filter quality factor is the inverse of the filter fractional bandwidth presented in equation 1.5. This equation suggests that to minimize the insertion loss, the resonator unloaded quality factor should be much higher than the filter quality factor. Therefore, realization of channel-select filter at the front-ends, i.e. very large Q_f, requires constituent resonators with much higher quality factor, compared to a band-select filter.
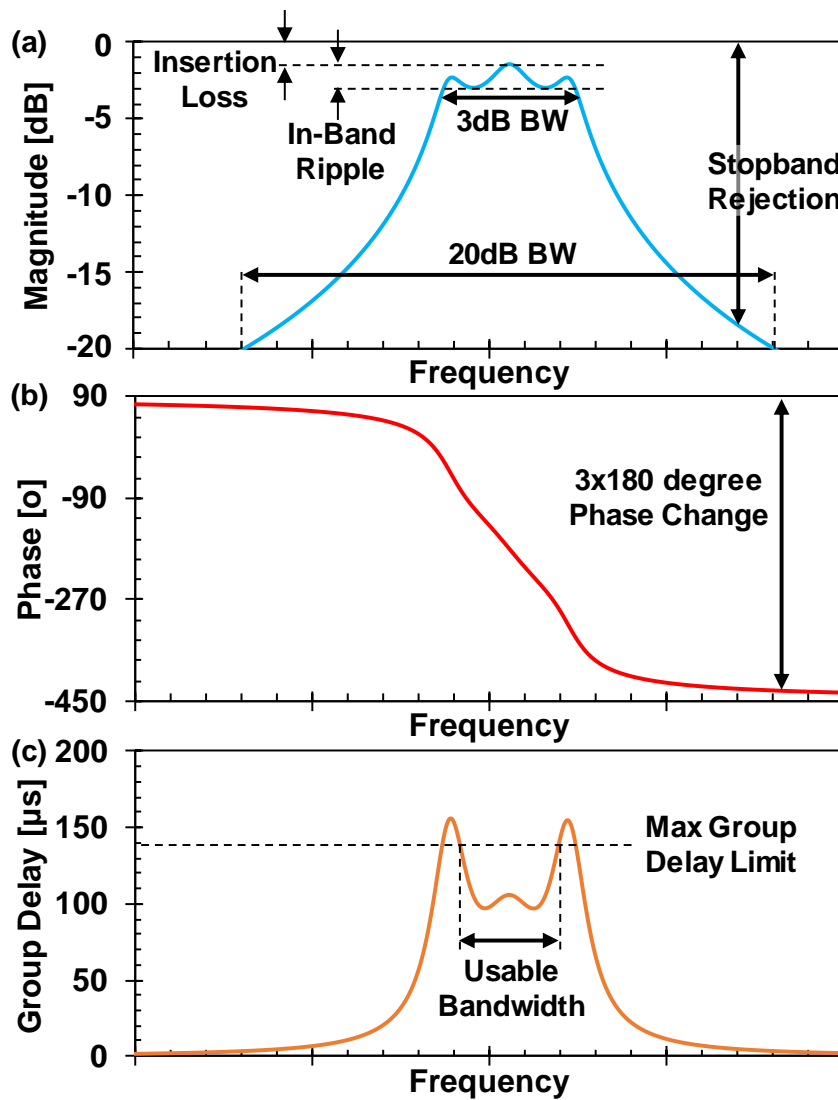
Figure 1.8: (a) Schematic description of (a) transmission amplitude, (b) phase, and (c) group delay response metrics used to specify a bandpass filter.

$$I.L. \propto \frac{Q_f}{Q_o} \tag{1.4}$$

$$Q_f = \frac{1}{PBW} = \frac{f_o}{BW_{3dB}} \tag{1.5}$$

Figure 1.10 presents the importance of the resonator Q for channel selection. The simulated wide-bandwidth band-select filter only requires quality factor of 1,000 to achieve insertion loss smaller than 1dB, while the narrow channel-select filter demands quality factor of more than 30,000.

1.3.2   RESONATOR ELECTROMECHANICAL COUPLING

The resonator electromechanical coupling (C_x/C_o), where the C_x is the resonator motional capacitance and C_o is the transducer static capacitance given in Figure 1.9, provides a powerful tool to gauge the resonator performance and determine the maximum filter bandwidth it can
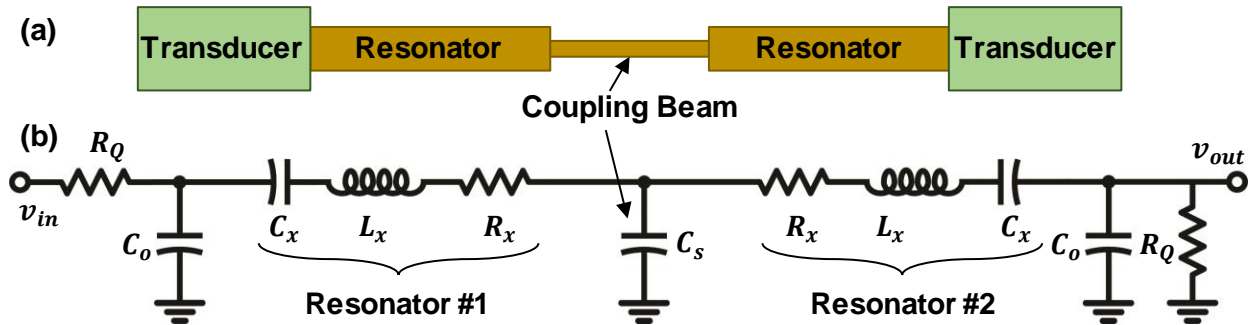
Figure 1.9: (a) Schematic description of general implementation topology of a band-pass filter consisting of a chain of discrete resonator tanks linked with coupling elements. (b) Electrical equivalent circuit representation of the generic filter.
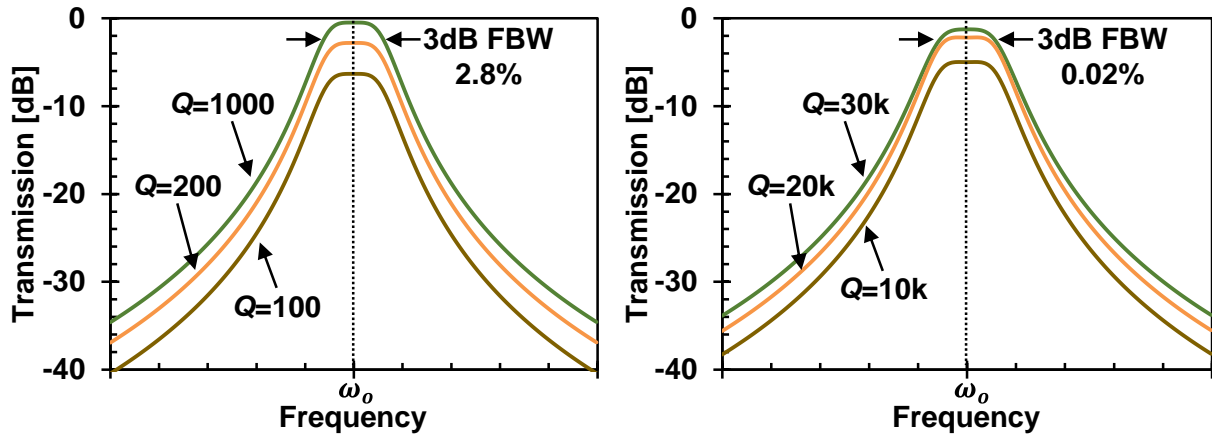
Figure 1.10: Simulated frequency spectrum for a 3rd order filter with (a) 2.8% bandwidth for a wideband band-select application, and (b) 0.02% bandwidth for a narrow band channel-select application for varying resonator tank Q's.

11

support without introduction of any distortion in the passband (*c.f.* Chapter 3). To realize a filter with flat passband and small in-band distortion, the constituent resonator (C_x/C_o) should be larger than the filter fractional bandwidth PBW, given in equation 1.5.

Figure 1.11 illustrates the effect of resonator (C_x/C_o) on the filter passband, where weak electromechanical coupling prevents ideal termination of the filter and introduces unacceptable distortion in the filter response. Narrow channel-select filters with fractional bandwidth of 0.1% or smaller does not demand very high (C_x/C_o), however, a filter bank comprises of several channel-select filters in parallel, as proposed in Figure 1.7, requires strong electromechanical coupling for proper termination of each filter [23].

1.3.3 RESONATOR IMPEDANCE

Although the resonator quality factor Q and electromechanical coupling (C_x/C_o) are primarily set by the resonator technology, the resonator impedance X_o given in equation 1.6 is a design parameter and is determined by the resonator area A_o. Here, ω_o, ε and d_o are filter center frequency, permittivity and the gap spacing, respectively. The resonator impedance and therefore, the resonator area are the design parameters to achieve the desired termination resistance R_Q, as given by equation 1.7 (*c.f.* Chapter 3). The communication standard sets the desired termination resistance R_Q and filter quality factor Q_f and the resonator electromechanical coupling (C_x/C_o) is determined primarily by the resonator technology.

$$X_o = \frac{1}{\omega_o C_o} = \frac{d_o}{\omega_o \varepsilon} \cdot \frac{1}{A_o} \tag{1.6}$$

$$R_Q = \left(\frac{Q_o}{Q_f} - 1\right) R_x \cong \frac{1}{Q_f} \cdot \frac{1}{\left(\frac{C_x}{C_o}\right)} \cdot \frac{1}{X_o} \tag{1.7}$$
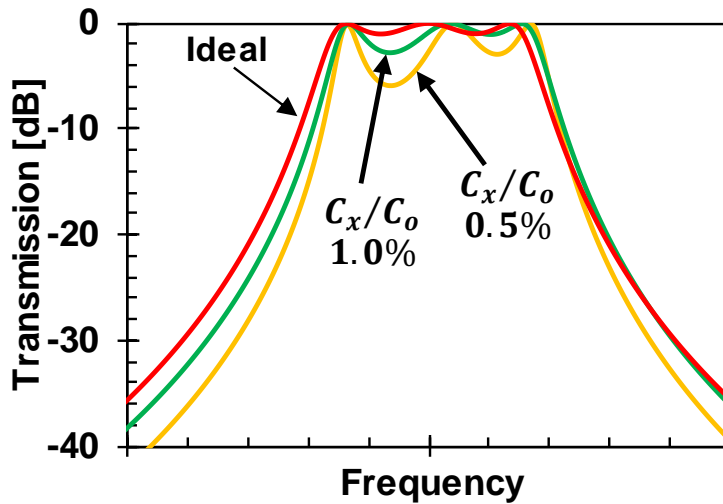
Figure 1.11: Simulated frequency response of a three-resonator RF channel-select filter with 1% fractional bandwidth for different resonator electromechanical coupling (C_x/C_o).

12

1.4 REVIEW OF RF CHANNEL-SELECT FILTERS

Equipped by the potential benefits of an RF channel-select receiver, numerous researchers have tried to realize RF channel selection to improve the system robustness and reliability and reduce the power consumptions [30]. These studies employ various resonator technologies such as capacitive [31] [32], piezoelectric [33] [34] [35] [36] and internal dielectric [37] [38]. To fully exploit the advantages of channel selection, the proposed resonator technology should provide different advantages, such as:

i) High quality factor: Q's of 10,000 or more is necessary for the filter realization with small insertion loss.
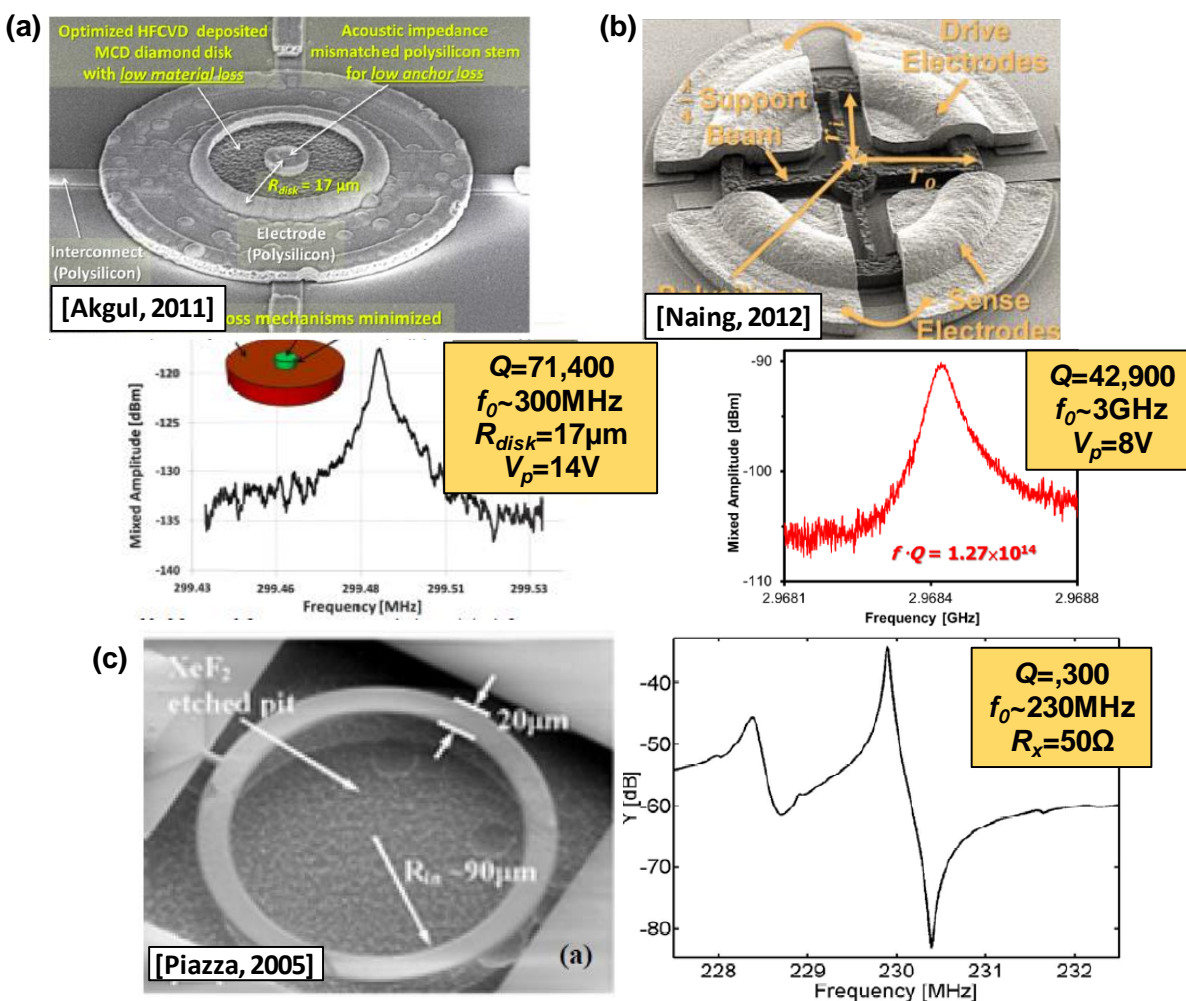
Figure 1.12: Previous works on capacitive transduced vibrating disks (a) and rings (b) exemplifies the high-Q of capacitive resonators at 300MHz and 3GHz respectively. (c) Piezoelectric vibrating rings offer strong coupling and small motional resistance, but with low Q.

ii) Strong electromechanical coupling: Resonator (C_x/C_o) much larger than the filter fractional bandwidth ensures perfect termination and distortion-free passband. Furthermore, strong coupling provides higher stopband rejection.

iii) Small footprint and CAD-amenable design: The application of channel selection at the RF demands realization of filter banks at the front-end to ensure full coverage of the spectrum. As a result, each filter should occupy small area and CAD design specifies the filter performance, especially the center frequency, to attain many different frequencies on a single chip with no need for complicated fabrication processes [39].

iv) Nonlinearity: The channel selection relaxes the nonlinearity requirements on the following stages, consequently, the filter nonlinear performance becomes the dominant factor in the overall system nonlinearity.

Figure 1.12 compares the performance of capacitive and piezoelectric resonators designed for channel-selection application. The capacitive ring resonator [40] and disk resonator [41] provide the high quality factor required by the channel selection at UHF and VHF. Capacitive resonator quality factor exceeds 150,000 at 60MHz [42] and reaches more than 50,000 at 3GHz [40]. Such high Q necessary for the low-IL filter is only offered by capacitive transduction. However, these capacitive resonators fall short in provision of very strong electromechanical coupling, contrary to the theoretical predictions. Application of high-k materials in the gap spacing
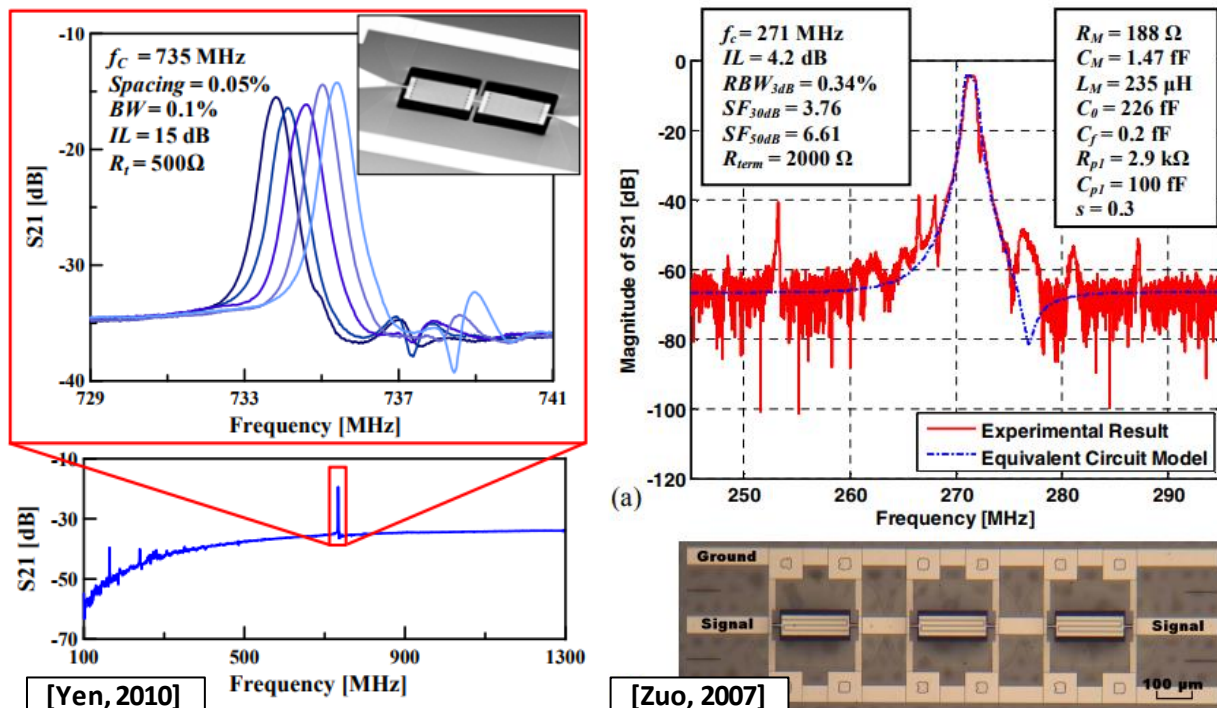
Figure 1.13: Previous vibrating channel-select filter work using piezoelectric actuation.

14

[43] [44]enhances the resonator (C_x/C_o), but this work will demonstrate the true power of sub-20nm gap spacing to provide sufficient electromechanical coupling.

In comparison, the piezoelectric resonators offer strong coupling on the order of 1-10% [45], but often suffer from quality factor smaller than 3,000. On the other hand, piezoelectric transduction does not offer sufficient tuning range, which is very important for the realization of narrow filters (*c.f.* Chapter 3). However, piezo actuation easily grants wide-band filters, where *Q*'s of only 500 to 1,000 is enough for realization of low-IL filters [14] [46]. Figure 1.13 presents two channel-select filters at 270MHz [33] and 735MHz [34] realized by piezoelectric resonators. As expected from the theory, these filters have unacceptably-high insertion loss due to the limitation of the piezoelectric resonator quality factor.

The capacitive micromechanical filters of Figure 1.14 at 163MHz [47] and 223MHz [48] achieve channel-selective bandwidth of 0.06% and 0.09%, respectively, with small insertion loss of 2.7dB. Such a small insertion loss is the direct consequence of application of high-*Q* capacitive resonators as the building block of these mechanical circuits. This work expands on the achievements of these capacitive channel-select filters to improve the filter roll-off by manipulating the transfer function loss poles through unconventional bridging scheme [47] [49].
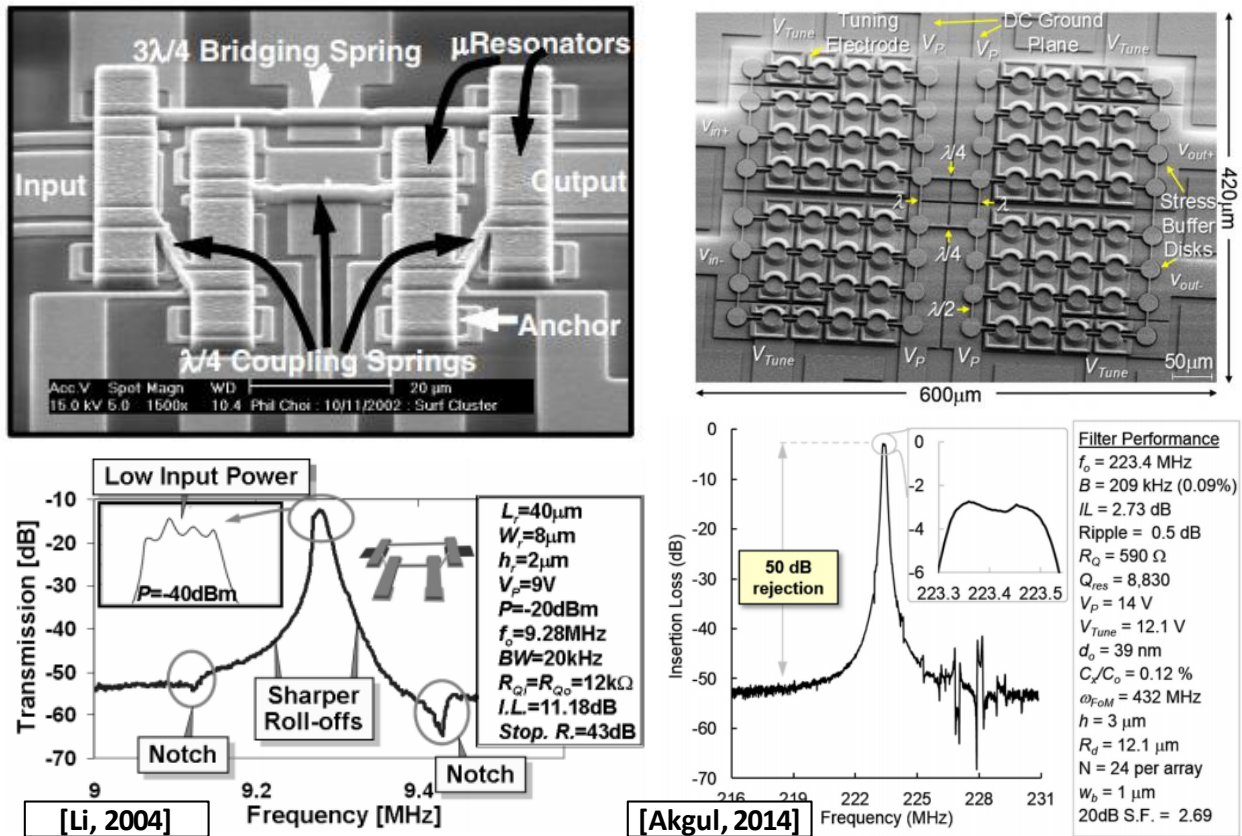
Figure 1.14: Previous work on capacitive actuated vibrating disk channel-select filters.

1.5 DISSERTATION OVERVIEW

This work focuses on channel-select filters at HF (3-30MHz) and attempts to improve the filter performance by strategic mechanical bridging between non-adjacent resonators. To do so, Chapter 2 introduces the high-Q micromechanical clamped-clamped beam (CC-beam) resonators that form the building block of such a filter. This chapter provides basics of the micromechanical resonators and capacitive transduction and then specializes the developed theory for the CC-beam resonators. The CC-beam resonators presented in this chapter offer quality factor of 15,100 and electromechanical coupling of more than 10%, all necessary for the successful demonstration of channel-select filters.

Chapter 3 employs these CC-beam resonators in a mechanical circuit to shape the desired transfer function. This chapter illustrates the formation of the transfer function poles by proper design of mechanical coupling beams and derives all the necessary expressions to investigate the effects of the resonator specifications on the filter performance.

Since the mechanical coupling beams play a vital role in the micromechanical filter design, Chapter 4 investigates the mechanical design of narrow coupling beams, for both extensional and flexural modes. This chapter provides new formulation for the mechanically coupled resonators and further expands our understandings on the coupling beam behaviors.

Equipped by the filter design procedure of Chapter 3 and the coupling beam characteristics of Chapter 4, Chapter 5 exploits strategic bridging between non-adjacent resonators to insert and manipulate loss poles in the filter transfer function and improve the filter passband-to-stopband roll-off. The third- and fourth-order micromechanical filters presented in this chapter deliver small percent bandwidth of 0.1% to 0.3% with insertion loss of only 1dB. These filters have very sharp roll-off characterized by 20dB shape factor of 1.84.

Chapter 6 investigates the nonlinearity sources in the capacitive transducers and offer insightful expressions on the micromechanical resonator and filter nonlinearity. These expressions suggest capacitive transducers should be able to provide sufficient nonlinear performances, required by the today's communication systems. The measured nonlinear performances of the filters presented in Chapter 5 confirm the findings of the developed theory.

To fully exploit the strong electromechanical coupling of CC-beam resonators, Chapter 7 demonstrates a seventh-order bridged micromechanical filter with remarkable roll-off marked by 20dB shape factor as small as 1.45, which is the best 20dB shape factor reported so far for any channel-select filter.

Lastly, Chapter 8 demonstrates a capacitive transducer with only 13.2nm of gap spacing between the structure and the electrode. Such a small gap spacing provides strong electromechanical coupling (C_x/C_o) of 1.6%, that enables the realization of high-order micromechanical filters at higher frequency.

Chapter 2 MICROMECHANICAL RESONATORS

This chapter presents the fundamental operation and basic equations governing clamped-clamped beam (CC-beam) resonators. A high-quality micromechanical resonator, like the CC-beam used in this work, is the building block of selective high-rejection micromechanical filters. These resonators [50] outperform other competing technologies such as LC-tanks [51], bulk acoustic wave (BAW) resonators [52], and surface acoustic wave (SAW) resonators [53] in terms of quality factor and hence, can provide the extreme selectivity required by channel-select filters, while introducing very small insertion loss. Since the velocity of acoustic waves are orders of magnitude smaller than the velocity of electromagnetic waves, and therefore, the acoustic wavelength is much larger for a given frequency, lumped element model is still a valid approximation to model the behavior of these resonators. This chapter presents the lumped element model for the main mode shape of the CC-beams and defines the effective stiffness, effective mass, electromechanical coupling, motional resistance, etc.

2.1 LUMPED ELEMENT MODEL

A single degree of freedom (SDF) mass-spring-damper system can model the mechanical vibration and capture the important frequency behavior of a micromechanical resonator without any need to use distributed model, since the acoustic waves has much larger wavelength than electromagnetic waves, for a given frequency [54]. Figure 2.1 shows two micromechanical resonators with their approximate dimension, the 40μm-long CC-beam has center frequency around 10MHz [55] and the contour-mode disk resonator with radius of 2.6μm has been used in 1GHz application [56]. The simple lumped element model of Figure 2.1 (c) can model both resonators and predict their behavior with excellent accuracy. The sinusoidal force *F(t)* acting on the lumped mass *m* induces mechanical motion in the SDF system, described by equation 2.1 [54]:

$$m_r \frac{d^2 x(t)}{dt^2} + b_r \frac{dx(t)}{dt} + k_r x(t) = F e^{j\omega t} \tag{2.1}$$

where ω is the angular frequency. This equation can be simplified to equation 2.2 in the steady state with the general solution given in equation 2.3:

$$-m_r \omega^2 X + b_r j\omega X + k_r X = F \tag{2.2}$$

$$X = \frac{F}{k_r - m_r \omega^2 + b_r j\omega} \tag{2.3}$$

where *X* and *F* are the phasors of mechanical motion and applied force, respectively.

Figure 2.1 (d) shows the magnitude and phase response of a general SDF system. The SDF response has a pole at natural resonance frequency ω_{nom}, defined in equation 2.4, and the resonator displacement at this frequency is Q times the displacement at zero frequency, as quality factor Q defined in the equation 2.5. Quality factor Q is a merit of energy dissipated in the resonator in one cycle relative to the stored energy in the system and determines the 3dB bandwidth of the resonator. Hence, the resonator response can be rearranged into the general form given in the equation 2.6.

$$\omega_{nom} = \sqrt{\frac{k_r}{m_r}} \tag{2.4}$$

$$Q = \frac{k_r}{b_r \omega_o} = \frac{m_r \omega_o}{b_r} = \frac{\sqrt{k_r m_r}}{b_r} \tag{2.5}$$

$$X = \frac{F}{k_r} \cdot \frac{1}{1 - \left(\frac{\omega}{\omega_o}\right)^2 + \frac{j}{Q}\left(\frac{\omega}{\omega_o}\right)}$$

$$|X| = \frac{F}{k_r} \cdot \frac{1}{\sqrt{\left(1 - \left(\frac{\omega}{\omega_o}\right)^2\right)^2 + \left(\frac{\omega}{Q\omega_o}\right)^2}} \tag{2.6}$$

$$\angle X = -\arctan\left(\frac{\frac{\omega}{Q\omega_o}}{1 - \left(\frac{\omega}{\omega_o}\right)^2}\right)$$

The frequency response of the mechanical SDF system, given in the equation 2.3 and 2.6, bears a resemblance to the electrical response of a series RLC tank circuit (Figure 2.1) as given in equation 2.7. The equivalency process described in equation 2.8 models a mass-spring-damper system as a series RLC tank circuit to harness the powerful computing and optimization capabilities developed for electrical circuits [57].

$$i_x = \frac{v_x}{j\omega l_x + r_x + \frac{1}{j\omega c_x}} = j\omega c_x v_x \cdot \frac{1}{1 - \left(\frac{\omega}{\omega_o}\right)^2 + \frac{j}{Q}\left(\frac{\omega}{\omega_o}\right)} \tag{2.7}$$

$$
\begin{aligned}
velocity &\leftrightarrow current & j\omega X &\leftrightarrow i_x \\
force &\leftrightarrow voltage & F &\leftrightarrow v_x \\
mass &\leftrightarrow indcutance & m_r &\leftrightarrow l_x \\
stiffness &\leftrightarrow \frac{1}{capacitance} & k_r &\leftrightarrow \frac{1}{c_x} \\
dampness &\leftrightarrow resistance & b_r &\leftrightarrow r_x
\end{aligned} \tag{2.8}
$$

To convert incoming RF power to mechanical force applied to the resonator, various electromechanical transduction techniques, such as capacitive [58], piezo-electric [59], piezo-resistive [60], thermal [61], etc., can be used. Since capacitive transduction, simplified in Figure 2.2, is the only technique that can provide quality factor in the order of 10,000 or more required by channel-select filter, this work employs gap-closing capacitive micromechanical resonators to develop frequency-selective filters.

The applied voltage to the capacitive transducer of Figure 2.2 induces electric field between the two parallel plates and the change in the stored energy in the electric field determines the applied forces on both plates, as given by equation 2.9. The applied force makes the suspended plate of the gap-closing transducer of Figure 2.2 move from the stationary position and changes the gap spacing between the two parallel plates. Neglecting the fringe capacitance, equations 2.10 and 2.11 provide the expressions for the change in the capacitance and the applied force in a gap-closing transducer with electrode area A and stationary gap spacing of d_o, respectively [57].

$$F(t) = \frac{1}{2}\Delta V^2 \frac{dC}{dx} = \frac{1}{2}(V_P + v_x \cos(\omega t))^2 \frac{dC}{dx} \qquad (2.9)$$
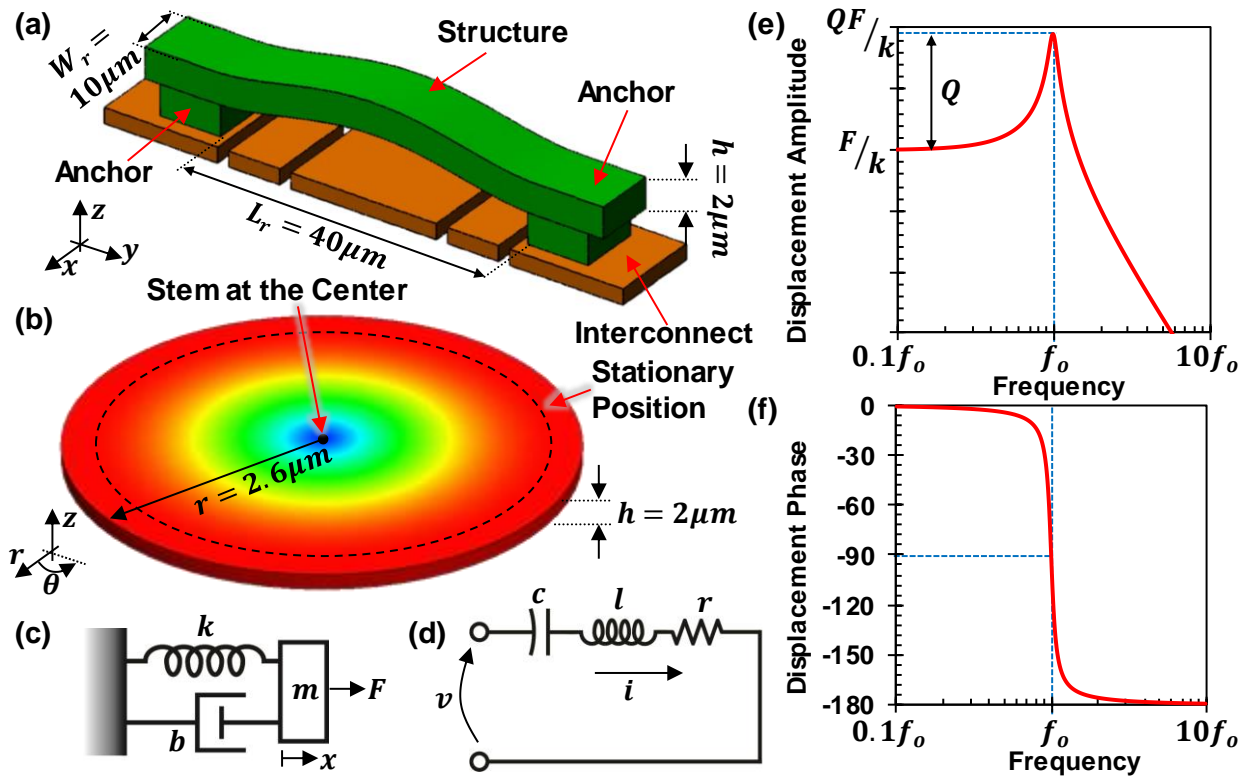
Figure 2.1: (a) Illustration of a clamped-clamped beam resonator centered at 10MHz and (b) a contour-mode disk resonator designed at 1GHz, with nominal dimension. Both resonators can be modeled by (c) lumped mechanical or (d) lumped electrical elements. The displacement of the micromechanical resonators of (a) and (b) follows the biquad transfer function of (2.6) shown in plots (e) and (f).

$$\frac{dC}{dx} = \frac{d}{dx}\left(\frac{\varepsilon A}{d_o - x}\right) = \frac{\varepsilon A}{(d_o - x)^2} = \frac{\varepsilon A}{d_o^2}\frac{1}{\left(1 - \frac{x}{d_o}\right)^2} \cong \frac{\varepsilon A}{d_o^2}\left(1 + 2\frac{x}{d_o} + 3\left(\frac{x}{d_o}\right)^2 + \cdots\right) \quad (2.10)$$

$$F(t) \cong \frac{1}{2}(V_P^2 + 2V_P v_x \cos(\omega t) + v_x^2 \cos^2(\omega t))\frac{\varepsilon A}{d_o^2}\left(1 + 2\frac{x}{d_o} + 3\left(\frac{x}{d_o}\right)^2 + \cdots\right)$$

$$F(t) \cong \frac{1}{2}V_P^2\frac{\varepsilon A}{d_o^2} + \left(V_P\frac{\varepsilon A}{d_o^2}\right)v_x \cos(\omega t) + V_P^2\frac{\varepsilon A}{d_o^3}x + \cdots \quad (2.11)$$

The first two terms of equation 2.11 are the constant and main sinusoidal mechanical force on the plates and determine the average and time-varying change in the gap spacing, respectively. The third term in the force expression depends on the displacement and follows hook's law. Hence, it will act as a spring force in the equation 2.2 and is known as electrical stiffness. Since this term subtracts from the resonator stiffness, it softens the system and lowers the resonance frequency, as suggested by the equations 2.13. The higher order terms contribute to the nonlinearity of the transducers and we will investigate their effect on device performance in Chapter 5.

$$k_e = V_P^2\frac{\varepsilon A}{d_o^3} \quad (2.12)$$

$$\omega_o = \sqrt{\frac{k}{m_r}} = \sqrt{\frac{k_r - k_e}{m_r}} = \omega_{nom}\sqrt{1 - \frac{k_e}{k_r}} \cong \omega_{nom}\left(1 - \frac{1}{2}\cdot\frac{k_e}{k_r}\right) \quad (2.13)$$

The change in the stored charge in the capacitor determines the input current into the transducer, as in equation 2.14. Equation 2.14 reduces to equation 2.15 in the steady state, which demonstrates that the input current i_{in} includes two terms: the first term i_{co} models the current of a static capacitor and the second term i_x depends on the velocity of the resonator.
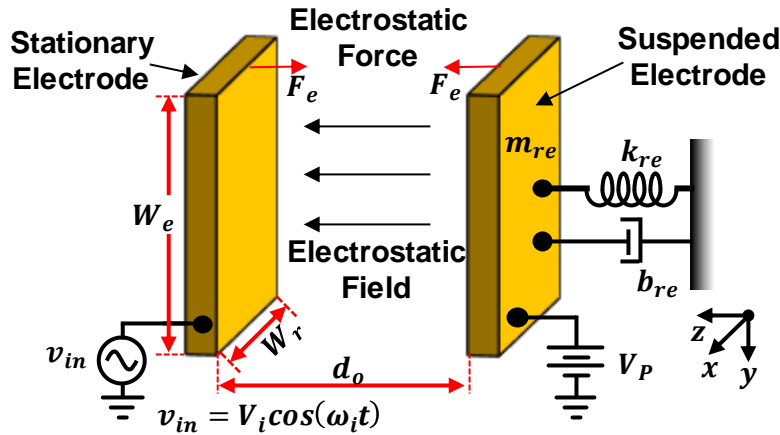
Figure 2.2: (a) Illustration of a parallel-plate capacitive transducer. The application of voltage bias source VP and time-varying voltage vin makes the suspended electrode vibrate around its stationary position by inducing time-varying electrostatic field.

$$i_{in}(t) = \frac{dQ}{dt} = \frac{d(C\,\Delta V)}{dt} = C\frac{d\Delta V}{dt} + \Delta V\frac{dC}{dt} = C\frac{d\Delta V}{dt} + \Delta V\frac{dC}{dx}\frac{dx}{dt} \tag{2.14}$$

$$i_{in} = j\omega C v_x + V_P \frac{dC}{dx} j\omega X \cong j\omega C v_x + \left(V_P \frac{\varepsilon A}{d_o^2}\right) j\omega X = i_{C_o} + i_x \tag{2.15}$$

Since the capacitive electromechanical transduction is a lossless process (the dielectric loss is negligible), an equivalent ideal transformer suits as the equivalent small signal electrical lumped model, as suggested by equation 2.16 and shown in the Figure 2.3. In this figure, the static capacitor C_o models the i_{Co} and the transformer forms the capacitive transducer equivalent model. The transformer ratio η_e, defined in equation 2.16, converts the small signal voltage to applied mechanical force.

$$\begin{bmatrix} F \\ j\omega X \end{bmatrix} = \begin{bmatrix} \eta_e & 0 \\ 0 & \dfrac{1}{\eta_e} \end{bmatrix} \begin{bmatrix} v_x \\ i_x \end{bmatrix}, \qquad \eta_e = V_P \frac{\varepsilon A}{d_o^2} \tag{2.16}$$

The total resonator stiffness determines the value of the equivalent capacitor $c_x = 1/(k_r - k_e)$ in the Figure 2.3 which can be decomposed into two capacitors in series $c_x = 1/k_r$ and $c_e = -1/k_e$, as shown in Figure 2.3. Here, c_x models the resonator mechanical stiffness and c_e predicts the change in the frequency by electrical stiffness. Further investigation of c_e, as shown in equation 2.17, suggests that moving the c_e to the other side of the transformer and replacing it with a series capacitor with negative capacitance value equal to the static capacitance of the transducer C_o simplifies this model, as shown in Figure 2.3 (c) [62].

$$c_e = \frac{-1}{k_e} = -\frac{d_o^3}{\varepsilon A V_P^2} = -\frac{\varepsilon A}{d_o}\left(\frac{d_o^2}{\varepsilon A\,V_P}\right)^2 = \frac{-C_o}{\eta_e^2} \tag{2.17}$$

The gap closing transducer has a very nonlinear characteristic, as suggested in equations 2.9-2.11. Applied voltage exerts mechanical force on the suspended electrode and makes it move closer to the other electrode. This decrease in the gap spacing increases dC/dx and boosts the applied force even further and reduces the gap more. The spring force can counter this positive feedback between applied force and the gap spacing and makes the gap to reach a steady state position, if the suspended electrode does not pass one third of initial gap spacing [57]. The voltage corresponding to this displacement is called pull-in voltage and applying any voltage larger than
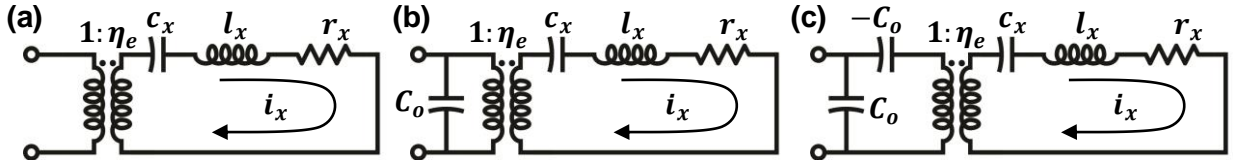
Figure 2.3: The development of electrical equivalent circuit: (a) the transformer models the transduction between input voltage and applied mechanical force, (b) Co represents the transducer intrinsic capacitance at the input, and (c) the negative capacitance at the input models the electrical stiffness and the change in the resonance frequency by bias voltage.

that makes the positive feedback strong enough, so that the suspended electrode catastrophically collapses to the other electrode. In other word, the electrical stiffness at pull-in voltage is equal to the mechanical stiffness and the system does not have any restoring force and is completely unstable. Equation 2.18 provides the expression for the pull-in voltage of a parallel plate capacitive transducer:

$$V_{pull-in} = \sqrt{\frac{8}{27} \cdot \frac{k_r d_o^3}{\varepsilon A}}$$

(2.18)

Figure 2.4 presents the final electrical equivalent circuit of any micromechanical resonator. The series RLC components form the familiar equivalent circuit used for Quartz [63] or Piezo [64] resonators, if transferred to the left side of the transformer. Equation 2.19 provides the expressions for the lumped elements L_x, C_x, C_o, and R_x. Figure 2.4 (b) shows the magnitude and phase of the input admittance of the derived model. The admittance has maximum where the series branch (including L_x, C_x and R_x) is in resonance and hence, called the series resonance frequency. When the parallel resonant tank (including L_x, C_x, C_o, R_x) is at resonance, the admittance reaches its minimum. In other word, the motional current from the resonator and the electrical current from the static capacitor are equal in magnitude and completely out of phase, therefore the output current is minimum and impedance is at maximum. The separation of series and parallel resonance frequencies, f_s and f_p, is a very important filter design parameter and determines the maximum resonator tunability and maximum achievable filter bandwidth. The analytical solution of f_s and f_p shows that the ratio (C_x/C_o), called electromechanical coupling strength, determines the separation between f_s and f_p. Here C_x and C_o are motional and static capacitance of the transducer, given by equations 2.8-2.16. The electromechanical coupling strength (C_x/C_o) represents the efficiency of
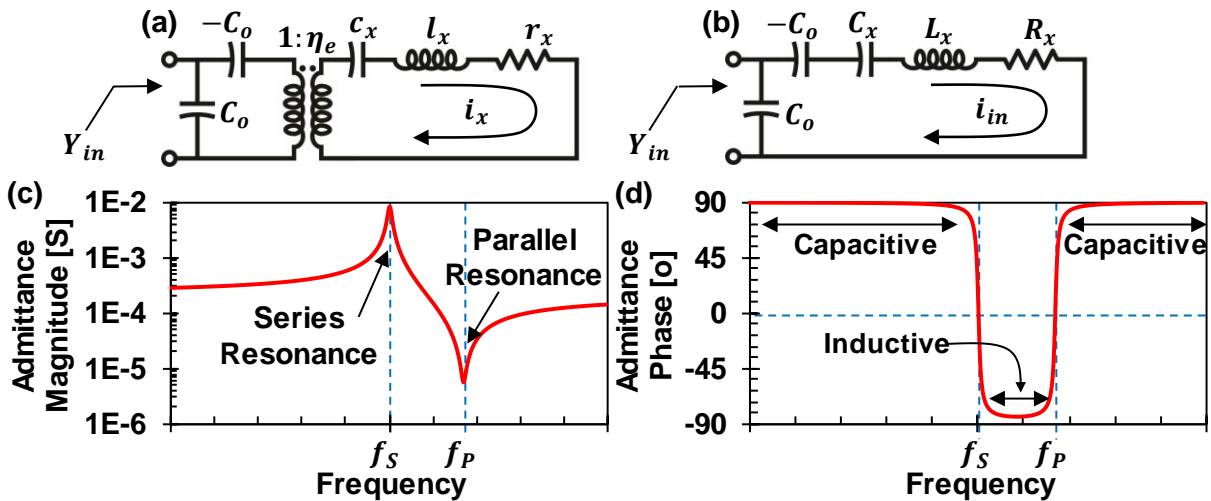
Figure 2.4: (a) Electrical equivalent circuit of a micromechanical resonator and (b) the equivalent circuit referred to the input. The input admittance of the micromechanical resonator shows the low-impedance series resonance and the high-impedance parallel resonance (c) with 180degrees of change in the phase (d). The resonator acts as an inductor between series and parallel resonances and a capacitor everywhere else.

22

energy conversion between electrical and mechanical domains. You might notice that the electromechanical coupling strength given in equation 2.20 is the same as the change in the resonance frequency of equation 2.13 due to electrical stiffness softening. In other word, transducer with stronger electromechanical coupling has larger tuning range, as suggested by 2.21.

$$L_x = \frac{l_x}{\eta_e^2} = m_r \frac{d_o^4}{(\varepsilon A V_P)^2} \qquad\qquad R_x = \frac{r_x}{\eta_e^2} = \frac{m_r \omega_o}{Q \eta_e^2} = \frac{m_r \omega_o}{Q} \frac{d_o^4}{(\varepsilon A V_P)^2}$$

$$C_x = c_x \eta_e^2 = \frac{1}{k_r} \frac{(\varepsilon A V_P)^2}{d_o^4} \qquad\qquad C_o = \frac{\varepsilon A}{d_o} \tag{2.19}$$

$$\frac{C_x}{C_o} = \frac{1}{k_r} \frac{\varepsilon A V_P^2}{d_o^3} \tag{2.20}$$

$$\omega_o = \omega_{nom} \sqrt{1 - \frac{k_e}{k_r}} = \omega_{nom} \sqrt{1 - \frac{C_x}{C_o}} \tag{2.21}$$

2.2 Clamped-Clamped Beam Resonators

Clamped-clamped beam (CC-beams) resonators [50] comprise of a long narrow beam anchored at both ends and suspended above the input electrode by gap spacing d_o, as shown in Figure 2.5. CC-beams were among the first resonators implemented in micro-size and used in frequency control and time-keeping applications, from kHz [50] [65] to 1GHz [66], as well as various sensors. This is indeed due to several exceptional characteristics of these resonators which made them attractive to the researchers across different fields:

- Simple processing: A simple three-mask surface micromachining process can realize CC-beams, as explained in the Section 2.3. This means low-cost fast-turnout process, invaluable to the fast-paced fields.
- Easy excitation: an electrode underneath the beam can efficiently excite the fundamental mode, without any need for complex electrode processing or choice of material.
- Spurious-free excitation: due to strong coupling of electric field to the fundamental mechanical mode, spurious modes do not get excited and wideband response is spurious free.
- High Q: CC-beams can provide high quality factor, in the order of 10,000 or more, up to VHF. Note that the CC-beam quality factor drops by frequency, as the anchor loss becomes dominant.
- Strong coupling: theoretically, CC-beams have strong electromechanical coupling strength on the order of 10%, up to VHF.
- Tunability: a set of separate electrodes underneath the CC-beam, as shown in Figure 2.5, can tune the resonance frequency of the resonator, with no need to change the

23

bias voltage V_P and therefore, no compromise in the main resonator parameters, such as C_x, R_x, etc.

- Low-velocity coupling: the mechanical coupling beams between CC-beams can be places anywhere along the beam length. Different joint location changes the effective stiffness and manipulates the system bandwidth (*c.f.* Chapter 3)

The application of fixed boundary condition at both ends into the Euler–Lagrange wave equation [54] determines the resonance frequency and results in the mode shape of equation 2.22 for the eigenvalue frequency of 2.23. Here, E and ρ are the Young modulus and the density of the material, respectively, and h and L_r are the thickness and length of the resonator, as shown in Figure 2.5. Note that the resonance frequency of a CC-beam does not depend on the width and this approximation is valid if the beam length is much larger than the width and the acoustic wave propagation is essentially a one-dimensional problem. The Figure 2.5 presents the analytical solution and the FEM simulation of the fundamental mode shape. The results of the previous section assumed that different parts of the resonator have the same displacement and velocity, however, this mode shape shows that the displacement of a CC-beam is a function of the location and therefore, we must modify those findings accordingly.

$$X_{mode}(y) = -1.01781\left\{\cos\left(4.73\frac{y}{Lr}\right) - \cosh\left(4.73\frac{y}{Lr}\right)\right\}$$
$$+ \left\{\sin\left(4.73\frac{y}{Lr}\right) - \sinh\left(4.73\frac{y}{Lr}\right)\right\} \tag{2.22}$$

$$f_{nom} = 1.03\sqrt{\frac{E}{\rho}} \cdot \frac{h}{L_r^2} \tag{2.23}$$
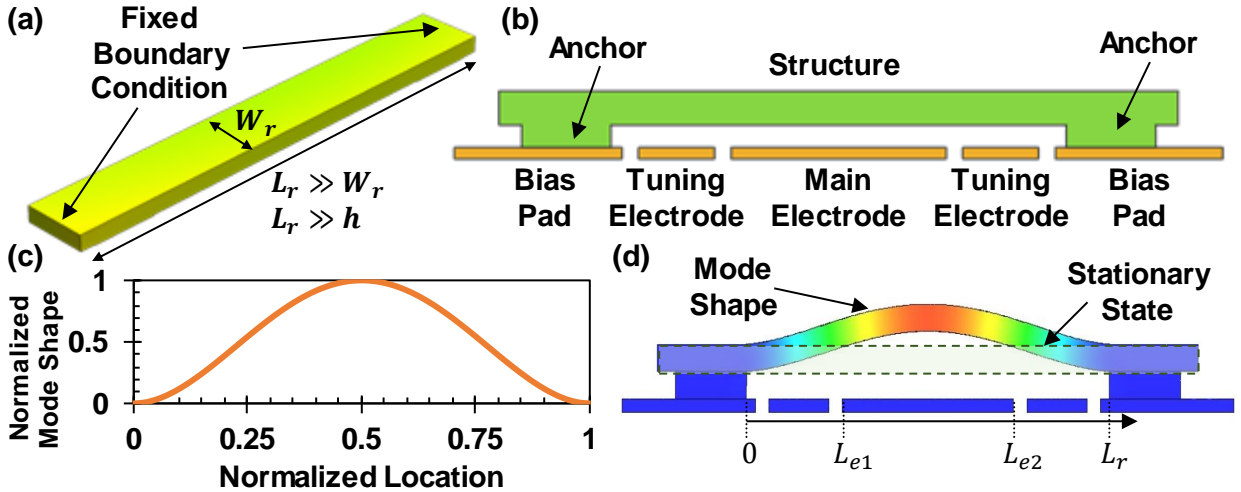
Figure 2.5: (a) An illustration of a general beam with fixed boundary condition on both ends and (b) a schematic of the CC-beam resonator of this work. The center electrode carries the main signal, while two small electrodes on both sides are used for fine tuning of the transfer function. (c) and (d) presents the CC-beam analytical mode shape and FEM simulation.

Although the resonator displacement and velocity are a function of location, the stored energy in the resonator is a universal parameter and should not depend on the location of interest. This argument suggest that also effective mass and effective stiffness of the resonator should be functions of the location to provide the constant stored energy in the resonator. The resonator velocity in the steady state is given in equation 2.24. The resonator total kinetic energy is the sum of kinetic energy in each infinitely-small differential volume of the resonator, as shown in equation 2.25. Since the CC-beam resonator is much longer than it is wide, the wave propagation is effectively a one-dimensional problem and the integration to find the total kinetic energy is only necessary in *y*-direction. For wide or thick resonators, the wave equation should be solved in 2D or 3D and the corresponding integration will be over a surface or volume, respectively. The effective mass models the resonator behavior in a given location and hence, it should predict the same amount of stored energy, independent of the point of interest. This argument suggests the expression of equation 2.26 for the resonator effective mass. This equation reduces to familiar expression $\rho W_r L_r h$ for a constant mode shape: the integration simply considers the contribution of the beam mass in different location in the total resonator response. Note the difference between the effective mass and the differential mass at a given location, while the differential mass is a physical parameter at that point and determines the amount of stored energy there, the effective mass is a merely modeling parameter and represents the total amount of the energy stored in the whole resonator.

$$V(y) = j\omega X_{mode}(y) \tag{2.24}$$

$$dKE(y') = \frac{1}{2} dm(y')|V(y')|^2 = \frac{1}{2}(\rho W_r h \, dy')\left(\omega^2 X_{mode}^2(y')\right)$$

$$KE_{total} = \int_0^{L_r} dKE(y') = \frac{1}{2}\rho W_r h \omega^2 \int_0^{L_r} X_{mode}^2(y')dy' \tag{2.25}$$

$$\frac{1}{2} m_r(y)|V(y)|^2 = KE_{total}$$

$$m_r(y) = \frac{2KE_{total}}{\omega^2 X_{mode}^2(y)} = \rho W_r h \frac{\int_0^{L_r} X_{mode}^2(y')dy'}{X_{mode}^2(y)} \tag{2.26}$$

The same analysis for potential energy can provide analytical expression for the effective stiffness. However, equation 2.4 provides simpler framework for the calculation of effective stiffness, as articulated in equation 2.27. It is a convention to report the effective mass and stiffness at the maximum displacement location. Maximum displacement of the CC-beam fundamental mode happens at the center of the resonator and equation 2.28 provides the corresponding effective mass m_{re} and effective stiffness k_{re}.

$$k_r(y) = \omega_o^2 m_r(y) = 41.883 \times EW_r \frac{h^3}{L_r^4} \frac{\int_0^{L_r} X_{mode}^2(y')dy'}{X_{mode}^2(y)} \tag{2.27}$$

25

$$m_{re} = m_r\left(\frac{L_r}{2}\right) = \rho W_r h \frac{\int_0^{L_r} X_{mode}^2(y')dy'}{2.613}$$

$$k_{re} = k_r\left(\frac{L_r}{2}\right) = 41.883 \times E W_r \frac{h^3}{L_r^4} \frac{\int_0^{L_r} X_{mode}^2(y')dy'}{2.613} \tag{2.28}$$

The applied bias voltage to the resonator applies a constant mechanical force to the suspended electrode and hence, bends the beam from the rest position and change the gap spacing. Since the performance of capacitive transducers is a strong function of the gap spacing, thorough investigation of the gap spacing due to beam bending is very important. Each differential slice of the capacitive transducer of Figure 2.5 applies some mechanical force on the suspended electrode and make it bend, determined by the gap at that location and the bias voltage. The total beam deformation will be the sum of these differential bending, applying the linear superposition assumption. The following assumptions can simplify this complicated static problem into a simple spring-force question:

- The static mode shape X_{static} is the same as the fundamental mode shape X_{mode} of 2.22.
- The parallel plate capacitor is a valid approximation for the electric field in each differential slice.
- The force from each differential slice bend the beam according to fundamental mode shape and hence, the problem simplifies into the identifying the maximum deflection at the beam center due to each differential force.
- The deflection at a given location is determined by the mechanical force and the effective stiffness at that location.

Equation 2.29 determines the deflection at y' due the electrostatic force of differential slice at y'. Note that the gap spacing in this equation is $d(y')$ and has to be found and is not equal to the initial gap spacing d_o. The deflection at point y' can be transferred to the beam center if divided by the mode shape at that point $X_{mode}(y')$, as shown in equation 2.30. The expression of equation 2.30 is the amplitude of deflection at the beam center due to the applied force at y' and hence, should be multiplied by $X_{mode}(y)$ to provide the expression for the deflection along the beam. Integrating over the electrode width provides the total deflection in the resonator due to the applied voltage, as presented in the equation 2.31. This equation is transcendental and self-recursive and does not have closed-form analytical solution.

$$\delta(y',y') = \frac{1}{2}\frac{V_P^2 \varepsilon W_r dy'}{k_r(y')\{d(y')\}^2} \tag{2.29}$$

$$\delta\left(\frac{L_r}{2},y'\right) = \frac{1}{2}\frac{V_P^2 \varepsilon W_r dy'}{k_r(y')\{d(y')\}^2}\frac{1}{X_{mode}(y')} \tag{2.30}$$

$$d(y) = d_o - \int_{L_{e1}}^{L_{e2}} \delta\left(\frac{L_r}{2}, y'\right) X_{mode}(y)$$

$$= d_o - \frac{1}{2} V_P^2 \varepsilon W_r \int_{L_{e1}}^{L_{e2}} \frac{1}{k_r(y')\{d(y')\}^2} \frac{X_{mode}(y)}{X_{mode}(y')} dy' \tag{2.31}$$

The same argument and assumptions can provide accurate expression for the electrical stiffness of the CC-beam, including beam deflection under bias voltage V_P. The contribution to the change in the resonance frequency from the differential slice at y' is given in the expression 2.32. Total electrical stiffness in the transducer will be the integration over the electrode width, presented in equation 2.33. Here, $k_r(y')$ acts as a weighting function, suggesting that the electrical stiffness near the anchor points where effective stiffness is extremely large, is negligible.

$$\frac{dk_e(y')}{k_r(y')} = V_P^2 \frac{\varepsilon W_r dy'}{\{d(y')\}^3} \frac{1}{k_r(y')} \tag{2.32}$$

$$k_e = \left(-V_P^2 \varepsilon W_r \int_{L_{e1}}^{L_{e2}} \frac{1}{\{d(y')\}^3} \frac{k_{re}}{k_r(y')} dy'\right) \tag{2.33}$$

Electrical stiffness softens the resonator and reduce the effective stiffness, therefore, the stiffness term in the equation 2.31 should be $k_r(y')$-k_e to capture this effect. On the other hand, calculation of electrical stiffness requires the gap spacing as a function of the location. Hence, equations 2.31 and 2.33 are mutually coupled and must be solved numerically together. Figure 2.6 provides an efficient recursive algorithm to solve this set of equations numerically. Initially it assumes there is no deflection in the beam and calculates the electrical stiffness and then use these numbers to calculate the deflection in the beam. This algorithm diverges at the pull-in voltage or beyond that and serves as an indication of the pull-in phenomena for the complex structures.

The transformer ratio η_e is the link between electrical and mechanical domain and thorough investigation of its dependence on beam mode shape is of utmost importance. Since considering the beam deflection in the equation 2.1 is not straightforward, it is more convenient to find η_e from equation 2.19. The input current into the device for a given input voltage at the resonance frequency determines the motional resistance R_x. Then, equation 2.19 can provide the expression for η_e. The electrostatic force of the differential slice at y' cause small displacement in the resonator at y', which can be converted to displacement at any point by using the same assumptions of the previous section. Equations 2.34 and 2.35 provide the displacement at y' and anywhere along the resonator, respectively, due to the force at y'. The total displacement is the sum of displacement from each differential segment along the electrode, as given in equation 2.36.

$$dX(y', y') = \frac{QF(y')}{k_r(y')} = \frac{Q}{k_r(y')} \frac{V_P \varepsilon W_r dy'}{\{d(y')\}^2} v_i \tag{2.34}$$

$$dX(y, y') = \frac{Q}{k_r(y')} \frac{V_P \varepsilon W_r dy'}{\{d(y')\}^2} \frac{X_{mode}(y)}{X_{mode}(y')} v_i \tag{2.35}$$

$$X(y) = \int_{Le1}^{Le2} dX(y, y') = \int_{Le1}^{Le2} \left(\frac{Q}{k_r(y')} \frac{V_P \varepsilon W_r}{\{d(y')\}^2} \frac{X_{mode}(y)}{X_{mode}(y')} v_i \right) dy' \tag{2.36}$$

The displacement transfer function of equation 2.36, induces motional current i_x, as shown in equation 2.15. Equation 2.37 presents the output motional current from the differential slice at y and the total output current is the sum of currents from each segment, given in equation 2.38. Since the resonator impedance is purely resistive at resonance, it represents the motional resistance R_x, as expressed in equation 2.39. Equation 2.18 can be used to factor out η_e and provides the analytical expression, given in equation 2.40. The double integration in the equation 2.40 originates from the coupling between electrical and mechanical domain; (1) applied voltage induces mechanical force, which makes the beam to move, (2) displacement of the suspended beam changes the transducer capacitance and generates output current.

$$di_x(y) = \frac{\omega_o V_P \varepsilon W_r dy}{\{d(y)\}^2} X(y) \tag{2.37}$$

$$i_x = \int_{Le1}^{Le2} di_x(y) = \int_{Le1}^{Le2} \left(\frac{\omega_o V_P \varepsilon W_r}{\{d(y)\}^2} \left\{ \int_{Le1}^{Le2} \left(\frac{Q}{k_r(y')} \frac{V_P \varepsilon W_r}{\{d(y')\}^2} \frac{X_{mode}(y)}{X_{mode}(y')} v_i \right) dy' \right\} \right) dy \tag{2.38}$$

$$\frac{1}{R_x} = \left(\frac{i_x}{v_i} \right) = \int_{Le1}^{Le2} \int_{Le1}^{Le2} \left(\frac{\omega_o Q}{k_r(y')} \frac{(V_P \varepsilon W_r)^2}{\{d(y)\}^2 \{d(y')\}^2} \frac{X_{mode}(y)}{X_{mode}(y')} \right) dy' dy \tag{2.39}$$

$$\eta_e = \sqrt{\frac{k_{re}}{\omega_o Q R_x}} = \sqrt{\int_{Le1}^{Le2} \int_{Le1}^{Le2} \left(\frac{k_{re}}{k_r(y')} \cdot \frac{(V_P \varepsilon W_r)^2}{\{d(y)\}^2 \{d(y')\}^2} \cdot \frac{X_{mode}(y)}{X_{mode}(y')} \right) dy' dy}$$

$$\eta_e = V_P \varepsilon W_r \int_{Le1}^{Le2} \left(\frac{1}{\{d(y)\}^2} \cdot \frac{X_{mode}(y)}{X_{mode}(L_r/2)} \right) dy \tag{2.40}$$

Similar arguments can provide an expression for the electromechanical coupling η_{et} of tuning electrodes, shown in Figure 2.5. The main electrode still drives the fundamental mode and therefore, X/v_i transfer function includes integration from L_{e1} to L_{e2}. On the other hand, the tuning electrodes generate the output current and the integration will be from L_{et1} to L_{et2}, shown in equation 2.41.
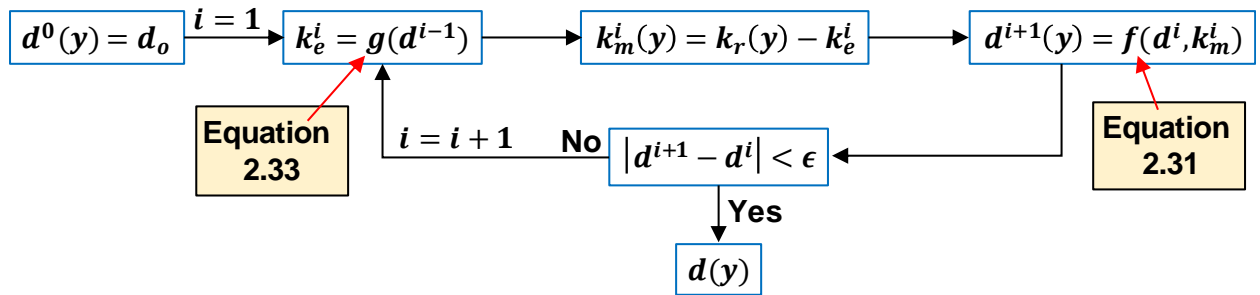
Figure 2.6: The flow chart used to calculate the accurate transformer ratio, gap spacing and electrical stiffness of the CC-beam resonator by considering the effects of the mode shape and beam bending due to the bias voltage.

28

$$\eta_{et} = \sqrt{\int_{L_{et1}}^{L_{et2}} \left(\frac{X_{mode}(y)}{\{d(y)\}^2} \right) dy \int_{L_{e1}}^{L_{e2}} \left(\frac{k_{re}}{k_r(y')} \cdot \frac{(V_P \varepsilon W_r)^2}{\{d(y')\}^2} \cdot \frac{1}{X_{mode}(y')} \right) dy'}$$

$$\eta_{et} = V_P \varepsilon W_r \sqrt{\int_{L_{et1}}^{L_{et2}} \left(\frac{1}{\{d(y)\}^2} \cdot \frac{X_{mode}(y)}{X_{mode}(Lr/2)} \right) dy \int_{L_{e1}}^{L_{e2}} \left(\frac{1}{\{d(y')\}^2} \cdot \frac{X_{mode}(y')}{X_{mode}(Lr/2)} \right) dy'}$$

(2.41)

The set of equations 2.23, 27, 28, 30, 33, 40 and 41 forms the general framework to thoroughly investigate and predict the frequency behavior of any CC-beam resonator and can provide the corresponding equations for other types of resonators. However, these equations are dependent on heavy numerical recursive solutions and are not suitable for implementation in the circuit simulators, such as Keysight ADS, for circuit analysis and optimizations. Since the initial resonator and filter design is based on the linear performance of the device under small input power, we can assume the beam deflection is negligible compared to initial gap d_o and then, simplify these equations. Also, referring to electrode width in terms of the ratio of the beam length it covers simplifies the equations and make the integration independent of resonator length. Equation 2.42 and 2.43 provide expressions for the electrode width, assuming there is no gap between the electrodes and electrodes cover the whole beam length, as suggested by equation 2.44. Equation 2.45 provides the mode shape for the normalized values of y to L_r. The simplified expressions for the electromechanical coupling η_e and η_{et} are given in equation 2.44 and 2.45, respectively.

$$W_e = \alpha_e L_r, \qquad L_{e1} = \frac{L_r - W_e}{2} = L_r \left(\frac{1 - \alpha_e}{2} \right), \qquad L_{e2} = \frac{L_r + W_e}{2} = L_r \left(\frac{1 + \alpha_e}{2} \right) \qquad (2.42)$$

$$W_{et} = \alpha_{et} L_r, \qquad L_{et1} = 0, \qquad L_{et2} = W_{et} = \alpha_{et} L_r \qquad (2.43)$$

$$\alpha_e + 2\alpha_{et} = 1 \qquad (2.44)$$

$$\tilde{X}_{mode}(y) = -1.01781\{\cos(4.73y) - \cosh(4.73y)\} + \{\sin(4.73y) - \sinh(4.73y)\} \qquad (2.45)$$

$$\eta_e = \frac{V_P \varepsilon W_r L_r}{d_o^2} \int_{\frac{1 - \alpha_e}{2}}^{\frac{1 + \alpha_e}{2}} \left(\frac{\tilde{X}_{mode}(y)}{\tilde{X}_{mode}(1/2)} \right) dy \qquad (2.46)$$

$$\eta_{et} = \frac{V_P \varepsilon W_r L_r}{d_o^2} \sqrt{\int_0^{\alpha_{et}} \left(\frac{\tilde{X}_{mode}(y)}{\tilde{X}_{mode}(1/2)} \right) dy \int_{\frac{1 - \alpha_e}{2}}^{\frac{1 + \alpha_e}{2}} \left(\frac{\tilde{X}_{mode}(y')}{\tilde{X}_{mode}(1/2)} \right) dy'} \qquad (2.47)$$

equations 2.48 and 2.49 provide the motional resistance R_x and electromechanical coupling strength (C_x/C_o) of a CC-beam resonator, respectively, based on the simplification of the previous section. As these equations suggest, the motional resistance R_x and electromechanical coupling (C_x/C_o) improves by increasing bias voltage V_P and reducing gap spacing d_o. Particularly, they are

29

very strong functions of the gap and gap spacing is a powerful knob to control the resonator performance. Equations 2.49 also suggests that coupling and motional resistance decreases by the resonance frequency and the appropriate choice of gap spacing and biasing voltage should compensate the degradation in the performance. The choice of electrode width α_e also changes the resonator performance, as shown in Figure 2.7. Although R_x decrease monotonically by increase in the electrode width, the electromechanical coupling reaches its maximum when the electrode covers 60% of the beam length. This optimum point is since the beam displacement near the anchor point is much smaller than the center and the contribution of this section to the motional capacitance C_x is negligible, while the contribution to the static capacitance C_o is the same. On the other hand, the choice of α_e determines the maximum transformer ratio η_{et} of the tuning electrodes, as predicted by equation 2.44 and 2.47 and shown in Figure 2.7 (c). Considering different tradeoffs, this work adopts α_e of 49% and α_{et} of 19.36%.

$$R_x = \frac{k_{re}}{Q\omega_o\eta_e^2} = \frac{\omega_o}{Q} \cdot \frac{\rho}{\varepsilon^2} \cdot \frac{d_o^4}{V_P^2} \cdot \frac{h}{W_r L_r} \cdot \frac{\int_0^1 \tilde{X}^2_{mode}(y)dy}{\left(\int_{\frac{1-\alpha_e}{2}}^{\frac{1+\alpha_e}{2}} \tilde{X}_{mode}(y)dy \right)^2} \tag{2.48}$$
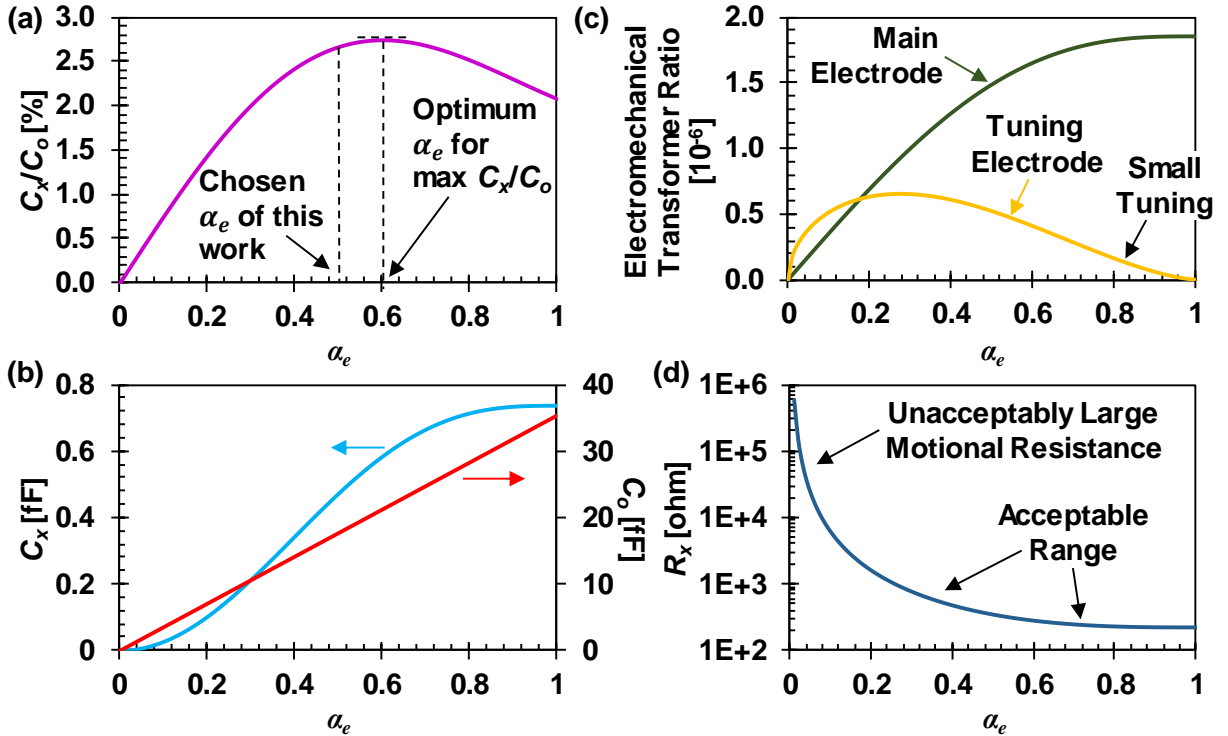
Figure 2.7: (a) The electromechanical coupling (C_x/C_o) as a function of normalized electrode width α_e. The coupling has maximum at $\alpha_e = 0.6$, since the resonator displacement near the anchor points is small and does not contribute to the output current, while the static capacitance linearly increases by the electrode width (b). The choice of electrode width should consider the amount of required tuning (c) and the resonator motional resistance (d). Wide electrode decreases the motional resistance in the expense of smaller tuning range. The optimum choice depends on the tradeoffs between (C_x/C_o), tuning range and R_x.

30

$$\frac{C_x}{C_o} = \frac{\eta_e^2}{k_{re}C_o} = \frac{1}{\omega_o^2} \cdot \frac{\varepsilon}{\rho} \cdot \frac{V_P^2}{d_o^3} \cdot \frac{1}{h\alpha_e} \cdot \frac{\left(\int_{\frac{1-\alpha_e}{2}}^{\frac{1+\alpha_e}{2}} \tilde{X}_{mode}(y)dy\right)^2}{\int_0^1 \tilde{X}^2_{mode}(y)dy} \tag{2.49}$$

There is an upper limit on the bias voltage to avoid catastrophic collapse of suspended electrode, as suggested by equation 2.18 and repeated in equation 2.50 for the CC-beam. Assuming the bias voltage is a fraction of the pull-in voltage, then equations 2.48 and 2.49 can be reorganized into equations 2.52 and 2.53 in order to capture all the limitations of CC-beam resonators. Equation 2.52 shows that in contrary to the common belief, capacitive resonator motional resistance decreases by frequency for a given thickness, assuming no degradation in the quality factor. More interestingly, equation 2.53 suggests that the electromechanical coupling strength is independent of CC-beam dimension and resonance frequency, and it is only determined by how close the bias voltage is to the fundamental limit and what the electrode covers what percentage of the beam.

$$V_{pull-in}^2 = \frac{\omega_o^2 \rho h d_o^3}{\varepsilon} \cdot \frac{\int_0^1 \tilde{X}^2_{mode}(y)dy}{\int_{1-\frac{\alpha_e}{2}}^{1+\frac{\alpha_e}{2}} \tilde{X}^2_{mode}(y)dy} \tag{2.50}$$

$$V_P = \alpha_V V_{pull-in} \tag{2.51}$$

$$R_x = \frac{1}{\alpha_V^2} \cdot \frac{1}{\omega_o Q\varepsilon} \cdot \frac{d_o}{W_r L_r} \cdot \frac{\int_{1-\frac{\alpha_e}{2}}^{1+\frac{\alpha_e}{2}} \tilde{X}^2_{mode}(y)dy}{\left(\int_{1-\frac{\alpha_e}{2}}^{1+\frac{\alpha_e}{2}} \tilde{X}_{mode}(y)dy\right)^2}$$

$$R_x = \frac{1}{2.544} \cdot \frac{1}{Q\varepsilon\alpha_V^2\sqrt{\omega_o}} \cdot \frac{d_o}{W_r\sqrt{h}} \cdot \frac{\int_{1-\frac{\alpha_e}{2}}^{1+\frac{\alpha_e}{2}} \tilde{X}^2_{mode}(y)dy}{\left(\int_{1-\frac{\alpha_e}{2}}^{1+\frac{\alpha_e}{2}} \tilde{X}_{mode}(y)dy\right)^2} \tag{2.52}$$

$$\frac{C_x}{C_o} = \frac{\alpha_V^2}{\alpha_e} \cdot \frac{\left(\int_{1-\frac{\alpha_e}{2}}^{1+\frac{\alpha_e}{2}} \tilde{X}_{mode}(y)dy\right)^2}{\int_{1-\frac{\alpha_e}{2}}^{1+\frac{\alpha_e}{2}} \tilde{X}^2_{mode}(y)dy} \tag{2.53}$$

Table 2.1 captures the design procedure presented here alongside the relevant governing equations with appropriate approximation for the choice of α_e of this work.

Table 2.1: Resonator Design Summary

Schematic	V_P V_T v_{in} **Input/Output Electrode** **Tuning Electrode** **Biasing Line**
Mode Shape	$X(y)$, W_t, W_e, W_t, O, L_{t1}, L_{e1}, L_{e2}, L_{t2}, L, y
Electric Equivalent Model*	i_{in}, v_{in}, X, P, C_o, $-C_o$, $1:\eta_e$, c_x, l_x, r_x, **Input/output Transducer**, T, P, C_t, $-C_t$, $1:\eta_{et}$, **Tuning Transducer**
Resonance Frequency	$$f_{\text{nom}} = 1.03\sqrt{\frac{E}{\rho}} \cdot \frac{h}{L_r^2}, \quad f_0 = f_{nom}\left[1 - \left(\frac{k_e}{k_m}\right)\right]^{1/2}$$ $$\left(\frac{k_e}{k_m}\right) = \int_{L_{e1}}^{L_{e2}} \frac{V_P^2 \cdot \varepsilon_0 \cdot W_r}{[d(y)]^3 \cdot k_m(y)}\,dy + 2\int_{L_{t1}-\frac{W_t}{2}}^{L_{t1}+\frac{W_t}{2}} \frac{V_P^2 \cdot \varepsilon_0 \cdot W_r}{[d(y)]^3 \cdot k_m(y)}\,dy$$ $$d(y) = d_0 - \frac{1}{2}\int_{L_{e1}}^{L_{e2}} \frac{V_P^2 \cdot \varepsilon_0 \cdot W_r}{[d(y')]^2 \cdot k_m(y')} \cdot \frac{X_{mode}(y)}{X_{mode}(y')}\,dy'$$
Effective Mass	$$m_r(y) = \frac{\rho \cdot W_r \cdot h}{[X_{mode}(y)]^2}\int_0^{L_r}[X_{mode}(y')]^2\,dy'$$ $$X_{mode}(y) = \zeta[\cos(ky) - \cosh(ky)] + [\sin(ky) - \sinh(ky)]$$ $$k = 4.730/L_r, \zeta = -1.01781$$ $$m_r(y) = 1.036\frac{\rho \cdot W_r \cdot h}{[X_{mode}(y)]^2}$$ $$m_{re} = m_r(L_r/2) = 0.3965(\rho \cdot W_r \cdot L_r \cdot h)$$
Effective Stiffness	$$k_m(y) = (2\pi f_{nom})^2 m_r(y), k_r(y) = (2\pi f_0)^2 m_r(y)$$ $$k_{re} = k_r\left(\frac{L_r}{2}\right) = 16.6057\left(E \cdot W_r \cdot \left(\frac{h}{L_r}\right)^3\right)$$
Transducer	$$\frac{\partial C}{\partial x} = \varepsilon_0 \cdot W_r \sqrt{\int_{L_{e1}}^{L_{e2}}\frac{X_{mode}(y)}{[d(y)]^2}\,dy\int_{L_{e1}}^{L_{e2}}\frac{k_{re}}{k_r(y')}\frac{1}{[d(y')]^2 X_{mode}(y')}\,dy'}$$ $$\frac{\partial C}{\partial x} \approx 0.8441\frac{\varepsilon_0 \cdot W_r \cdot W_e}{d_o^2}$$ $$\frac{\partial C_t}{\partial x} = \varepsilon_0 \cdot W_r \sqrt{\int_{L_{t1}-\frac{W_t}{2}}^{L_{t1}+\frac{W_t}{2}}\frac{X_{mode}(y)}{[d(y)]^2}\,dy\int_{L_{e1}}^{L_{e2}}\frac{k_{re}}{k_r(y')}\frac{1}{[d(y')]^2 X_{mode}(y')}\,dy'}$$ $$\frac{\partial C_t}{\partial x} \approx 0.7028\frac{\varepsilon_0 \cdot W_r \cdot W_t}{d_o^2}$$
Motional RCL	$$\eta_e = V_P\frac{\partial C}{\partial x}, \eta_{et} = |V_P - V_T|\frac{\partial C_t}{\partial x}$$ $$C_o = \frac{\varepsilon_0 W_r W_e}{d_o}, C_t = \frac{\varepsilon_0 W_r W_t}{d_o}$$ $$r_x = \frac{\sqrt{k_{re}m_{re}}}{Q}, l_x = m_{re}, c_x = \frac{1}{k_{re}}$$

2.3 EXPERIMENTAL RESULTS

CC-beam resonators were fabricated using a previously described vertical gap surface-micromachining process [55], summarized by the process cross-sections in Figure 2.8, with some modifications to incorporate a damascene process to enable a thick, low resistance interconnect layer. Fabrication starts with deposition of 2μm-thick silicon dioxide and 400nm-thick silicon nitride on the silicon substrate to electrically isolate different interconnects. Then 1.5μm-thick oxide is deposited and patterned using a

| | Oxide | Nitride | Sac. Ox. | Poly Int. | Poly Str. |
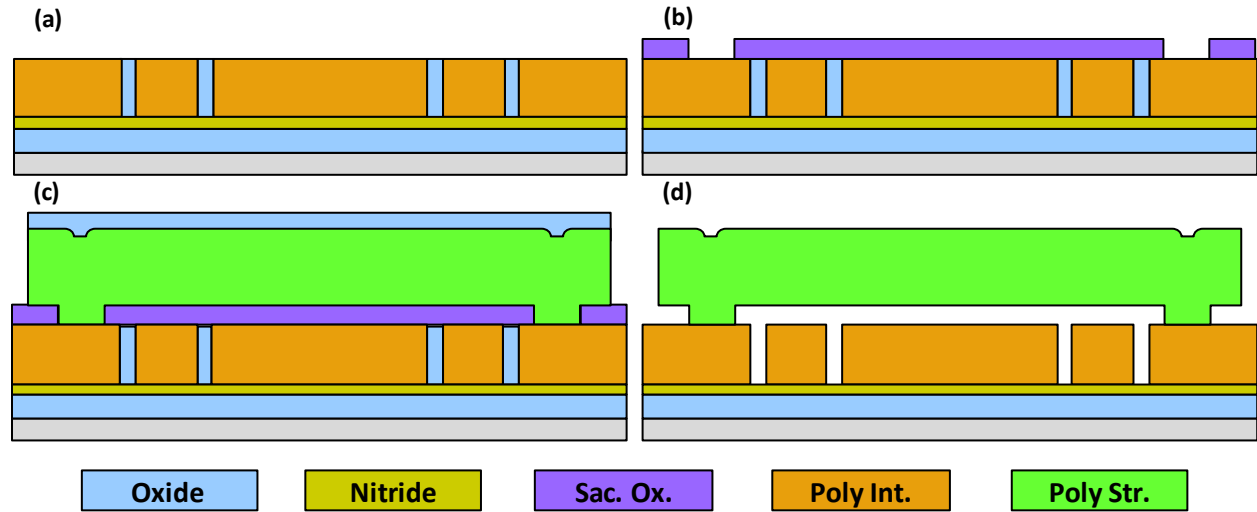
Figure 2.8: (a)-(d) Cross-sections of the fabrication process flow used for the third- and forth-order bridged filter of this work.
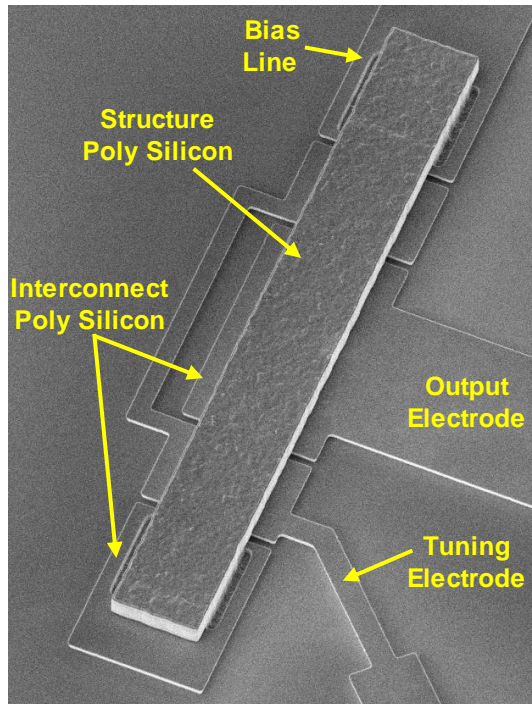
Figure 2.9: SEM photograph of a released CC-beam resonator.

Table 2.2: Resonator Data Summary

Parameters	Simulation	Measurement	Units
Young's Modulus, E	150	150	GPa
Density, ρ	2,300	2,300	kg/m^3
Length, L_r	40	40.8	μm
Width, W_r	8	8	μm
Thickness, h	2	1.985	μm
Electrode-to-Resonator Gap, d_o	150	140	nm
Resonant Frequency, f_{nom}	9.141	8.720	MHz
DC-Bias Voltage, V_P	5	5	V
Resonant Frequency, f_o	9.121	8.694	MHz
Quality Factor, Q	10,000	15,100	—
Effective Mass, m_r	582.9 x10^{-15}	590.2x10^{-15}	kg
Effective Stiffness, k_m	1.923x10^3	1.771x10^3	N/m
Effective Stiffness, k_r	1.914x10^3	1.761x10^3	N/m
Effective Damping, c_r	3.34x10^{-9}	2.13x10^{-9}	Ns/m
Input Electrode Width, W_e	20	20	μm
Tuning Electrode Width, W_t	7.9	7.9	μm
Electromech. Coupling, η_e	320x10^{-9}	386.5x10^{-9}	C/m
Electromech. Coupling, η_t	17.5x10^{-9}	20.1x10^{-9}	C/m
Equivalent Resistance, R_x	30.67	14.29	kΩ
Equivalent Inductance, L_x	5.35	3.95	H
Equivalent Capacitance, C_x	0.056	0.084	fF
Static Overlap Capacitance, C_o	16.9	18.1	fF
Electromech. Coupling, C_x/C_o	0.331	0.464	%

33

negative interconnect mask to form a mold for the interconnect. Deposition of 2μm-thick insitu-doped polysilicon and polishing down to the oxide yields to the thick interconnects of Figure 2.8 (a). This damascene process removes all the structure topography, allowing for more precise definition of resonator center frequency. Next, 150nm of sacrificial oxide is deposited and patterned to open anchor vias, as shown in Figure 2.8(b), followed by successive depositions of 2μm-thick structural phosphorous-doped-polysilicon and 500nm of oxide hard mask material, respectively. Patterning via the filter structure mask and etching then yields Figure 2.8 (c). A wet dip in hydrofluoric acid then releases devices, leaving free standing structures, such as shown in Figure 2.8(d).

Figure 2.9 presents the SEM of a released CC-beam micromechanical resonator and Table 2.2 summarizes the resonator designed dimensions and extracted characteristics of this work.

Figure 2.10 (a) presents the measurement circuitry used to characterized the released CC-beam resonator. This pseudo-two port configuration allows transmission measurement for the frequency characterization of the device, instead of reflection measurement offered by one-port. Figure 2.10 (b) shows the frequency response of the CC-beam at 5V, demonstrating the strong peak and good rejection a CC-beams can offer. This resonator has quality factor of 15,100 extracted by fitting to a Lorentzian function. As suggested by equation 2.48, the motional
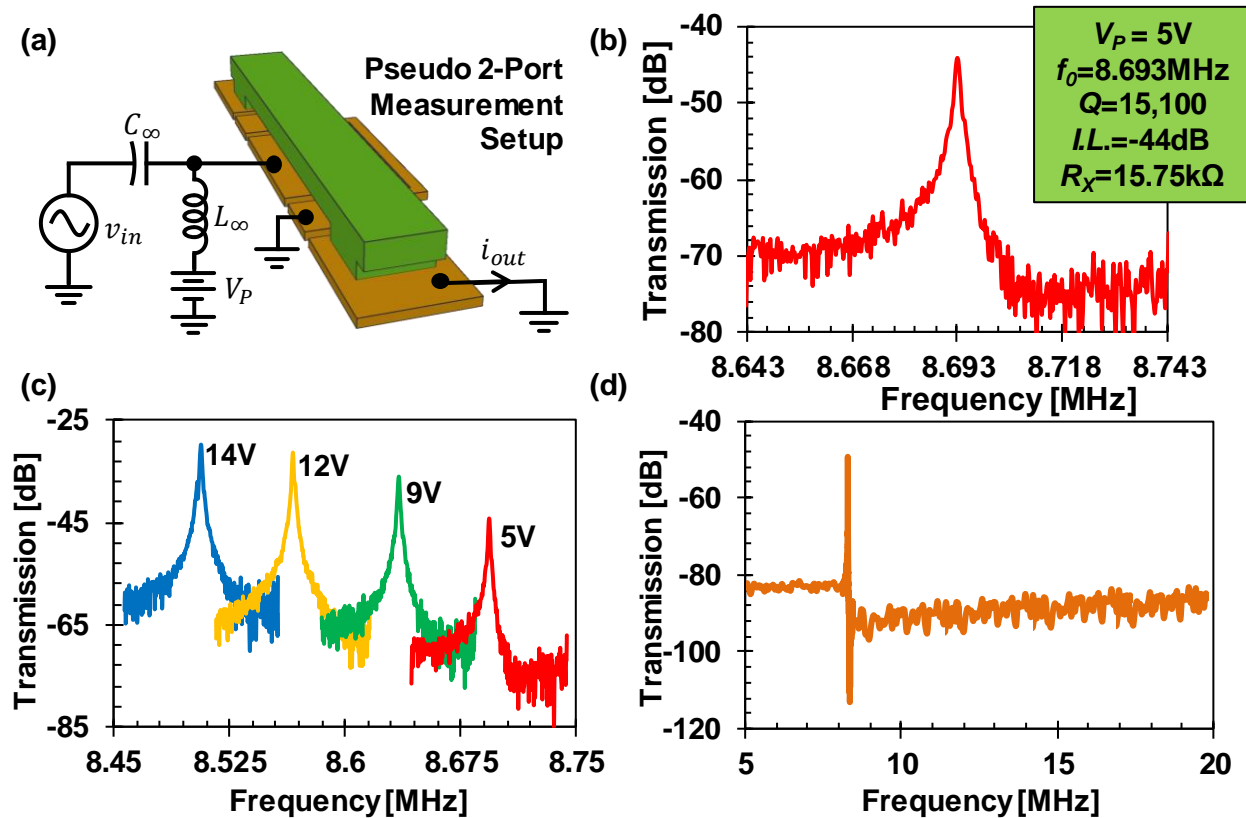
Figure 2.10: (a) Illustration of a CC-beam resonator in a typical pseudo two-port operation scheme and (b) its measured frequency response at 5V. (c) The increase in the bias voltage VP shifts the resonance frequency due to electrical stiffness and improves the insertion loss. (d) Wideband measurement of the resonator shows a spurious-free frequency response.

34

resistance of the resonator should decrease by bias voltage square and hence, the insertion loss decreases accordingly, confirmed by the graphs of Figure 2.10 (c). Figure 2.10 (d) demonstrate the wideband performance of the resonator and as mentioned in the previous section, the configuration for the CC-beam fundamental mode excitation does not excite spurious modes and the wideband respond is extremely clean.

Figure 2.11 (a), derived from Figure 2.10 (c), presents the resonance frequency of the resonator for different bias voltage V_P. The stiffness softening due to electrical stiffness shifts the resonance to lower frequency, as suggested by equation 2.333. The f_o-V_P plot is a unique feature of the capacitive resonator: the extrapolated resonance frequency at zero volt determines the resonator dimension and the graph curvature is distinctive to the gap spacing. This resonator has gap spacing of 142nm and beam height of 1.84μm, as reported in Table 2.2. However, the resonator insertion loss and the motional resistance, shown in Figure 2.11 (b), do not follow the equation 2.48 at higher bias voltages and seem to plateau at 1kΩ. This saturation in the motional resistance is due to finite conductivity of the interconnect layer. Modified lumped model in Figure 2.11 (c) with 500Ω series resistance with each line creates more realistic model and predicts the behavior of the Figure 2.11 (b) very well. This series resistance also loads the original quality factor of the resonator, as suggested by equation 2.54. Here, γ includes all the design and material parameters.

$$Q_{Loaded} = \frac{\omega_o L_x}{R_x + 2R_P} = \frac{Q_o}{1 + \frac{2R_P}{R_x}} = \frac{Q_o}{1 + \gamma V_P^2} \tag{2.54}$$
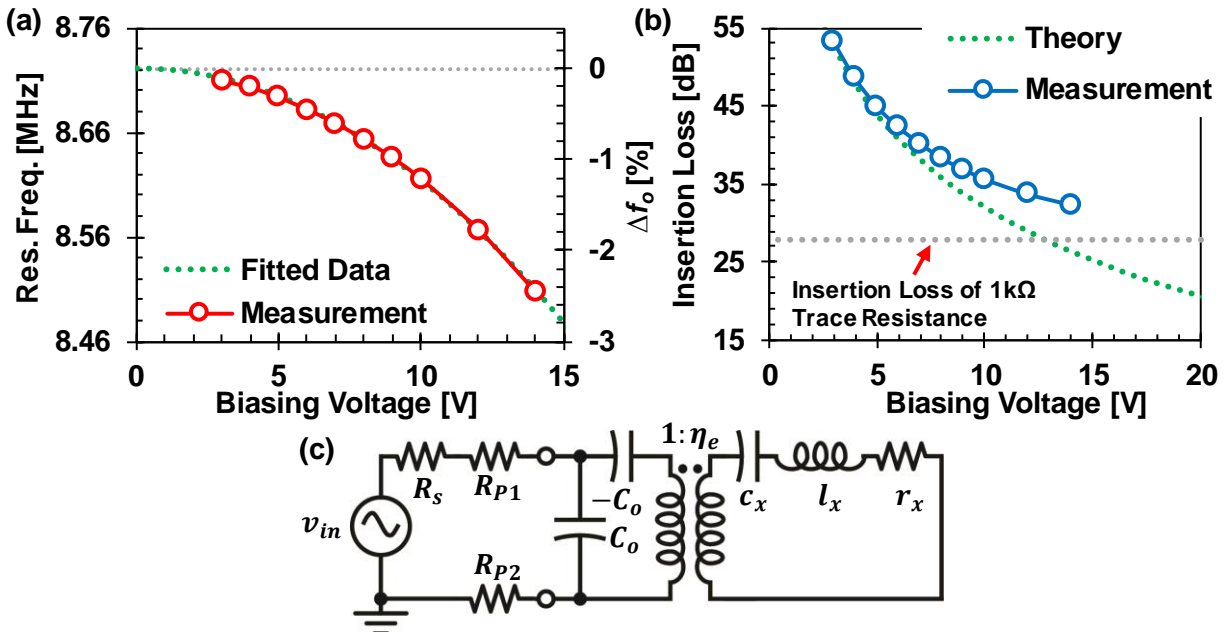
Figure 2.11: (a) The CC-beam resonance frequency and (b) insertion loss as a function of bias voltage VP. The measured insertion loss is higher than the value predicted by the developed model, since the model does not take the series interconnect resistance into account. (c) Electrical equivalent circuit with corresponding series resistance at each port.

The same pseudo two-port measurement circuitry determined the electromechanical coupling strength (C_x/C_o) of another released CC-beam resonator. Initially, the gap spacing was extracted from the f_o-V_P plot, shown in Figure 2.12 (a, b), and found to be 220nm. This gap spacing should support (C_x/C_o) of 2.9% at 20V of bias voltage, according to the equation 2.49. Figure 2.12 (c) presents the measured coupling strength (C_x/C_o) of this resonator based on the series and parallel frequencies, provided in equation 2.19, and as expected, this resonator can provide coupling on the order of 10% and more, which outperforms any competing technologies at these frequencies. The combination of high quality factor and strong coupling makes CC-beam resonators an excellent choice for realization of front-end filters or high-precision oscillators at HF. The product of these two parameters, $k^2_{eff}.Q$, is usually used to evaluate the performance of
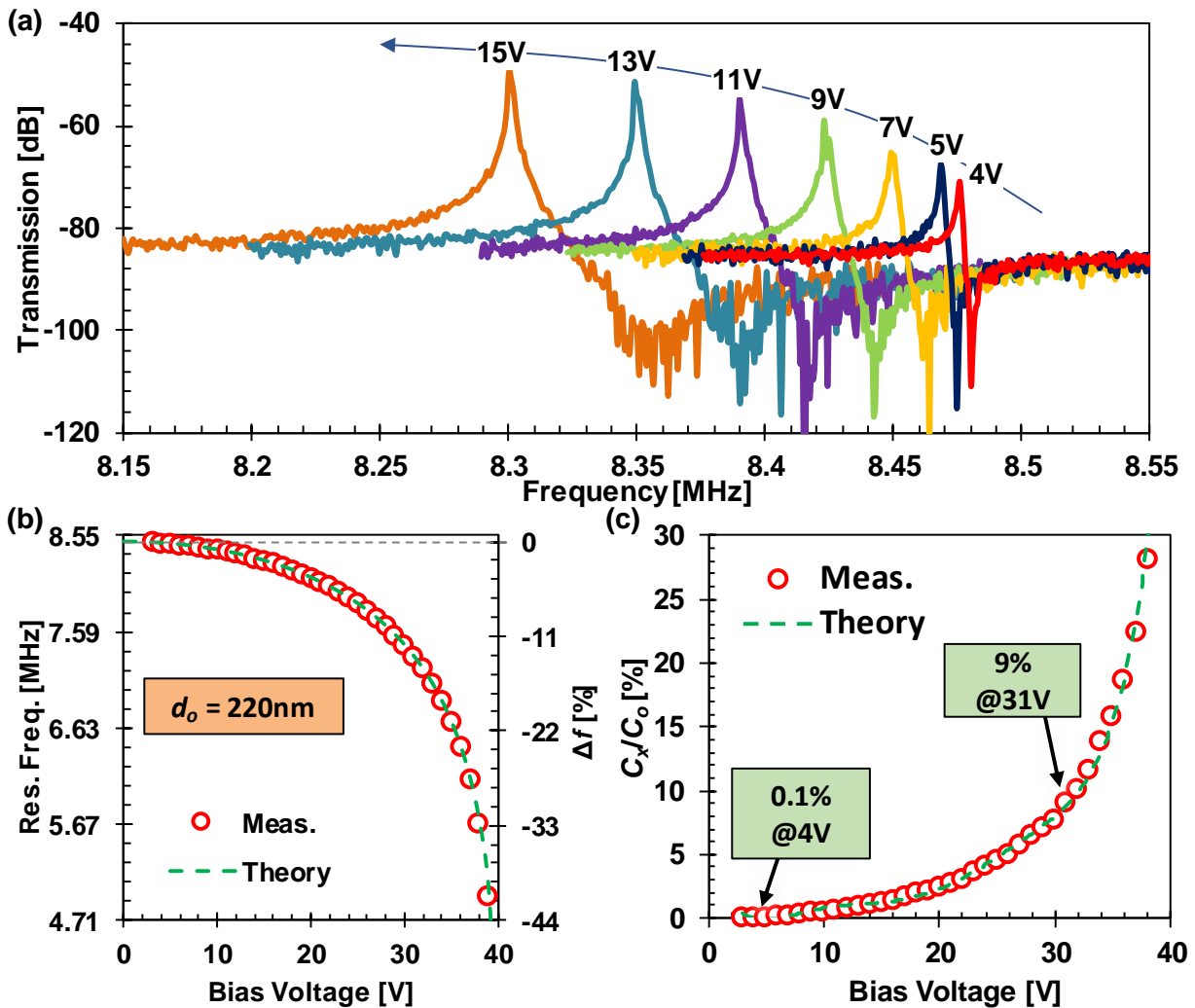
Figure 2.12: (a) The frequency response of a CC-beam resonator for different bias voltages. (b) The resonator center frequency for different bias voltage, derived from (a), which translates to gap spacing of 220nm. (c) The electromechanical coupling strength (C_x/C_o) derived from series and parallel resonance frequencies, as a function of bias voltage. This resonator offers (C_x/C_o) of 9%, matched to the prediction of the analytical equations.

36

resonators and compare different technologies. The CC-beam resonator of this work with $k^2_{eff} \cdot Q$ of 1,350 at 31V outperforms other competing technologies.

$$k^2_{eff} \cdot Q_o \cong 1.2 \left(\frac{C_x}{C_o}\right) Q_o \tag{2.55}$$

Chapter 3 MECHANICALLY-COUPLED MICROMECHANICAL FILTERS

This chapter introduces the basics of filter synthesis and design and discusses the importance of different filter specification and the formal procedure to achieve those goals. Selective low-insertion loss filters are required for both transmitter and receiver systems, to prevent transmitting high-power signals into other users' channels and to improve the sensitivity and range of the receiver. Current technologies exploit band-select BAW [14] or SAW [53] filters to filter out out-of-band interferers. The capacitive micromechanical resonators can provide channel-level filtering due to their extraordinary quality factor and coupling. The implementation of such a channel-select filter can further improve transceiver performance and greatly reduce the power consumption. This chapter introduces the design of channel-select filters by mechanical coupling of identical resonators and presents the design procedures and measurement results of a 2nd-order filter. Moreover, the micromechanical filters presented here can be monotonically integrated with standard CMOS process to improve the performance and reduce the cost [67].

3.1 FILTER SPECIFICATIONS AND RESONATOR REQUIREMENTS

A micromechanical resonator such as the one presented in the previous chapter has a biquad frequency response and although very useful in frequency-selection application [25], the offered bandwidth is not sufficient for any data-transfer application. Addition of more poles on the *s*-plane of the system eigenvalues can flatten the passband and achieve the desired bandwidth, as shown in Figure 3.1. A proper design of a third-order filter, such as one shown in Figure 3.1 (c), should achieve small insertion loss, large out-of-band rejection, and desired 3dB bandwidth, all by proper placement of the system poles. A selective filter also should have sharp passband-to-stopband roll-off, characterized by 20dB shape factor defined by equation 3.1. 20dB shape factor will be unity for the ideal brick-wall filter and is larger than one for any other implementations. Group delay models the dispersion behavior of the system and determines the system delay for different frequencies. Therefore, flat and minimum group delay design might be very important, depending on the application and system requirements.

$$SF_{20dB} = \frac{BW_{20dB}}{BW_{3dB}} \qquad (3.1)$$

There are various techniques to implement the system pole configuration shown in Figure 3.1 (d). This work adopts the mechanically-coupled cascaded-resonator technique which uses

several identical resonators coupled via mechanical beams to achieve the required filter response. This technique offers numerous advantages:

- All the resonating tanks have the same resonance frequency (i.e. dimension) and there is no need for very good absolute processing tolerances to determine the resonance frequency of each tank. Surface micromachining techniques have excellent relative local tolerances and hence, the resonance frequency of all the tanks will be identical, even though they might be off the initial designed value [68].
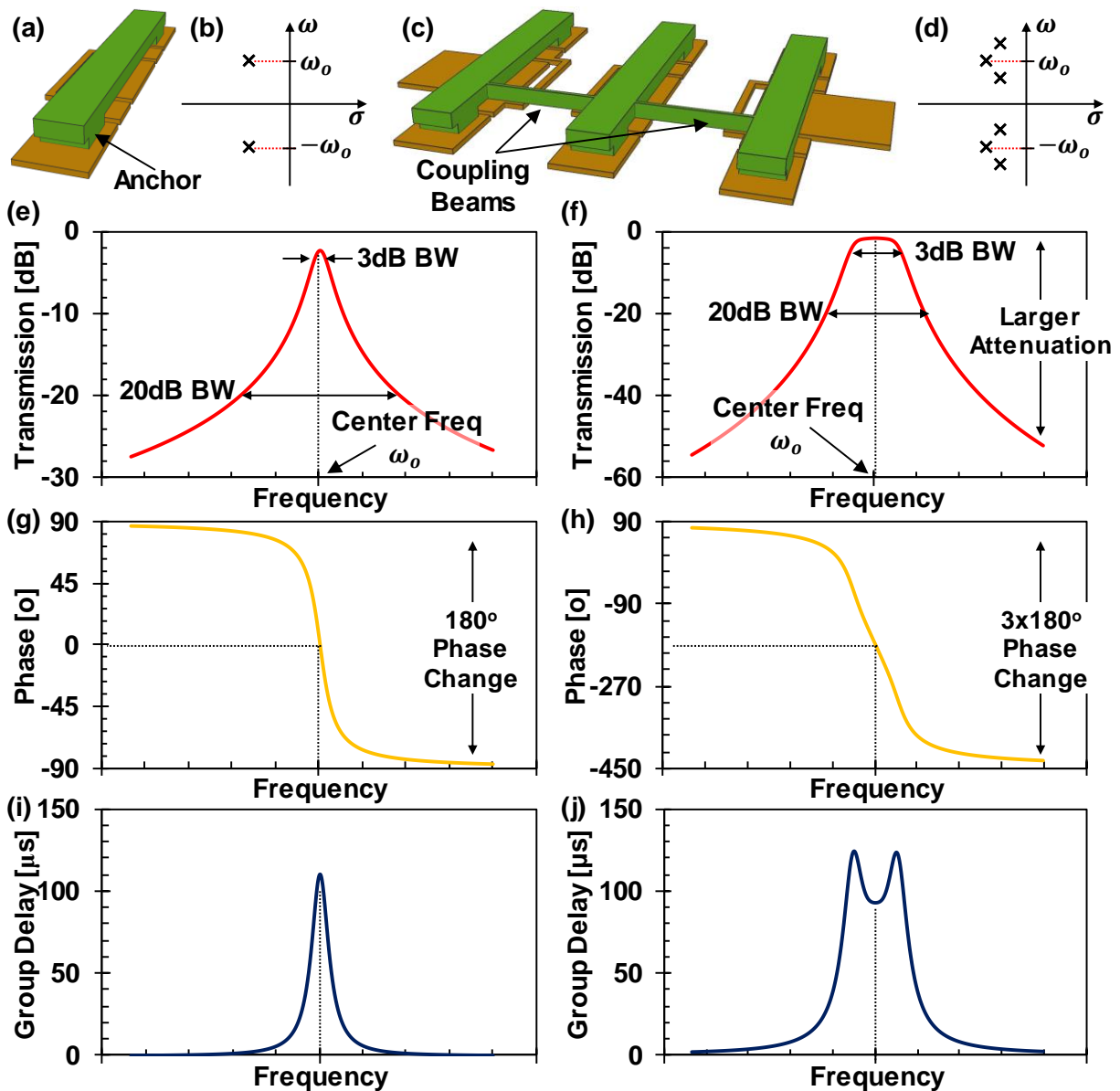
Figure 3.1: A single micromechanical resonator (a) and a third-order micromechanical filter (b) and their corresponding poles and zeros on the complex plane (b, d), transmission magnitude (e, f), phase (g, h) and group delay (i, j).

- The filter bandwidth is determined by mechanical design of coupling beams and not affected by electrical circuits [55].
- All the signal processing is happening in the mechanical domain and the system is less susceptible to the capacitive, inductive or resistive parasitic components.
- You can eliminate feedthrough path by non-conductive coupling beams, while the main signal in mechanical domain can pass through. Therefore, the out-of-band rejection can be improved even more.

3.1.1 QUALITY FACTOR REQUIREMENTS

The insertion loss is the most important specification of a front-end filter; it directly affects the efficiency of the transmitter and the power consumption of the power amplifier and also determines the receiver sensitivity and changes the signal-to-noise ratio and increases the receiver noise figure instantly.

The insertion loss of a filter realized by any techniques is primarily determined by the quality factor of each resonating tank and the filter percent bandwidth, as shown in equation 3.2. Here, Q_o is the unloaded quality factor of the identical resonating tanks and Q_f is a measure of filter bandwidth in comparison to its center frequency. This equation suggests that to realize a channel-select filter with small percent bandwidth, one needs resonating tanks with higher quality factor to minimize the insertion loss. Figure 3.3 presents a channel-select and a band-select filter with
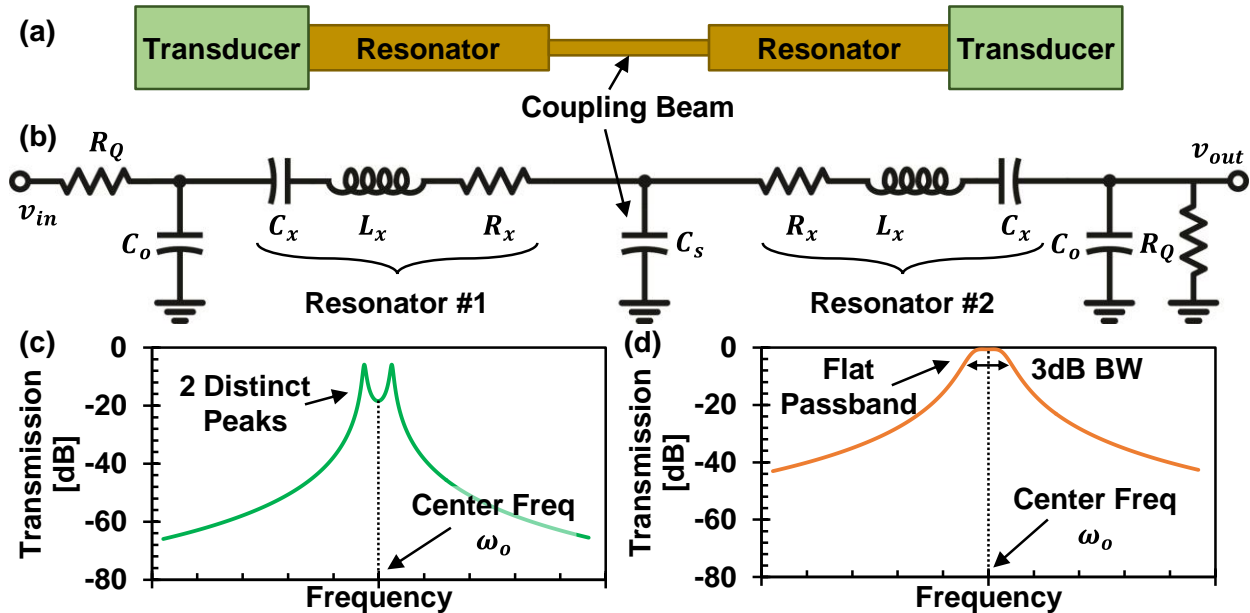
Figure 3.2: (a) Schematic description of general implementation topology of a bandpass filter consisting of a chain of discrete resonator tanks linked with coupling elements. (b) Electrical equivalent circuit representation of the generic filter network with LCR tanks representing the resonator elements and shunt capacitors modeling the coupling between adjacent resonators. (c) The two mode peaks that ensue from the coupled high Q resonators. (d) Terminated filter response after proper termination.

40

different resonator Q_o. As shown in this figure, a 2.8%-wide band-select filter only requires Q_o of 1000 to achieve insertion loss of 0.5dB, while a 0.02%-wide channel-select filter needs quality factor higher than 30,000 to obtain 1dB insertion loss. This highlights the importance of high quality factor for implementing RF channel-select filters, while the conventional band-select filters used in today's wireless handsets can perform with Q_o as low as 1000, or so.

$$IL \propto \frac{1}{Q_o \cdot PBW} = \frac{Q_f}{Qres}$$
$$PBW = \frac{1}{Q_f} = \frac{BW}{f_o}$$

(3.2)

3.1.2 ELECTROMECHANICAL COUPLING STRENGTH REQUIREMENTS

The electromechanical coupling strength (C_x/C_o) is a measure of the ratio of motional current at the output relative to the electrical feedthrough current via capacitive coupling and determines the proper termination resistance at the filter outputs and the maximum achievable out-of-band rejection; the stronger coupling the smaller required R_Q and the higher stopband rejection. Here, the termination resistance R_Q at the filter output loads the quality factor of the constituent resonators and flatten the rigged passband.

Hypothetically, if the resonating tanks of Figure 3.2 did not have any shunt capacitance C_o, there was no limit on the termination resistance and only the mechanical response of the system limits the stopband rejection. On the other hand, any transducer, capacitive or piezoelectric, has finite capacitance at the input, inherent to the fundamental operation of that transducer. The static capacitance C_o forms a lowpass filter at the input and output of the filter, with corner frequency given in equation 3.3, which attenuates the frequency components of the motional current above
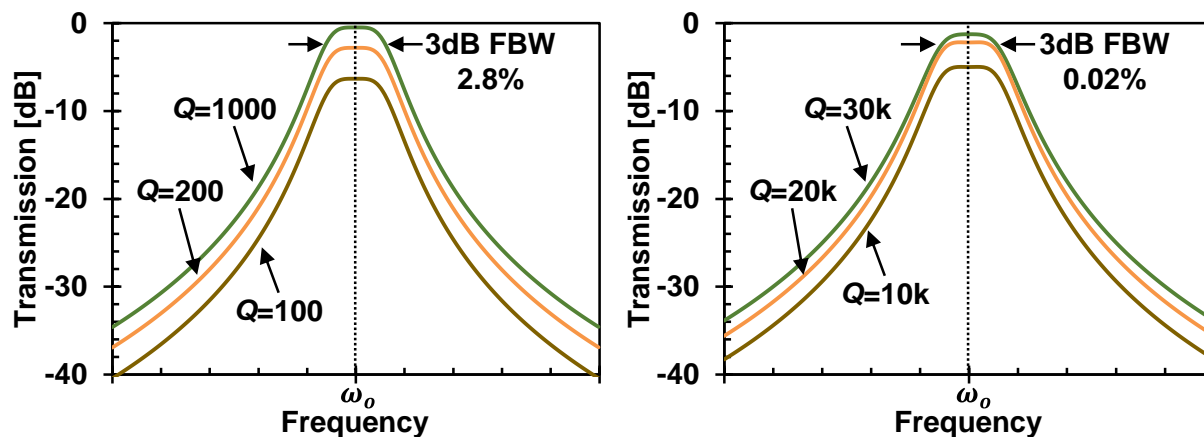
Figure 3.3: Simulation of a band-select filter (left) and a channel-select filter (right) with different constituent resonator unloaded quality factor.

41

f_{FOM}. To avoid any distortion in the signal within the bandpass frequency of the filter, the corner frequency of this lowpass filter f_{FOM} should be much higher than the filter center frequency. Equation 3.4 translates this requirements into resonator specifications and shows that the resonator electromechanical coupling (C_x/C_o) should be higher than the filter percent bandwidth. The expression used to evaluate R_Q will be explained in the following Section.

$$f_{FOM} = \frac{1}{2\pi R_Q C_o} = \frac{\omega_o Q_f C_x}{2\pi C_o}$$

$$R_Q = \frac{1}{\omega_o C_x Q_f}$$

(3.3)

$$f_{FOM} \gg f_o, \qquad \frac{C_x}{C_o} \gg \frac{1}{Q_f}, \qquad \frac{C_x}{C_o} \gg PBW$$

(3.4)

Figure 3.4 demonstrates the effect of electromechanical coupling (C_x/C_o) on the filter passband response. As suggested by equation 3.4, a wider filter requires stronger coupling for proper termination and minimum distortion in the filter response. The simulated 1% filter of Figure 3.4 (b) needs coupling of 1.5% or more, while the channel-select filter with 0.02% fractional
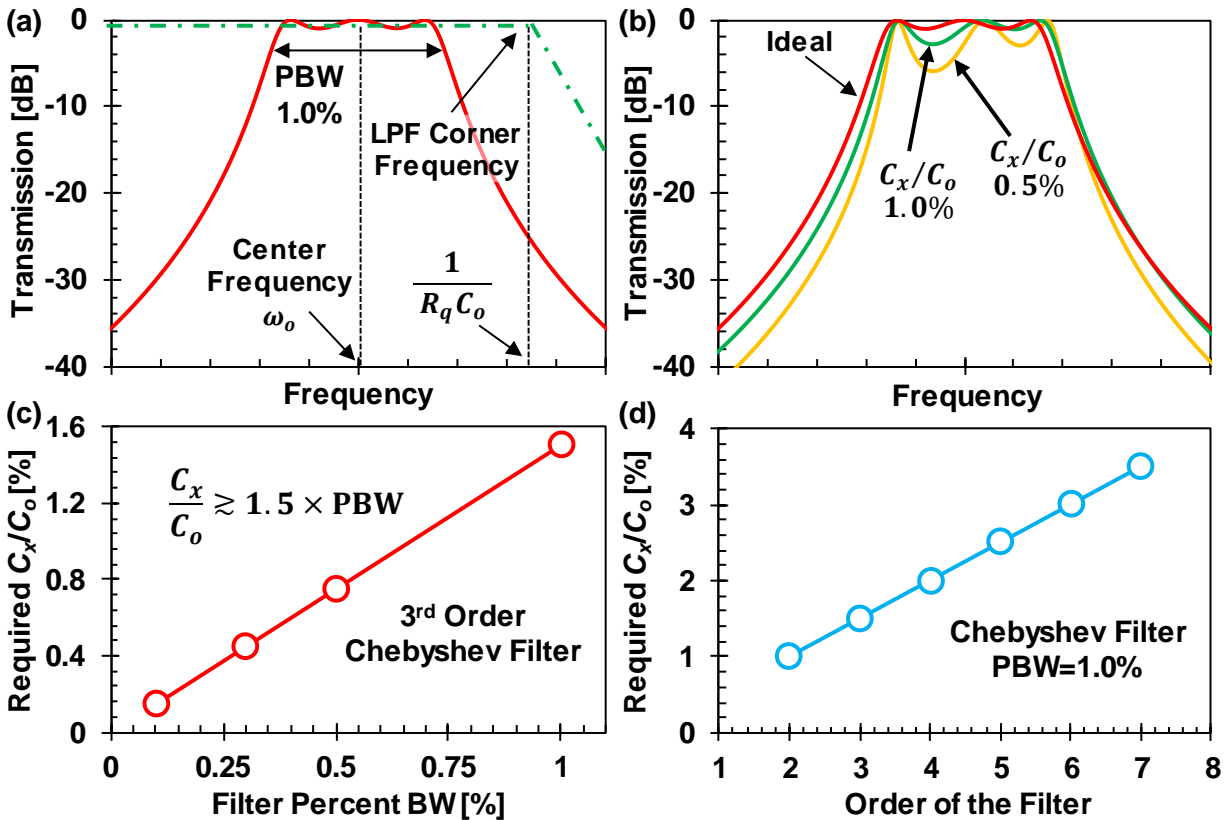
Figure 3.4: (a) Simulation of a third-order Chebyshev micromechanical filter and the low-pass filter formed at the filter input and output by intrinsic capacitance C_o and termination resistance R_Q, (b) terminated filters with different constituent resonator electromechanical coupling strength (C_x/C_o), (c) minimum coupling required for proper filter termination as a function of (c) filter bandwidth and (d) filter order.

bandwidth requires only 0.03%. The simulated third-order Chebyshev filter of this figure needs the coupling at least 1.5 times larger than fractional bandwidth to achieve in-band distortion smaller than 1dB.

3.1.3　REQUIREMENTS ON THE FABRICATION TOLERANCE

The resonating tanks of a cascaded filter, such as one shown in Figure 3.2, have identical resonance frequencies and then the mechanical coupling beam will make the system poles described in Figure 3.1 (d). The resonance frequency of a capacitive micromechanical resonator, like the CC-beam described in Chapter 2, is determined primarily by material properties, Young modulus and density, and physical dimensions, such as length and height for a CC-beam. Any mismatch in the resonance frequency of the constituent resonators of Figure 3.2 result in the distortion in the passband, since the system poles on the *s*-plane are off the designed location. This mismatch can be due to the fabrication tolerances across the wafer after photolithography or etching steps. For example, different exposure across the wafer can cause the anchor openings to be smaller or larger than the designed value and therefore, change the resonance frequency of the CC-beam resonator according to equation 2.23. The simulation results of Figure 3.5 suggest that the mismatch between resonator center frequencies should not exceed the fractional bandwidth of the filter to keep the distortion in an acceptable range. This requirement does not limit the implementation of band-select filters, since the fabrication variations in a modern facility is usually much better than the 3-6% fractional bandwidth of a band-select filter. On the other hand, this requirement dictates the variation on the order of 0.01% or so for a channel-select filter, which is not easily achievable and increases the fabrication costs dramatically. This tight variation
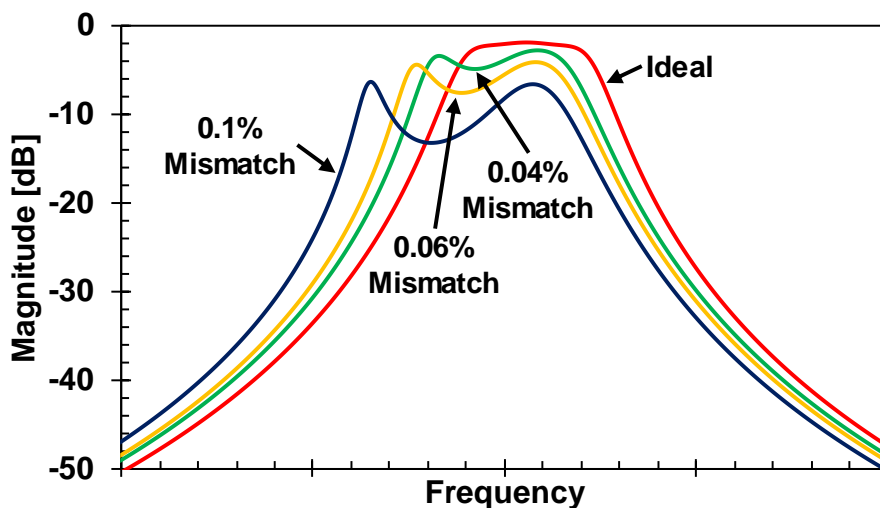
Figure 3.5: The filter response of Figure 3.2 relies on the identical resonance frequencies of constituent resonators. Small mismatch between the resonators introduces large distortion in the filter passband.

43

requirement and cost consideration were one of the most important obstacles for the implementation of channel-select filters in consumer's electronics. Some researchers have suggested different post-processing trimming techniques to compensate for the fabrication variations, though in expense of time and cost. Fortunately, the CC-beam resonators used in this work have wide tuning range via electrical stiffness, as discussed in Section 2.2. The tunability of individual resonators in a filter bank was the key to the success of this work and will be discussed in more details in the following chapters.

3.2 LUMPED ELECTRICAL AND MECHANICAL MODELS OF THE MICROMECHANICAL FILTER

The micromechanical filters of this work are much like the filter configuration of Figure 3.2 and use high-quality resonating tanks, described in Chapter 2, mechanically coupled via flexural coupling beams. Figure 3.6 presents a 2nd-order filter comprising of two identical CC-beam resonators and a flexural coupling beam. The length of the coupling beam is usually the quarter of the acoustic wavelength at the frequency of interest. This quarter-wavelength design makes the filter response more robust against fabrication tolerances and helps the balanced distribution of coupling mass and stiffness between two resonators. The design of coupling beam will be covered in more details in the following chapter. Three springs attached to the resonating tanks in the mechanical domain, shown in Figure 3.6 (b), or equivalently three capacitors shown in Figure 3.6 (c) model the quarter-wavelength coupling beam. The coupling length L_s should satisfy $H_6 = 0$ for quarter-wavelength design. Here, I_s, W_s, and h are the coupling beam moment of inertia, width and height and ρ, E are material density and Young modulus, respectively.

$$H_6 = \sinh \alpha \cos \alpha + \cosh \alpha \sin \alpha = 0 \tag{3.5}$$
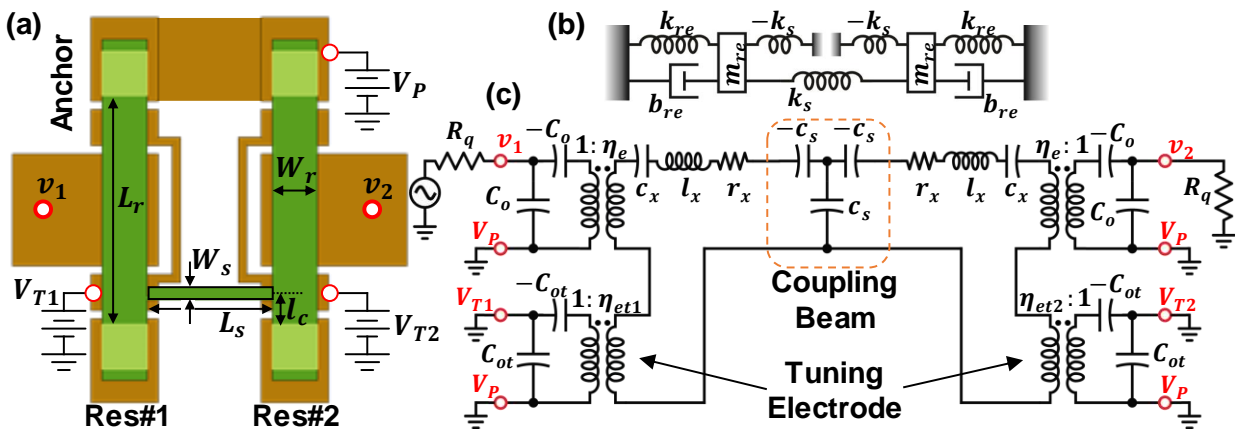
Figure 3.6: (a) Illustration of a 2CC-beam filter with biasing and tuning circuitry, (b) mechanical equivalent model of the 2nd-order filter coupled by quarter-wavelength coupling beams, (c) and its electrical equivalent circuit. The model includes ideal transformers to model the tuning electrodes, as well as the main input/output electrodes.

$$\alpha^4 = \frac{\rho}{E} \cdot \frac{W_s h L_s^4}{I_s} \cdot \omega^2 = 12 \frac{\rho}{E} \cdot \frac{L_s^4}{h^2} \cdot \omega^2, \qquad I_s = \frac{W_s h^3}{12}$$

$$k_s = \frac{E I_s \alpha^3 (\sin \alpha + \sinh \alpha)}{L_s^3 (\cos \alpha \cosh \alpha - 1)}$$

$$c_s = \frac{1}{k_s}$$

(3.6)

The mechanical system of Figure 3.6 (b) has two distinct mass with corresponding displacement amplitude and hence, has two degrees of freedom. Equations 3.7 formulate the steady-state response of this system for the applied force at the input. Since the system has two degrees of freedom, it will have two distinct eigenvalues and corresponding eigenvectors, as presented in equation 3.8. This calculation of eigenvalues assumes the loss in the system is very small and the resonating tanks have high quality factor. Equation 3.8 implies that the resonators are vibrating in phase at the first eigenvalue and out of phase at the second one and the resonators have equal displacement amplitude in both eigenvectors. These are direct consequences of quarter-wavelength coupling beam design. Assuming the coupling beam is much smaller than the main resonators and consequently, it is more compliant, equation 3.9 can approximate the eigenvalue resonance frequencies to find the fractional bandwidth $\Delta\omega/\omega_o$. This equation suggests that the separation between the resonance frequencies depends on the ratio between the resonator and coupling beam stiffness values and these two resonances are equally spaced around the center frequency of the resonating tanks ω_o. Therefore, the mechanical design of the system determines the system bandwidth; for a channel-select filter with tiny fractional bandwidth the resonator should be much stiffer than the coupling beam.

$$\begin{cases} -m\omega^2 X_1 + bj\omega X_1 + kX_1 - k_s X_2 = F_1 \\ -m\omega^2 X_2 + bj\omega X_2 + kX_2 - k_s X_1 = 0 \end{cases}$$

$$\begin{bmatrix} k - m\omega^2 + bj\omega & -k_s \\ -k_s & k - m\omega^2 + bj\omega \end{bmatrix} \begin{bmatrix} X_1 \\ X_2 \end{bmatrix} = \begin{bmatrix} F_1 \\ 0 \end{bmatrix}$$

$$\begin{bmatrix} X_1/F_1 \\ X_2/F_1 \end{bmatrix} = \frac{1}{(k - m\omega^2 + bj\omega)^2 - k_s^2} \begin{bmatrix} k - m\omega^2 + bj\omega \\ k_s \end{bmatrix}$$

$$\begin{bmatrix} X_1/F_1 \\ X_2/F_1 \end{bmatrix} = \frac{1}{([k - k_s] - m\omega^2 + bj\omega)([k + k_s] - m\omega^2 + bj\omega)} \begin{bmatrix} k - m\omega^2 + bj\omega \\ k_s \end{bmatrix}$$

(3.7)

$$\omega_{o1}^2 = \frac{k - k_s}{m}, \qquad \begin{bmatrix} X_1/F_1 \\ X_2/F_1 \end{bmatrix} \cong \frac{1}{2bj\omega} \begin{bmatrix} +1 \\ +1 \end{bmatrix}$$

$$\omega_{o2}^2 = \frac{k + k_s}{m}, \qquad \begin{bmatrix} X_1/F_1 \\ X_2/F_1 \end{bmatrix} \cong \frac{1}{2bj\omega} \begin{bmatrix} -1 \\ +1 \end{bmatrix}$$

(3.8)

$$\omega_{o1} = \sqrt{\frac{k - k_s}{m}} = \omega_o \sqrt{1 - \frac{k_s}{k}} \cong \omega_o \left(1 - \frac{1}{2} \cdot \frac{k_s}{k}\right)$$

(3.9)

$$\omega_{o2} = \sqrt{\frac{k + k_s}{m}} = \omega_o \sqrt{1 + \frac{k_s}{k}} \cong \omega_o \left(1 + \frac{1}{2} \cdot \frac{k_s}{k}\right)$$

$$\frac{\Delta\omega}{\omega_o} = \frac{\omega_{o2} - \omega_{o1}}{\omega_o} = \frac{k_s}{k}$$

The analysis of electrical lumped model in Figure 3.6 (c) results in the same conclusions. Investigation of the impedance Z, admittance Y, or other metrics for any types of input or output can determine the circuit eigenvalues. Here, the study of system impedance for short-circuited input and output simplifies the analysis due to the high-level of symmetry in the system. Due to this symmetry, the motional current in each mesh should be equal. If the motional currents are in phase, the net current through the center branch is zero and can act as a short circuit, shown in Figure 3.7 (b). At this mode, the coupling beam effectively reduces the effective stiffness of each resonating tanks and reduces the resonance frequency. On the other hand, if the motional currents in both meshes are out of phase, the current in the center branch is twice the current in each mesh. Hence, by splitting the coupling capacitance C_s into two parallel capacitors with twice the
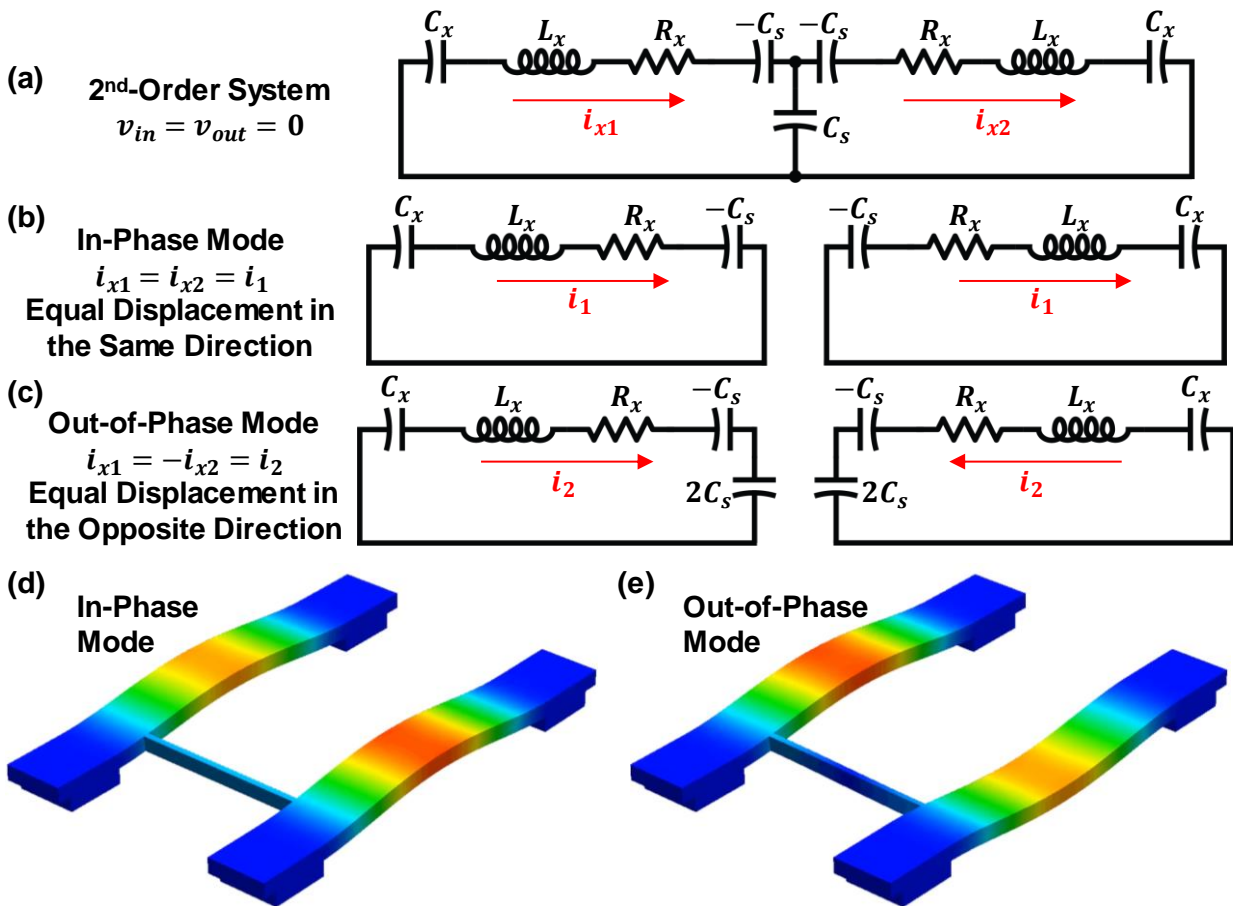
Figure 3.7: (a) Simplified 2nd-order filter with grounded input and output. The system has two distinct mode shapes: (1) when the current in both branches are equal and in phase, therefore there is no current through Cs and the center point is effectively ground; (2) when both currents are equal and in opposite directions.

capacitance value, the meshes can be separated as shown in Figure 3.7 (c). Equation 3.10 states the resonance frequencies of the series *RLC* tanks of each mode. This analysis shows the eigenvalues are spaced equally on both side of the resonator f_o and the ratio between resonator and coupling beam motional capacitance determines the fractional bandwidth.

$$\omega_{o1} = \sqrt{\frac{1}{L_x(C_x||-C_s)}} = \sqrt{\frac{C_s - C_x}{L_x C_x C_s}} = \omega_o \sqrt{1 - \frac{C_x}{C_s}} \cong \omega_o \left(1 - \frac{1}{2} \cdot \frac{C_x}{C_s}\right)$$

$$\omega_{o2} = \sqrt{\frac{1}{L_x(C_x||C_s)}} = \sqrt{\frac{C_s + C_x}{L_x C_x C_s}} = \omega_o \sqrt{1 + \frac{C_x}{C_s}} \cong \omega_o \left(1 + \frac{1}{2} \cdot \frac{C_x}{C_s}\right) \tag{3.10}$$

$$\frac{\Delta\omega}{\omega_o} = \frac{\omega_{o2} - \omega_{o1}}{\omega_o} = \frac{C_x}{C_s}$$

3.2.1   LOW-VELOCITY COUPLING

Equations 3.9 and 3.10 suggest that a channel-select filter with tiny fractional bandwidth requires the resonator to be much stiffer than the coupling beam and the desired system bandwidth determines this ratio. Equation 3.11 presents the coupling beam stiffness at the filter center frequency f_o. Since the material properties and device height are determined by the resonator design and quarter-wavelength design fixes α, the coupling beam width is the only design parameter to engineer the coupling beam stiffness and filter fractional bandwidth. However, the practical fabrication consideration limits the minimum achievable width. As a result, the resonator stiffness serves as the other design parameter to control the fractional bandwidth. But the resonator stiffness determines the system pole locations and hence, the filter design comprise the tradeoff between different specifications.

$$k_s = \left(\frac{E\rho^3}{12}\right)^{1/4} \cdot \frac{(\sin\alpha + \sinh\alpha)}{(\cos\alpha\cosh\alpha - 1)} \cdot (h\omega_o)^{3/2} \cdot W_s$$

$$k_s = 8.846 \cdot \frac{(\sin\alpha + \sinh\alpha)}{(\cos\alpha\cosh\alpha - 1)} \cdot EW_s \left(\frac{h}{L_r}\right)^3 \tag{3.11}$$

On the other hand, equation 2.27 suggests that a CC-beam resonator has different effective stiffness along the beam length and has a minimum at the beam center where the displacement amplitude is maximum and then approaches to infinity near the anchor points where the resonator displacement is very small, as shown in Figure 3.8 (b). The stiffness ratio in the equation 3.9 is essentially between the coupling beam stiffness and the effective stiffness of the resonator at the joint location. Therefore, the joint location l_c is a powerful design parameter to determine the filter fractional bandwidth, as presented in Figure 3.8 (c). The choice of coupling location is referred to as low-velocity coupling and can decouple the system pole design from the filter bandwidth and provides another degree of freedom for proper filter design.

The *RLC* resonating tanks in Figure 3.6 are typically modeled at the center of the CC-beam with equivalent values given in equations 2.28 and therefore, the current in each meshes is equivalent to resonator velocity at the beam center. An ideal transformer can provide the velocity conversion from the beam center to the coupling location l_c. Equation 3.11 provide the expression for the required velocity conversion. Figure 3.8 (d) presents the simulated fractional bandwidth as a function of coupling location and illustrates the need for near-anchor attachment of the coupling beam to achieve channel selection.

$$i\left(\frac{L_r}{2}\right) = \eta_c i(l_c)$$

$$\eta_c = \frac{i\left(\frac{Lr}{2}\right)}{i(l_c)} = \frac{X\left(\frac{L_r}{2}\right)}{X(l_c)} = \sqrt{\frac{k_r(l_c)}{k_r\left(\frac{L_r}{2}\right)}} = \sqrt{\frac{k_r(l_c)}{k_{re}}} \tag{3.12}$$

Note that the equations 3.9-10 are derived without any restriction on the filter type and system pole locations. Equation 3.9 should be modified to equation 3.13 to include the required pole distribution for different filter types to achieve a given filter bandwidth. Here, k_i is the normalized coupling coefficient and depends on the filter type (i.e. Butterworth, Chebyshev, etc.). The normalized coupling coefficients are tabulated in filter synthesis cook books [27].

$$\frac{\Delta\omega}{\omega_o} = \frac{1}{k_i} \cdot \frac{k_s}{k_{rc}} \tag{3.13}$$
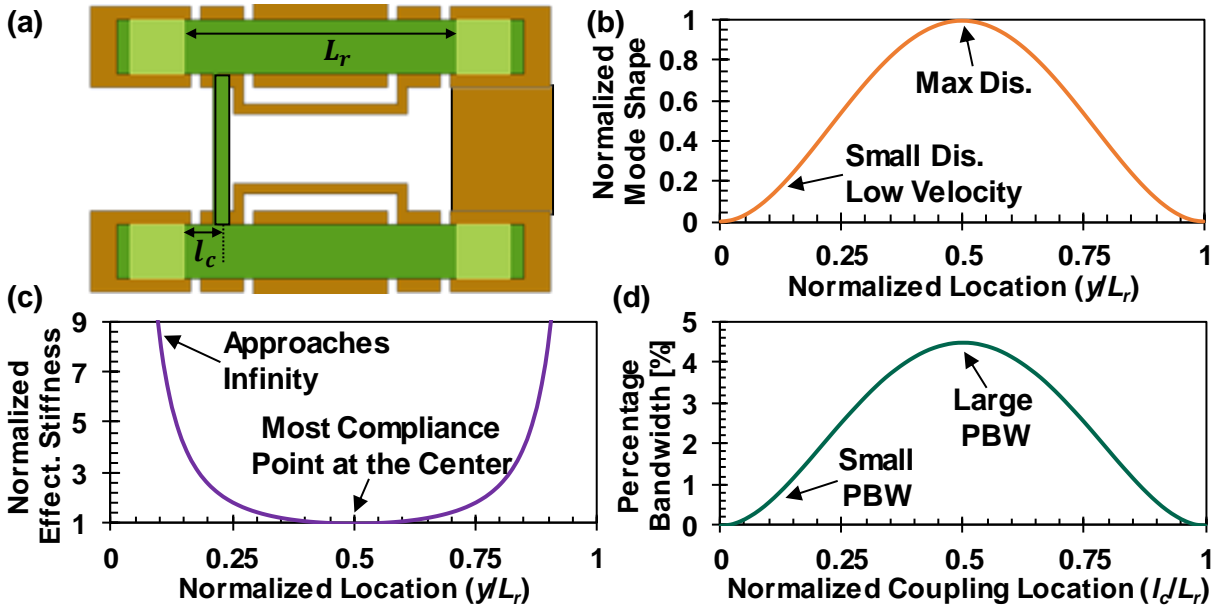
Figure 3.8: (a) The relative position of the quarter-wavelength coupling beam to the resonator length, (b) normalized resonator mode shape alongside the beam length, (c) the resonator effective stiffness normalized to the stiffness at the center, (d) the eigenmode separation as a function of the relative coupling beam position.

3.2.2   TERMINATION RESISTANCE

The micromechanical 2nd-order filter of Figure 3.6 comprises of micromechanical resonators with quality factor as high as 10,000 or more. Such a high-quality factor makes the corresponding eigenvalue transfer functions extremely frequency selective and the final filter transfer function has substantial and unacceptable ripple in the passband. Note that the phase difference between two eigenmodes are essential to achieve the final filter response; both eigenmodes are in phase
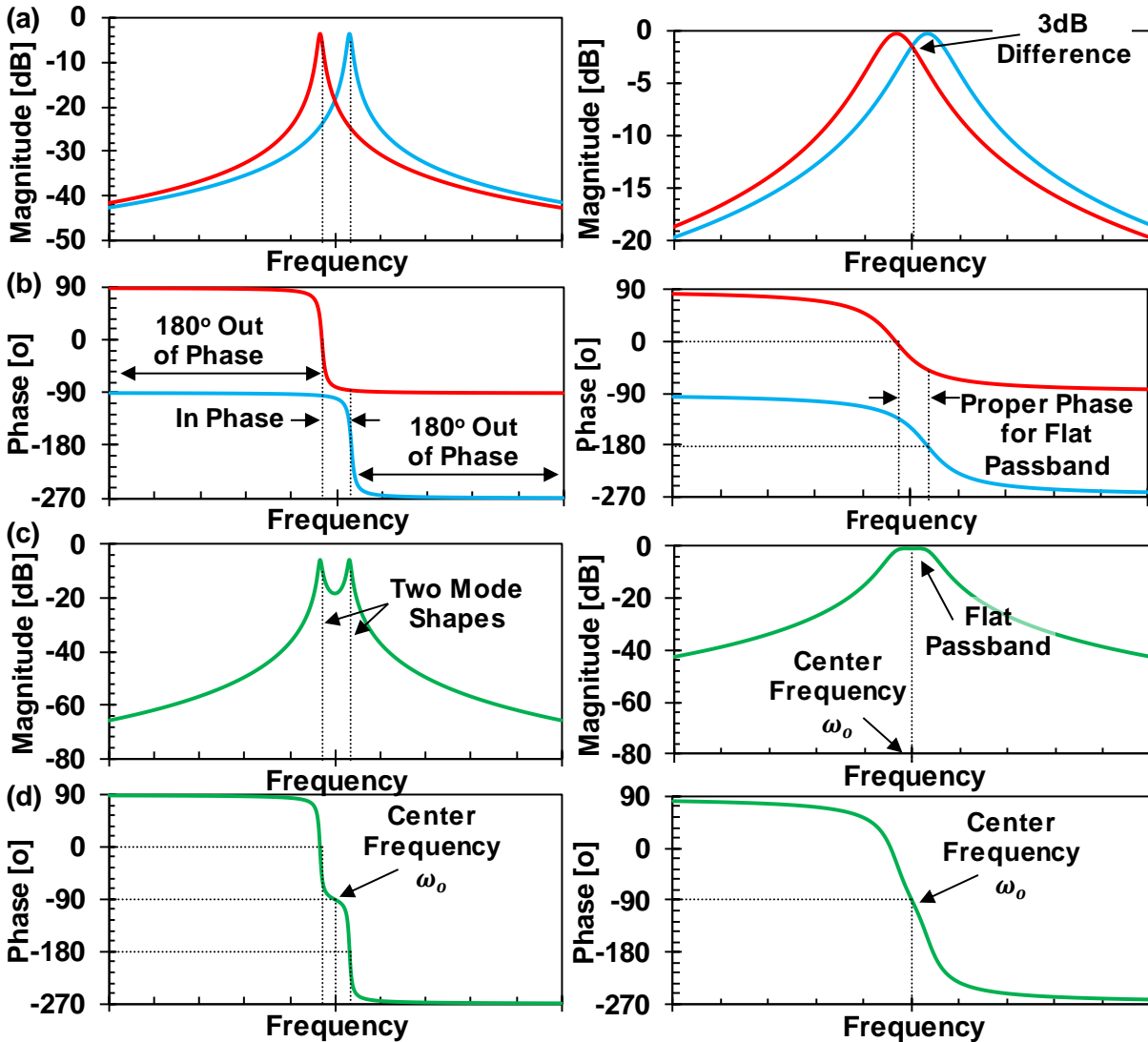
Figure 3.9: Formation of 2nd-order filter response from the two mode shapes of figure 3.6. Filter including high-Q resonators on the left and controlled-Q resonator on the right. Magnitude and phase of the mode shape response and the final filter response are shown in (a-b) and (c-d) respectively. Addition and subtraction of the displacement where the mode shapes are in phase and out of phase, result in the smaller insertion loss in the passband and larger stopband rejection. Proper Q-control via termination resistance is required for flat passband response.

within the passband and hence, their amplitudes add constructively, while they are out of phase outside the passband and subtract from each other, as shown in Figure 3.9.

To minimize the passband ripple, the eigenmode amplitudes at the center frequency f_o should be half of their maximum amplitude, at f_{o1} and f_{o2}. This argument suggests that the quality factor Q of the constituent resonator should be loaded such that each eigenmode has the same bandwidth as the filter [26]. In other word, the loaded quality factor Q_L of the input and output resonators should be the same as filter quality factor Q_f. Equation 3.14 provides the expression for the required termination resistance R_Q. Note that this argument has ignored the filter type and the expression 3.14 should be modified to equation 3.15 to account for requirements of different filter types. Here, q_n is a modification factor that depends on the filter type and can be found in filter synthesis cookbooks [27]. Figure 3.9 shows the formation of the flat-passband filter response by proper termination.

$$Q_L = Q\left(\frac{R_x}{R_x + R_Q}\right) = \frac{\omega_o}{\Delta\omega} = Q_f \rightarrow R_Q = R_x\left(\frac{Q}{Q_f} - 1\right) \tag{3.14}$$

$$R_Q = R_x\left(\frac{Q}{q_n Q_f} - 1\right) \tag{3.15}$$

The simple electrical circuit of Figure 3.10 approximates the filter transfer function within the passband by its motional resistances. This circuit can estimate the filter insertion loss, as shown in equation 3.16. This equation implies that to achieve a filter with small insertion loss, the unloaded quality factor of the constituent resonators Q_o should be much larger than the filter quality factor Q_f. For instance, to maintain the insertion loss smaller than 1dB, the resonator quality factor should be 10x the filter quality factor, as shown in Figure 3.10 (b). This expression provides further explanation why channel-select filter with very small fractional bandwidth and large Q_f, require high-quality factor resonators.

The required termination resistance of a filter with small insertion loss can be approximated by the equation 3.17: (1) the first term in this equation is determined by the filter specifications and the application of interest, (2) the second term is the resonator electromechanical coupling strength and is mainly determined by the technology, (3) the third term is the native impedance of
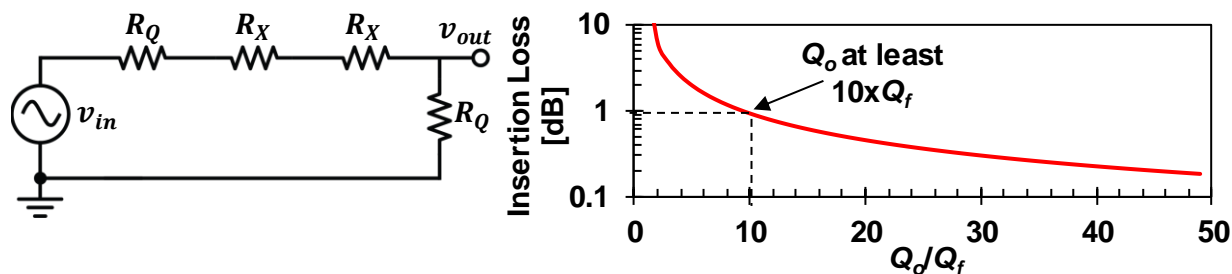
Figure 3.10: (a) Electrical equivalent circuit of a 2nd-order filter, approximated at the passband. (b) Filter insertion loss as a function of the resonator unloaded quality factor Q_o, relative to the filter quality factor Q_f.

the resonator define as the impedance of the static capacitance at the filter center frequency $Z_o = 1/\omega_o C_o$. For a given application and resonator technology, the native impedance is the only design parameter to achieve a desired termination resistance and depends on the resonator area. Resonator width W_r determines the native impedance of a CC-beam resonator, since the resonator length L_r and gap spacing d_o are determined by center frequency and the fabrication limits. Note that the resonator quality factor Q does not affect the termination resistance, only the passband insertion loss.

$$IL = -20 \log\left(\frac{R_Q}{R_Q + R_x}\right) = 20 \log\left(1 + \frac{R_x}{R_Q}\right) = 20 \log\left(\frac{1}{1 - \frac{q_n Q_f}{Q}}\right) \tag{3.16}$$

$$R_Q = \frac{1}{\omega_o Q C_x}\left(\frac{Q}{q_n Q_f} - 1\right) \cong \frac{1}{q_n Q_f} \cdot \frac{1}{\left(\frac{C_x}{C_o}\right)} \cdot \frac{1}{\omega_o C_o} \tag{3.17}$$

3.2.3 RESONATOR ELECTRICAL TUNING

The realization of channel-select filter with tiny fractional bandwidth asks for fabrication variation beyond the capability of current surface micromachining techniques, as explained in section 3.1.3. The inherent electrical tuning capability of capacitive resonators by electrical stiffness provides a solution to compensate the fabrication tolerances without any need for post-fabrication processes such as laser trimming [69], selective etching [70], selective deposition [71], etc. Hence, it is of utmost importance to accurately model the electrical tuning and confirm the sufficiency of tuning range provided by tuning electrodes to overcome any fabrication variations. Figure 3.11 presents the complete lumped electrical circuit to accurately model and design a micromechanical filter, like the one in Figure 3.6. Note that both terminals of tuning transformers are grounded, since they are connected to constant DC voltage sources, V_P and V_T.
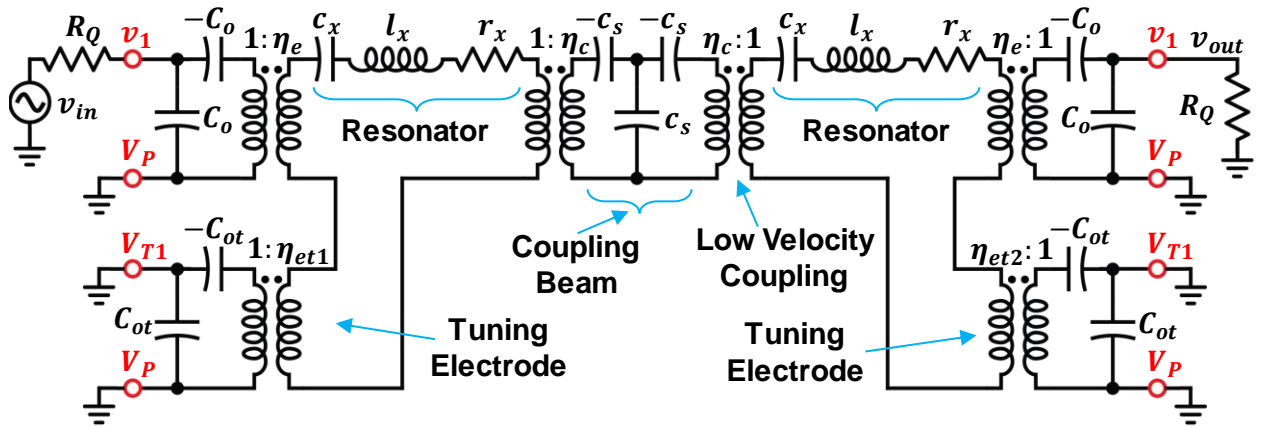
Figure 3.11: Complete electrical circuit modeling the 2nd-order CC-beam filter.

Table 3.1 captures the design procedure presented here alongside the relevant governing equations with appropriate approximation.

3.3 EXPERIMENTAL RESULTS

The procedure of Table 3.1 has been used to design a channel-select filter with 0.15% fractional bandwidth at 10MHz. Table 3.2 summarizes the designed and simulated parameters and dimensions of this filter and the damascene fabrication process of Figure 2.8 were used to make it. Figure 3.12 shows the SEM picture of a released device with the proper measurement circuitry. Since the designed termination resistance of this filter is different than 50Ω termination of commercial vector network analyzers (VNA), on-chip resistors should be used to properly terminate the filter. However, simple on-chip resistors in series with the VNA, as shown in Figure 3.12 (b), will form a resistor divider at the output and degrade the performance excessively. The trans-impedance amplifier of Figure 3.12 (c) or the unity buffer of Figure 3.12 (d) can provide proper filter termination and impedance matching at the same time and prohibit any performance degradation. In a real-world application, the stage following the filter, such as a low-noise amplifier LNA, will deliver the termination resistance and there will be no need for external resistors or any amplifiers.

Table 3.1: Summary of micromechanical filter design procedure
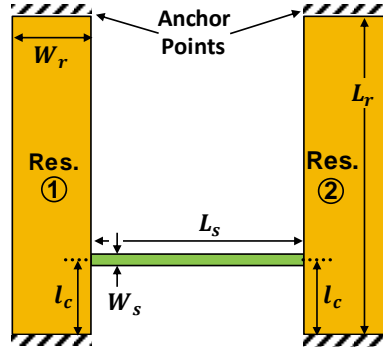
Given/Set Values	Procedure/Objective	Relevant Design Equations for a Given Parameter
Filter Schematic: Given and Set Values: 1. Resonator dimensions and equivalent lumped mechanical/electrical parameters from Table2.1. 2. Filter type such as Inverse Chebyshev response in this example. 3. Normalized filter coupling coefficients k_{sij} and loaded q_i of Inverse Chebyshev response from filter cookbooks [27]. 4. Set designed filter bandwidth BW. 5. Filter coupling locations l_{ci}. 6. Choose proper W_{sij} for coupling beam.	Obtain lumped equivalent mechanical parameters for CC-beam resonator.	Use Table 2:1 to obtain m_{re}, k_{re}, and c_{re}.
	Find filter coupling coefficients k_{sija}, k_{sijb}, and k_{sijc} where i and j denote adjacent resonators. Determine dimensions W_{sij} and L_{sij} for filter coupling beams.	$$k_s = \eta_c^2 k_{re}\left(\frac{BW}{f_o}\right)k_q$$
		where k_{re} is the resonator effective stiffness at the center and η_c is the low-velocity transformation.
		Solve equation 3.5 for $\lambda/4$ coupling (1st root) to find L_s.
		Use equation 3.11 for k_s and optimize the solution for W_s and the low-velocity transformation η_c.
	Obtain mechanical response using the model of fig***.	Use Figure 3.6 (b) to plot mechanical frequency response
	Determine equivalent circuit parameters for CC-beam resonator and coupling/bridging beams.	Use equations 2.19 to determine the equivalent electrical model shown in Figure 3.11.
		$$c_s = \frac{1}{k_s}$$
	Determine the termination resistance R_Q.	$$R_Q = \left(\frac{Q}{q_i Q_{fltr}} - 1\right)R_x$$ Where R_x is the resonator motional impedance, Q is the unloaded resonator quality factor, and $Q_{fltr}=f_0/$BW.
	Determine filter insertion IL.	$$IL = 20\log\left(1 + \frac{R_Q}{R_x}\right)$$
	Obtain electrical frequency response using the model of Figure 3.11.	Insert all the required parameters of Figure 3.11 and use any circuit simulator to simulate filter frequency response such as Figure 3.9

Figure 3.13 presents the measured frequency performance of this 2nd-order channel-select filter. The filter is centered at 8.6MHz and has tiny fractional bandwidth of 0.15%. The in-band insertion loss is 1dB achieved by 10kΩ termination resistance. This filter has out-of-band rejection of 42dB and 20dB shape factor of 2.56.

The channel-select filter of Figure 3.13 were initially designed to be centered at 10MHz, for a 2.2μm-thick structural poly process. However, the final deposited polysilicon was only 1.8μm thick and therefore, the micromechanical resonators and filters were centered at 8.6MHz. The different structural thickness changed the center frequency, but it did not affect the quarter-wavelength design. In-depth investigation of equation 3.4 reveals that parameter α only depends on the resonator length and not on the coupling beam height or width, hence, the required coupling beam length for quarter-wavelength design does not change by the structure height. On the other hand, the coupling beam stiffness k_s changes by the structure height as suggested by equation 3.11, but the dependency on the height is the same as the resonator stiffness k_{re} (equation 2.28) and hence, the change in the structure height does not affect the fractional bandwidth neither.

$$H_6 = \sinh \alpha \cos \alpha + \cosh \alpha \sin \alpha = 0 \tag{3.18}$$
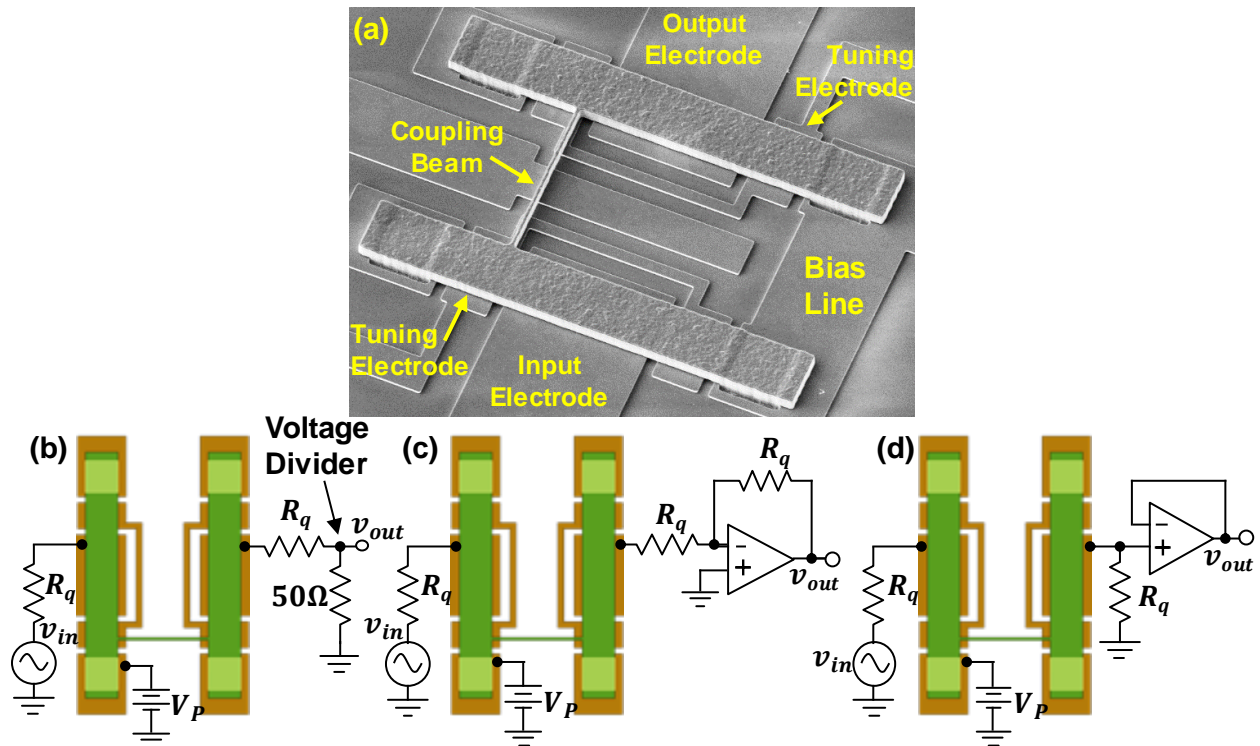
Figure 3.12: (a) SEM photo of the released 2nd-order CC-beam filter and the measurement circuitry: on-chip resistor in series with the VNA (b), trans-impedance buffer (c), unity-gain buffer (d). Application of (b) will degrade the output signal due to the formation of the voltage divider at the output. Any RQ larger than 50 requires output buffers offered in (c) or (d).

$$\alpha = \sqrt[4]{\frac{\rho}{E} \cdot \frac{W_s h L_s^4}{I_s}} \cdot \omega_o^2 = 4.735 \left(\frac{L_s}{L_r}\right)$$

3.3.1 OUT-OF-BAND REJECTION LIMITS

Comparison of the experimental frequency response of Figure 3.13 to the simulation results of Figure 3.11 shows that the filter out-of-band rejection far from the center frequency does not follow the prediction of neither electrical nor mechanical lumped models and the rejection is very limited. The lumped models presented in Figure 3.6 and Figure 3.11 neglect the electrical feedthrough in the filter structure: there is a capacitive coupling between the input and output electrodes and resonators and the coupling beams provide the resistive paths from the input to the output electrodes, as shown in Figure 3.14. This electrical feedthrough path limits the out-of-band rejection to the feedforward signal through the capacitive-resistive path. The constant bias voltage source V_P should ground the capacitor C_o terminal and short the feedforward path to ground, as shown in Figure 3.11, but the bias line has finite resistance and it is not a perfect short to ground. The electrical model of Figure 3.14 modifies the one in Figure 3.11 to account for the finite resistance of the bias line. This modification does not change the filter passband response, since the feedthrough signal power is orders of magnitudes weaker than the motional signal. However, this feedforward path dominates the filter response far-from the center frequency, and hence, sets the limits on the out-of-band rejection. Figure 3.14 (d) presents the effective electrical model far from the center frequency and Figure 3.14 (b) shows the simulation results of the out-of-band rejection for different values of feedthrough capacitance and resistances. Equation 3.19 provides the expression for out-of-band rejection derived from the model of Figure 3.14 (e).

$$Rej = 20 \log \left| \frac{R_Q^2 + R_1^2 + 2\left(R_Q R_1 + R_Q R_2 + R_1 R_2\right) + \left(R_Q + R_1 + R_2 + \frac{1}{j\omega_o C_o}\right)\frac{1}{j\omega_o C_o}}{2 R_2 R_Q} \right| \quad (3.19)$$

V_P = 4V	
f_0 = 8.579MHz	
BW = 13kHz	
PBW = 0.15%	
R_q = 10kΩ	
I.L. = -1dB	
Ripple < 2dB	
Stop. Rej. = 42dB	
20dB Sh. F. = 2.56	
P_{in} = -40dBm	
Press. = 1mTorr	
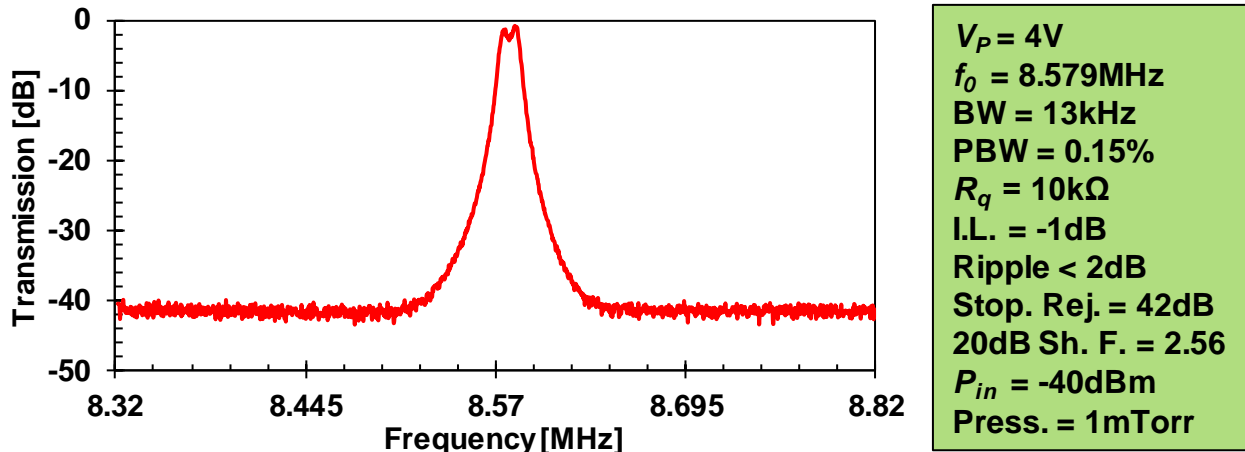
Figure 3.13: The frequency response of the 2CC resonator of Figure 3.12.

Equation 3.17 suggests how rejection can be improved, considering that C_o and R_Q are determined by the filter design procedures and have finite values:

i)   Ideal Interconnect:

An ideal bias line with very small resistance, i.e. $R_{b2} \approx 0$, can improve the rejection by shorting the electrical feedforward signal to small-signal ground. A highly-doped thick-poly interconnect can reduce the resistance of the bias line. On the other hand, implementation of metal interconnect can eliminate the rejection problem, at the cost of fabrication complexity and galvanic issues in the release process.

ii)   Non-Conductive Coupling Beams:

The capacitors in the model of Figure 3.14 presented for the out-of-band rejection are inherent to the working principles of capacitive transducers and not eliminable. On the other hand, the resistive path through the coupling beams is not deep-rooted in the capacitive transduction and hence, replacing the coupling beams with non-conductive material, i.e. $R_{b3} \rightarrow \infty$, can break the resistive path and improve the out-of-band rejection. The implementation of this non-conductive coupling beam was not investigated in this work and can be the subject of further study.

iii) Differential Mechanical Circuits:
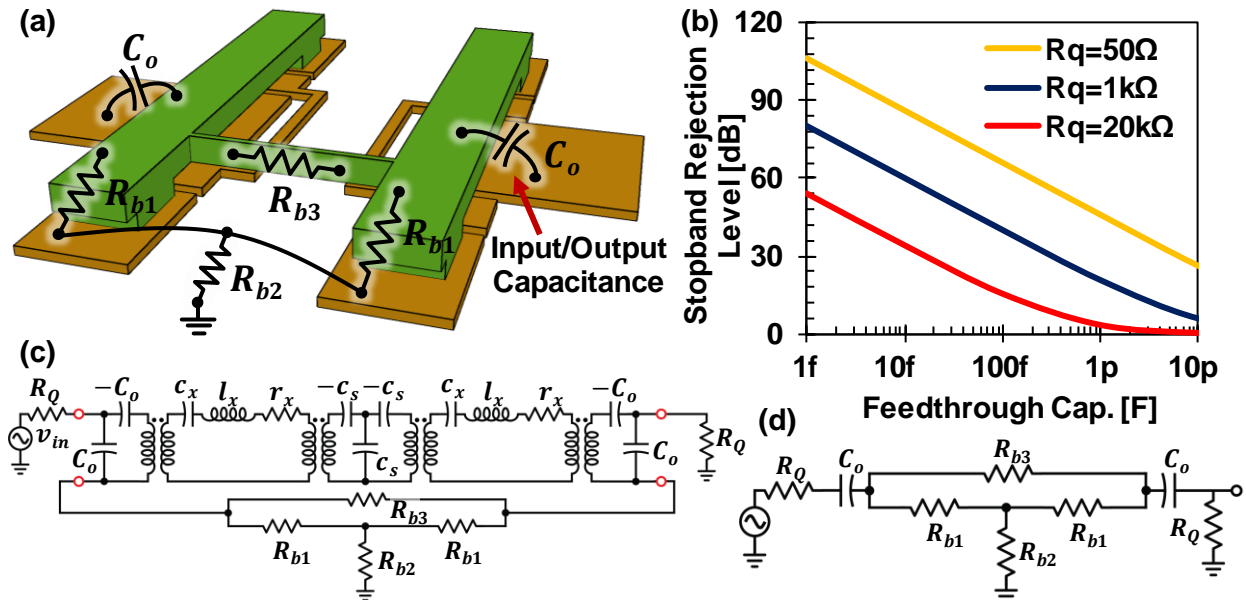
Figure 3.14: (a) Illustration of the parasitic capacitance and resistance in the system which limits the filter wideband rejection. (b) Simulation of stopband rejection as a function of parasitic capacitance and filter termination resistance R_Q. (c) The overall filter electrical equivalent circuit of the filter including the parasitic elements and (d) the simplified equivalent circuit outside the passband, for stopband rejection simulation.

A mechanical circuit with differential input and output can theoretically cancel out all the feedthrough signal due to the phase difference in different paths. Differential mechanical filters such as the one implemented in [48], improved the out-of-band rejection up to 10-20dB. The implementation of differential filters was not investigated in this work and can be the topic of further study.

Table 3.2: Filter Data Summary

Parameter	2CC Design		Units
	Design/Sim.	Meas.	
Center Frequency, f_o	8.469	8.081	MHz
Resonator Q	10,000	15,100	—
Bandwidth, BW	11.1	10.7	kHz
Percent Bandwidth, (BW/f_o)	0.131	0.132	%
Filter DC-Bias, V_P	30	21	V
Loaded q_i^*	1.0	--	—
Normalized Filter Coupling Coef., k	0.674	--	—
Filter Coupling Beam Length, L_s	22.3	--	μm
Filter Coupling Beam Width, W_s	0.75	--	μm
Coupling/Bridging Beam Thickness, h	2	1.985	μm
Resonator Mass @ I/O, m_{re}	5.829×10^{-13}	5.902×10^{-13}	kg
Resonator Stiffness @ I/O, k_{re}	1.923×10^3	1.772×10^3	N/m
Resonator Damping @ I/O, c_{re}	3.036×10^{-9}	1.841×10^{-9}	Ns/m
Filter Coupling Location, l_c	4.1, 3.6	4.5, 4.0	μm
Coupling Beam Stiffness, k_{sa}	-109.56	87.72	N/m
Coupling Beam Stiffness, k_{sc}	109.56	103.09	N/m
Filter Coupling Capacitance, c_{sa}	-0.0091	-0.0114	F
Filter Coupling Capacitance, c_{sc}	0.0091	0.0097	F
Mechanical Transformer Turn Ratio at l_c, η_c	8.03, 10.18	7.04, 8.071	C/m
Equivalent Inductance, l_x	5.829×10^{-13}	5.902×10^{-13}	H
Equivalent Capacitance, c_x	4.323×10^{-4}	5.644×10^{-4}	F
Equivalent Resistance, r_x	3.036×10^{-9}	1.841×10^{-9}	Ω
Electromechanical Coupling Coefficient, η_e	1.833×10^{-6}	1.409×10^{-6}	C/m
Calculated Equivalent Resistance, R_x	0.904	1.018	kΩ
Calculated Equivalent Inductance, L_x	0.173	0.297	H
Calculated Equivalent Capacitance, C_x	2.12	1.257	fF
Static Overlap Capacitance, C_o	9.44	10.12	fF
Electromechanical Coupling C_x/C_o	22.5	12.42	%
Termination Resistance, R_Q	11	12	kΩ
Insertion Loss, IL	0.3	1.2	dB
20 dB Shape Factor	2.07	2.08	—
Stopband Rejection, SR	90	40	dB
Loss Pole position, $|f_{loss\,pole} - f_o|/f_o$	0.369	0.297	%

Chapter 4 MECHANICAL COUPLING BEAMS

The cascaded filter design procedure presented in Chapter 3 elaborated on the importance of the mechanical beam design. While the constituent micromechanical resonators determine the filter center frequency, the design of mechanical coupling beams determine the filter bandwidth and more importantly, the filter type. Moreover, coupling beams with length equivalent to the half-wavelength are frequently used to couple identical resonators in order to increase the resonator area and reduce the effective motional resistance in filter or oscillator applications. Therefore, more detailed and thorough understanding of the coupling beam frequency behavior and its impact on the system poles is necessary. This chapter introduces the extensional and flexural beam mechanical model and provides accurate analytical solutions in comparison to the conventional approximate solutions.

4.1 COUPLING BEAM MECHANICAL MODEL

The design of coupling beams of Figure 4.1 is complicated, since beside the effective stiffness, they have finite effective mass that have to be considered. The coupling beam mass is not negligible, especially for the micromechanical system where the static mass of coupling beams is in the same order as the resonator static mass and if neglected, can introduce unwanted distortion in the passband. A simple mass-spring model, like the one in Figure 4.2, does not accurately represent the narrow long coupling beams used often in micromechanical filters, since the phase at both side of the beam is significantly different and this model does not capture the phase difference. A long coupling beam at high frequency, such as the extensional and flexural beams shown in Figure 4.1, can be modeled by an acoustic transmission line, an equivalent concept to the electromagnetic transmission line, in order to precisely capture the important phase difference at both ends [72].

A distributed mechanical system can model the acoustic transmission line, in comparison to electromagnetic transmission line. A distributed system such as the one shown in Figure 4.2 (b) determines the frequency response and phase difference, but it is impractical for the filter design and optimization procedure. From the filter design perspective, the details of acoustic wave phase and amplitude alongside the coupling beam is extraneous and a simple model that can predict the phase and amplitude of the force and velocity at one end relative to the other one is sufficient. Analytical solution to the Euler–Lagrange wave propagation equation provides the *ABCD* matrix model for an acoustic transmission line, equivalent to EM, given in equation 4.1.

$$\begin{bmatrix} f_1 \\ \dot{x}_1 \end{bmatrix} = \begin{bmatrix} A & B \\ C & D \end{bmatrix} \begin{bmatrix} f_2 \\ \dot{x}_2 \end{bmatrix} \tag{4.1}$$

The expression in equation 4.2 and 4.3 presents the solution for the extensional and flexural coupling beams of Figure 4.2. Here, β, v_p and Z_o are the acoustic wavenumber, velocity and

impedance, ρ and E are material density and Young modulus, W_s, h and L_s are coupling beam width, height and length, respectively.

$$\begin{bmatrix} f_1 \\ \dot{x}_1 \end{bmatrix} = \begin{bmatrix} \cos(\beta L_s) & jZ_o \sin(\beta L_s) \\ \dfrac{j}{Z_o} \sin(\beta L_s) & \cos(\beta L_s) \end{bmatrix} \begin{bmatrix} f_2 \\ \dot{x}_2 \end{bmatrix}$$

$$\beta = \frac{\omega}{v_P} = \frac{\omega}{\sqrt{\dfrac{E}{\rho}}}, \qquad Z_o = W_s h \sqrt{E\rho}$$

(4.2)
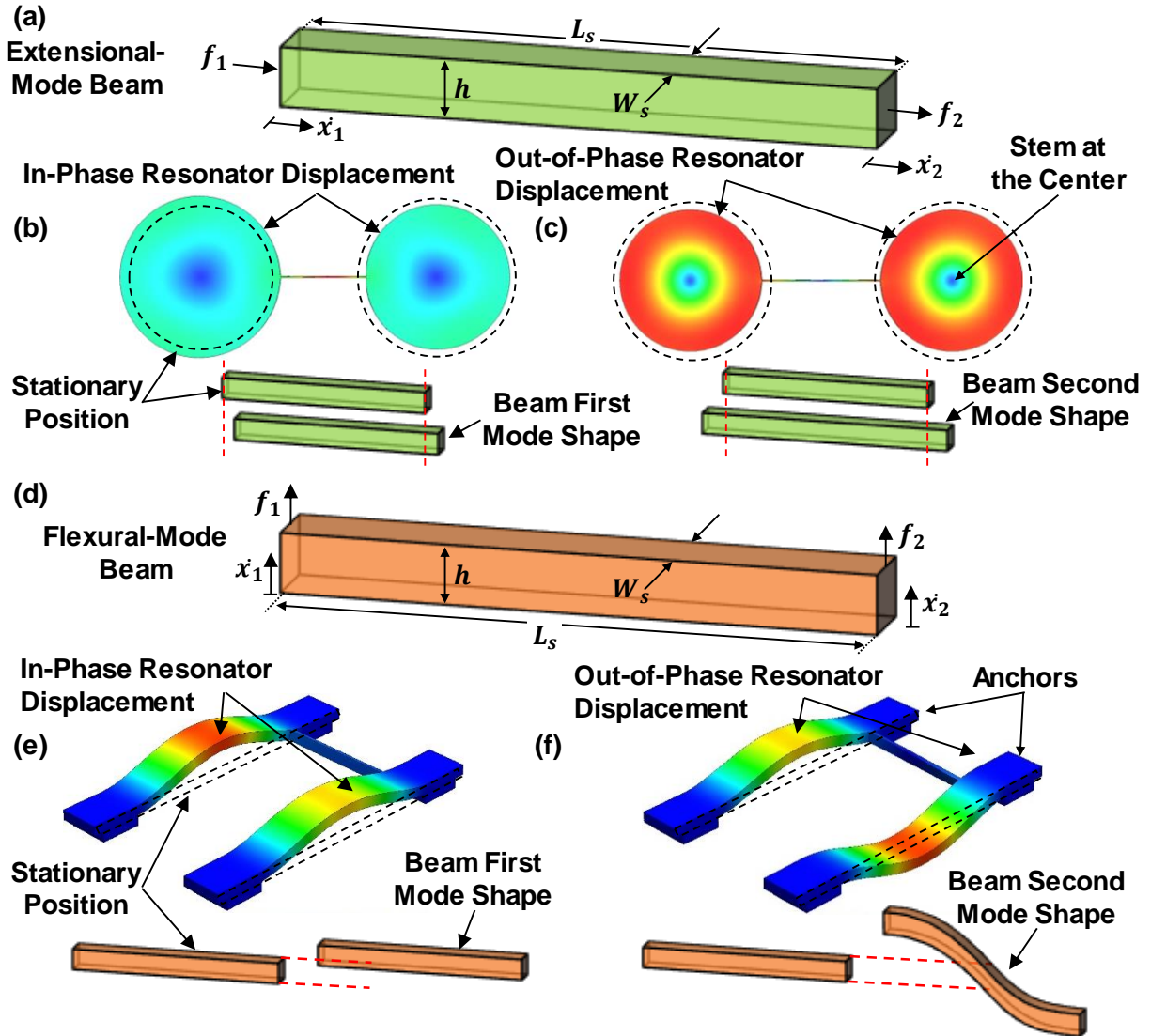
Figure 4.1: (a) Illustration of an extensional-mode coupling beam and (b) the in-phase and (c) out-of-phase modes of a 2 contour-mode disk system. The coupling beam has average displacement when vibrating in phase, while it is expanding and contracting around the center in the out-of-phase mode. (d) Schematic of a flexural-mode coupling beam and the applied forces, (e) the in-phase mode shape of a 2 CC-beam system, and (f) the out-of-phase mode shape. The in-phase coupling beam has average vertical displacement and has a nodal point at the center when in out-of-phase mode.

$$\begin{bmatrix} f_1 \\ \dot{x}_1 \end{bmatrix} = \begin{bmatrix} \dfrac{H_6}{H_7} & -\dfrac{2EI_s\alpha^3 H_1}{j\omega L_s^3 H_7} \\[2ex] -\dfrac{j\omega L_s^3 H_3}{EI_s\alpha^3 H_7} & \dfrac{H_6}{H_7} \end{bmatrix} \begin{bmatrix} f_2 \\ \dot{x}_2 \end{bmatrix}$$

$$\alpha^4 = L_s^4 \left(\frac{\rho W_s h \omega^2}{EI_s} \right), \qquad I_s = \frac{1}{12} W_s h^3$$

$$H_1 = \sinh \alpha \cdot \sin \alpha, \qquad H_3 = \cosh \alpha \cdot \cos \alpha - 1$$
$$H_6 = \sinh \alpha \cdot \cos \alpha + \cosh \alpha \cdot \sin \alpha, \qquad H_7 = \sin \alpha + \sinh \alpha$$

(4.3)

The determinant of *ABCD* matrices in equations 4.2 and 4.3 is equal to one, and hence, a T network of mechanical impedances can represent them, as shown in Figure 4.2, in analogy to EM transmission line. The *ABCD* matrix of this *T* network is given in equation 4.4 and by comparison to coupling beam *ABCD* matrices, different impedances can be found. Figure 4.2 presents the lumped mechanical model of a 2nd-order mass-spring system with a *T* network representing the coupling beam. Equation 4.5 provide the effective stiffness values of the *T* network. Equation 4.6 provides the steady-state matrix representation of the mechanical system of Figure 4.2 and the two eigenvalues of the system are given in the equation 4.7. Note that the stiffness terms k_{sa} and k_{sc} in the system pole expressions, i.e. equation 4.7, are also frequency dependent.

$$\begin{bmatrix} f_1 \\ \dot{x}_1 \end{bmatrix} = \frac{1}{Z_c} \begin{bmatrix} Z_a + Z_b & Z_a Z_b + Z_b Z_c + Z_c Z_a \\ 1 & Z_b + Z_c \end{bmatrix} \begin{bmatrix} f_2 \\ \dot{x}_2 \end{bmatrix}$$

$$Z_a = \frac{A-1}{C}, \qquad Z_b = \frac{D-1}{C} = \frac{A-1}{C}, \qquad Z_c = \frac{1}{C}$$

(4.4)

$$\frac{k_{sa}}{j\omega} = Z_a = Z_b, \qquad \frac{k_{sc}}{j\omega} = Z_c$$

(4.5)

$$\begin{bmatrix} (k_{re} + k_{sa} + k_{sc}) - m_{re}\omega^2 & -k_{sc} \\ -k_{sc} & (k_{re} + k_{sa} + k_{sc}) - m_{re}\omega^2 \end{bmatrix} \begin{bmatrix} X_1 \\ X_2 \end{bmatrix} = \begin{bmatrix} F_1 \\ F_2 \end{bmatrix}$$

(4.6)

$$\text{1}^{\text{st}} \text{ Eigenvalue: } m_{re}\omega^2 - (k_{re} + k_{sa}) = 0$$
$$\text{2}^{\text{nd}} \text{ Eigenvalue: } m_{re}\omega^2 - (k_{re} + k_{sa} + 2k_{sc}) = 0$$

(4.7)

4.2 EXTENSIONAL-MODE COUPLING BEAM

Comparison of equation 4.5 and 4.2 can provide the effective stiffness values k_{sa} and k_{sc} for an extensional coupling beam and is given in equation 4.8. Substituting these terms in equation 4.7 delivers the system eigenvalue expressions, given in equation 4.9. Note that these expressions have nonlinear trigonometric dependencies on the frequency, which should not be ignored in the general case. For any given coupling beam length L_s, each eigenvalue expression has infinite solutions, though the solutions far from the resonator center frequency do not contribute to the system passband and can be neglected. Figure 4.3 presents the solutions of these equations for different coupling beam length, calculated for a disk resonator centered at 132MHz. The system bandwidth shown in Figure 4.3 (c) is defined as the frequency difference between two nearest

modes. The acoustic wave at 132MHz has wavelength of 61µm for the given material properties and as evident from this figure, the system bandwidth has minima at $(2n+1)\lambda/4$ equivalent length and maxima at $n\lambda/2$. The detailed description of maximum and minimum bandwidth will be presented in the following sections.

$$k_{sa} = -\omega Z_o \tan\left(\frac{1}{2}\beta L_s\right) = -\omega Z_o \tan\left(\frac{1}{2}\frac{\omega L_s}{v_P}\right)$$

$$k_{sc} = \omega Z_o \csc(\beta L_s) = \omega Z_o \csc\left(\frac{\omega L_s}{v_P}\right)$$

(4.8)

1st Eigenvalue:

$$m_{re}\omega^2 - k_{re} + \omega Z_o \tan\left(\frac{1}{2}\frac{\omega L_s}{v_P}\right) = 0$$

2nd Eigenvalue:

$$m_{re}\omega^2 - k_{re} - \omega Z_o \cot\left(\frac{1}{2}\frac{\omega L_s}{v_P}\right) = 0$$

(4.9)

The conventional approach to solve this system of equations used to be approximating the frequency term in the trigonometric functions by resonator center frequency ω_o, so the equations have closed-form solutions given in equation 4.10. Figure 4.3 (b, d, f) show the system poles for different coupling beam length. These figures highlight the differences between the solutions of equation 4.9 and 4.10: (1) the approximate solution fails to recognize infinite solutions for a given coupling length and only provide two, (2) the system bandwidth approaches infinity at $n\lambda/2$. Figure 4.4 presents the system bandwidth derived from the both approaches described above and reveals the error in the approximation method: around the $(2n+1)\lambda/4$ coupling length, there are two eigenvalues close to the center frequency and hence, the solutions from the approximation method are very close to the exact solutions. On the other hand, the eigenvalues are far from each other at
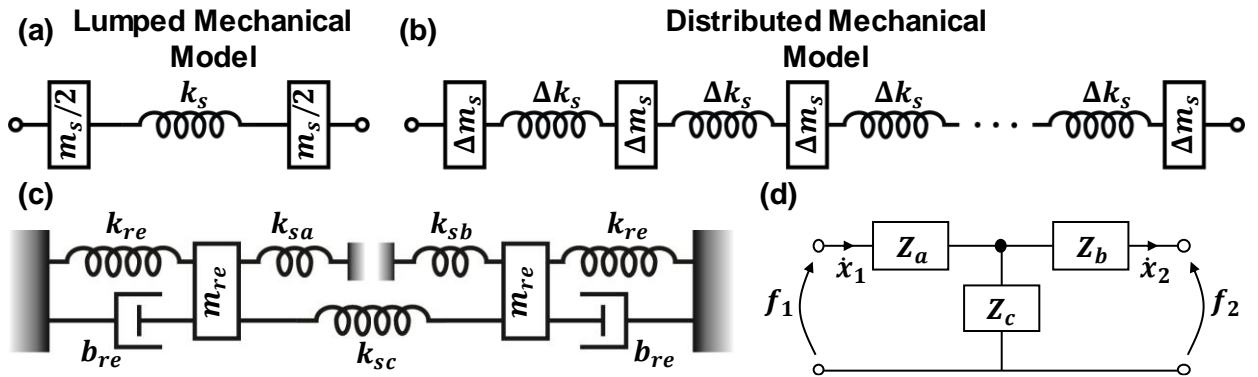
Figure 4.2: (a) Lumped and (b) distributed mechanical models of coupling beams. Lumped mechanical model does not capture the wave propagation and phase difference across the coupling beam. The distributed model can be represented by a transmission line in mechanical (c) or electrical domain (d).

$n\lambda/2$ and hence, the approximation method does not work and sets one of the system eigenvalues at infinity, making the bandwidth approaching the infinity.
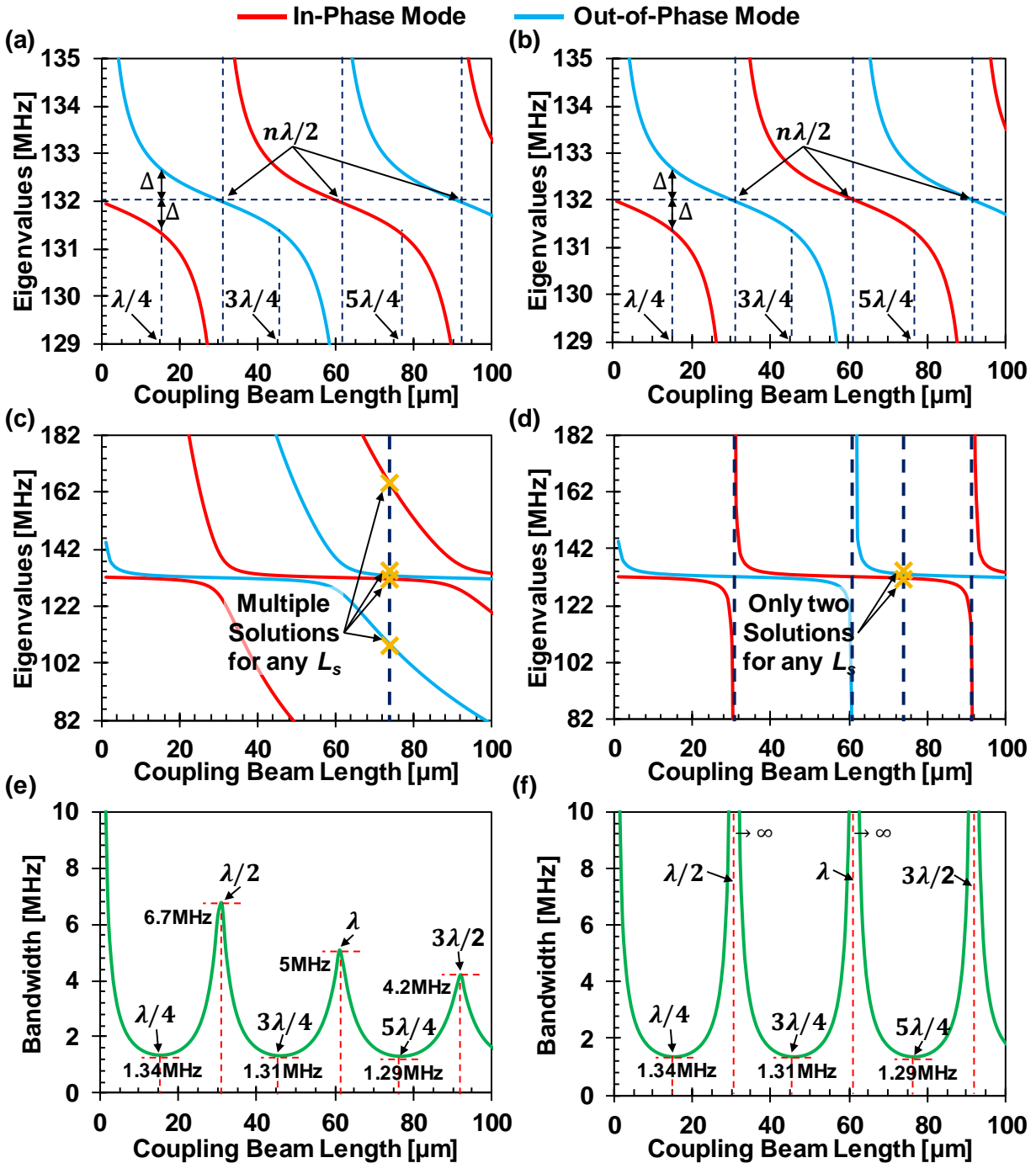
Figure 4.3: The eigenvalues of a 2nd-order system with extensional-mode coupling beam (a-d) and the corresponding system bandwidth (e, f). The solution to the equations 4.9 and 4.10 are presented in (a, c, e) and (b, d, f), respectively. Both equations predict similar bandwidth near quarter-wavelength, but deviate near half-wavelength. Equation 4.9 has multiple solutions for any given length, while equation 4.10 provides only two.

$$\omega_1 = \sqrt{\frac{1}{m_{re}}\left(k_{re} - \omega_o Z_o \tan\left(\frac{1}{2}\frac{\omega_o L_s}{v_P}\right)\right)}$$

$$\omega_2 = \sqrt{\frac{1}{m_{re}}\left(k_{re} + \omega_o Z_o \cot\left(\frac{1}{2}\frac{\omega_o L_s}{v_P}\right)\right)}$$

(4.10)

4.2.1 QUARTER-WAVELENGTH EXTENSIONAL BEAM

As mentioned in the previous section, the system bandwidth has a minimum when the coupling beam length is equivalent to a quarter-wavelength transmission line, $(2n+1)\lambda/4$. The investigation of equation 4.7 and 4.8 can provide the mathematical foundation for this result. The difference between the both eigenvalues is due to the k_{sc} term and minimizing this term gives the smallest system bandwidth. k_{sc} effective stiffness is minimize whenever $\sin(\beta L_s)=1$ or $L_s=(2n+1)\lambda/4$. Equation 4.11 and 4.12 provide the system poles and the *ABCD* matrix for such a coupling length. Here, both poles are close to center frequency and hence $\omega_1 \approx \omega_o$ and $\omega_2 \approx \omega_o$ have been used to derive the final expressions. Quarter-wavelength design sets the poles equally spaced from the resonator center frequency and the ABCD matrix is similar to the quarter-wavelength EM transmission line, i.e. provides the impedance transformation given in equation 4.13. Moreover, the system bandwidth has the least dependency on the coupling beam length around quarter-wavelength points and hence, the design encompassing these coupling lengths are more robust against process variation.

$$\frac{\omega_1}{\omega_o} = \sqrt{1 + \left(\frac{\omega_o Z_o}{2k_{re}}\right)^2} - \frac{\omega_o Z_o}{2k_{re}} \cong 1 - \frac{\omega_o Z_o}{2k_{re}}$$

$$\frac{\omega_2}{\omega_o} = \sqrt{1 + \left(\frac{\omega_o Z_o}{2k_{re}}\right)^2} + \frac{\omega_o Z_o}{2k_{re}} \cong 1 + \frac{\omega_o Z_o}{2k_{re}}$$

(4.11)

$$\begin{bmatrix} f_1 \\ \dot{x}_1 \end{bmatrix} = \begin{bmatrix} 0 & jZ_o \\ \dfrac{j}{Z_o} & 0 \end{bmatrix} \begin{bmatrix} f_2 \\ \dot{x}_2 \end{bmatrix}$$

(4.12)

$$Z_{in} = \frac{Z_o^2}{Z_L}$$

(4.13)

4.2.2 HALF-WAVELENGTH EXTENSIONAL BEAM

The system bandwidth of Figure 4.3 has a maximum for coupling lengths equivalent to $n\lambda/2$, since $\sin(\beta L_s)=0$ and k_{sc} approaches infinity. Equation 4.14 defines the equivalent length defined at the resonator center frequency an equation 4.15 provides the characteristic expressions for the

eigenvalue calculation. Although this equation does not have analytical solutions, but it has two solutions of interest: $\omega_2=\omega_o$ for odd values of n and $\omega_1=\omega_o$ for even values of n, as shown in equation 4.16. This equation suggests for half-wavelength coupling beams one of the system eigenvalues will be exactly equal to the resonator center frequency and the coupling beam pushes the other eigenvalue far from the center frequency, depending on the value of Z_o and k_{re}. However, the other eigenvalue will not be at infinity, as expected from the approximation method of equation 4.10. The frequency behavior of the coupling beam can explain the finite value of this mode: the length of coupling beam is equivalent to half-wavelength at a certain frequency and as the other mode is getting further and further from f_o, the coupling length does not behave as a half wavelength transmission line anymore. Equations 4.17 and 4.18 provide the ABCD matrix and impedance transformation of the half-wavelength extensional coupling beam. Note that these two equations are only valid for the mode exactly at ω_o. Equation 4.18 suggests that half-wavelength coupling does not contribute to the impedance of the system and hence, it is widely used for arraying identical resonators to achieve low-R_x mechanical system, with no introduction of new modes into the system response.

$$\sin(\beta L_s)]_{@\omega_o} = 0 \rightarrow \frac{\omega_o L_s}{v_P} = n\pi \tag{4.14}$$
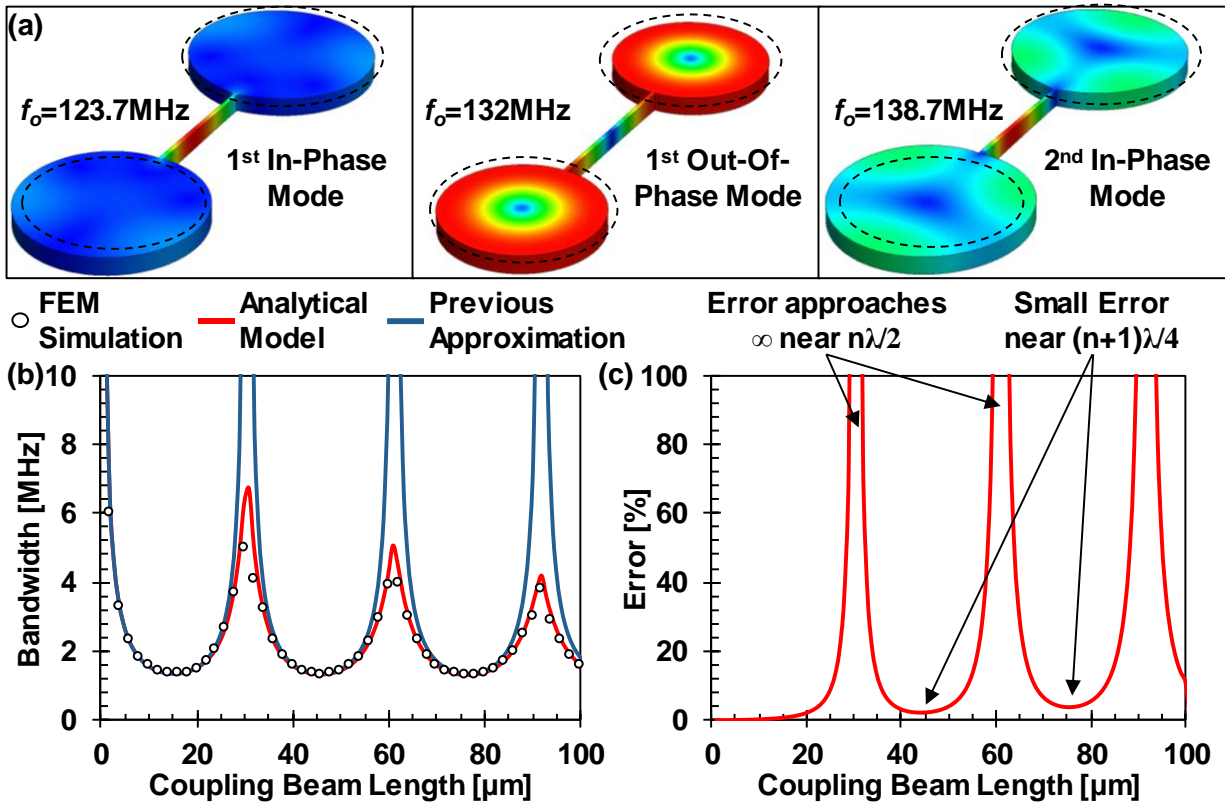
Figure 4.4: (a) FEM simulation of a 2nd-order system including contour mode disks and half-wavelength extensional coupling beams. (b) Comparison of solutions to equations 4.9 and 4.10 to FEM simulations. (c) Equation 4.10 prediction deviate from equation 4.9 and FEM simulations.

63

$$\left(\frac{\omega_1}{\omega_o}\right)^2 + \left(\frac{\omega_1}{\omega_o}\right)\frac{\omega_o Z_o}{k_{re}}\tan\left(\frac{n\pi}{2}\frac{\omega_1}{\omega_o}\right) - 1 = 0$$

$$\left(\frac{\omega_2}{\omega_o}\right)^2 - \left(\frac{\omega_2}{\omega_o}\right)\frac{\omega_o Z_o}{k_{re}}\cot\left(\frac{n\pi}{2}\frac{\omega_1}{\omega_o}\right) - 1 = 0$$

(4.15)

$$odd\ n: \begin{cases} \left(\frac{\omega_1}{\omega_o}\right)^2 + \left(\frac{\omega_1}{\omega_o}\right)\frac{\omega_o Z_o}{k_{re}}\tan\left(\frac{n\pi}{2}\frac{\omega_1}{\omega_o}\right) - 1 = 0 \\ \omega_2 = \omega_o \end{cases}$$

(4.16)

$$even\ n: \begin{cases} \omega_1 = \omega_o \\ \left(\frac{\omega_2}{\omega_o}\right)^2 - \left(\frac{\omega_2}{\omega_o}\right)\frac{\omega_o Z_o}{k_{re}}\cot\left(\frac{n\pi}{2}\frac{\omega_1}{\omega_o}\right) - 1 = 0 \end{cases}$$

$$\begin{bmatrix} f_1 \\ \dot{x}_1 \end{bmatrix} = \begin{bmatrix} 1 & 0 \\ 0 & 1 \end{bmatrix}\begin{bmatrix} f_2 \\ \dot{x}_2 \end{bmatrix}$$

(4.17)

$$Z_{in} = Z_L$$

(4.18)

4.3 FLEXURAL-MODE COUPLING BEAM

Comparison of the flexural beam ABCD matrix given in equation 4.3 and effective stiffness expressions of equation 4.4 and 4.5 delivers the corresponding stiffness expressions of equation 4.19. These effective stiffness expressions provide the eigenvalue problems, given in equation 4.20. Note that the terms α, H_3, H_6 and H_7 are also frequency dependent and should not be considered a constant value. The eigenvalue expressions of equation 4.19 have infinite solutions for any given coupling length Ls, as shown in Figure 4.5. This figure presents the eigenvalues of the system for a CC-beam resonator at 10MHz.

$$k_{sa} = EI_s\left(\frac{\alpha}{L_s}\right)^3\frac{H_7 - H_6}{H_3}$$

$$k_{sc} = -EI_s\left(\frac{\alpha}{L_s}\right)^3\frac{H_7}{H_3}$$

(4.19)

$$\alpha^4 = L_s^4\left(\frac{\rho W_s h}{EI_s}\right)\omega^2$$

1st Eigenvalue:

$$m_{re}\omega^2 - k_{re} - EI_s\left(\frac{\alpha}{L_s}\right)^3\frac{H_7 - H_6}{H_3} = 0$$

2nd Eigenvalue:

(4.20)

$$m_{re}\omega^2 - k_{re} + EI_s\left(\frac{\alpha}{L_s}\right)^3\frac{H_7 + H_6}{H_3} = 0$$

The substitution of ω by ω_o can transform the transcendental equations of 4.20 into a 2nd-order polynomial problem given in 4.21, as done conventionally by designers. This approximation is only valid when both poles are very close to ω_o, i.e. the quarter-wavelength design, but fails severely around maximum bandwidth, as shown in Figure 4.6.
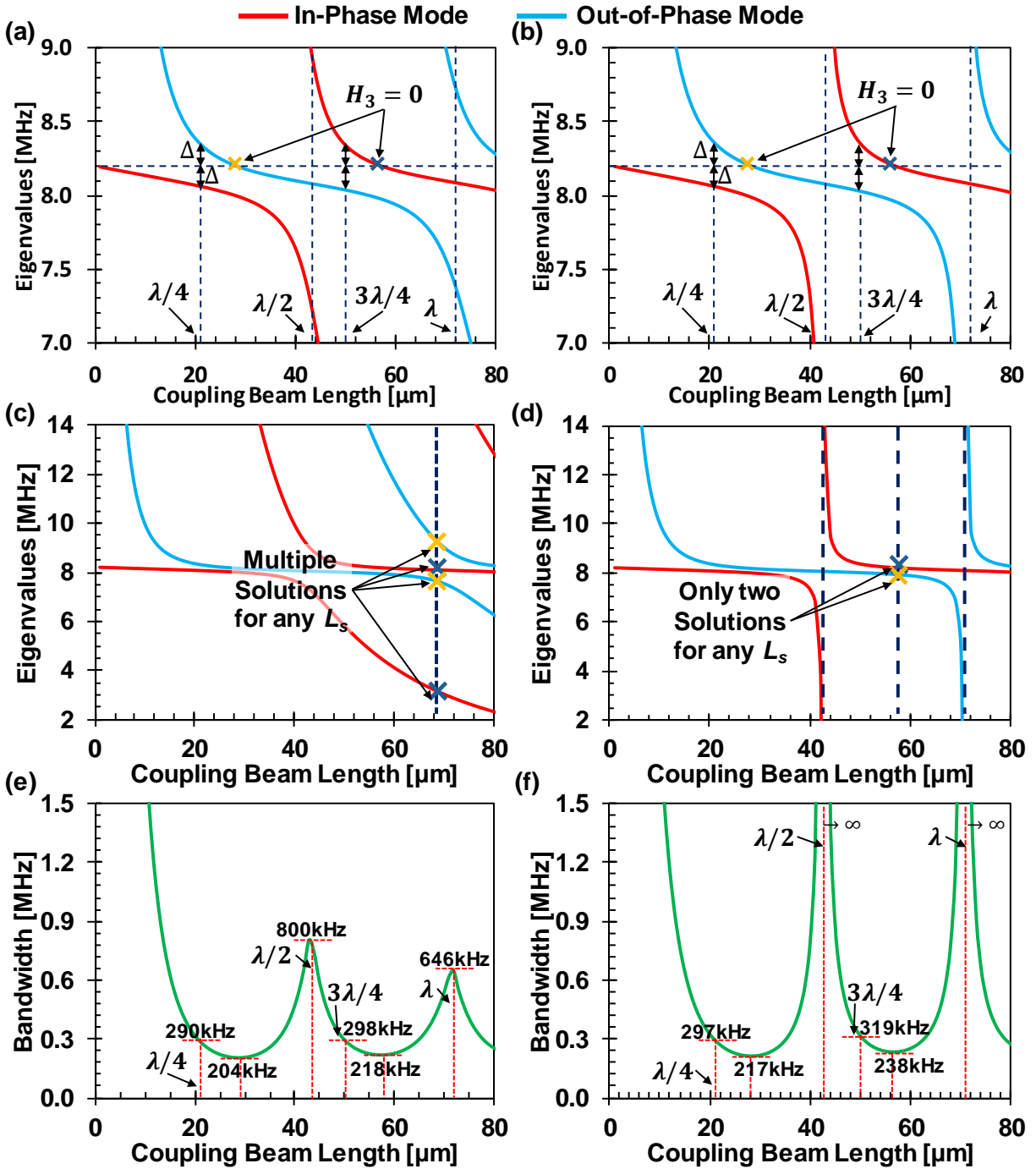
Figure 4.5: The eigenvalues of a 2nd-order system with flexural-mode coupling beam (a-d) and the corresponding system bandwidth (e, f). The solution to the equations 4.19 and 4.20 are presented in (a, c, e) and (b, d, f), respectively. Both equations predict similar bandwidth near quarter-wavelength, but deviate near half-wavelength. In contrast to extensional mode, the minimum bandwidth does not happen at quarter-wavelength and the system eigenvalue is not equal to f_o at half-wavelength.

$$\alpha_o^4 = L_s^4 \left(\frac{\rho W_s h}{EI_s}\right) \omega_o^2$$

1st Eigenvalue:

$$m_{re}\omega^2 - k_{re} - EI_s \left(\frac{\alpha_o}{L_s}\right)^3 \frac{H_7 - H_6}{H_3} = 0 \tag{4.21}$$

2nd Eigenvalue:

$$m_{re}\omega^2 - k_{re} + EI_s \left(\frac{\alpha_o}{L_s}\right)^3 \frac{H_7 + H_6}{H_3} = 0$$

4.3.1   QUARTER-WAVELENGTH FLEXURAL BEAM

In analogy to electromagnetic transmission line, the *ABCD* matrix main diagonal elements will be zero at quarter-wavelength equivalent length. This requires $H_6=0$ and the solutions of this equation corresponding α and coupling length L_s equivalent to quarter wavelength, as shown in equation 4.22. Other than zero which is the trivial solution of this equation, the first, second and third solutions of this equations provides the corresponding coupling length for $\lambda/4$, $3\lambda/4$, and $5\lambda/4$, respectively. Equation 4.23 provides the system poles for quarter-wavelength design. As evident from this equation and shown in the Figure 4.5, the eigenvalues are symmetric around resonator center frequency ω_o.

$$H_6 = \sinh \alpha \cdot \cos \alpha + \cosh \alpha \cdot \sin \alpha = 0 \rightarrow \alpha = 0, 2.365, 5.498, 8.639, \ldots \tag{4.22}$$

$$\left(\frac{\omega_1}{\omega_o}\right)^2 = \sqrt{1 + \frac{EI_s}{k_{re}}\left(\frac{\alpha}{L_s}\right)^3 \frac{H_7}{H_3}} \cong 1 + \frac{1}{2}\frac{EI_s}{k_{re}}\left(\frac{\alpha}{L_s}\right)^3 \frac{H_7}{H_3}$$

$$\left(\frac{\omega_2}{\omega_o}\right)^2 = \sqrt{1 - \frac{EI_s}{k_{re}}\left(\frac{\alpha}{L_s}\right)^3 \frac{H_7}{H_3}} \cong 1 - \frac{1}{2}\frac{EI_s}{k_{re}}\left(\frac{\alpha}{L_s}\right)^3 \frac{H_7}{H_3} \tag{4.23}$$

4.3.2   HALF-WAVELENGTH FLEXURAL BEAM

The definition of half wavelength for a flexural beam is not straightforward. As shown in the previous section, the *ABCD* matrix of a half-wavelength design is an identity matrix. On the other hand, the elements B and C in the flexural beam *ABCD* matrix have different dependencies on α and coupling length L_s and hence, there is no choice of coupling length that could make both terms equal to zero, as shown in equation 4.24. Note that since H_3 appears in the eigenvalue expressions of equation 4.20, and makes the effective beam stiffness approach infinity when $H_3=0$, it is expected that H_3 determines the half-wavelength design.

$$B = 0 \rightarrow H_1 = \sinh \alpha \cdot \sin \alpha = 0 \rightarrow \alpha = 0, 3.142, 6.283, 9.425, \ldots$$
$$C = 0 \rightarrow H_3 = \cosh \alpha \cdot \cos \alpha - 1 = 0 \rightarrow \alpha = 0, 4.730, 7.853, 10.996, \ldots \tag{4.24}$$

i) *Case for $H_3=0$*

When the element *C* in the *ABCD* matrix is zero, it increases the effective stiffness vastly and hence, attempts to pull the system poles apart from each other and set one of them at infinity. The constraint $H_3=0$ given in equation 4.24 determines the corresponding α and coupling length L_s. Using trigonometric formulas and some algebraic manipulation can simplify the eigenvalue problems of equation 4.20 for $\lambda/2$ and λ equivalent length, as shown in equation 4.25. Note that the roots of equation $H_3=0$ given in equation 4.24 should not be used to determine the 1st eigenvalue of $\lambda/2$ or 2nd eigenvalue of λ equivalent length, since the roots of this equations are very far from the resonator center frequency ω_o and the coupling beam is not equivalent to half wavelength at those frequencies. Therefore, the exact equations given in 4.20 should be solved to find the corresponding eigenvalue. If the coupling beam was half-wavelength equivalent for all the frequencies, that would have pushed one of the poles to infinity, as expected from the approximation method.

Although the solutions of $H_3=0$ set the poles furthest from each other and determine the maximum for system bandwidth, they are not quite similar to half-wavelength behavior in electromagnetics. As explained earlier, these solutions do not change the *ABCD* matrix into identity matrix and none of the solutions of the eigenvalue problem is exactly at resonator center frequency ω_o, as observed in extensional coupling beam. Hence, application of half-wavelength
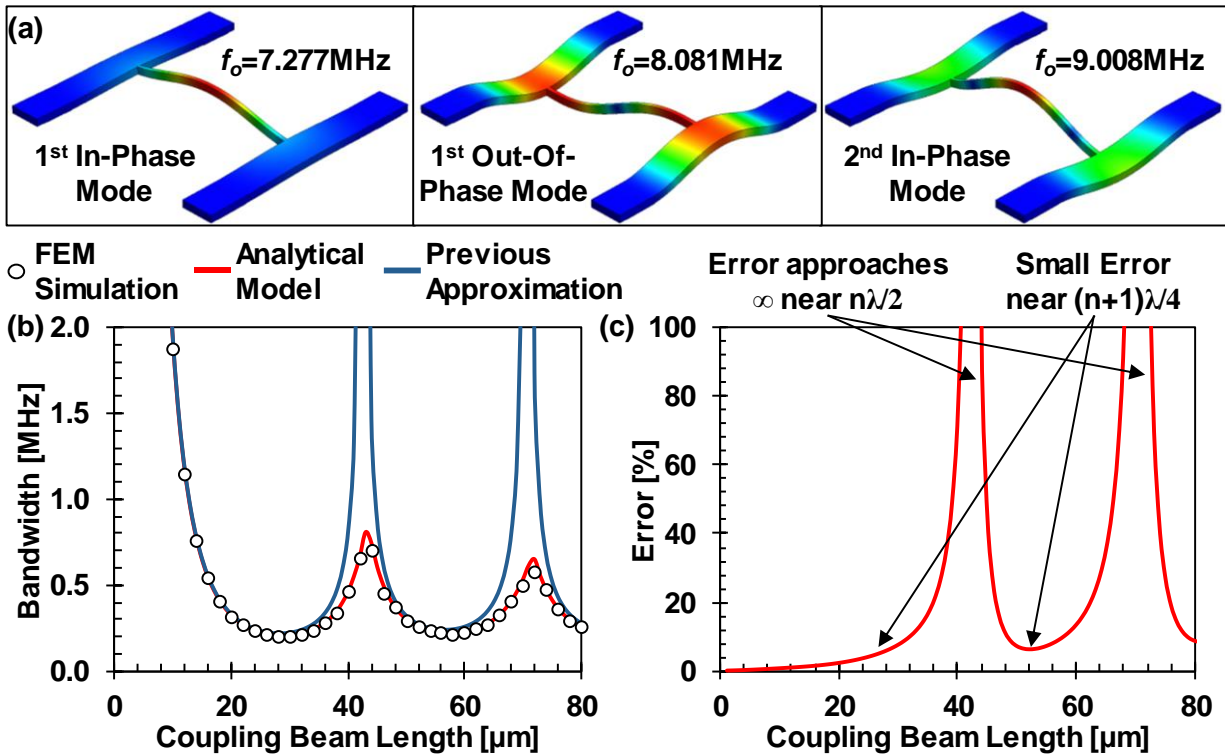

Figure 4.6: (a) FEM simulation of a 2nd-order system including CC-beam resonators and half-wavelength flexural coupling beam. (b) Comparison of solutions to equations 4.19 and 4.20 to FEM simulations. (c) Equation 4.20 prediction deviate from equation 4.19 and FEM simulations.

67

flexural coupling beam in resonator arrays to make the structure stiffer and motional resistance smaller should be with careful investigation and thorough analysis.

$$L_s]_{@\omega_o} \equiv \frac{\lambda}{2}, \frac{3\lambda}{2}, \dots, \frac{(2n+1)\lambda}{2} \qquad\qquad L_s]_{@\omega_o} \equiv \lambda, 2\lambda, \dots, n\lambda$$

<div style="display:flex">

1st Eigenvalue:

$$\left(\frac{\omega_1}{\omega_o}\right)^2 - 1 - \frac{EI_s}{k_{re}}\left(\frac{\alpha}{L_s}\right)^3 \frac{H_7 - H_6}{H_3} = 0$$

1st Eigenvalue: $\alpha = 7.853, 14.137, \dots$

$$\left(\frac{\omega_1}{\omega_o}\right)^2 - 1 - \frac{EI_s}{k_{re}}\left(\frac{\alpha}{L_s}\right)^3 = 0 \qquad (4.25)$$

2nd Eigenvalue: $\alpha = 4.730, 10.996, \dots$

$$\left(\frac{\omega_2}{\omega_o}\right)^2 - 1 + \frac{EI_s}{k_{re}}\left(\frac{\alpha}{L_s}\right)^3 = 0$$

2nd Eigenvalue:

$$\left(\frac{\omega_2}{\omega_o}\right)^2 - 1 + \frac{EI_s}{k_{re}}\left(\frac{\alpha}{L_s}\right)^3 \frac{H_7 + H_6}{H_3} = 0$$

</div>

ii) Case for H₁=0

For the values of $\alpha = n\pi$, the element B of the *ABCD* matrix will vanishes to zero, however the corresponding coupling beam length is not equivalent to any special cases in the electromagnetic transmission line. This constraint simplifies the expressions for the H_i terms, as shown in equation 4.20 and the eigenvalue problems, as in equation 4.21. Since the hyperbolic functions in these expressions approaches unity very fast (equation 4.22), the eigenvalue expressions of 4.21 can be simplified even further, as presented in equation 4.27. This equation suggests that for the case $H_1=0$, one of the eigenvalues is exactly at resonator center frequency and the other one is particularly close to the ω_o, since the coupling beam effective stiffness is minimum. Exceptionally, the minimum bandwidth of the flexural coupling beam occurs at a length L_s other than equivalent quarter wavelength, and the system has a pole equal to ω_o, at a coupling length other than the equivalent half wavelength.

$$\begin{bmatrix} f_1 \\ \dot{x}_1 \end{bmatrix} = \begin{bmatrix} (-1)^n & 0 \\ -\dfrac{j\omega L_s^3 H_3}{EI_s \alpha^3 H_7} & (-1)^n \end{bmatrix} \begin{bmatrix} f_2 \\ \dot{x}_2 \end{bmatrix}$$

$$\alpha = n\pi \rightarrow \begin{cases} H_1 = 0, & H_3 = (-1)^n \cosh(n\pi) - 1 \\ H_6 = (-1)^n \sinh(n\pi), & H_7 = \sinh(n\pi) \end{cases} \qquad (4.26)$$

<div style="display:flex">

even n

1st Eigenvalue:

$$\left(\frac{\omega_1}{\omega_o}\right)^2 - 1 = 0$$

2nd Eigenvalue:

$$\left(\frac{\omega_2}{\omega_o}\right)^2 - 1 + \frac{EI_s}{k_{re}}\left(\frac{n\pi}{L_s}\right)^3 \frac{2\sinh(n\pi)}{\cosh(n\pi) - 1} = 0$$

odd n

1st Eigenvalue:

$$\left(\frac{\omega_1}{\omega_o}\right)^2 - 1 + \frac{EI_s}{k_{re}}\left(\frac{n\pi}{L_s}\right)^3 \frac{2\sinh(n\pi)}{\cosh(n\pi) + 1} = 0 \qquad (4.27)$$

2nd Eigenvalue:

$$\left(\frac{\omega_2}{\omega_o}\right)^2 - 1 = 0$$

</div>

68

$$\frac{\sinh(n\pi)}{\cosh(n\pi) \pm 1} \cong 1, \qquad for\ n = 1,2,3, \ldots \tag{4.28}$$

1st Eigenvalue:
$$\left(\frac{\omega_1}{\omega_o}\right)^2 - 1 = 0$$

2nd Eigenvalue:
$$\left(\frac{\omega_2}{\omega_o}\right)^2 - 1 + \frac{2EI_s}{k_{re}}\left(\frac{n\pi}{L_s}\right)^3 = 0$$

1st Eigenvalue:
$$\left(\frac{\omega_1}{\omega_o}\right)^2 - 1 + \frac{2EI_s}{k_{re}}\left(\frac{n\pi}{L_s}\right)^3 = 0$$

2nd Eigenvalue:
$$\left(\frac{\omega_2}{\omega_o}\right)^2 - 1 = 0$$

$$(4.29)$$

4.3.3 GENERAL MODEL FOR FLEXURAL COUPLING BEAM

A flexural coupling beam, like the one Figure 4.1, might have torsional displacement, beside the main displacement in the *z*-direction. Figure 4.7 presents the general displacement of a flexural beam. Therefore, a flexural coupling beam conveys rotation θ, angular velocity $d\theta/dt$ and bending moment *M*, in addition to linear displacement *x*, velocity *v*, and force *F*. The general equation describing flexural-mode coupling is very complicated, since it includes all these parameters, i.e. angular velocity $d\theta/dt$, bending moment *M*, linear velocity *v*, and force *F*, and model how they interact with each other. Equation 4.30 presents the *ABCD* matrix for a thin flexural beam. The derivatives of the resonator displacement mode shape, such as one in equation 2.21, provide the expressions for the angular velocity and the bending moments.

$$\begin{bmatrix} F_1 \\ M_1 \\ v_1 \\ \dot{\theta}_1 \end{bmatrix} = \frac{1}{2} \begin{bmatrix} H_9 & -\dfrac{\alpha}{L_s}H_8 & -\dfrac{EI_s\alpha^3}{j\omega L_s^3}H_7 & -\dfrac{EI_s\alpha^2}{j\omega L_s^2}H_{10} \\ \dfrac{L_s}{\alpha}H_7 & H_9 & \dfrac{EI_s\alpha^2}{j\omega L_s^2}H_{10} & -\dfrac{EI_s\alpha}{j\omega L_s}H_8 \\ \dfrac{j\omega L_s^3}{EI_s\alpha^3}H_8 & \dfrac{j\omega L_s^2}{EI_s\alpha^2}H_{10} & H_9 & -\dfrac{L_s}{\alpha}H_7 \\ -\dfrac{j\omega L_s^2}{EI_s\alpha^2}H_{10} & \dfrac{j\omega L_s}{EI_s\alpha}H_7 & \dfrac{\alpha}{L_s}H_8 & H_9 \end{bmatrix} \begin{bmatrix} F_2 \\ M_2 \\ v_2 \\ \dot{\theta}_2 \end{bmatrix} \tag{4.30}$$

This work exploits low-velocity coupling, i.e. the flexural coupling beams are attached to the main resonators close to the anchor points where the resonator displacement and rotation is very small. Therefore, the simplified *ABCD* matrix of equation 4.3 provides accurate model for the filter design procedure. Implementation of wide-bandwidth filters with coupling location close to the resonator center point requires thorough analysis and investigation of torsional stiffness on the filter response.
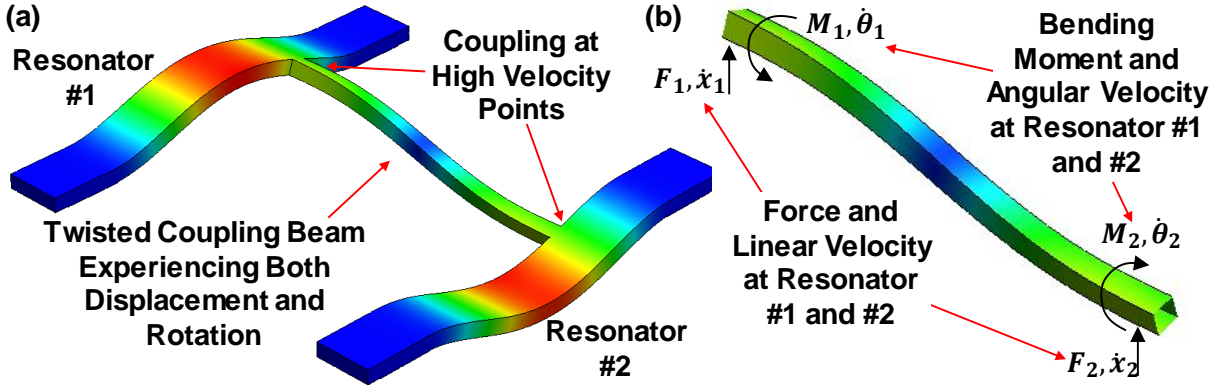
Figure 4.7: (a) Illustration of a 2 CC-beam mechanical system with flexural-mode coupling beams attached at high-velocity point. (b) The phase difference in the CC-beam displacements twists the coupling beam and induces rotation.

4.4 EXPERIMENTAL RESULTS

Figure 4.8 presents the SEM images of the fabricated mechanical structures of Figure 4.1 in order to characterize extensional and flexural coupling beams. The constituent contour-mode disk resonators of Figure 4.8 (a) have radius of 20µm and are centered at 132MHz. The CC-beam resonators in the array of Figure 4.8 (b) are 40µm long and have resonance frequency of 8.2MHz. Numerous copies of the disk and CC-beam structures with different coupling length laid out to investigate the demonstrated analysis of extensional and flexural coupling beams, respectively. The process flow of Chapter 2 was used to fabricate the CC-beam mechanical structure and a conventional 5-mask process described in detail in [50] were adopted to fabricate the disk arrays. Figure 4.8 (c) presents the wideband frequency response of a disk array with 30µm long extensional coupling beam. As suggested by the analysis of section 4.2, the system has more than two eigenvalues. Figure 4.8 (e) shows the measured bandwidth of the system as a function of the coupling length. The two-disk array bandwidth has minimum and maximum at the coupling length equivalent to quarter and have wavelength, respectively. However, the half-wavelength bandwidth is finite and the system poles are not at infinity, in contrast to conventional model. The theory presented in the section 4.2 matches the behavior of the system, as shown in the Figure 4.8 (e). Figure 4.8 (d) presents the frequency response of a CC-beam array with coupling length of 40µm which clearly shows the three resonance frequencies of the system, although the coupling beam is equivalent to half wavelength. Figure 4.8 (f) shows the bandwidth of the resonator array for different flexural coupling beam length. As expected, the minimum bandwidth does not happen at quarter wavelength and also the bandwidth is not infinity at half wavelength equivalent coupling beam.
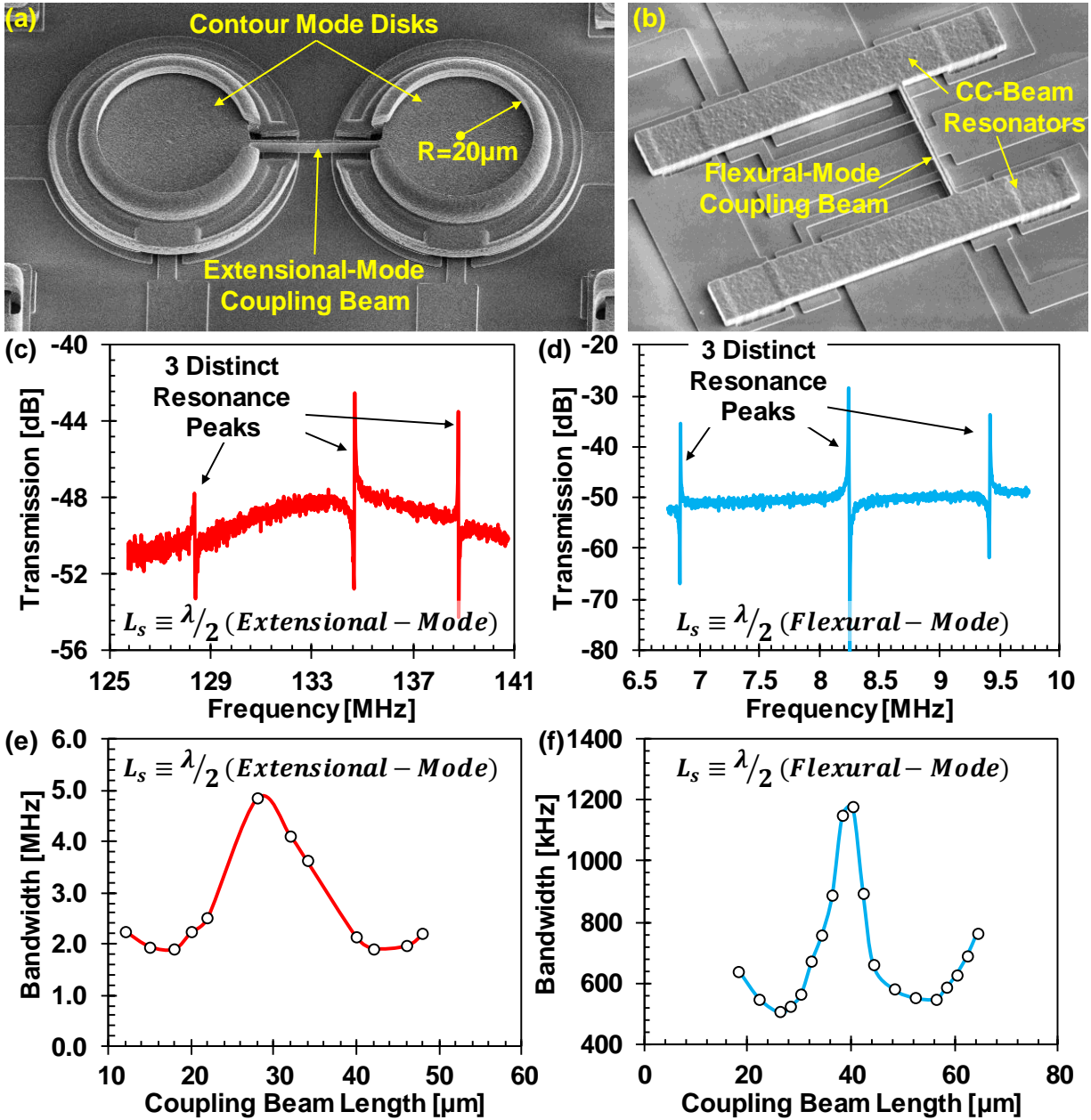
Figure 4.8: SEM photographs of a contour-mode disk resonator array (a) and a CC-beam resonator array (b) fabricated to test the models developed in this chapter. The frequency response of the disk array with half-wavelength extensional-mode coupling beam (c) and CC-beam array with flexural-mode coupling beam (d), show the three distinct resonance peaks near f_o, as predicted by the developed models. The corresponding system bandwidth as a function of the coupling beam length for the disk array (e) and the CC-beam array (f).

Chapter 5 BRIDGED MICROMECHANICAL FILTERS

This chapter presents the bridging technique to control the filter frequency response. The bridging between non-adjacent resonators introduces transmission zeros in the filter frequency response and is able to manipulate the filter passband-to-stopband roll-off via the relative distance of the loss poles to passband [47] [73]. The optimum design of the non-adjacent bridging can sharpen the roll-off and improve the filter 20dB shape factor. The high-order micromechanical filters demonstrated in this chapter exploit this technique to achieve 20dB shape factor of 1.84, with small insertion loss of 1dB. The introduced loss poles provide extra 10dB rejection at the adjacent channels to further relieve the nonlinearity requirements on the following stages, such as LNAs.

5.1 FILTER TYPES AND TRANSMISSION ZEROS

The micromechanical filters presented in Chapter 3 consist of several identical micromechanical resonators coupled via thin extensional- or flexural-mode beams. This mechanical coupling makes a system with several degrees of freedom and hence, splits the system eigenmodes around the resonator center frequency f_o, as explained in details in Chapter 4. This filter design procedure is capable of implementing any all-pole filter type, such as Butterworth, Chebyshev, or Gaussian by proper choice of normalized coupling coefficient k_i. However, this technique does not produce any transfer function zeros, as confirmed by the system transfer function derived in Chapter 3 and 4, and hence, is not capable of prototyping other filter types such as Inverse Chebyshev or Elliptic. These filter types are of interest due to the fast passband-to-stopband roll-off offered by the placement of loss poles, i.e. transfer function zeros, very close to the passband, as shown in Figure 5.1.

The series and parallel resonances of the constituent resonators of a conventional ladder filter structure generate the transmission zeros required for the Inverse Chebyshev prototype [26]. However, the coupled mechanical structure of this work does all the signal processing in the mechanical domain and hence, the series and parallel resonances could not generate any transmission zeros. In order to introduce and manipulate loss poles, this work adopts simple and well-known trick in signal processing: if there are two feedforward paths from the system input to the output with different phase, i.e. time delay, the system transfer function will have a zero, as shown in Figure 5.2. Therefore, the filters of this work exploits bridging between non-adjacent resonators, i.e. the input and output resonators, to implement the second feedforward path from the input to the output, shown in the Figure 5.3.

Figure 5.4 presents the frequency shaping characteristics that each presented micromechanical filter generates. For comparison, Figure 5.4 presents a conventional non-bridged design, again, alongside its frequency shaping characteristic. As shown, each of these filters consists of several CC-beam resonators coupled mechanically by soft flexural-mode beams, all suspended 140nm above the substrate. Conducting strips underlie the central region of each end resonator serve as capacitive transducer electrodes positioned to induce resonator vibration in a direction perpendicular to the substrate. Of the three different designs in Figure 5.4, (a), (c) and (d) are three-resonator filters, while (b) and (d) are four-resonator filters.

Figure 5.4 also presents the circuit needed to operate any one of the filters in Figure 5.4. Here, a dc-bias V_P is applied to the suspended filter structure, and an ac input voltage v_i is applied through a properly-valued input termination resistor R_Q to the input electrode. This combined input generates an electrical force between the input electrode and the conductive resonator that induces vibration of the input resonator when the frequency of v_i is within the passband of the mechanical filter. This vibrational energy is imparted to the center and output resonators via the coupling springs, causing them to vibrate as well. Vibration of the output resonator creates a dc-biased, time varying capacitor between the conductive resonator and output electrode, which sources a motional output current i_o. The motional current is then directed to the output termination resistor R_Q, which converts the current to an output voltage and loads the Q of the output resonator so as to flatten the jagged passband (to be described later via Figure 5.17) of the mechanical system into the desired flat passband, shown in Figure 5.4 (f, g, h).
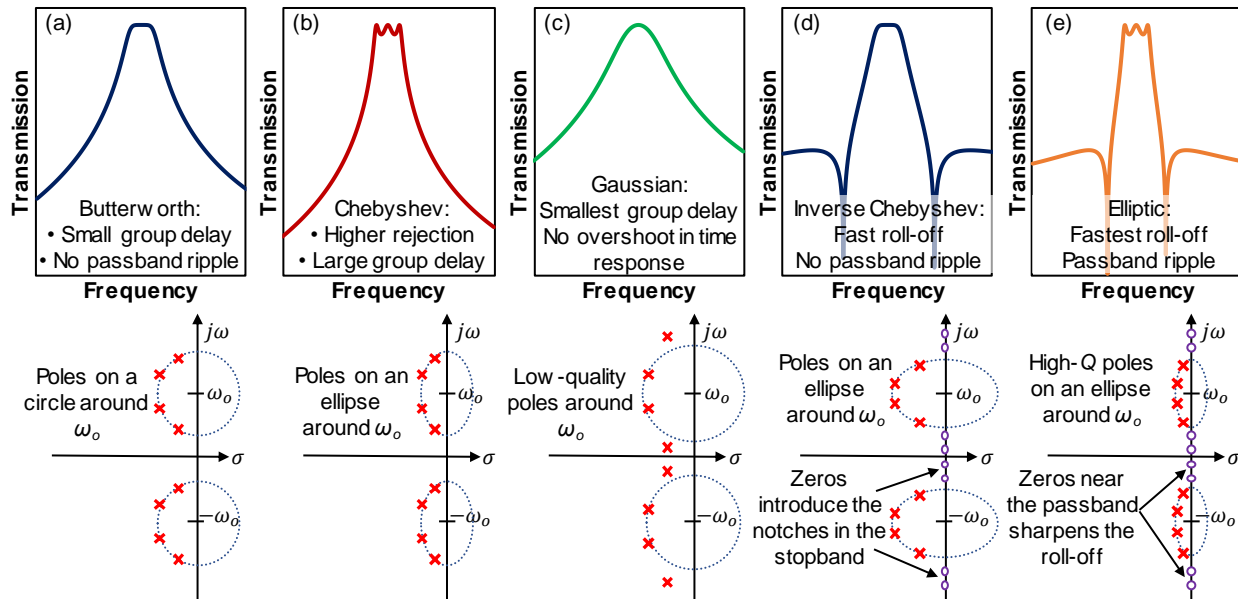

Figure 5.1: The frequency response and system pole and zero placement on the s-plane for (a) Butterworth, (b) Chebyshev, (c) Gaussian, (d) Inverse Chebyshev, and (e) Elliptic filters. The transmission zeros placed very close to the passband sharpen the roll-off for an Inverse Chebyshev or Elliptic filter.

73

Since it is the output resonator that delivers the final electrical output signal in this filter, the key to attaining a desired frequency shaping response is to control the mechanical inputs imparted to the output resonator by the coupling beam(s) attached to it. Before this work [47] [73], all previous deterministically designed micromechanical filters [55] [28] utilized only coupling between adjacent resonators, shown in Figure 5.4 (a) and (b), meaning that only one coupling beam controlled the motion of the output resonator, resulting in frequency characteristics with monotonic stopbands, as shown in Figure 5.4 (f, g, h). In contrast, the bridged filters of this work employ a more general coupling scheme, where non-adjacent resonators are now linked. As shown, non-adjacent resonator coupling is achieved by offsetting the inner resonators from the outer ones to allow direct mechanical coupling of outer resonators in the same structural layer (i.e., without the need for a third layer of polysilicon). As depicted in Figure 5.4, some of the filter variants use angled adjacent-resonator coupling beams in order to minimize the length of the non-adjacent resonator coupler. For example, by using angled adjacent-resonator couplers, the design of (c) can use a quarter-wavelength (λ/4) non-adjacent resonator coupler, whereas the straight adjacent-resonator coupler design of (d) must use a three-quarter-wavelength (3λ/4) coupler. Even with an angled coupler, the 4-resonator filter design of (e) still requires a 3λ/4 non-adjacent resonator coupling beam.

In each filter structure, the new non-adjacent resonator linkage introduces a feedforward path that generates loss poles in the filter transfer function, leading to a faster roll-off from passband to stopband, as shown in Figure 5.4, which plots the expected frequency characteristics

$$H_1(s) = \frac{1}{\frac{s}{P_1} + 1}$$

$$H_2(s) = \frac{1}{\frac{s}{P_2} + 1}$$

$$\frac{Y}{X}(s) = H_1(s) + H_2(s) = \frac{1}{\frac{s}{P_1} + 1} + \frac{1}{\frac{s}{P_2} + 1}$$

$$\frac{Y}{X}(s) = \frac{\frac{s}{Z} + 1}{\left(\frac{s}{P_1} + 1\right)\left(\frac{s}{P_2} + 1\right)} \quad \boxed{\text{Zero due to different delay}}$$
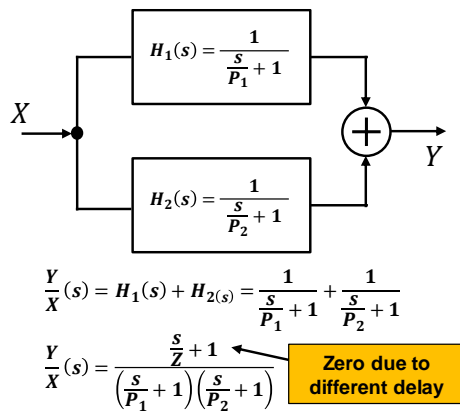
Figure 5.2: A system comprising two feedforward paths from the input to the output with different time delay, or equivalently with different poles in the transfer functions, has a loss pole in the system overall transfer function. The loss pole will be generated even if each feedforward path transfer function does not have any zeros.
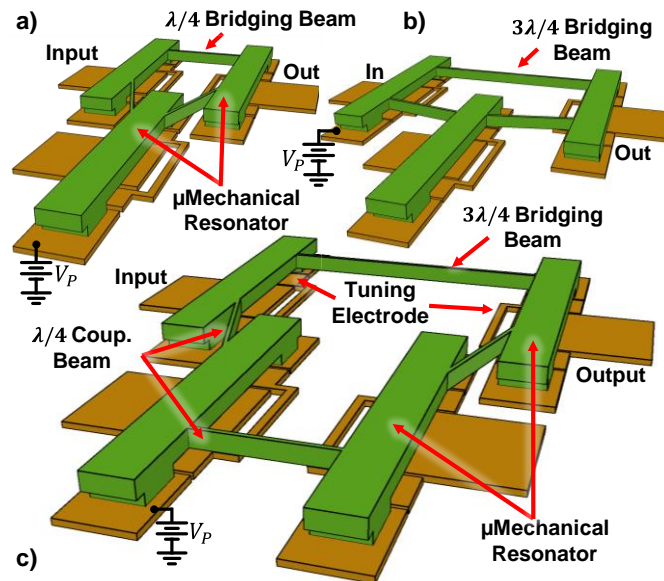
Figure 5.3: Schematics for the three bridged micromechanical filter designs realized in this work. (a) 3CC filter with λ/4 bridging beam design (3CC λ/4). (b) 3CC filter with 3λ/4 bridging beam design (3CC 3λ/4). (c) 4CC filter with 3λ/4 bridging beam design (4CC 3λ/4).

corresponding to the different filter structures at the top of Figure 5.3. Here, loss poles are seen to occur either above or below the passband of a 3 CC-beam bridged filter design, depending upon whether its coupling beam dimensions correspond to a quarter-wavelength or to three-quarter-wavelengths, respectively. The 4 CC-beam bridged filter design, on the other hand, achieves two loss poles on each side of its passband with a symmetrical frequency response. In all cases, the loss poles provide sharper passband-to-stopband roll-offs and greater stopband rejection in their respective filter transfer functions.

5.2 BRIDGED FILTER DESIGN CONCEPT

Generating a loss pole in a mechanical filter's passband essentially amounts to minimizing (or zeroing out, if possible) the velocity of the resonator(s) that feed the output electrode. One way to achieve this (employed here) is to couple more than one force into the output resonator and design the phase difference such that the forces maintain the desired passband response, but cancel one another at the desired loss pole frequency, which is generally outside the passband. This can
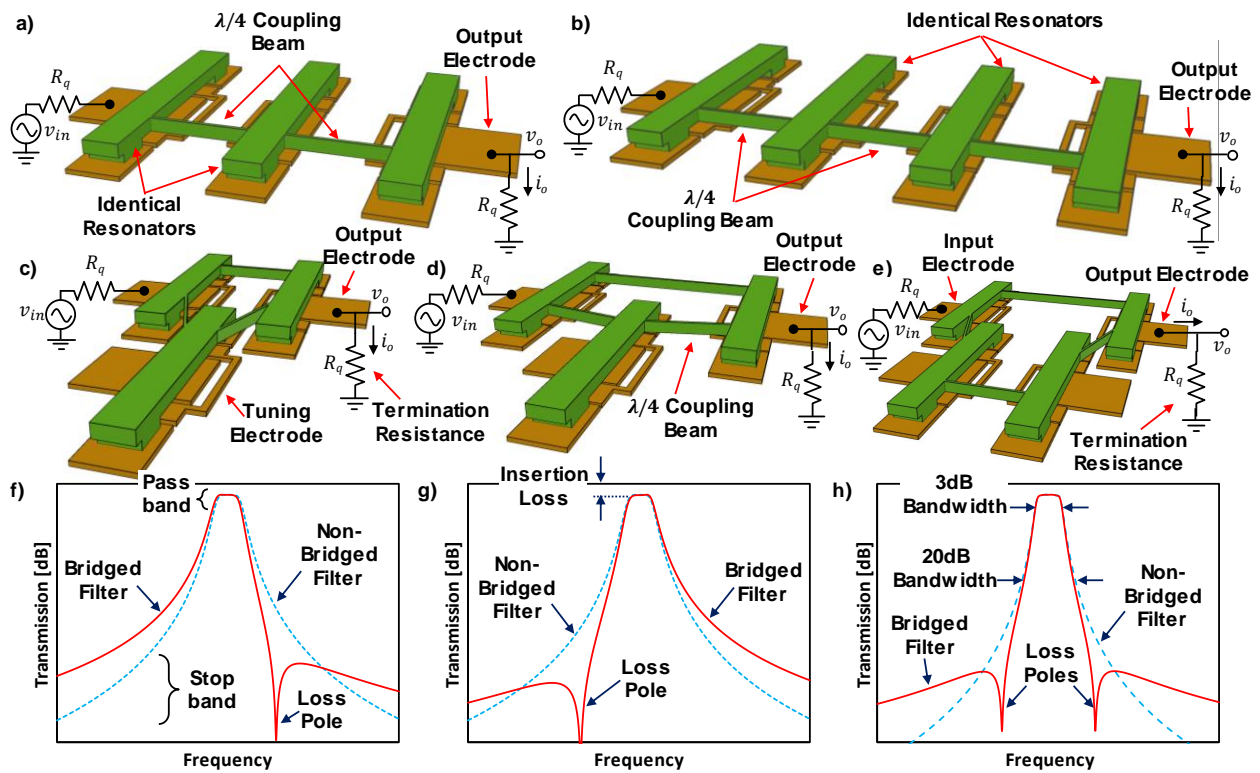
Figure 5.4: Conventional monotonic third-order (a) and fourth-order (b) CC-beam filters compromising identical resonators coupled with quarter-wavelength beams. Modified filter design introducing bridging between non-adjacent resonators to create and control transfer function loss poles along with required measurement circuitry (c-e). $\lambda/4$ bridging of 3CC filter (c) will introduce loss pole above the passband (f), while $3\lambda/4$ 3CC filter (d) has loss pole below the passband (g). The 4CC $3\lambda/4$ bridged filter (e) has symmetric frequency response with loss poles on both side (h). The loss pole improves passband-to-stopband roll-off and reduces 20dB shape factor defined as BW_{20dB}/BW_{3dB}.

75

be accomplished in the mechanical domain by attaching two coupling beams to the output resonator that generate (or at least do not disturb) the desired passband response, but that apply forces with opposite phase when the input frequency is at the desired loss pole location. To illustrate that this is exactly what a bridged filter does, Figure 5.5 presents the (unterminated) mechanical frequency response of the Figure 5.3 (b) filter with finite element mode shape simulations at the filter pole and loss pole locations, clearly showing displacement of the output resonator at the filter pole (i.e., peak) locations, but none at the loss pole frequency.

In the actual implementation, each coupling beam connects the output resonator and an intermediate resonator, which means each beam can be thought of as belonging to its own sub-filter (within the whole filter structure). The response of the output resonator can then be seen as a superposition of the responses of the sub-filters.

The physical implementation of the above is perhaps best illustrated by examining more closely the hierarchical structure of the filter of Figure 5.3 (b). Pursuant to this, Figure 5.6 again presents mode shapes at various locations on the mechanical frequency response, but this time splits up the filter of Figure 5.3 (b) into two main functional blocks, each comprising a non-bridged filter in its own right, one using two clamped-clamped beam (CC-beam) resonators and coupled by the $3\lambda/4$ bridging beam; the other using three CC-beam resonators, each coupled by adjacent $\lambda/4$ beams; and each to be called 2CC $3\lambda/4$ and 3CC $\lambda/4$ monotonic filters, respectively, as shorthand for the remainder of the paper. Here, the resonators are labeled with numbers to better indicate that resonators 1 and 3 are shared between the two sub-filter structures.

Figure 5.7 plots the magnitude and phase of the force-to-velocity transfer functions for the two sub-filters on the same plot, assuming each filter is driven at resonator #1 (i.e., the input
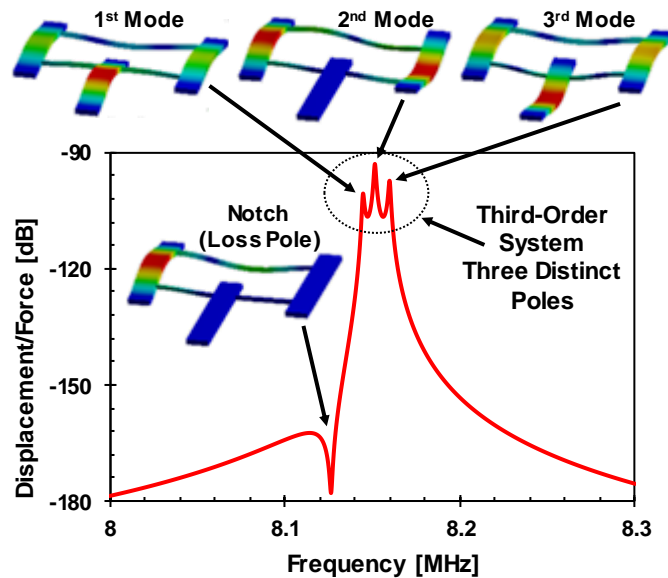
Figure 5.5: Harmonic analysis via ANSYS for a 3CC $3\lambda/4$ bridged μmechanical filter of Figure 5.3 (b). A unity mechanical force is applied to the input resonator and the output resonator displacement is probed.

resonator) and sensed at resonator #3 (i.e., the output resonator). The motion of the output resonator #3 is the most important among all the resonators as it delivers the output current and the total filter response. As shown in Figure 5.7, the response of the two sub-filters are out of phase below the center frequency f_o, and in phase above it. This means that the forces imparted to the output resonators by the coupling beams of the respective 2CC $3\lambda/4$ and 3CC $\lambda/4$ sub-filters will oppose one another when coupled to the same output resonator in the final filter. The mode shapes at various frequencies shown in Figure 5.6 further confirm the relative phasing between sub-filter output resonators. In particular, at the point below the filter center frequency where the magnitudes of the sub-filter force-to-velocity transfer functions are equal, the mode shapes of the sub-filters are such that their resonator #3 motions are equal and opposite. Thus, when superposed in the complete filter structure, their motions cancel completely, and the little or no motion of the output resonator (i.e., resonator #3) leads to little or no current generation between resonator #3 and the output electrode, hence a loss pole in the overall filter transfer function.

Figure 5.6: ANSYS-simulated mode shapes of 3CC- and 2CC-beam filters with $\lambda/4$ and $3\lambda/4$ filter couplers, respectively, showing the amplitude subtraction below the passband due to the 180º out-of-phase motions of resonator #3 and the amplitude addition above the passband since both of resonator #3 vibrate in-phase.
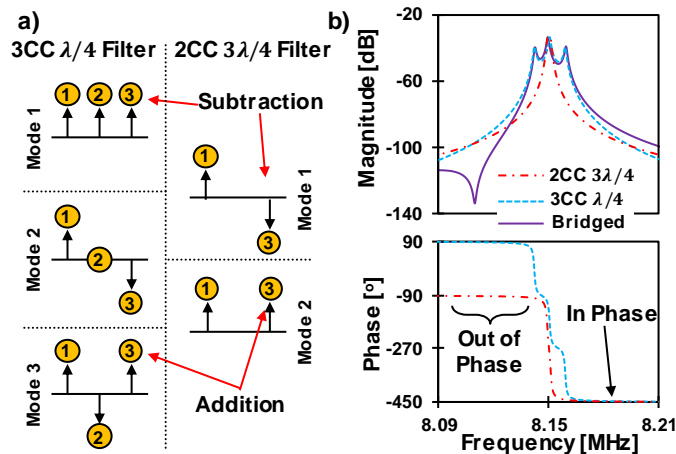
Figure 5.7: (a) Phase relationships between resonators in 3- and 2-resonator coupled systems where $\lambda/4$ and $3\lambda/4$ filter couplers are used, respectively. (b) Frequency transfer functions of 2- (blue dash line) and 3-resonator filters (red dot line), together with the expected 3-resonator bridged filters (black solid line), clearly show the superposition in the end resonators of the first two filters to generate the loss pole below the passband to achieve 3CC $3\lambda/4$ bridged filter response.

As shown in Figure 5.7, above the filter center frequency, the responses of its two- and three-resonator sub-filter constituents are in phase, therefore, add to each other at the corresponding frequencies. Thus, no loss pole is formed, and the addition actually hurts the rejection at upper passband frequencies, but achieves the expected behavior for a bandpass filter with a single lower passband loss pole. As with previous filters, the jagged passband response seen in Figure 5.6 can be flattened (or reduced to a desired ripple) by terminating the filter with the correct value of impedance, as shown in Figure 5.17.

To observe the loss pole effect of the bridged filter shown in Figure 5.3 (b), Figure 5.5 finally presents the force-to-displacement frequency response of the output resonator for a 3CC $3\lambda/4$ bridged filter using ANSYS, clearly showing the loss pole below the passband. For this simulation, a unit mechanical force is applied on the input resonator of the bridged filter and the harmonic analysis obtains the displacement of the output resonator at the center. As mentioned above, the three mode shapes of the monotonic 3CC $\lambda/4$ filter of Figure 5.4 (a) form the passband, while the output resonator is stationary at the loss pole frequency due to the cancellation of induced displacement from parallel paths.

As is evident from the analysis of third-order filter with $3\lambda/4$ bridging beam, the formation of the transfer function loss pole is the result of phase difference between the two parallel paths from the input to the output. This phase difference depends on the bridging beam lengths as well as the order of the main filter [15]. For instance, the second-order filter with three-quarter-wavelength ($3\lambda/4$) bridge has an out-of-phase mode shape at lower frequencies compare to the in-phase mode shape (Figure 5.6) resulting in the loss poles below the filter passband. On the other hand, the in-phase mode shape of a second-order filter with a $\lambda/4$ bridging beam happens at lower frequencies compared to the out-of-phase one, as shown in Figure 5.8, expecting the loss pole to
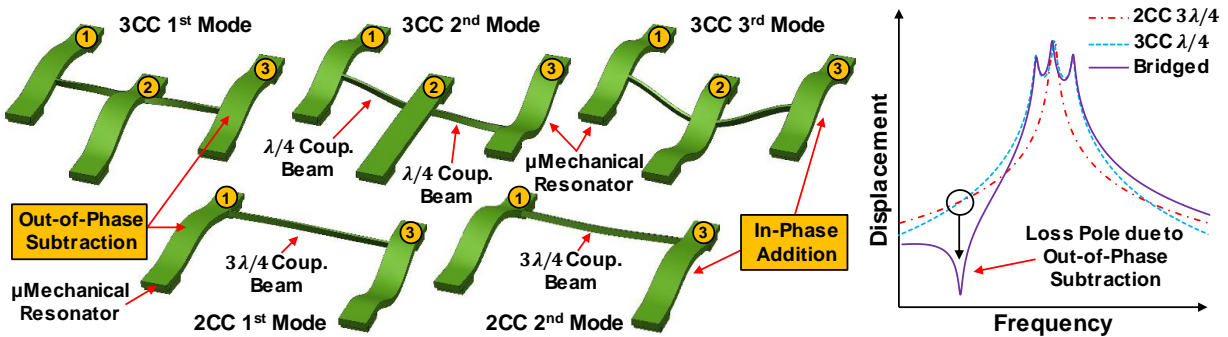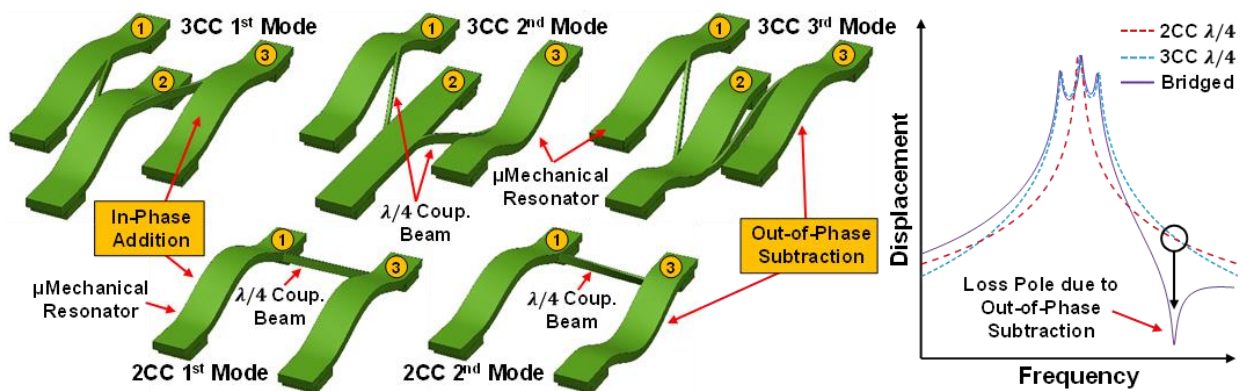

Figure 5.8: ANSYS-simulated mode shapes of 3CC- and 2CC-beam filters both with $\lambda/4$ filter couplers, showing the amplitude addition above the pass-band due to the in-phase motions of resonator #3 and the amplitude subtraction above the passband since both of resonator #3 vibrate 180º out-of-phase. The mechanical frequency response of the 2CC $\lambda/4$, 3CC $\lambda/4$ and 3CC $\lambda/4$ bridged filters shown on the right illustrate the loss pole generation furthermore.

happen above the passband. Hence, the design of the bridging beam (i.e., phase shift element) can precisely control the amplitude addition or subtraction between two or more filter structures.

Figure 5.8 and Figure 5.9 present the operation of a three clamped-clamped beam filter with quarter-wavelength (i.e., $\lambda/4$) bridging beam, such as in Figure 5.3 (a), to achieve a loss pole above its passband. In normal operation of a non-bridged three-resonator filter, such as in Figure 5.4 (a), with all quarter-wavelength filter couplers (i.e., 3CC $\lambda/4$ monotonic filter), the electrostatic force from the capacitive transduction drives #1 (input) resonator, and the overall response consists of mechanical modes depicting in the Figure 5.8, where the #3 (output) resonator vibrates in-phase with #1 resonator at first and third mode. In contrast, in a two-resonator filter with quarter-wavelength coupler (i.e., 2CC $\lambda/4$ monotonic filter), output (#3) resonator vibrates in-phase and out-of-phase with the input (#1) resonator at the first and second mode, respectively. Hence, based on the linear vibration theory, the superimposed displacement of the output (#3) resonator diminishes at the frequencies above the passband and enhances below the passband. The phase response of Figure 5.9 illustrates the loss pole formation by signal cancellation due to the out-of-phase dis-placements of parallel paths.

Figure 5.4 (h) presents the frequency response of a four clamped-clamped beam bridged filter with $3\lambda/4$ bridging beam and two loss poles below and above the passband, which yields to
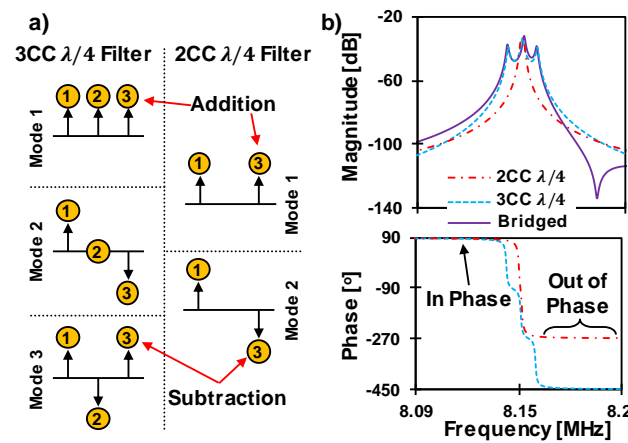
Figure 5.9: (a) Phase relationships between resonators in 3- and 2-resonator coupled systems via all $\lambda/4$ filter couplers. (b) Frequency transfer functions of 2- (blue dash line) and 3-resonator filters (red dot line), together with the expected 3-resonator bridged filters (black solid line), clearly show the superposition in the end resonators of the first two filters to generate the loss pole above the passband to achieve 3CC $\lambda/4$ bridged filter response.
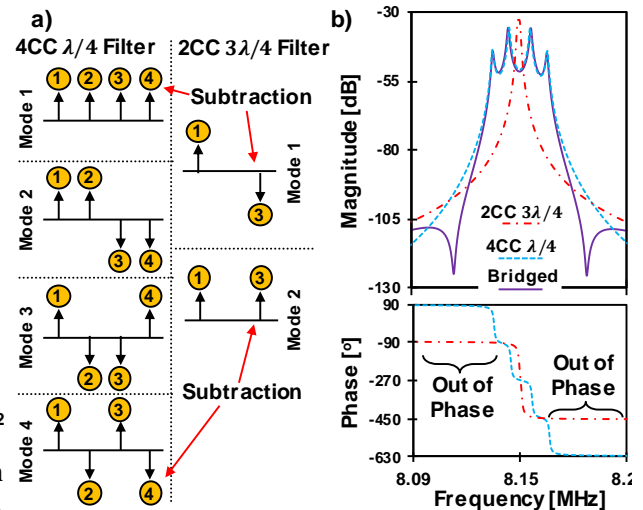
Figure 5.10: (a) Phase relationships between resonators in 4- and 2-resonator coupled systems where $\lambda/4$ and $3\lambda/4$ filter couplers are used, respectively. (b) Frequency transfer functions of 2- (blue dash line) and 4-resonator filters (red dot line), together with the expected 4-resonator bridged filters (black solid line), clearly show the superposition in the end resonators of the first two filters to generate the loss poles below and above the passband to achieve 4CC $3\lambda/4$ bridged filter response.

79

symmetric frequency characteristic. Figure 5.10 explains the formation of these two loss poles via the mode shapes and phase difference of the parallel paths. The monotonic fourth-order filter of Figure 5.4 (b) has four distinct mode shapes shown in Figure 5.10, where the output (#4) resonator is in-phase with the input (#1) resonator at the first and second mode shape, and vibrates out-of-phase at the second and fourth mode shapes. On the other hand, the output resonator of the second-order filter with $3\lambda/4$ coupling vibrates out-of-phase and in-phase with the input resonator at the first and second modes, respectively. Hence, the displacement of the output (#4) resonator cancels out on both side of the passband due to this out-of-phase displacement. The phase responses of fourth- and second-order filters, shown in Figure 5.10, demonstrate the loss pole formation clearly. The small vibration amplitude compared to the gap spacing allows the superposition of the motions from both monotonic filters by simple application of linear algebra, not only providing a straightforward analysis but facilitating the design of all the bridged filters in this work.

5.3 BRIDGED FILTER DESIGN AND MODELING

Due to the good matching tolerance, but poor absolute tolerance, of the planar fabrication technology used to construct the subject micromechanical filters, it is advantageous to design filters so that their constituent resonators have identical un-coupled frequencies, and then just let the coupling beams pull their frequencies apart to generate a passband [12], as explained in details in Chapters 3 and 4. In such a design, the center frequency of the filter is determined primarily by the (identical) resonance frequencies of its constituent resonators, while the bandwidth (i.e. the spacing between modes) is determined largely by the ratio of the stiffness of its coupling springs to the effective stiffness of the CC-beam resonator. Figure 5.5 presents finite element simulations depicting the mode shapes corresponding to each of the three mode frequencies of the filter in Figure 5.3 (b). For the coupled three-resonator system of Figure 5.3 (b), the frequency of each vibration mode corresponds to a distinct peak in the force-to-displacement frequency characteristic and to a distinct, physical mode shape of the coupled mechanical system as shown in Figure 5.5. In the lowest frequency mode, all resonators vibrate in phase; in the middle frequency mode, the center resonator ideally remains motionless, while the end resonators vibrate 180° out of phase; and finally, in the highest frequency mode, each resonator is phase-shifted 180° from its adjacent neighbor. Without proper impedance matching, the complete mechanical filter exhibits the jagged passband seen in the mechanical simulations of Figure 5.14 which will be described later. Proper impedance matching (described in Chapter 4) in the form of termination resistors designed to lower the Q's of the input and output resonators by specific amounts are required to flatten the passband and achieve a more recognizable filter characteristic, such as in Fig. 5.4.

For mass balance reasons, as well as achieving a more robust design against fabrication tolerances [12], a filter design with identical resonators is best achieved using coupling beams with dimensions that correspond to single- or multiple-quarter-wavelengths at the filter center frequency. Thus, as mentioned earlier, each of the three bridged filter designs implemented here,

and shown in Figure 5.1, utilizes quarter-wavelength (λ/4) couplers between adjacent resonators, and either λ/4 or 3λ/4 (for longer distances) coupling beams to connect non-adjacent resonators. The design variations include

    i) A 3 CC-beam filter using a λ/4 bridging beam (3CC λ/4 bridged filter of Figure 5.4 (c)) with a loss pole above the passband as shown in Figure 5.4 (f).

    ii) A 3 CC-beam filter using a 3λ/4 bridging beam (3CC 3λ/4 bridged filter of Figure 5.4 (d)) with a loss pole below the passband as shown in Figure 5.4 (g).

    iii) A 4 CC-beam filter using a 3λ/4 bridging beam (4CC 3λ/4 bridged filter of Figure 5.4 (e)) with two loss poles as shown in Figure 5.4 (h).

Although employing identical resonators and quarter-wavelength coupling beams are beneficial, it exerts geometrical restrictions on the bridged filter design, as mentioned in the previous section. For instance, there are two quarter-wavelength coupling beams and one CC-beam resonator between input (#1) and output (#3) resonator of a third-order monotonic filter (Figure 5.4 (a)), while the λ/4 bridging requires only a quarter-wavelength distance between the input and output resonators. Hence, to accommodate differences in coupling beam path lengths in designs (a) and (c), angled beams are utilized to preserve λ/4 adjacent-resonator coupling. Since the analytical model of a flexural coupling beam in [15] and low-velocity coupling technique of [72] are derived for the right-angled attachment of the coupling beam, bridged filter design with angled coupling beam requires more careful study.

Extensive finite element simulations by CoventorWare showed very little deviation from the standard model for the design parameters of this work. Particularly, the quarter-wavelength design of the coupling beams makes the filter composition more robust to the attachment angles. In addition, the coupling at low velocity point where the effective stiffness of the resonator is considerably large, masks small deviations in the coupling beam stiffness. Any future designs either for wide-bandwidth filters (coupling at high-velocity point) or employing other coupling lengths (other than quarter-wavelength) will require extra and thorough investigations of the coupling design.

Simple mechanical models for the filters of Figure 5.3 can be attained by first recognizing that each filter is merely a multi-degree of freedom mechanical system that can be equated in narrow frequency bands to a lumped parameter mechanical circuit, as explained in detail in Chapter 4. The conventional monotonic mechanical filters such as 4-resonator and 2-resonator filters can be modeled as 4-degree and 2-degree of freedom mechanical systems shown in Figure 5.11 (b) and (c), respectively, where each mass-spring-damper system represents a resonator, while each coupling beam, including the bridging beam, corresponds to a π-network of mechanical springs. Then, the actual filter structure of Figure 5.3 (c), which is the superposition of filter structures in Figure 5.11 (b) and (c), can be explicitly equated to the equivalent mechanical circuit

shown in Figure 5.11 (a) with the same equivalent lumped values. The bridging beam connecting the input and output resonators provides a feedforward path that generates the desired loss poles.

The lumped mechanical model of Figure 5.11 (and those of the other designs in Figure 5.3) has the equation of motion given in 5.1, where $[M]$, $[C]$, and $[K]$ are the mass, damping, and stiffness matrices, respectively, x is the displacement vector of the resonators, and F is the electrostatic force applied to the input resonator, as described in Chapter 2. For mechanically coupled systems like the one in Figure 5.11, each matrix in (5.1) can be expressed in a specific form as 5.2 and 5.3 where F_1 is the only electrostatic force applied to the input resonator of this mechanical system and is generated by the dc bias voltage V_P and ac signal source v_i. All the mechanical coupling beams connecting adjacent and non-adjacent resonators in any filter of Figure 5.3 are designed to be equivalent to the quarter-wavelength. Chapter 4 meticulously presented the flexural-mode beams and showed that $k_{sa}=-k_{sc}$ for any quarter wavelength design. Therefore, the diagonal elements of the $[K]$ matrix can be simplified as $k_{ii}=k_{re}$, assuming identical resonator stiffness. Since all the resonators are identical and have the same effective mass, stiffness and resonance frequency, the eigenmode problem in 5.1, 5.2, and 5.3 can be simplified to equation 5.4, where ω_o and k_{re} are resonator center frequency and effective stiffness, respectively. The damping coefficient $[C]$ has been neglected in this equation, since the resonators have very high Q and the damping does not affect the resonance frequency. This equation emphasizes on the fact that the system eigenvalues will be centered around resonator resonance frequency and the ratio of coupling beam effective stiffness k_{sc} and resonator effective stiffness k_{re} determines their relative distance to ω_o.

$$[M]\ddot{x} + [C]\dot{x} + [K]x = F \tag{5.1}$$

$$[M] = \begin{bmatrix} m_{re1} & 0 & 0 & 0 \\ 0 & m_{re2} & 0 & 0 \\ 0 & 0 & m_{re3} & 0 \\ 0 & 0 & 0 & m_{re4} \end{bmatrix}, [C] = \begin{bmatrix} c_{re1} & 0 & 0 & 0 \\ 0 & c_{re2} & 0 & 0 \\ 0 & 0 & c_{re3} & 0 \\ 0 & 0 & 0 & c_{re4} \end{bmatrix} \tag{5.2}$$

$$[K] = \begin{bmatrix} k_{11} & k_{12} & k_{13} & k_{14} \\ k_{21} & k_{22} & k_{23} & k_{24} \\ k_{31} & k_{32} & k_{33} & k_{34} \\ k_{41} & k_{42} & k_{43} & k_{44} \end{bmatrix}$$

$$k_{11} = k_{re1} + k_{s12a} + k_{s12c} + k_{sBa} + k_{sBc}$$
$$k_{22} = k_{re2} + k_{s12a} + k_{s12c} + k_{s23a} + k_{s23c}$$
$$k_{33} = k_{re3} + k_{s23a} + k_{s23c} + k_{s34a} + k_{s34c}$$
$$k_{44} = k_{re4} + k_{s34a} + k_{s34c} + k_{sBa} + k_{sBc}$$
$$k_{12} = k_{21} = -k_{s12c}, \qquad k_{23} = k_{32} = -k_{s23c}$$
$$k_{34} = k_{43} = -k_{s34c}, \qquad k_{14} = k_{41} = -k_{sBc}$$
$$k_{13} = k_{31} = k_{24} = k_{42} = 0$$
$$x = [x_1 \quad x_2 \quad x_3 \quad x_4]^T, F = [F_1 \quad 0 \quad 0 \quad 0]^T \tag{5.3}$$

$$k_{re} \begin{bmatrix} 1 - \left(\dfrac{\omega}{\omega_o}\right)^2 & -\dfrac{k_{s12c}}{k_{re}} & 0 & -\dfrac{k_{sBc}}{k_{re}} \\[2mm] -\dfrac{k_{s12c}}{k_{re}} & 1 - \left(\dfrac{\omega}{\omega_o}\right)^2 & -\dfrac{k_{s23c}}{k_{re}} & 0 \\[2mm] 0 & -\dfrac{k_{s23c}}{k_{re}} & 1 - \left(\dfrac{\omega}{\omega_o}\right)^2 & -\dfrac{k_{s34c}}{k_{re}} \\[2mm] -\dfrac{k_{sBc}}{k_{re}} & 0 & -\dfrac{k_{s34c}}{k_{re}} & 1 - \left(\dfrac{\omega}{\omega_o}\right)^2 \end{bmatrix} \begin{bmatrix} X_1 \\ X_2 \\ X_3 \\ X_4 \end{bmatrix} = \begin{bmatrix} 1 \\ 0 \\ 0 \\ 0 \end{bmatrix} F_1 \qquad (5.4)$$

Solution of (5.1) provides the force-to-displacement transfer function (i.e., X/F) for each resonator of a given filter. Here, it can be shown mathematically that the bridged filter structure of Figure 5.11 (a) is the superposition of monotonic filter structures in Figure 5.11 (b) and (c): where $(X_4/F_1)_{4CC}$ and $(X_4/F_1)_{2CC}$ present the force-to-displacement transfer functions of the 4CC and 2CC monotonic filters shown in Figure 5.11 (b) and (c), respectively. Generation of the loss pole is due to the signal cancellation (i.e., (5.5) = 0) between two parallel paths, therefore, the frequency of
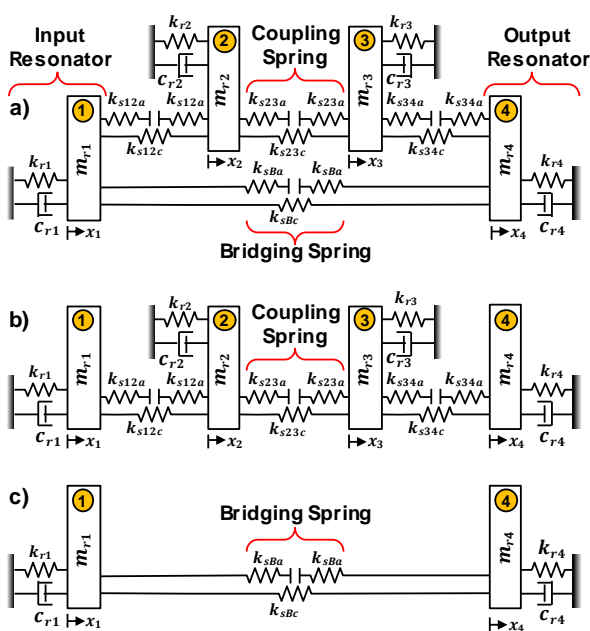
Figure 5.11: Equivalent lumped mechanical model for a bridged 4 CC-beam μmechanical filter (a). Equivalent lumped mechanical models for (b) 4CC-beam and (c) 2CC-beam μmechanical filters. Here, each λ/4 or 3λ/4 coupling spring is represented by a set of three springs: one positive adjoining spring, and two negative grounded springs, so as to simulate the canceling effect of quarter-wavelength design.
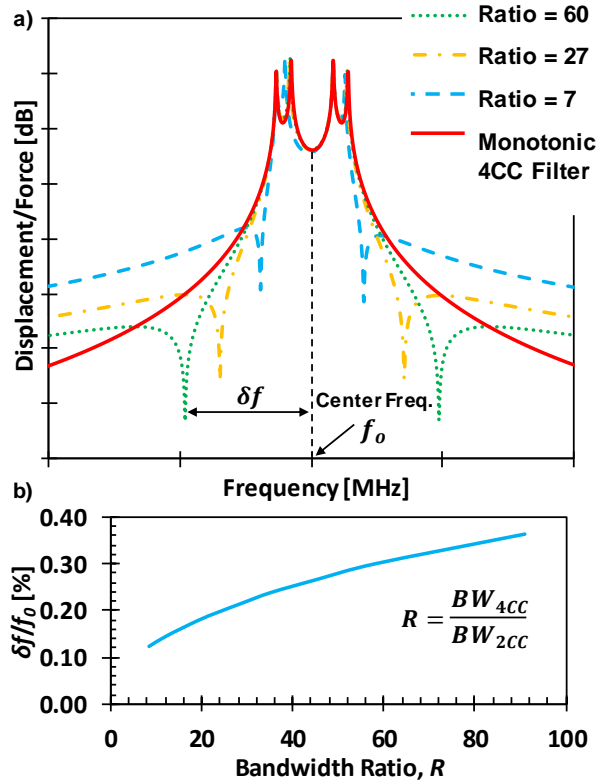
Figure 5.12: Simulated frequency response spectra for the equivalent lumped mechanical models of Fig. 10 (a) for different bandwidth ratio R. The width and coupling location of the bridging beam control the loss pole frequency. As the bandwidth ratio R increases, the loss poles move further from the passband (b).

the loss pole can be obtained by solving equation 5.6. Equation 5.7 and 5.8 provide the eigenvalue equation of the 4CC and 2CC monotonic filter of Figure 5.11 (b) and (c). Note that to capture the effect of the low-velocity coupling, the resonator effective stiffness should be calculated at the coupling location and therefore, the resonator effective stiffness k_{re} in the equation of motion in 5.4 has been modified to $\eta_c^2 k_{re}$. The velocity transform ratio η_c transfers the resonator effective stiffness from the center to the coupling location, as suggested in Chapter 3 and also given in equation 5.9.

The solution to 5.6 and the relative position of the loss pole to the filter center frequency depends on the ratio of 4CC and 2CC filter bandwidth, as shown in Figure 5.12. As mentioned earlier, the separation of modes in a mechanically-coupled system, which is proportional to the filter bandwidth, depends on the ratio between the resonator effective stiffness at the coupling location $\eta_c^2 k_{re}$ and the coupling beam stiffness k_{sc}. Equation 5.7 shows that the filter bandwidth and passband composition determine the required coupling stiffness, and the coupling stiffness sets the problem of optimum design for coupling beam width and the joint location, while the resonator dimensions and coupling beam lengths are determined by the filter center frequency and the choice of structure thickness, as explained in more detailed in Chapter 2 and 3. Similar approaches apply to the 3CC bridged filters in Figure 5.3 (a) and (b) to determine their loss pole.

$$\left(\frac{X_4}{F_1}\right)_{4CC-Bridged} = \left(\frac{X_4}{F_1}\right)_{4CC} + \left(\frac{X_4}{F_1}\right)_{2CC} \tag{5.5}$$

$$\left(\frac{X_4}{F_1}\right)_{4CC} = -\left(\frac{X_4}{F_1}\right)_{2CC} \tag{5.6}$$

As previously stated, the relative distance of the loss pole from the filter center frequency depends on the ratio of 4CC and 2CC filter bandwidth $R=BW_{4CC}/BW_{2CC}$. The width W_{sij} and the joint location l_{cl-3} of coupling beams between adjacent resonators determines the overall filter passband composition and therefore BW_{4CC}. Consequently, bandwidth of second-order filter BW_{2CC}, and therefore the stiffness of the bridging beam is the only design variable for loss pole optimization, i.e. the loss pole frequency is determined by W_{sB} and l_{cB}.

$$k_{re}\begin{bmatrix} 1-\left(\frac{\omega}{\omega_o}\right)^2 & -\dfrac{k_{s12c}}{\eta_{c12}^2 k_{re}} & 0 & 0 \\[2ex] -\dfrac{k_{s12c}}{\eta_{c12}^2 k_{re}} & 1-\left(\frac{\omega}{\omega_o}\right)^2 & -\dfrac{k_{s23c}}{\eta_{c23}^2 k_{re}} & 0 \\[2ex] 0 & -\dfrac{k_{s23c}}{\eta_{c23}^2 k_{re}} & 1-\left(\frac{\omega}{\omega_o}\right)^2 & -\dfrac{k_{s34c}}{\eta_{c34}^2 k_{re}} \\[2ex] 0 & 0 & -\dfrac{k_{s34c}}{\eta_{c34}^2 k_{re}} & 1-\left(\frac{\omega}{\omega_o}\right)^2 \end{bmatrix}\begin{bmatrix} X_1 \\ X_2 \\ X_3 \\ X_4 \end{bmatrix}_{4CC} = \begin{bmatrix} 1 \\ 0 \\ 0 \\ 0 \end{bmatrix}F_1 \tag{5.7}$$

$$k_{re}\begin{bmatrix} 1-\left(\dfrac{\omega}{\omega_o}\right)^2 & -\dfrac{k_{sBc}}{\eta_{cB}^2 k_{re}} \\ -\dfrac{k_{sBc}}{\eta_{cB}^2 k_{re}} & 1-\left(\dfrac{\omega}{\omega_o}\right)^2 \end{bmatrix}\begin{bmatrix} X_1 \\ X_4 \end{bmatrix}_{2CC} = \begin{bmatrix} 1 \\ 0 \end{bmatrix}F_1 \tag{5.8}$$

$$\eta_c = \sqrt{\dfrac{k_r(l_c)}{k_{re}}} = \dfrac{X_{mode}\left(\dfrac{L_r}{2}\right)}{X_{mode}(l_c)} \tag{5.9}$$

Figure 5.12 (a) presents the output resonator displacement of the 4CC bridged filter for different bandwidth ratio R, acquired by varying the coupling location l_{cB}. As the bandwidth ratio R decreases, the loss poles move closer to the passband and make the passband-to-stopband roll-off steeper. However, as the loss poles approach the passband, they compromise the out-of-band rejection and also affect the passband poles and introduce ripples in the passband. On the other hand, the larger the bandwidth ratio R, the further the loss poles are from the passband, until they do not affect the passband-to-stopband roll-off anymore. The optimum design of loss pole location requires careful examination of constraints set by the application and different trade-offs between out-of-band rejection, passband-to-stopband roll-off, passband composition and ripples, etc.

Figure 5.13 presents simulated frequency characteristics for each of the bridged filter designs explored in this work using their lumped parameter mechanical models as the one shown in Figure 5.11. Among the three design variations, the 4CC $3\lambda/4$ design demonstrates the best filter shape factor and the largest stopband rejection, albeit the use of more mechanical links and resonators. Figure 5.14 presents the simulated pole/zero plot for the input-to-output resonator transfer function
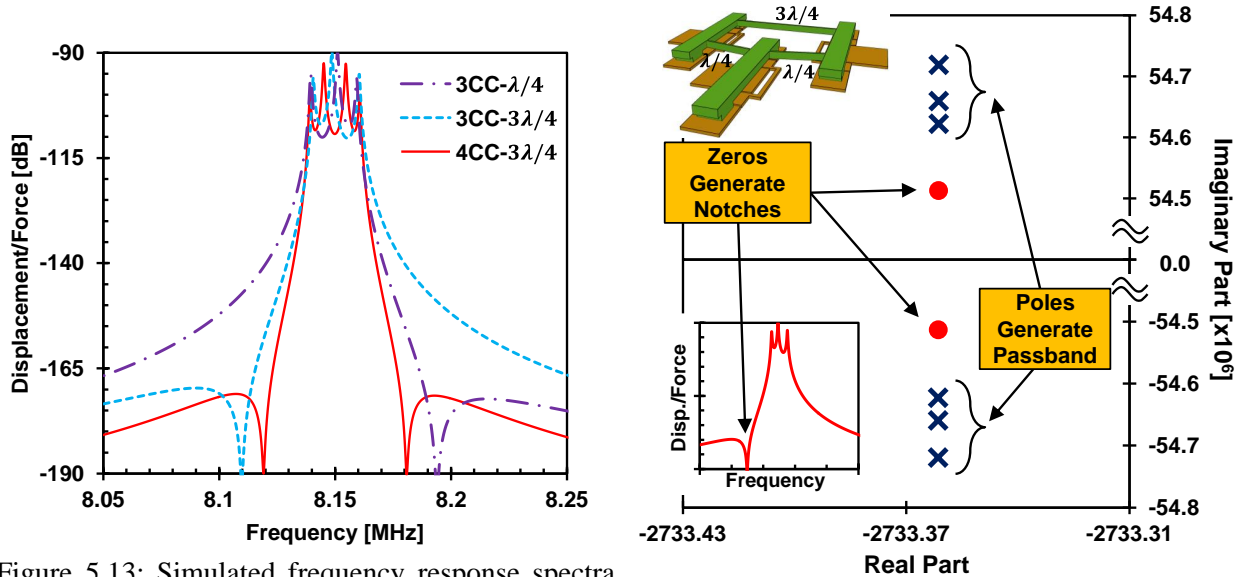
Figure 5.13: Simulated frequency response spectra for the equivalent lumped mechanical models for each of the filters of Fig. 1.

Figure 5.14: Pole/zero, i.e. root locus, plot of a transfer function derived from the mechanical vibration model of the output resonator in a 4CC $3\lambda/4$ bridged μmechanical filter.

for the 4CC $3\lambda/4$ bridged filter of Figure 5.3 (b) and modeled by 5.1, along with the actual transfer function plot. Here, the poles correspond to the mode shapes that combine to form the passband of this bridged filter, while the zeros generate the notch profile in its frequency response. The mechanical passband response is jagged at this point, but will be flattened out into an eventual filter passband by properly terminating the input and output resonators. The number of mechanical resonance modes with closely spaced frequencies is equal to the number of resonators used in the filter.

5.4 ELECTRICAL EQUIVALENT CIRCUIT

Although the described mechanical circuit model is helpful in gaining an analytical understanding of bridged filter operation, an electrical equivalent circuit model would give more insight on design verification and evaluation in actual communication systems, since it would allow the use of the abundant and well-developed electrical circuit simulators in existence, such as Keysight ADS [19]. The electrical equivalent circuit can be derived by mere analogy to the mechanical circuit of Chapter 2 and 3, where each mass is replaced by an inductor, each spring by a capacitor, and each damper by a resistor.

Using this approach, Figure 5.15 presents the electrical equivalent circuit for the 3CC $\lambda/4$ design of Figure 5.3 (a). As shown, each resonator originally represented by a mass-spring-damper is now modeled by an LCR circuit. The coupling beams are mechanical transmission lines, which are equated to T networks of energy storage elements by a combination of positive and negative valued capacitors to emphasize the quarter-wavelength cancellation nature of the coupling beams,
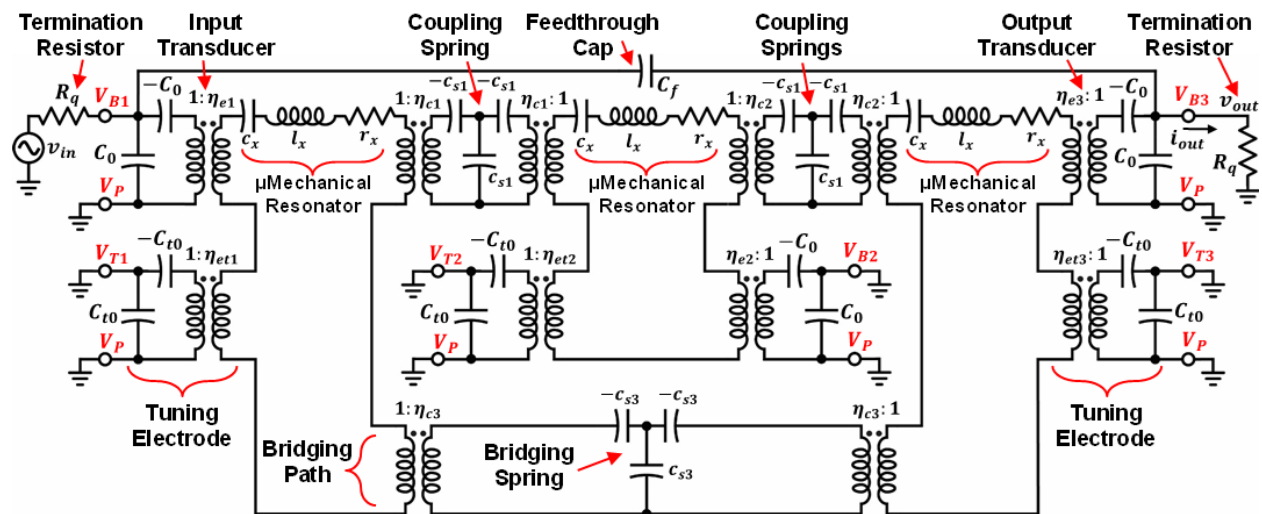
Figure 5.15: Equivalent electrical circuit for a 3CC-beam µmechanical bridged filter. Resonators and coupling beams are presented as LCR tanks and transmission line T-network model, respectively. Transformers with turn ratio ηe model the capacitive transducers (main and tuning electrode) and with turn ratio ηc represents low-velocity coupling. The negative capacitors at the input/output transducers model electrical stiffness and its voltage dependency accurately.

as described in Chapter 4. Note that Figure 5.15 clearly shows the bridging connection as a feedforward path in the electrical domain.

The frequency response of the mechanical circuit of Figure 5.13 has jagged passband due to the high quality factor Q of the constituent resonator tanks and it does not satisfy the frequency selection requirement expected from a filter. Hence, termination resistors shown in Figure 5.15 are required to load the Q's of the input and output resonators and form the desired passband shown in Figure 5.16. The value of the required termination resistor depends on the filter quality factor $Q_f=f_o/BW$, resonator electromechanical coupling coefficient C_x/C_o and the resonator static reactance $\omega_o C_o$, as developed in equation 3.15 and repeated in 5.10. Here q_i is a normalized parameter and depends on the filter type and order and can be looked up from a filter cookbook [20]. Desired value of termination resistance R_Q can be obtained by the optimum design of gap spacing d_o and bias voltage V_P, and resonator area $A=W_r L_r$.

$$R_Q = R_x \left(\frac{Q}{q_n Q_f} - 1 \right) \cong \frac{1}{q_n Q_f} \cdot \frac{1}{\left(\frac{C_x}{C_o} \right)} \cdot \frac{1}{\omega_o C_o} \tag{5.10}$$

Figure 5.16 demonstrates the properly terminated frequency characteristics of the bridged filters of Figure 5.1 (a-c), matching the expected frequency characteristics for each of the three designs. As shown, the 3CC design has one loss pole, which occurs above the passband when a $\lambda/4$ bridging beam is used, and below when a $3\lambda/4$ is used. The 4CC design achieves two loss poles with a $3\lambda/4$ bridging beam. As advertised, the frequency responses are similar to those of the mechanical simulations of Figure 5.13, except these show flat passbands and the actual (small) filter insertion loss, since they are properly terminated with R_Q. Like the response in mechanical

Figure 5.16: ADS-simulated frequency characteristics for the bridged 3CC $\lambda/4$, 3CC $3\lambda/4$, and 4CC $3\lambda/4$ micromechanical filters of Figure 5.3 all properly terminated, and using electrical equivalent circuits based on the topology of Figure 5.15.

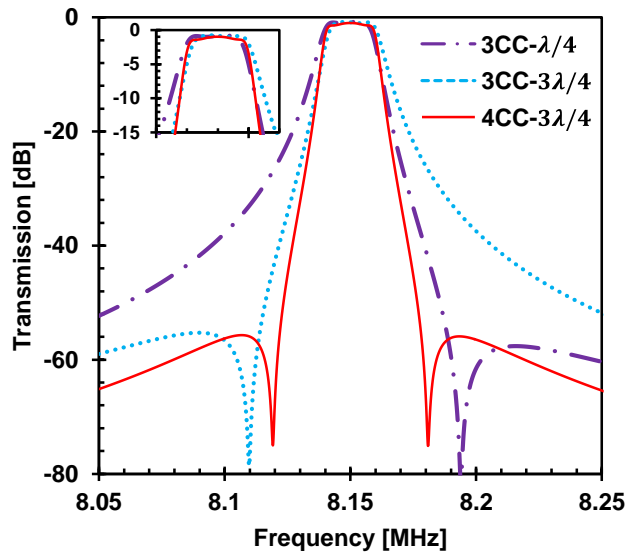domain, the 4CC 3λ/4 design exhibits the best filter shape factor among the three, although it has slightly larger insertion loss.

5.5 BRIDGED FILTER DESIGN EXAMPLE

Synthesis techniques for coupled resonator filters are well-established, and normalized values for their transfer function coefficients are readily available from data tabulated in filter cookbooks [20]. To better outline the exact design procedure, Table 5.1 presents a step-by-step summary of the design procedure for a 4CC 3λ/4 bridged micromechanical filter and specifies all needed dimensions and equations. Since the constituent resonator of a bridged filter is chosen

Table 5.1: 4CC 3λ/4 Bridged Filter Design (Using CC-Beams) Equation Summary.

Given/Set Values	Procedure/Objective	Relevant Design Equations for a Given Parameter
	Obtain lumped equivalent mechanical parameters for CC-beam resonator.	Use Table 2.1 to obtain m_{re}, k_{re}, and c_{re}.
Bridged Filter Schematic:	Find filter coupling coefficients k_{sija}, k_{sijb}, and k_{sijc} where i and j denote adjacent resonators. Determine dimensions W_{sij} and L_{sij} for filter coupling beams.	$k_{sij} = \eta_{cij}^2 k_{re}\left(\dfrac{BW}{f_o}\right)k_{ij}$ (T5. 1)
		where k_{re} is the resonator effective stiffness at the center and η_c is the low-velocity transformation.
		$k_{sija} = k_{sijb} = -k_{sijc} = -k_{sij}$ (T5. 2)
		Solve equation 4.22 for λ/4 coupling (1st root) using α to find L_{sij}.
		Use equation 4.19 for k_{sa} and optimize the solution for W_{sij} and the low-velocity transformation η_{ci}.
	Determine dimension L_{sb} for bridging beam. Find bridging coupling coefficients k_{sa}, k_{sb}, and k_{sc}.	Repeat (T5.2) again but choose 2nd root to obtain α for 3λ/4 coupling and solve for L_{sB}
		Obtain k_{sBa}, k_{sBb}, and k_{sBc} for optimum placement of the loss pole and solve for W_{sB} and η_{cB}.
	Obtain mechanical response (the model of Figure 5.11)	Use 5.1-5.9 to plot mechanical frequency response such as Figure 5.12.
Given and Set Values:	Determine equivalent circuit parameters for CC-beam resonator and coupling / bridging beams.	Use equations 2.19 to determine the equivalent electrical model shown in Figure 5.15.
7. Resonator dimensions and equivalent lumped mechanical/electrical parameters from Table 2.2.		$c_{sija} = c_{sijb} = -c_{sijc} = \dfrac{1}{k_{sij}}$ (T5. 3)
8. Filter type such as Inverse Chebyshev response in this example. 9. Normalized filter coupling coefficients k_{sij} and loaded q_i of Inverse Chebyshev response from filter cookbooks [27]. 10. Set designed filter bandwidth BW. 11. Filter coupling/bridging locations l_{ci}. 12. Choose proper W_{sij} for bridging beam.	Design for the optimum value of the termination resistance R_Q, resonator desing paramter, and the required area of the input/output resonators. Iterate these steps to achieve the desired values.	$R_Q = R_x\left(\dfrac{Q}{q_n Q_f} - 1\right) \cong \dfrac{1}{q_n Q_f}\cdot\dfrac{1}{\left(\dfrac{C_x}{C_o}\right)}\cdot\dfrac{1}{\omega_o C_o}$ Where R_x is the resonator motional impedance, Q is the unloaded resonator quality factor, and $Q_f = f_o$/BW, C_x/C_o is the resonator electromechanical coupling strength, C_o is the input/output static capacitance and ω_o is the resonator center frequency. (T5. 4)
	Determine filter insertion IL.	$IL = 20\log\left(\dfrac{R_Q + R_x}{R_Q}\right)$ $IL = 20\log\left(\dfrac{1}{1 - \dfrac{q_n Q_f}{Q}}\right)$ (T5. 5)
	Obtain electrical frequency response using the model of Figure 5.15	Insert all the required parameters of Figure 5.15 and use any circuit simulator to simulate filter frequency response such as Figure 5.16.

Bridged Filter Schematic labels: Anchor Points, l_{c2}, l_{c2}, L_{s12}, L_{s34}, Res. ②, Res. ③, L_{s23}, W_{s12}, W_{s34}, l_{c1}, l_{c1}, l_{c3}, l_{c3}, W_{s23}, Res. ①, Res. ④, W_{sB}, L_{sB}, l_{cB}, l_{cB}

corresponding to Table 2.1, resonator dimensions, material properties, electrode-to-resonator gap spacing d_o, center frequency f_o, equivalent lumped mechanical/electrical parameters, and shunt capacitance C_o are determined before implementing filter modeling. Next, specific type of bandpass filters, such as Butterworth, Chebyshev, linear phase, Gaussian, or Legendre, can be chosen with desired passband ripple in [27]. In this work, pseudo-Inverse Chebyshev filter response with designated filter bandwidth BW is utilized to enhance filter shape factor but, on the other hand, suffer relatively larger passband ripples. The normalized coupling coefficients k_{ij} and loaded q's (i.e., q_i) of a designated bandpass filter can be found from filter cookbook [27] and here tabulated in Table 5.2. The normalized coupling coefficients k_{ij} now can be denormalized into filter coupling coefficients using (T5.1) while the coupling spring constants k_{sija}, k_{sijb}, and k_{sijc} are determined via (T5.2) as well due to quarter wavelength design. The quarter-wavelength design presented in Chapter 4 determines the coupling beam length L_{sij} between adjacent resonators. The choice of coupling beam width W_{sij} and joint location $l_{c1\text{-}3}$ is an optimization problem to achieve normalized coupling stiffness k_{sij}, while considering fabrication constraints.

The bridging beam between the non-adjacent resonators is equivalent to three-quarter wavelength and the second root of equation 4.21 (i.e. $H_6{=}0$) determines the length L_{sB} of the bridging beam. The mechanical frequency characteristic of Figure 5.15 can be simulated using 5.1-5.4 with abovementioned parameters. Finally, the optimum design of bridging beam width W_{sB} and its location l_{cB} determines the loss pole location and filter roll-off.

To achieve terminated frequency response of a given bridged filter, all the electrical parameters of Figure 5.15 are required to attain flat passband and real insertion loss as shown Figure 5.16. Therefore, equivalent circuit parameters of the constituent resonator of a bridged filter are calculated from Table 2.1 and Table 5.2. The mechanical transformer turns ratio η_{ci} coupling and bridging locations l_{ci}, can be obtained from 5.16 while electromechanical coupling coefficient η_e are attained via 2.46 The desired termination resistance R_Q determines the optimum choice of gap spacing d_o for a certain bias voltage V_P. Finally, the frequency response of such a bridged filter can be simulated using model of Figure 5.15 applied into any circuit simulator, like Keysight ADS [74], to obtain flattened passband and real insertion loss.

5.6 FABRICATION AND EXPERIMENTAL RESULTS

The designed filter of Figure 5.3 were fabricated by the three-mask surface micromachining process described in Chapter 2. Figure 5.17-Figure 5.19 present SEM's for fabricated versions of each design.

Figure 5.20 presents two measurement setups to properly terminate the filter response. Since the filters of this work require termination resistance of 10kΩ, the available 50Ω-matched network analyzer cannot provide required loading and therefore, off-chip resistors R_Q, shown in Figure 5.20, are essential. But having a series resistance at the output of the filter buries the output signal

because of the voltage divider formed between R_Q and 50Ω internal impedance of the network analyzer. Having a unity-gain trans-impedance amplifier (Figure 5.20 (a)) or a buffer (Figure 5.20 (b)) at the output of the filter can eliminate that voltage divider and acts as an active matching network. The virtual ground of the amplifier inverting terminal effectively nulls out parasitic shunt capacitance, greatly improving the measurable bandwidth of the trans-impedance amplifier (Figure 5.20 (a)). Both measurement circuitries have been used to characterize the filter responses in this work and no perceivable difference was observed.

Figure 5.21-Figure 5.23 present frequency characteristics for each design, measured under 1mTorr vacuum using a
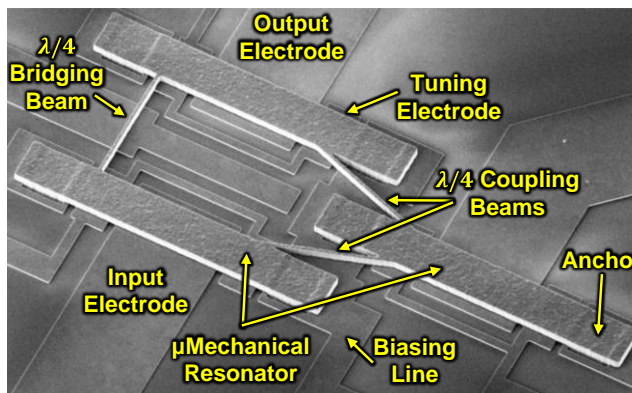
Figure 5.17: Scanning electron micrograph (SEM) of released 3CC $\lambda/4$ bridged micromechanical filter. Each constituent resonator in the filter has its own tuning electrode to maximize the tuning range of the final filter transfer function.

Figure 5.19: Scanning electron micrograph (SEM) of a 4CC $3\lambda/4$ bridged μmechanical filter with separate tuning electrode underneath each resonator.

Figure 5.18: Scanning electron micrograph (SEM) of a 3CC $3\lambda/4$ bridged μmechanical filter, depicting $\lambda/4$ coupling beams and $3\lambda/4$ bridging beam.
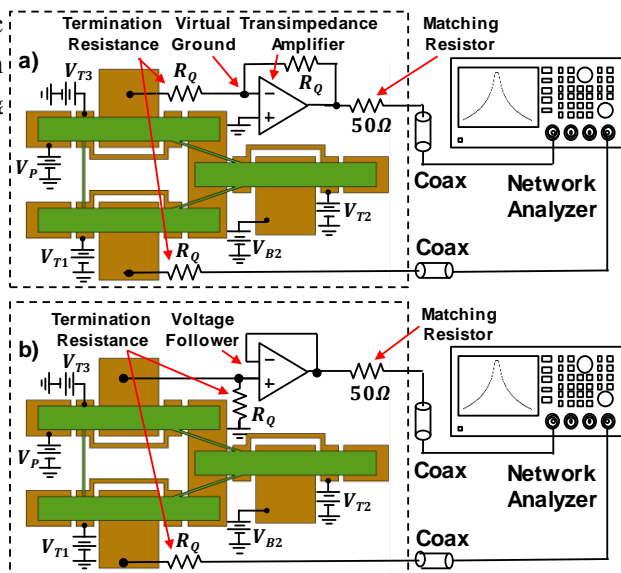
Figure 5.20: Test setup with trans-impedance (a) and unity buffer (b) illustrating the filter termination scheme, showing detail connections of operational amplifier circuit and measurement instrumentation for a bridged filter.

90

custom-built vacuum chamber together with a network analyzer, and using the indicated bias configurations of Figure 5.20, where V_P is applied to the filter structure, and V_{Ti} are tuning voltages of individual resonators. Since the main electrodes of the resonator #2 in 3CC filter and of the resonators #2 and #3 in 4CC filter do not act as input/output transducers, they have been used as extra tuning pad with indicated voltage sources V_{Bi}.

As shown in Figure 5.21, the 3CC $\lambda/4$ design achieves an insertion loss of only 1.2 dB for a 0.13% bandwidth centered at 8.08 MHz, with 40 dB of stopband rejection, and a (notch) loss pole above the passband, as expected, achieving 20-dB shape factor of 2.08, much better than achieved previously in [12], and also providing extra 12 dB rejection. From Figure 5.22, the 3CC $3\lambda/4$ design achieves an insertion loss of 1 dB for a 0.12% bandwidth centered at 8.18 MHz, with a loss pole be-low the passband and a shape factor of 2.03. Figure 5.23 characterized the 4CC $3\lambda/4$ design which achieves an insertion loss of 1 dB for a 0.32% bandwidth centered at 8.074 MHz, with 40 dB stopband rejection and a shape factor of 1.84.
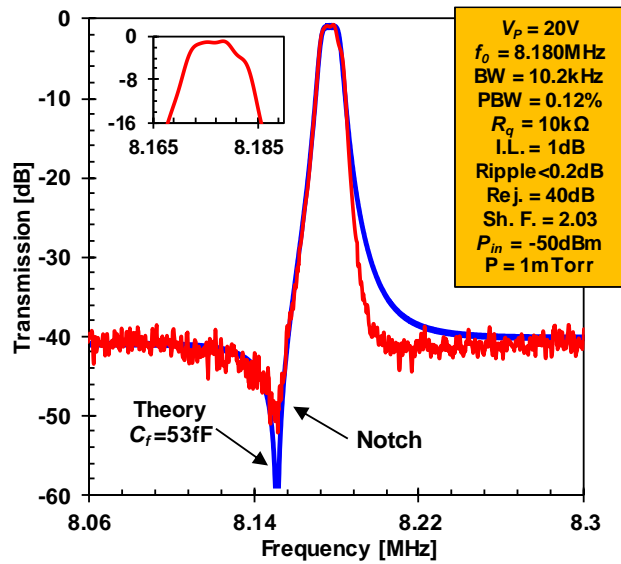
Figure 5.22: Measured frequency characteristic for 3CC $3\lambda/4$ bridged micromechanical filter of Figure 5.18.
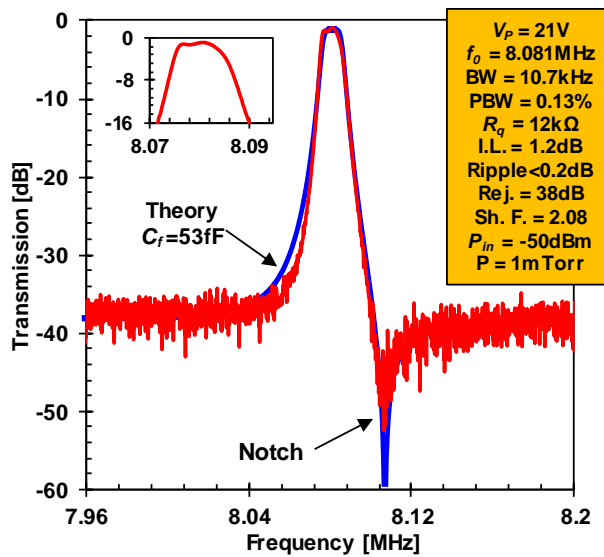
Figure 5.21: Measured frequency characteristic for 3CC $\lambda/4$ bridged micromechanical filter of Figure 5.17.
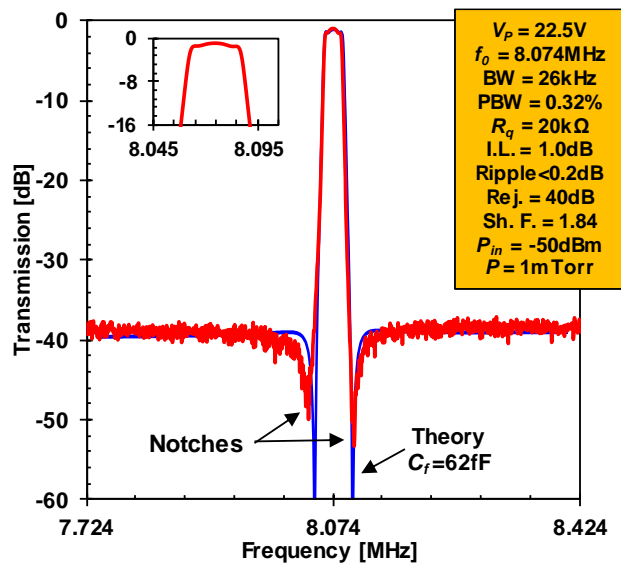
Figure 5.23: Measured frequency characteristic for the 4CC $3\lambda/4$ bridged micromechanical filter of Figure 5.19.

91

The narrow-band filters presented so far are capable of exclusively selecting a channel within a desired band. However, in any practical application, the receiver should be able to communicate via any designated channel (Figure 5.24 (a)). A RF switch followed by a filter bank [21] like the one shown in Figure 5.24 (b) is capable of selecting any desired channel, though in expense of a huge footprint. Recently, application of tunable filters (Figure 5.24 (c)) have been the subject of extensive research and various methods have been developed, usually in expense of extra fabrication steps, large footprints or including off-chip components [75]. The voltage-dependent electrical stiffness [62] provides tuning capability for capacitive transducers free of charge and the tuning electrodes underneath each constituent resonators of this work offer tuning capability for individual poles and zeros of the filter transfer function. Figure 5.24 (d) presents the tuning capability of the 3CC $3\lambda/4$ bridged filter of this work. The bias voltage V_P shifts the filter center frequency and then tuning voltages V_{T1-3} and V_{B2} minimize any passband ripple by tuning individual resonators. This filter has remarkable tuning resolution of 80kHz/V, which translates to tuning range of 1%/V.

e)	Filter #3	Filter #2	Filter #1
V_P	22V	21V	20V
f_0	7.998MHz	8.080MHz	8.159MHz
BW (PBW)	8.7kHz (0.11%)	10.5kHz (0.13%)	11.3kHz (0.14%)
PBW	0.11%	0.13%	0.14%
Sh. F.	2.37	2.14	2.07
V_{T1}, V_{T2}	-0.36V, 0.15V	-0.42V, 0.18V	-.022V, 0.33V
V_{T3}, V_{B2}	-0.02V, 0.45V	0.00V, 0.11V	-0.69V, 0.64V
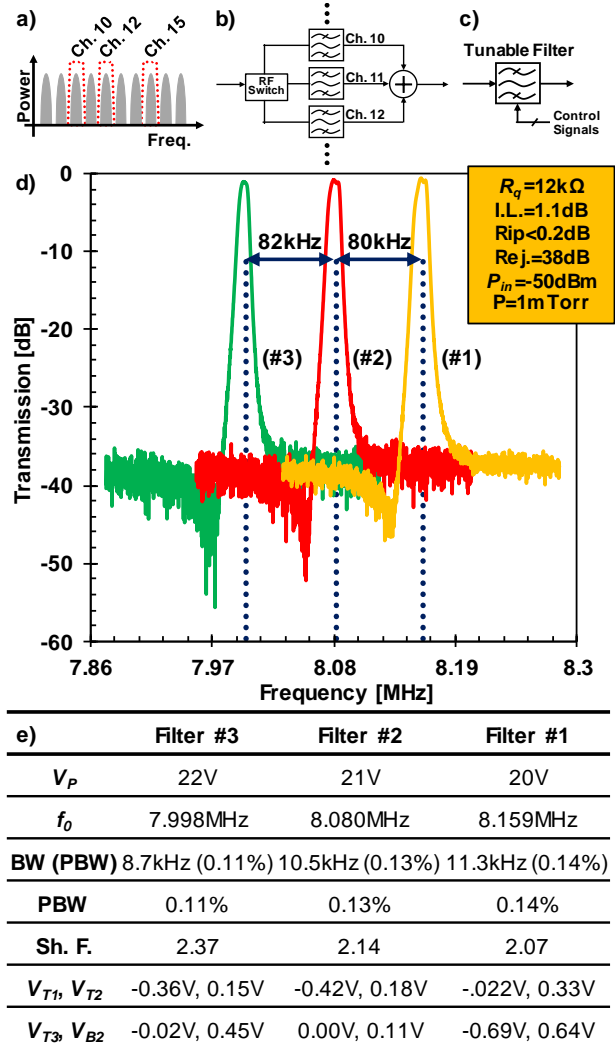
Figure 5.24: The receiver should be able to select between different channels available in the band (a). Combination of a RF switch and a filter bank (b) is capable of choosing appropriate channels, in expense of big foot-print, while a tunable filter provides selectivity and flexibility (c). Intrinsic tuning capability of capacitive transducers offers the ultimate solution (d). The bias voltage changes the center frequency and the tuning voltages correct any passband ripple (e).

92

Table 5.2: Bridged Filter Design Summary

Parameter	3CC $\lambda/4$ Design		3CC $3\lambda/4$ Design		4CC $3\lambda/4$ Design		Units
	Design/Sim.	Meas.	Design/Sim.	Meas.	Design/Sim.	Meas.	
Center Frequency, f_o	8.469	8.081	8.469	8.180	8.469	8.074	MHz
Resonator Q	10,000	15,100	10,000	15,100	10,000	15,100	—
Bandwidth, BW	11.1	10.7	11.1	10.2	27.3	26	kHz
Percent Bandwidth, (BW/f_o)	0.131	0.132	0.131	0.125	0.322	0.322	%
Filter DC-Bias, V_P	30	21	30	20	30	22.5	V
Loaded $q_i{}^*$	1.0	--	1.0	--	0.7654	--	—
Normalized Filter Coupling Coef., $k_{12}{}^*$	0.674	--	0.674	--	0.597	--	—
Normalized Filter Coupling Coef., $k_{23}{}^*$	0.419	--	0.419	--	0.431	--	—
Normalized Filter Coupling Coef., $k_{34}{}^*$	--	--	--	--	0.465	--	—
Filter Coupling Beam Length, L_{s12}, L_{s23}, L_{s34}	22.3	--	22.3	--	22.3	--	μm
Bridging Beam Length, L_{s13}, L_{s14}	22.3	--	51.8	--	51.8	--	μm
Filter Coupling Beam Width, W_{s12}, W_{s23}, W_{s34}	0.75	--	0.75	--	0.75	--	μm
Bridging Beam Width, W_{sb}	0.75	--	0.75	--	0.75	--	μm
Coupling/Bridging Beam Thickness, h	2	1.985	2	1.985	2	1.985	μm
Resonator Mass @ I/O, m_{re}	5.829×10^{-13}	5.902×10^{-13}	5.829×10^{-13}	5.902×10^{-13}	5.829×10^{-13}	5.902×10^{-13}	kg
Resonator Stiffness @ I/O, k_{re}	1.923×10^3	1.772×10^3	1.923×10^3	1.772×10^3	1.923×10^3	1.772×10^3	N/m
Resonator Damping @ I/O, c_{re}	3.036×10^{-9}	1.841×10^{-9}	3.036×10^{-9}	1.841×10^{-9}	3.036×10^{-9}	1.841×10^{-9}	Ns/m
Filter Coupling Location, l_{c1-3}	4.1, 3.6	4.5, 4.0	4.1, 3.6	4.5, 4.0	5.1, 4.65, 4.75	5.5, 5.05, 5.15	μm
Bridging Location, l_{cb}	2.2	2.6	2.2	2.6	2.3	2.7	μm
Coupling Beam Stiffness, k_{s12a}, k_{s23a}, k_{s34a}	-109.56	87.72	-109.56	87.72	-109.56	87.72	N/m
Coupling Beam Stiffness, k_{s12c}, k_{s23c}, k_{s34c}	109.56	103.09	109.56	103.09	109.56	103.09	N/m
Bridging Beam Stiffness, k_{sb}	-109.56	87.72	125.68	214.42	125.68	214.42	N/m
Bridging Beam Stiffness, k_{sb}	109.56	103.09	-125.68	-155.09	-125.68	-155.09	N/m
Filter Coupling Capacitance, c_{s12a}, c_{s23a}, c_{s34a}	-0.0091	-0.0114	-0.0091	-0.0114	-0.0091	-0.0114	F
Filter Coupling Capacitance, c_{s12c}, c_{s23c}, c_{s34c}	0.0091	0.0097	0.0091	0.0097	0.0091	0.0097	F
Bridging Capacitance, c_{sb}	-0.009	-0.0114	0.008	0.0047	0.008	0.0047	F
Bridging Capacitance, c_{sb}	0.009	0.0097	-0.008	-0.0064	-0.008	-0.0064	F
Mechanical Transformer Turn Ratio at l_{c1-3}, η_{c1-3}	8.03, 10.18	7.04, 8.071	8.03, 10.18	7.04, 8.071	5.44, 6.40, 6.16	4.93, 5.73, 5.54	C/m
Mechanical Transformer Turn Ratio at l_{cb}, η_{cb}	25.65	19.39	25.65	19.39	23.57	18.06	C/m
Equivalent Inductance, l_x	5.829×10^{-13}	5.902×10^{-13}	5.829×10^{-13}	5.902×10^{-13}	5.829×10^{-13}	5.902×10^{-13}	H
Equivalent Capacitance, c_x	4.323×10^{-4}	5.644×10^{-4}	4.323×10^{-4}	5.644×10^{-4}	4.323×10^{-4}	5.644×10^{-4}	F
Equivalent Resistance, r_x	3.036×10^{-9}	1.841×10^{-9}	3.036×10^{-9}	1.841×10^{-9}	3.036×10^{-9}	1.841×10^{-9}	Ω
Electromechanical Coupling Coefficient, η_e	1.833×10^{-6}	1.409×10^{-6}	1.833×10^{-6}	1.330×10^{-6}	1.833×10^{-6}	1.532×10^{-6}	C/m
Calculated Equivalent Resistance, R_x	0.904	1.018	0.904	1.151	0.904	0.852	kΩ
Calculated Equivalent Inductance, L_x	0.173	0.297	0.173	0.334	0.173	0.25	H
Calculated Equivalent Capacitance, C_x	2.12	1.257	2.12	1.105	2.12	1.52	fF
Static Overlap Capacitance, C_o	9.44	10.12	9.44	10.12	9.44	10.12	fF
Electromechanical Coupling Cx/C_o	22.5	12.42	22.5	10.92	22.5	15.0	%
Termination Resistance, R_Q	11	12	11	10	22	20	kΩ
Insertion Loss, IL	0.3	1.2	0.3	1.0	0.3	1.0	dB
20 dB Shape Factor	2.07	2.08	2.07	2.03	1.42	1.84	—
Stopband Rejection, SR	90	40	90	40	90	40	dB
Loss Pole position, $|f_{loss\,pole} - f_o|/f_o$	0.369	0.297	0.354	0.367	0.406, 0.411	0.421, 0.396	%

*From filter cookbooks [27].

Chapter 6 NONLINEARITY IN MICROMECHANICAL RESONATORS AND FILTERS

Channel-select filters like those presented in Chapter 5, capable of rejecting all interferer signals relax the dynamic range requirements on subsequent stages, e.g., the LNA and the mixer, thereby greatly reduce the receiver power consumption. However, the degree of interferer suppression depends strongly on the linearity of the filter, which if not sufficiently linear, can also generate intermodulation spurs even after rejecting interferers.

Pursuant to determining the linearity of high-order capacitive-gap micromechanical filters, this chapter represents a complete analytical formulation for the IIP3 of such devices and then verifies the formulation via experimental measurement on the 3rd- and 4th-order bridged filters. With IIP3 on the order of 36dBm for 400-kHz tone separations, these filters possess sufficient linearity for a large range of HF RF front-end or IF applications.

6.1 SYSTEM NONLINEARITY

The general filter design procedure developed so far presumes the micromechanical filters as a linear system, i.e. the output of the system is a mere scaled version of the input at exactly the given tone, shown in Figure 6.1 (a). However, any practical system entails some nonlinearity and this nonlinearity is most conveniently modeled by a Taylor series given in equation 6.1, where x and y are input and output and a_is describe system behavior [17]. In general, the system input is not a pure sinusoidal signal at a given frequency, and hence, the system response to a general input such as the one given in equation 6.2 is required for complete understanding of the system. Here, two interferer signals at frequencies ω_1 and ω_2 add to the desired signal at frequency ω_o.

$$y = a_o + a_1 x + a_2 x^2 + a_3 x^3 + \cdots \tag{6.1}$$
$$x = S_o \cos(\omega_o t) + S_1 \cos(\omega_1 t) + S_2 \cos(\omega_2 t) \tag{6.2}$$

When this signal passes through a nonlinear transfer function of the form in (6.1), the output includes not only a scaled version of the input, but also spurious signals at frequencies not present in the original input. Specifically, inserting (2) into (1), harmonics as well as inter-modulation components arise:

    i.   The odd-order nonlinearities contribute to the DC offset at the output, which affect the operational point of the following stages. In a capacitive transducer, these terms modify the bias voltage V_P and therefore, the system performance such as center

frequency f_o or electromechanical coupling strength (C_x/C_o) might change by strong input signal.

ii.   Third-order nonlinearity also modifies the main output terms and effectively changes the system linear gain a_1. In most practical cases, $a_1a_3 < 0$ and therefore, the system gain reduces at large input power.

iii. Second-order intermodulation between input tones produces very low frequency terms at the output and causes the slow-varying fluctuations at the output.

iv.   Harmonics of the input tones at $n\omega_i$, although are at much higher frequencies and can be filtered out easily, but they might cause unwanted oscillation in the following stages and more importantly, they might affect other systems operating at or near those frequencies.

v.   Third-order intermodulation produces output tones very close to the desired frequency ω_o. Specially, if the tones are spaced equally, i.e. $\omega_1-\omega_o = \omega_2-\omega_1 = \pm\Delta\omega$, then $2\omega_1-\omega_2 = \omega_o$ and the intermodulation tone is exactly at the desired frequency disturbing the desired signal detection. The intermodulation term can be considered as noise at the output degrading the system signal-to-noise ratio SNR. The intermodulation term can completely mask the desired signal, for strong enough tones at the input.
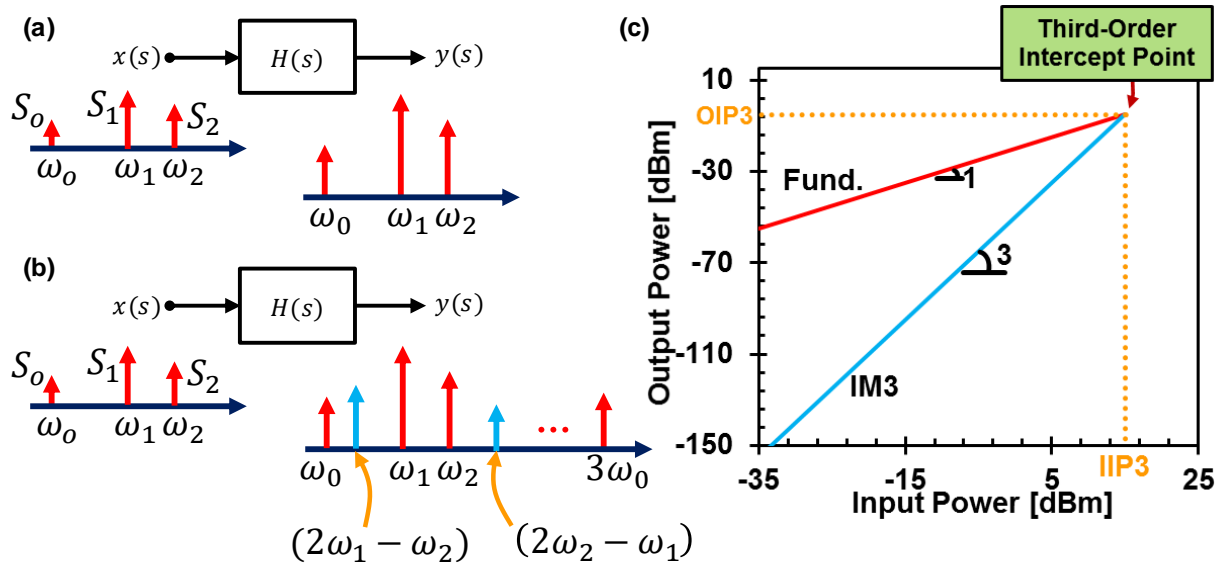
Figure

Figure 6.1: (a) Perspective-view schematics for the three bridged micromechanical filter designs used in this work to measure nonlinearity in capacitive-gap filters and their frequency characteristics. (b) Two-tone experiment setup showing needed biasing, excitation, and sensing circuits along with CC beam dimensions. Tones are spaced equally from each other and from the center frequency of the filter.

$$y = a_o + \frac{a_2}{2}\{S_o^2 + S_1^2 + S_2^2\} + \cdots \qquad\qquad i$$

$$+a_1\{S_o \cos(\omega_o t) + S_1 \cos(\omega_1 t) + S_2 \cos(\omega_2 t)\} + \frac{3}{4}a_3 S_o \cos(\omega_o t) + \cdots \quad ii$$

$$+a_2\{S_o S_1 \cos((\omega_o - \omega_1)t) + S_o S_2 \cos((\omega_o - \omega_2)t) + \cdots\} \qquad iii \quad (6.3)$$

$$+\frac{a_2}{2}\{S_o^2 \cos(2\omega_o t) + \cdots\} + \frac{a_3}{2}\{S_o^3 \cos(3\omega_o t) + \cdots\} + \cdots \qquad iv$$

$$+\frac{3}{4}a_3\{S_1^2 S_2 \cos((2\omega_1 - \omega_2)t) + S_1^2 S_2 \cos((2\omega_1 + \omega_2)t)\} + \cdots \qquad v$$

These five terms summarize different consequences of the system nonlinearity on the system performance and characteristic and advocate the need to reduce the nonlinear coefficients a_2 and a_3 to suppress the undesired effects. Particularly, intermodulation between two equispaced input tones can produce output terms at frequencies near the desired signal, which is not distinguishable from the desired tone at all. This third-order intermodulation component, IM3, can directly impact the signal-to-noise ratio of the desired channel and eventually mask the channel completely, if the system nonlinearity is too large. Hence, *IM3* distortion must be constrained below a minimum acceptable value.

Since the intermodulation term grows by the input power cube while the linear term grows proportional to the input power, their extrapolated lines intercept at some point, as shown in Figure 6.1. The third-order input intercept point (*IIP3*), the common measure of the third order nonlinearity, is defined as the input power level at which the extrapolated intermodulation component has the same power as the fundamental output, when all the input tones have equal power level. In general, a larger IIP3 indicates smaller nonlinearity (or better linearity) in a given system, as suggested by equation 6.4, and hence smaller intermodulation component generation, which is a design goal of communication systems.

$$a_1 S_o = \frac{3}{4}a_3 S_o^3 \rightarrow S_o = \sqrt{\frac{4}{3} \cdot \left|\frac{a_1}{a_3}\right|} \qquad\qquad (6.4)$$

As shown in Figure 6.2, while a micromechanical channel-select filter attenuates out-of-channel interferer signals, its nonlinearity can still result in intermodulation components at its output that corrupt the desired signal, which motivates the necessity to design for maximum filter *IIP3*. Note that interferer signals for a channel-select filter are outside the filter pass-band.

6.2 CAPACITIVE-GAP TRANSDUCER NONLINEARITY

Nonlinearity in either resonator stiffness [76] or capacitive-gap transduction [77] is often the most important contributors to filter nonlinearity. The former becomes significant when large

displacement induces non-negligible internal strain in the resonator, which manifests as a stiffness nonlinearity. Since interferer signals are out-of-channel for a channel-select filter, the induced displacement is generally very small, so the stiffness nonlinearity is negligible. Therefore, transducer nonlinearity which translates to input force nonlinearity generates the intermodulation term of a channel-select filter.

The parallel-plate capacitor described in Chapter 2 can simplify the derivation of the micromechanical resonator nonlinear terms. The findings of this section will be expanded for the micromechanical filters in the following sections.

The transducer takes as input a dc voltage V_P applied to one electrode and an *ac* excitation voltage v_i applied to the other. The free electrode moves in response to the force F generated by the input voltage combination following a biquad frequency response of Figure 6.3, where the electrode effective stiffness k_{re} and quality factor Q determine the maximum displacement according to equation 6.4 and 6.5, where ω_o is the resonance frequency. The mechanical force F is due to the electrostatic actuation and the equation 6.6 provides the linear displacement-to-voltage transfer function for a single tone input at frequency ω and amplitude of V_o. Here, η_e is the electromechanical coupling introduced in Chapter 2.

$$\frac{X}{F}(\omega) = \frac{1}{k_{re}} \Theta(\omega) \tag{6.5}$$

$$\Theta(\omega) = \frac{1}{1 - \left(\dfrac{\omega}{\omega_o}\right)^2 + \dfrac{j\omega}{Q\omega_o}} \tag{6.6}$$

$$\frac{X}{V_o}(\omega) = \frac{\eta_e}{k_{re}} \Theta(\omega) \tag{6.7}$$

The nonlinearity in the transduction force is due to the nonlinear nature of the gap-closing capacitive transducers, like the one shown in Figure 6.3. Equation 6.7 provides the total actuation
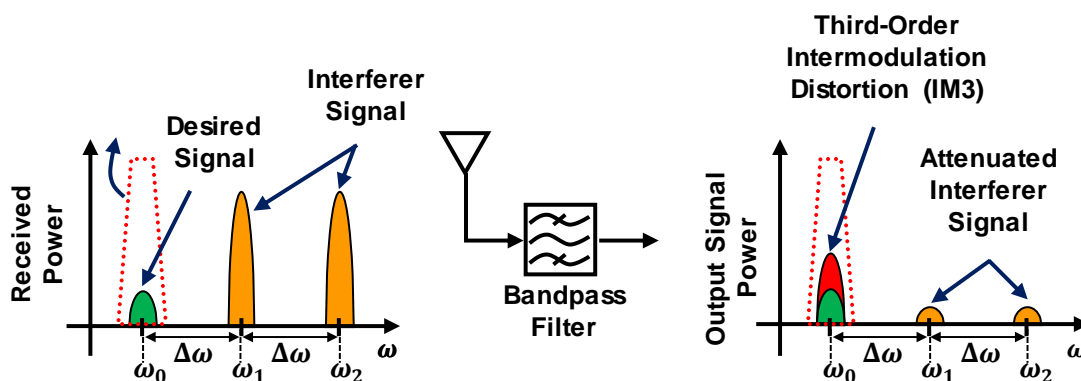

Figure 6.2: While a channel-select filter attenuates out-of-band interferer signals, filter nonlinearity can still produce a troublesome intermodulation component at the output, especially if interferers are $\Delta\omega$ and $2\Delta\omega$ away from desired signal, for which the IM3 component will be exactly at ω_o and can deteriorate receiver signal-to-noise ratio, *SNR*.

force F_{tot} that drives the resonator to move a displacement x and clearly shows the nonlinear dependency of the actuation force F_{tot} on the input voltage v_i and the resonator displacement x. For purposes of IIP3 determination, the input voltage comprises the sum of two out-of-band signals with equal amplitude V_o. Without loss of generality, we can assume ω_1 and ω_2 are chosen such that $2\omega_1-\omega_2=\omega_o$, as in equation 6.9. Application of this input voltage induces small resonator displacement X_1 and X_2 at the corresponding frequencies which can be found from equation 6.6. Nonlinear interaction between these displacements and the input voltages produces a displacement spur at ω_o via third-order intermodulation terms, as discussed in the previous section and shown in Figure 6.4. Hence, the total resulting resonator displacement takes the form given in equation 6.10, where the amplitude of the displacement at ω_o to be determined later. The phase terms ϕ_1 and ϕ_2 are necessary for the general equation of motion that includes the damping term b_{re}, and if ω_1 and ω_2 are far enough from the center frequency ω_o, they can be approximated by 0 or $-\pi$, for $\omega_1,\omega_2<\omega_o$ and $\omega_1,\omega_2>\omega_o$ respectively. Equation 6.11 provides the displacement expression for the latter case, assuming high-Q micromechanical resonators and defining $\Theta_1= \Theta(\omega_1)$ and $\Theta_2=\Theta(\omega_2)$.

$$F_{tot} = \frac{1}{2}(V_P - v_i)^2 \frac{dC}{dx} = \frac{1}{2}(V_P - v_i)^2 \frac{d}{dx}\left(\frac{\varepsilon A}{d_o - x}\right)$$

$$F_{tot} = \frac{1}{2}(V_P - v_i)^2 \frac{d}{dx}\left(C_o\left(1 - \frac{x}{d_o}\right)^{-1}\right) \tag{6.8}$$

$$F_{tot} = \frac{1}{2}(V_P - v_i)^2 \frac{C_o}{d_o}\left(1 + \frac{2x}{d_o} + \frac{3x^2}{d_o^2} + \frac{4x^3}{d_o^3} + \cdots\right)$$

$$v_i = v_1 + v_2 = V_o \cos(\omega_1 t) + V_o \cos(\omega_2 t) \tag{6.9}$$

$$\omega_1 = \omega_o + \Delta\omega, \qquad \omega_2 = \omega_o + 2\Delta\omega \tag{6.10}$$

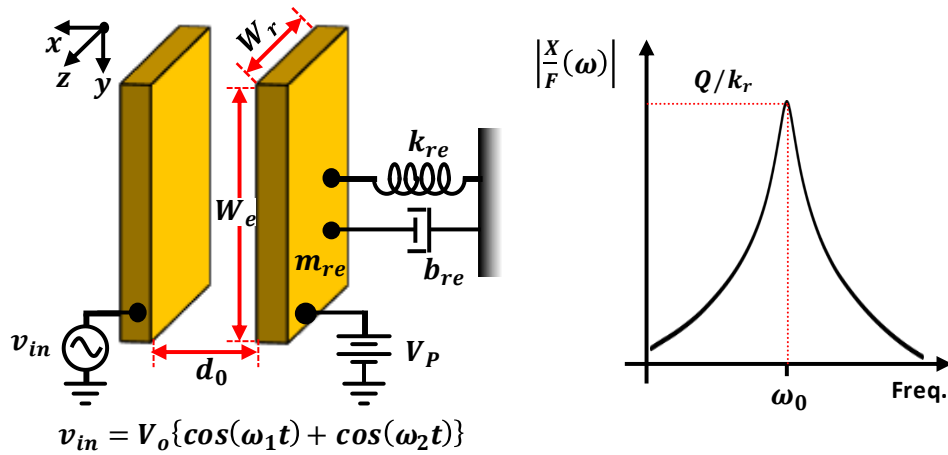$$v_{in} = V_o\{cos(\omega_1 t) + cos(\omega_2 t)\}$$

Figure 6.3: Simplified schematic of a parallel-plate capacitive-gap transducer. The moving plate with effective stiffness and mass of k_{re} and m_{re}, respectively, produces the bandpass biquad frequency response shown on the right.

$$x = x_o + x_1 + x_2 = X_o \cos(\omega_o t + \phi_o) + X_1 \cos(\omega_1 t + \phi_1) + X_2 \cos(\omega_2 t + \phi_2)$$

$$X_1 = \frac{\eta_e V_o}{k_{re}} |\Theta(\omega_1)| = \frac{\eta_e V_o}{k_{re}} |\Theta_1|, \qquad X_2 = \frac{\eta_e V_o}{k_{re}} |\Theta(\omega_2)| = \frac{\eta_e V_o}{k_{re}} |\Theta_2| \tag{6.11}$$

$$\phi_o = \frac{\pi}{2}, \qquad \phi_1 = \phi_2 = -\pi$$

$$x = x_o + x_1 + x_2 \cong X_o \sin(\omega_o t) - X_1 \cos(\omega_1 t) - X_2 \cos(\omega_2 t) \tag{6.12}$$

$$X_1 = \frac{\eta_e V_o}{k_{re}} |\Theta_1|, \qquad X_2 = \frac{\eta_e V_o}{k_{re}} |\Theta_2|$$

Substituting equations 6.8 and 6.10 into the actuation force expression of equation 6.7 determines the displacement amplitude at the resonance frequency ω_o due to third-order intermodulation of two off-resonance signals at ω_1 and ω_2. As suggested by equation 6.7, third-order intermodulation can be originated from different interactions between input voltages v_i and resonator displacement x. Equation 6.12 provides all the possible combination of v_is and x_is that generate third-order intermodulation at ω_o assuming the condition of equation 6.9. Since the input voltage v_i and the associated displacement x is relatively small, equation 6.13 neglects all higher order terms of equation 6.12, without introducing substantial error in the calculation. Substituting the displacement term from the equation 6.11, equation 6.14 presents the third-order intermodulation force that induces displacement resonator at ω_o. Here, A is the capacitor area defined by $A=W_r W_e$ from Figure 6.3. Further investigation of this equation suggests that it can be simplified by application of electromechanical coupling strength (C_x/C_o), as shown in equation 6.15. Since the coupling strength is usually on the order of a few % or less, the last term will dominate the expression in the parenthesis.

$$F_{IM3} = \frac{C_o}{2d_o} \left(\begin{array}{c} V_P^2 \left(\frac{12}{d_o^3} x_1^2 x_2 \right) + V_p v_1 \left(\frac{12}{d_o^2} x_1 x_2 \right) + V_p v_2 \left(\frac{6}{d_o^2} x_1^2 \right) \\[6pt] + v_1^2 \left(\frac{2}{d_o} x_2 + \frac{4}{d_o^3} (x_2^3 + 3x_o^2 x_2 + 3x_1^2 x_2) \right) + v_2^2 \left(\frac{12}{d_o^3} x_1^2 x_2 \right) \\[6pt] + v_1 v_2 \left(\frac{4}{d_o} x_1 + \frac{8}{d_o^3} (x_1^3 + 3x_o^2 x_1 + 3x_1 x_2^2) \right) + \cdots \end{array} \right) \tag{6.13}$$

$$F_{IM3} = \frac{C_o}{2d_o} \left(\begin{array}{c} V_P^2 \left(\frac{12}{d_o^3} x_1^2 x_2 \right) + V_p v_1 \left(\frac{12}{d_o^2} x_1 x_2 \right) + V_p v_2 \left(\frac{6}{d_o^2} x_1^2 \right) \\[6pt] + v_1^2 \left(\frac{2}{d_o} x_2 \right) + v_1 v_2 \left(\frac{4}{d_o} x_1 \right) \end{array} \right) \tag{6.14}$$

$$F_{IM3} = V_o^3 \frac{V_P (\varepsilon A)^2}{4d_o^5 k_{re}} \left(\begin{array}{c} 6 \frac{V_P^4 (\varepsilon A)^2}{d_o^6 k_{re}^2} |\Theta_1|^2 |\Theta_2| - 3 \frac{V_P^2 \varepsilon A}{d_o^3 k_{re}} (2|\Theta_1||\Theta_2| + |\Theta_1|^2) \\[6pt] + (2|\Theta_1| + |\Theta_2|) \end{array} \right) \tag{6.15}$$

$$F_{IM3} = V_o^3 \frac{V_P(\varepsilon A)^2}{4d_o^5 k_{re}} \left(6\left(\frac{C_x}{C_o}\right)^2 |\Theta_1|^2|\Theta_2| - 3\left(\frac{C_x}{C_o}\right)(2|\Theta_1||\Theta_2| + |\Theta_1|^2) \atop +(2|\Theta_1| + |\Theta_2|) \right) \tag{6.16}$$

The third-order input intercept point (*IIP3*) is defined as the input power for which the third-order modulation *IM3* term is equal to the fundamental term. Assuming the nonlinearity associated with current generation at the output transducer is negligible compared to those associated with force generation at the input transducer, equating F_{IM3} (6.15) to the fundamental force F_{fund} (6.16) when exciting the resonator at ω_o, and then solving for V_o, yields the expression for input voltage V_{IIP3}, as given in (6.17). Recognizing that the linear force component is the corresponding input power, IIP_3, then takes the form given in equation 6.18 where R_T is the total resistance in the system, seen at the input, dominated by the resonator motional resistance R_x. substituting for the motional resistance, equation 6.19 delivers the *IIP3* point of a capacitive micromechanical resonator. Note that this expression is linear, while *IIP3* is usually been reported in dBm by proper conversion.

$$F_{fund} = V_P V_o \frac{\varepsilon A}{d_o^2} \tag{6.17}$$

$$V_{IIP3}^2 = \frac{\frac{4d_o^3 k_{re}}{\varepsilon A}}{\left(6\frac{V_P^4(\varepsilon A)^2}{d_o^6 k_{re}^2}|\Theta_1|^2|\Theta_2| + 3\frac{V_P^2 \varepsilon A}{d_o^3 k_{re}}(2|\Theta_1||\Theta_2| + |\Theta_1|^2) + (2|\Theta_1| + |\Theta_2|) \right)} \tag{6.18}$$

$$V_{IIP3}^2 = \frac{\frac{4d_o^3 k_{re}}{\varepsilon A}}{\left(6\left(\frac{C_x}{C_o}\right)^2|\Theta_1|^2|\Theta_2| + 3\left(\frac{C_x}{C_o}\right)(2|\Theta_1||\Theta_2| + |\Theta_1|^2) + (2|\Theta_1| + |\Theta_2|) \right)} \tag{6.19}$$
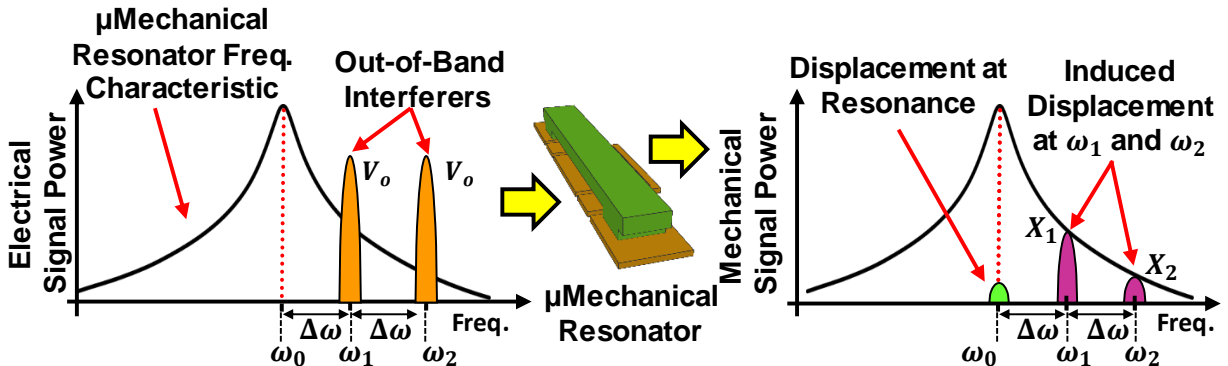

Figure 6.4: Simulated frequency response spectra for an (a) unterminated and (b) terminated third-order filter alongside those for the three constituent resonators. Loading of resonator *Q* by termination reduces in-band displacement, but also reduces out-of-band attenuation. Still, the terminated filter provides more out-of-band rejection than a stand-alone resonator, which increases *IIP3*.

$$IIP_3 = \frac{V_{IIP3}^2}{2R_T} \cong \frac{V_{IIP3}^2}{2R_x} \tag{6.20}$$

$$IIP_3 = \frac{2Q\omega_o \cdot \frac{V_P^2 \varepsilon A}{d_o}}{\left(6\frac{V_P^4(\varepsilon A)^2}{d_o^6 k_{re}^2}|\Theta_1|^2|\Theta_2| + 3\frac{V_P^2 \varepsilon A}{d_o^3 k_{re}}(2|\Theta_1||\Theta_2| + |\Theta_1|^2) + (2|\Theta_1| + |\Theta_2|)\right)} \tag{6.21}$$

$$IIP_3 = \frac{2Q\omega_o \cdot \frac{V_P^2 \varepsilon A}{d_o}}{\left(6\left(\frac{C_x}{C_o}\right)^2|\Theta_1|^2|\Theta_2| + 3\left(\frac{C_x}{C_o}\right)(2|\Theta_1||\Theta_2| + |\Theta_1|^2) + (2|\Theta_1| + |\Theta_2|)\right)} \tag{6.22}$$

A careful examination of equation (6.20 and 6.21) shows that *IIP3* is dependent on not only material properties, but also resonator and electrode geometry. In particular, *IIP3* increases with V_P, A and d_o and it is not strongly dependent on k_{re}. The resonator quality factor affects the *IIP3* in two ways: (1) higher *Q* devices rejects out-of-band signal more effectively and therefore suppress Θ_1 and Θ_2, (2) the motional resistance of the resonator decreases by *Q* and hence, for a given V_{IIP3}, it improves *IIP3*. Note that equation 6.19 is valid for a resonator with motional resistance much larger than the system impedance. If R_x is on the same order as the 50Ω system impedance, this equation should be modified to include the matching at the input and resonator loading by the system impedance.

Figure 6.5 presents different dependencies of *IIP3* (equation 6.20) and V_{IIP3} (equation 6.17) on different design parameters. As expected, V_{IIP3} is not a strong function of quality factor *Q*, while *IIP3* improves by *Q* due to decrease in the resonator motional resistance R_x, as shown in Figure 6.5 (a). Figure 6.5 (b) the complex dependency of *IIP3* on the transducer gap spacing: *IIP3* monotonically decreases by gap spacing for large bias voltages while it improves by the gap spacing for the small V_P. The resonator coupling (C_x/C_o) is considerably large for large V_P and small gap spacing and therefore, the first term in the denominator of 6.20 and 6.21 dominates. In this case, *IIP3* is proportional to do^5 and small gap spacing degrades the nonlinearity. On the other hand, for small voltages the last term in the denominator dominates and hence, *IIIP3* is inversely proportional to do and small gap spacing improves the linearity. Note that for small gap, smaller bias voltage is required to achieve strong electromechanical coupling and hence, reducing the gap spacing improves the linearity of the system while providing better performance. Wider resonators linearly increase the capacitor's area *A* and also the resonator effective stiffness (equation 2.22). Therefore, V_{IIP3} does not change by the resonator width while *IIP3* improves by W_r due to the reduction in the resonator motional resistance R_x, as shown in Figure 6.5.

Figure 6.5 (c) provides more insights into the tradeoff between the gap spacing, the bias voltage V_P and the resonator linearity *IIP3*. Although *IIP3* increases monotonically with V_P for

large gaps, there is an optimum bias voltage for small gap resonators. For small V_P and do the *IIP3* increases by V_P^2. On the other hand, as V_P increases and the first denominator term of 6.20 grows and dominates the denominator and as a result, *IIP3* decreases by $1/V_P^2$.
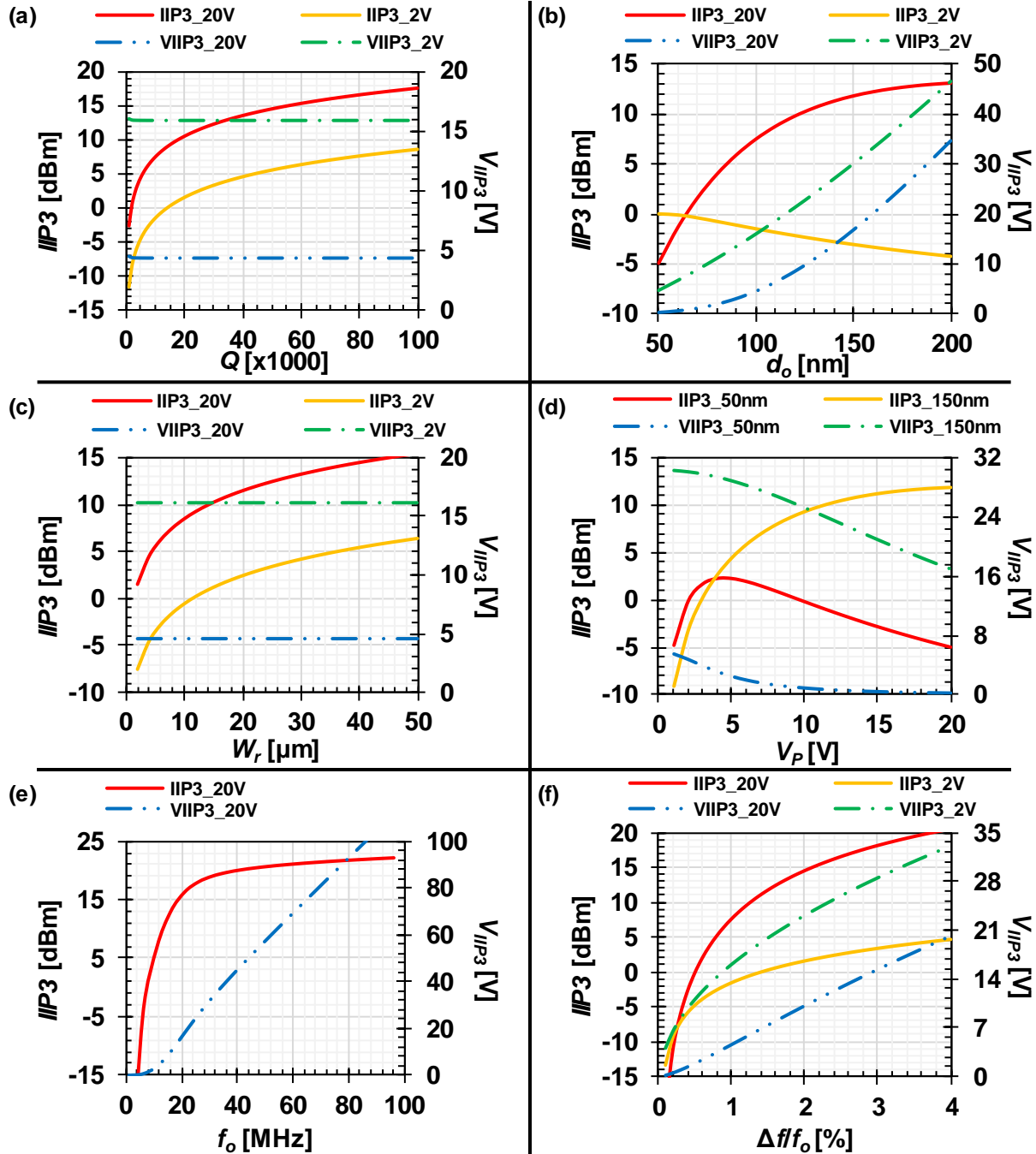

Figure 6.5: The third-order intermodulation point *IIP3* and V_{IIP3} as a function of (a) resonator quality factor Q, (b) transducer gap spacing d_o, (c) resonator width W_r, (d) transducer bias voltage V_P, (e) resonator center frequency f_o, (f) the tone spacing $\Delta f/f_o$. The parameters used in all the simulations are: Q=10k, $\Delta f/f_o$=1%, f_o=13MHz, k_{re}=12kN/m, d_o=100nm, W_e=20um, W_r=8um, V_P=20V (unless specified otherwise).

102

As suggested by equation 6.20 and shown in Figure 6.5 (e), *IIP3* improves linearly by the resonator center frequency. Although not evident from equation 6.17, V_{IIP3} increases with the center frequency, as the resonator becomes stiffer at higher frequencies. For this simulation, the resonator height was constant and the resonator length determines the center frequency. As the interferer signals move further from the center frequency, the micromechanical resonator provides more attenuation and hence, reduces the induced displacement, as suggested by equation 6.5 as shown in Figure 6.5 (f).

6.3 FILTER CONSIDERATION IN IIP3 CALCULATION

Although the parallel-plate approximation is still valid for a capacitive-gap micromechanical filter as shown in Figure 6.6, the *IIP3* expression requires two major modifications to account for the following.

6.3.1 TOTAL RESISTANCE

Proper termination is essential to minimize in-channel ripple and attain a flat passband. Before termination, the resonator *Q*'s are too large and the filter passband consists of distinct peaks, as shown in Figure 6.7 (a). The termination resistance needed to flatten the passband of a filter with center frequency f_o, bandwidth *B*, and small insertion loss is:
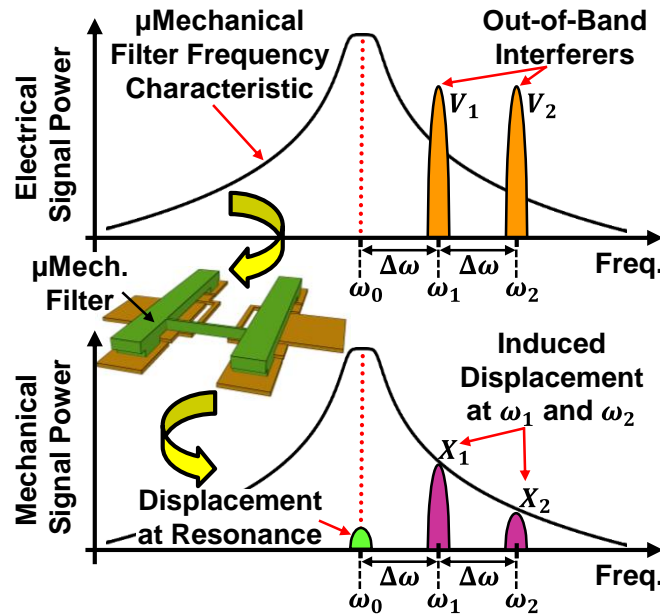

Figure 6.6: Schematic description of IM3 generation by two interferer signals going through a filter transfer function. The interaction between out-of-band motion induced by these interferers and input voltage can intro-duce an in-band input force and corresponding displacement. The un-desirable IM3 displacement results even with no input at resonance.

$$R_Q = \left(\frac{Q}{q_i Q_f} - 1\right) R_x \cong \frac{Q}{q_i Q_f} R_x = \frac{k_{re}}{q_i Q_f \eta_e^2 \omega_o}$$

$$R_x = \frac{k_{re}}{Q\eta_e^2 \omega_o}$$

(6.23)

where $Q_f = f_o/B$ is the filter fractional bandwidth. In contrast to the single resonator case, these termination resistors R_Q dominate the resistance in the system, so $R_T \sim R_Q$ in equation (16) when calculating the *IIP3* of filters. This argument suggests that the resonator quality factor in the equation 6.20 and 6.21 should be replaced by the expression $q_i Q_f$ (i.e. the product of the filter fractional bandwidth and the filter normalization factor.

6.3.2   HIGH-ORDER MECHANICAL SYSTEM:

The equation of motion (6.5) describes only single resonators, whereas the micromechanical filters of this work comprise several resonators linked by coupling beams, as explained in previous chapters. Solving the complete mechanical system yields transfer functions listed in filter cook books, such as [27]. For example, the transfer function of a second-order filter coupled by quarter-wavelength coupling beams takes the form given in equations 6.18 and 6.19. Here, P_{BW} is the filter fractional bandwidth. Note that terminating the filter with R_Q loads the quality factors of the constituent resonators, which is why Q_f appears in (6.19) instead of the resonator quality factor Q. The loading effect reduces resonator displacement at resonance ($X_o \propto Q/k_{re}$) and reduces out-of-band rejection leading to larger out-of-band displacements X_1 and X_2. However, compared with a similarly terminated stand-alone resonator, the high-order transfer function of a multi-resonator filter shown in Figure 6.7 provides a larger out-of-band attenuation that reduces out-of-band displacement, decreasing *IM3*, hence improving *IIP3*.

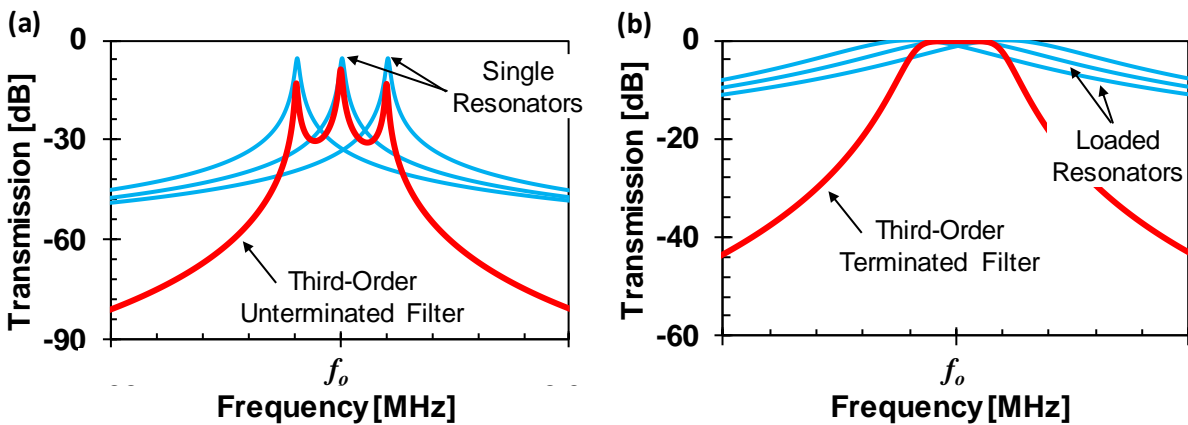

Figure 6.7: Simulated frequency response spectra for an (a) unterminated and (b) terminated third-order filter alongside those for the three constituent resonators. Loading of resonator Q by termination reduces in-band displacement, but also reduces out-of-band attenuation. Still, the terminated filter provides more out-of-band rejection than a stand-alone resonator, which increases *IIP3*.

$$\frac{X}{F}(\omega) = \frac{1}{k_{re}} \Theta(\omega) \tag{6.24}$$

$$\Theta(\omega) \cong \frac{P_{BW}}{\left(1 - \frac{(\omega/\omega_o)^2}{1 + P_{BW}} + \frac{j(\omega/\omega_o)}{Q_f}\right)\left(1 - \frac{(\omega/\omega_o)^2}{1 - P_{BW}} + \frac{j(\omega/\omega_o)}{Q_f}\right)} \tag{6.25}$$

$$P_{BW} = \frac{BW}{f_o}, \qquad Q_f = \frac{f_o}{BW}$$

6.4 COMPLETE FORMULATION FOR IIP3

While the parallel-plate capacitor approximation provides an analytical solution and design insight for the effect of third-order nonlinearities, it neglects phenomena such as beam bending due to dc-bias voltage and location-dependent effective stiffness. This can introduce errors in the IIP3 calculation.

V_P-induced beam bending results in C_o and d_o that are not constant, but rather functions of location on the y-axis given by d(y) in equation 2.22. On the other hand, the effective resonator stiffness is also location dependent and changes according to the mode shape at the point of interest. For similar reasons, X_1 and X_2 vary along the beam length (the y-axis in Figure 6.8), approaching zero near the anchors. In general, with knowledge of the peak displacement (at the beam midpoint) governed by the resonator lumped model, displacements at other beam locations follow from the resonator mode shape. To correctly determine the total actuation force F_{tot}, the differential intermodulation force components dF_{IM3} in infinitesimal regions dy at locations y should be integrated over the entire beam length.

Since effective stiffness increases dramatically moving away from the beam center, displacement is a strong function of location. This phenomenon can result in a V_{IIP3} value twice as large as that derived using a simple parallel-plate approximation. Including these modifications is essential to better explain the experimental results.
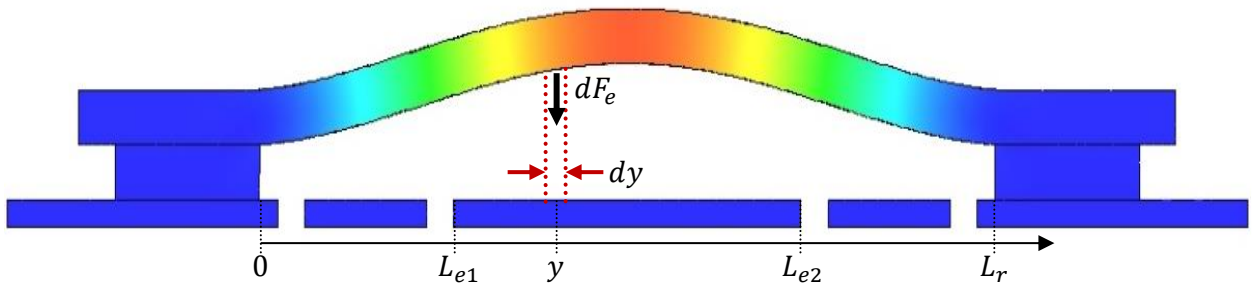

Figure 6.8: The accurate modeling of the resonator nonlinearity requires considering the resonator mode shape and location-dependent effective stiffness. The third-order intermodulation force dF_{IM3} should be calculated from the electrostatic force dF_e over the infinitesimal length dy and then integrated over the electrode width, from L_{e1} to L_{e2}.

6.5 MEASUREMENT RESULTS

Figure 6.9 (a) shows the pseudo 2-port setup used for the nonlinearity measurement on the CC-beam resonator of Chapter 2. The power combiner at the input couples the two signals at $\omega1$ and $\omega2$ from different sources and then a bias-T feeds the input signal to the beam structure. As expected from the equation 6.3, the intermodulation term grows with the input power cube, while the fundamental signal grows linearly, and the intersection determines the third-order intercept point. Figure 6.9 (b) and (c) present the intermodulation measurement for bias voltages of 5V and 7.5V, respectively. The resonator bias at 5V shows *IIP3* of 19.6dBm, 31.16dBm, and 34.57dBm for tone spacing of 0.2%, 1% and 5%, respectively. The same resonator shows *IIP3* of 4.71dBm, 20.91dBm and 32.7dBm when biased at 7.5V. Figure 6.9 (c) summarizes the *IIP3* measurements for different tone spacing, showing the suppression of nonlinearity term as the interfering signals move further from the center frequency.
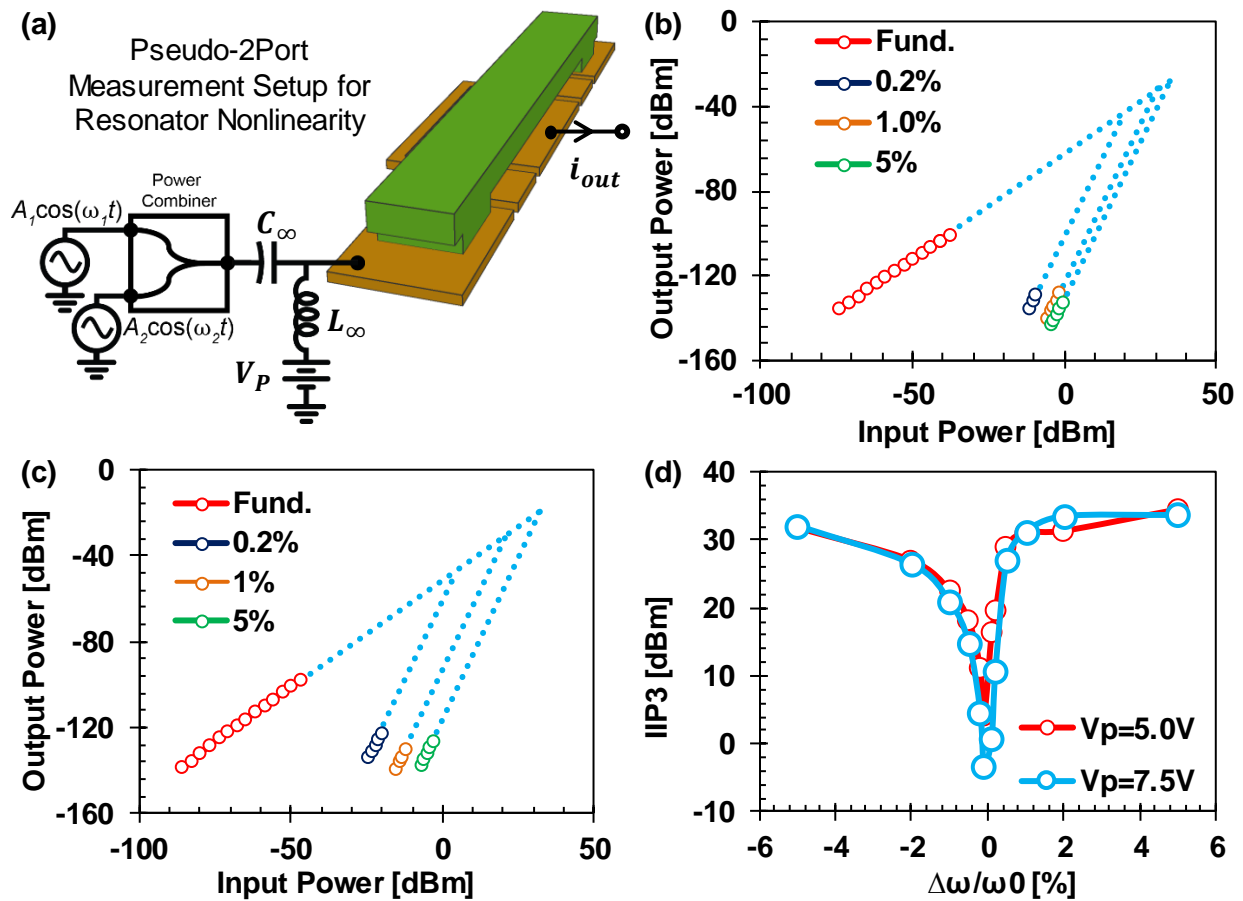

Figure 6.9: (a) The pseudo-2 port setup for resonator nonlinearity measurement. (b) Third-order input intercept point *IIP3* measurements of the CC-beam micromechanical resonator at bias voltage of (c) 5V and (d) 7.5V for different tone spacing. (d) measured IIP3 versus percent tone separation ($\Delta\omega/\omega_o$) for a terminated 3CC-λ/4 filter.

Figure 6.10 (a) shows the nonlinearity measurement setup for the CC-beam bridged filters presented in Chapter 5, and also presents *IIP3* measurements on (b) a 3CC-3λ/4 bridged filter and (c) a 4CC-3λ/4 bridged filter. Here, a spectrum analyzer measured the output power response to two-tone inputs with frequency spacings like those pictured in Figure 6.1. These filters show (b) an *IIP3* of 17dBm for a tone separation of 125kHz; and in (c), *IIP3*'s of 22.7dBm and 27dBm for tone separations of 80 and 160kHz, respectively.

The expression for out-of-band spurious-free dynamic range takes the form [17] of equation 6.20 for a system limited by the thermal noise. Here, SNR_{min} is the minimum signal-to-noise ratio
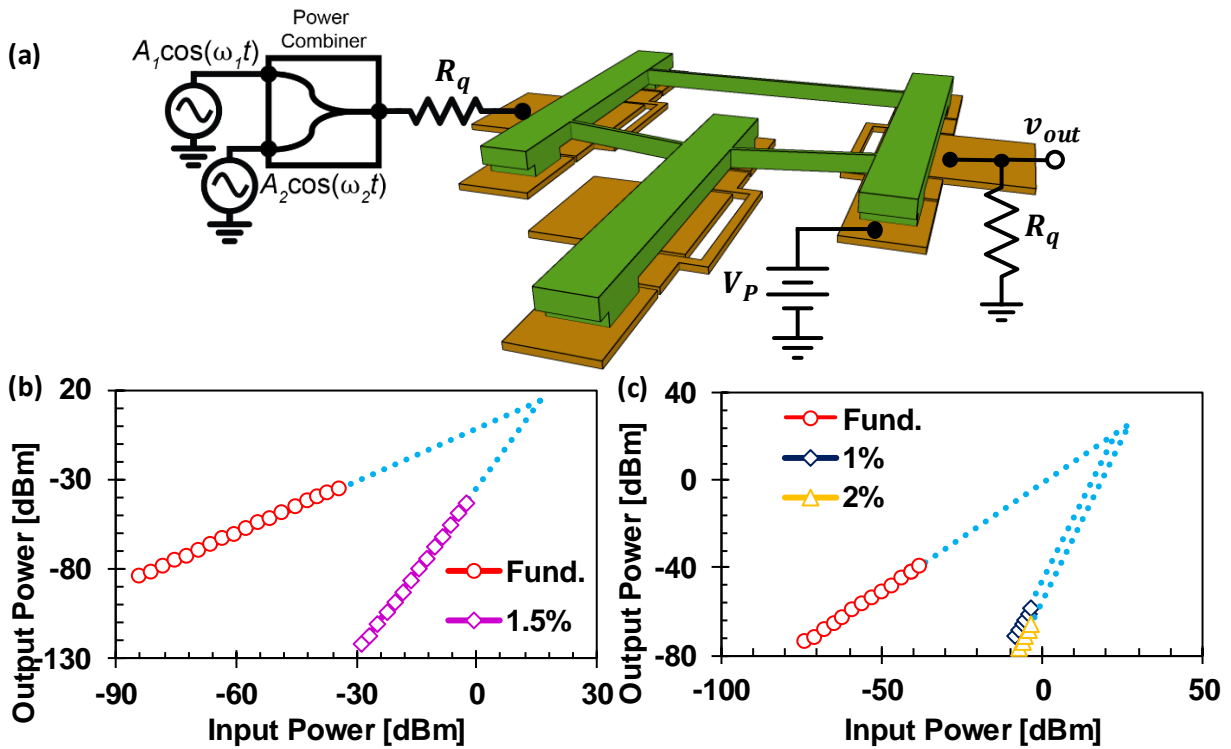

Figure 6.10: (a) Third-order input intercept point *IIP3* measurement setup for 3CC-3λ/4 bridged filter. (b) 3CC-3λ/4 and (c) 4CC-3λ/4 bridged micromechanical filter nonlinearity measurement.
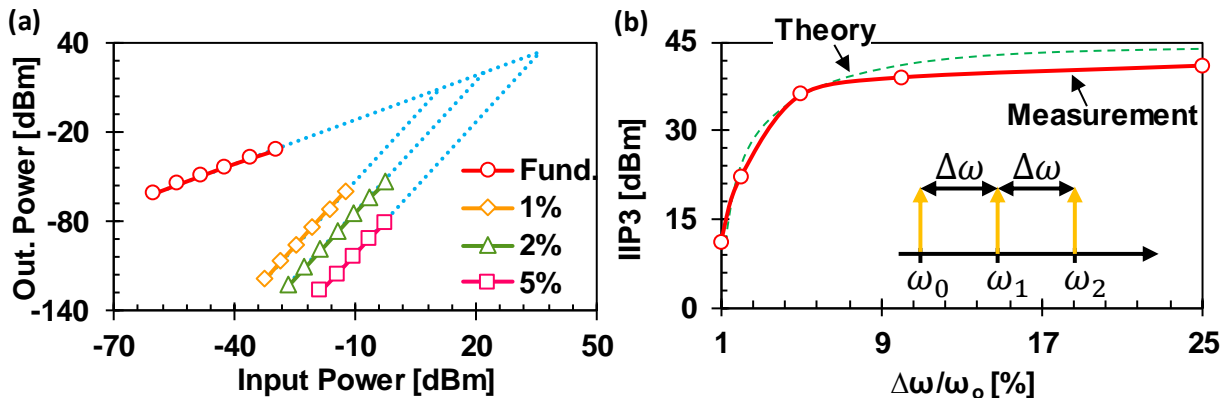

Figure 6.11:: (a) Two-tone measurement with tone separations of 80, 160 and 400kHz and (b) measured *IIP3* versus percent tone separation ($\Delta\omega/\omega_o$) for a terminated 3CC-λ/4 filter.

required by the system to detect and demodulate the desired signal. Assuming SNR_{min} =10dB, these *IIP3*s correspond to *SFDR*'s of 89.94dB for the 3CC-3λ/4 bridged filter with 125kHz tone separation; and 91dB and 93.9dB for the 4CC-3λ/4 bridged filter with 80 and 160kHz tone separations, respectively

$$SFDR = \frac{2}{3}\Big(\ IIP3 + 174dBm - IL - 10\log_{10}(BW)\ \Big) - SNR_{min} \qquad (6.26)$$

Figure 6.11 presents *IIP3* measurements on a 3CC-λ/4 bridged micromechanical filter. Specifically, (a) shows two-tone measurements for different tone spacings, while (b) plots measured *IIP3* as a function of percent tone spacing ($\Delta\omega/\omega_o$). As expected, as out-of-band interferers move further away from the center frequency, induced displacements X_1 and X_2 decrease and *IIP3* increases. This filter achieves *IIP3* of 11dBm, 22dBm and 36dBm corresponding to *SFDR*'s of 85.67dB, 93dB and 102.34dB for tone separations of 80, 160 and 400kHz, respectively. These *IIP3*s are more than 30dBm higher than previous marks for single resonators.

Chapter 7 7TH-ORDER SHARP-ROLL-OFF BRIDGED MICROMECHANICAL FILTERS

The bridging technique established in the previous chapters empowered the demonstration of 3rd- and 4th-order micromechanical filter with sharp passband-to-stopband roll-off. However, there is no reason for this technique to be limited to the presented filter types, and to the offered bridging scheme between the input and the output resonators. To demonstrate the capability of this technique to provide desired filter transfer function, this chapter introduces a seventh-order micromechanical filter with the steepest roll-off among the reported MEMS-based filters at HF. This shape factor arises from not only the sheer order of the filter, governed by seven coupled clamped-clamped beam resonators, but also from strategic bridging of its non-adjacent 1st, 4th, and 7th resonators to generate loss poles that further steepen the roll-off from passband to stopband. The steepness of this filter's roll-off greatly increases the density of available channels in HF radios for military and Ham applications, as well as future sensor network applications enabled by these results.

The availability of high-order filters in millimeter sizes at HF, if possible, would likely spur vibrant activity in not only military and Ham radios, but also in a much bigger ultra-low power sensor network arena, especially if dense packing of channels becomes possible.

7.1 HIGH-ORDER FILTERS

Application of small frequency filters with millimeter dimensions, like the ones introduced in the previous chapters, lowers the power consumption of any receiver front-end due to their ability to remove unwanted interfering signals. On the other hand, piezo-based filters of similar size are more difficult to construct for the much lower HF range, spanning frequencies from 3-30MHz, since wavelengths (acoustic or electrical) are much larger at these frequencies. To further
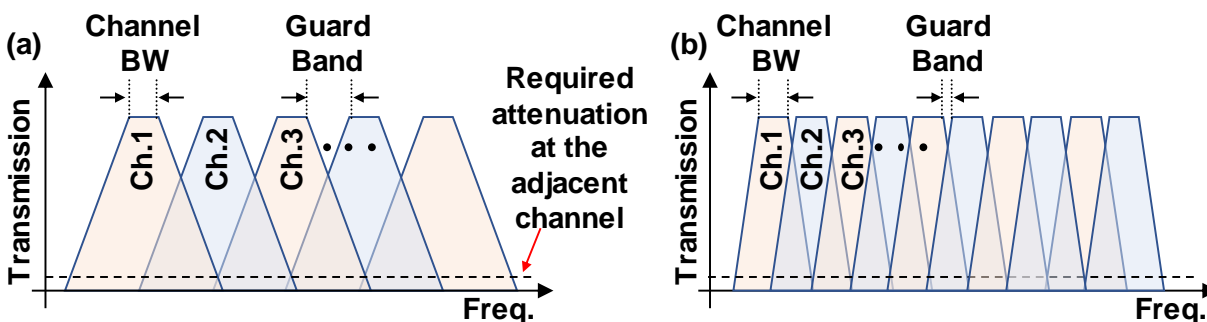

Figure 7.1: The required attenuation at the adjacent channel determines the minimum guard band necessary for the system. A system with sharp roll-off filters (b) increases the spectrum utilization efficiency, compared to a system with large passband to stopband roll-off (a).

complicate matters, the piezoelectric technologies normally employed for GHz filters lack the electromechanical coupling strength to support high-order filters at HF [34] [35] [36] [78].

Application of filters with sharper roll-off increases the spectrum utilization efficiency. Any telecommunication standard puts limits on the minimum filter attenuation at the adjacent channel (or band) to prevent crosstalk between different channels (or bands) and avoid jamming by nearby
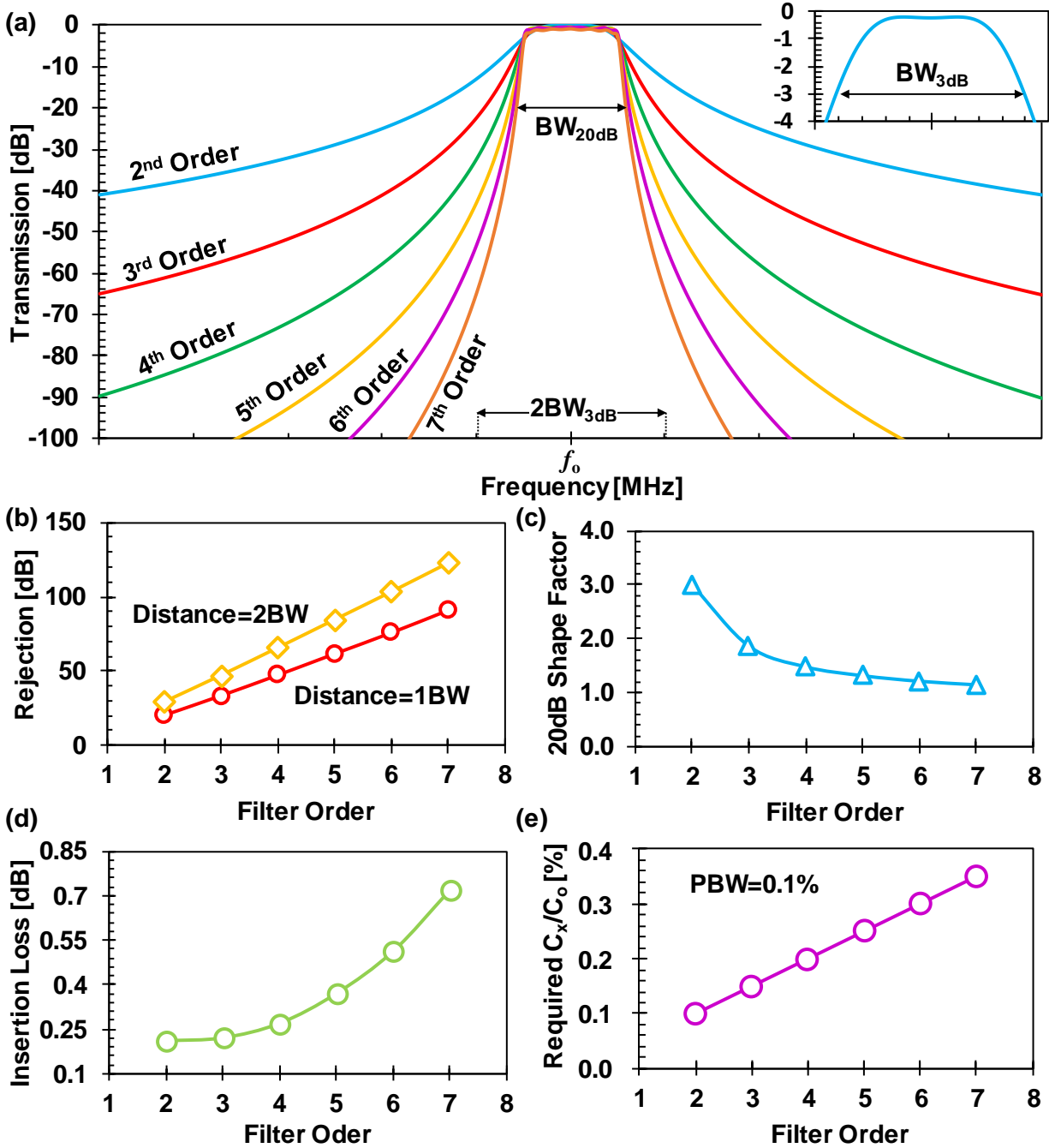

Figure 7.2: (a) Higher-order filters provide sharper roll-off and larger stopband rejection (b), quantified as the 20dB shape factor defined by BW20dB/BW3dB (c). However, higher order filters have slightly larger insertion loss (d) and require larger Cx/Co for proper termination (e).

transceivers. Due to theoretical and practical limitation, no filter can provide brick wall frequency response and hence, it is essential to allow guard bands between adjacent channels (or bands) to achieve the required attenuation, as shown in Figure 7.1 (a). Utilization of filters with sharp passband-to-stopband roll-off can decrease the required guard band and noticeably improve the spectrum utilization efficiency, as presented in Figure 7.1 (b).

Increasing the order filter, i.e. having more resonant tank in the mechanical system, improves the out-of-band rejection and steepens the passband-to-stopband roll-off, as shown in Figure 7.2 (a). Each stage of resonating tank adds to the attenuation of the out-of-band signal and hence, increase the overall filter rejection, as shown in (b). Here, the typical filter rejection is measured at two different distances from the passband corners: a bandwidth away and twice the filter bandwidth from the filter edge. This increase in the rejection also boosts the filter roll-off; higher out-of-band rejection and similar in-band attenuation suggests faster roll-off from passband to stopband. The 20dB shape factor defined in equation 7.1 quantifies the filter roll-off by comparing the filter bandwidth at 3dB and 20dB attenuation. An ideal brick-wall filter response would have shape factor of unity. Figure 7.2 (c) shows the improvement in the shape factor by the increase in the filter order. However, increasing the number of resonating tanks in the system implies more loss in the system and slightly increase in the filter in-band insertion loss, as shown in (d). Also, higher-order filter requires constituent resonators with stronger electromechanical coupling C_x/C_o for proper filter termination, shown in (e).

$$20dB \text{ } Shape \text{ } Factor = \frac{BW_{20dB}}{BW_{3dB}} \tag{7.1}$$

7.2 ELECTROMECHANICAL COUPLING REQUIREMENTS

Attaining a channel-selecting response requires not only constituent resonators with high Q to reduce in-band insertion loss, but also resonators with high electromechanical coupling to push the corner frequency of the low-pass RC filters formed at the input and output well beyond the filter center frequency, as explained in Chapter 3. The electromechanical coupling strength (C_x/C_o) of the input and output resonators depends on their static capacitance C_o and the effective stiffness of the system, as in equation 7.2. However, mechanical coupling of the identical resonators changes the effective stiffness of the system.
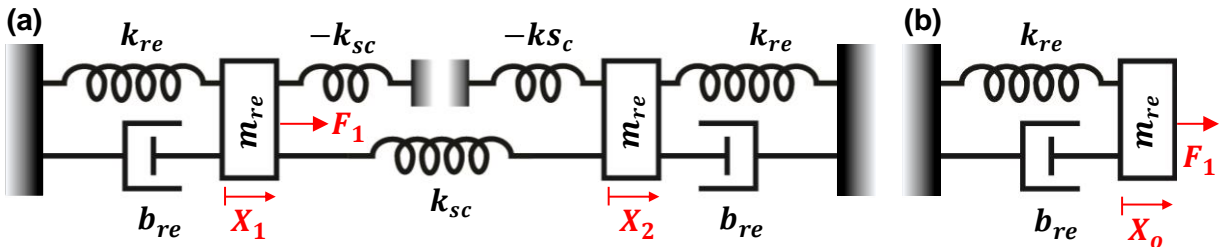

Figure 7.3: The mechanical lumped-element model of (a) a quarter-wavelength second-order micromechanical filter and (b) a single resonator.

111

Equation 7.3 provides the equation of a motion for a generic second-order filter, such as one shown in the Figure 7.3 (a), coupled mechanically by quarter-wavelength coupling beams. Here, the resonator effective stiffness k_{re} and effective mass m_{re} determines the resonator center frequency ω_o and the normalized coupling beam effective stiffness k_{sc}/k_{re} governs the system bandwidth ω_1 and ω_2. Equation 7.5 presents the displacement of the constituent resonators at the system eigenvalues and shows that a given force makes induces displacement exactly half the displacement of a single resonator, given in equation 7.6.

The smaller resonator displacement suggests that the second-order system is effectively twice stiffer than a single resonator and therefore, for a given input/output transducer parameters, i.e. static capacitance C_o and transformer ratio η_e, a second-order filter has half the electromechanical coupling strength (C_x/C_o) of a single resonator. This argument suggests that for the proper filter termination, the constituent resonator of higher order system should have stronger coupling coefficient compared to a lower order system, as shown in figure 7.2 (e).

$$\frac{C_x}{C_o} = \frac{k_{re}}{\eta_e^2 C_o} \tag{7.2}$$

$$k_{re}\begin{bmatrix} 1 - \left(\frac{\omega}{\omega_o}\right)^2 + \frac{j}{Q}\frac{\omega}{\omega_o} & -\frac{k_{sc}}{k_{re}} \\ -\frac{k_{sc}}{k_{re}} & 1 - \left(\frac{\omega}{\omega_o}\right)^2 \frac{j}{Q}\frac{\omega}{\omega_o} \end{bmatrix}\begin{bmatrix} X_1 \\ X_2 \end{bmatrix} = \begin{bmatrix} F_1 \\ 0 \end{bmatrix} \tag{7.3}$$

$$\begin{bmatrix} X_1 \\ X_2 \end{bmatrix} = \frac{1}{\left(1 - \left(\frac{\omega}{\omega_o}\right)^2 + \frac{j}{Q}\frac{\omega}{\omega_o} + \frac{k_{sc}}{k_{re}}\right)\left(1 - \left(\frac{\omega}{\omega_o}\right)^2 + \frac{j}{Q}\frac{\omega}{\omega_o} - \frac{k_{sc}}{k_{re}}\right)}\begin{bmatrix} 1 - \left(\frac{\omega}{\omega_o}\right)^2 + \frac{j}{Q}\frac{\omega}{\omega_o} \\ \frac{k_{sc}}{k_{re}} \end{bmatrix}\frac{F_1}{k_{re}} \tag{7.4}$$

$$\omega_1 = \omega_o\left(1 - \frac{k_{sc}}{k_{re}}\right)^{1/2}, \qquad \omega_2 = \omega_o\left(1 + \frac{k_{sc}}{k_{re}}\right)^{1/2} \tag{7.5}$$
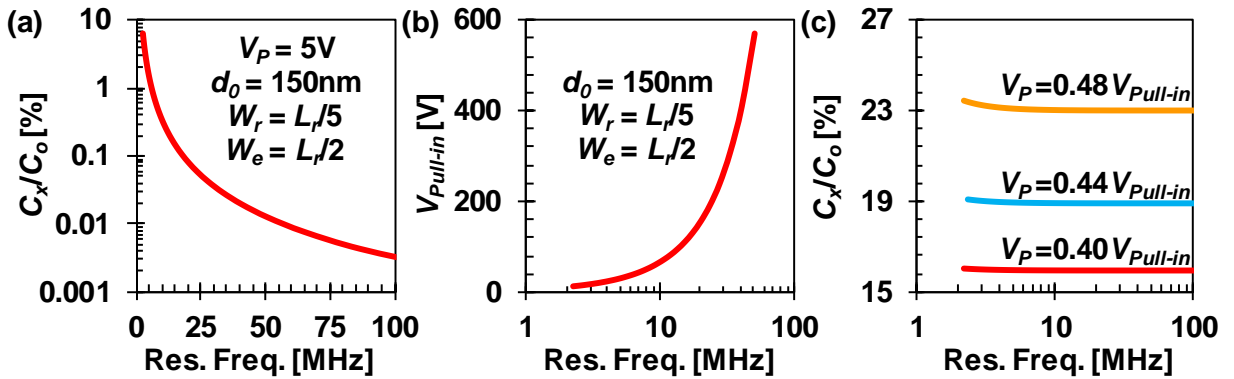

Figure 7.4: Electromechanical coupling for V_P=5V and d_o=150nm, b) resonator pull-in voltage, and c) electromechanical coupling for $V_P=\alpha_V.V_{Pull-in}$, all versus CC-beam resonance frequency.

$$\begin{bmatrix} X_1 \\ X_2 \end{bmatrix}_{\omega_1} = \frac{1}{2} \cdot \frac{QF_1}{jk_{re}} \begin{bmatrix} 1 \\ 1 \end{bmatrix}, \qquad \begin{bmatrix} X_1 \\ X_2 \end{bmatrix}_{\omega_2} = \frac{1}{2} \cdot \frac{QF_1}{jk_{re}} \begin{bmatrix} -1 \\ 1 \end{bmatrix}$$

$$X_o]_{\omega_o} = \frac{QF_1}{jk_{re}} \tag{7.6}$$

The CC-beam introduced in Chapter 2 is capable of providing strong electromechanical coupling coefficient in the order of 10% or more, predicted by equation 2.22 and demonstrated by the measurements of Figure 2.22. The expression for coupling coefficients of capacitive transducers repeated in equation 7.7 advises that there are quite a few knobs to improve the coupling, such as bias voltage V_P and gap spacing d_o, and suggests that the coupling drops rapidly by the center frequency ω_o (Figure 7.4 (a)). However, the resonator pull-in voltage, which sets the upper limit on the bias voltage, also increases by the frequency. Therefore, if one lifts the constant V_P restriction, then the drop in (C_x/C_o) becomes much more gradual, or even disappears. Use of $V_{Pull-in}$ in yields (C_x/C_o) curves like those in Figure 7.4 (c), which are now flat with frequency, with large values >15% across the plotted frequency range. Whether or not a voltage as high as 600V for 50MHz is practical in a real application, 25V at 10 MHz is practical. So, if not at GHz frequency, capacitive-gap transducers easily best AlN piezoelectric transducers in the HF range [45], and by rather large margins, e.g., 16.7% vs. 1%. Armed with this insight, the filter design of this work employs capacitive-gap transducers with resonator-to-electrode gap spacing of 137nm, which with a dc bias of 22.5V applied to the beams achieves a very large (C_x/C_o)~17% to implement high-order micromechanical filters.

$$\frac{C_x}{C_o} = \frac{\eta_e^2}{k_{re}C_o} = \frac{1}{\omega_o^2} \cdot \frac{\varepsilon}{\rho} \cdot \frac{V_P^2}{d_o^3} \cdot \frac{1}{h\alpha_e} \cdot \frac{\left(\int_{1-\frac{\alpha_e}{2}}^{1+\frac{\alpha_e}{2}} \tilde{X}_{mode}(y)dy \right)^2}{\int_0^1 \tilde{X}^2_{mode}(y)dy} \tag{7.7}$$

$$\frac{C_x}{C_o} = \frac{\alpha_V^2}{\alpha_e} \cdot \frac{\left(\int_{1-\frac{\alpha_e}{2}}^{1+\frac{\alpha_e}{2}} \tilde{X}_{mode}(y)dy \right)^2}{\int_{1-\frac{\alpha_e}{2}}^{1+\frac{\alpha_e}{2}} \tilde{X}^2_{mode}(y)dy} \tag{7.8}$$

7.3 MICROMECHANICAL FILTER DESIGN

Figure 7.5 presents the perspective view schematic of the seventh-order micromechanical filter of this work. As shown, this filter comprises seven clamped-clamped beam (CC-beam) flexural-mode resonators linked by numerous quarter-wavelength flexural-mode coupling beams to generate a 7-pole filter response. The feedforward path between the input and output resonators of this filter is more complicated than the simple bridging technique used in Chapter 5. The bridging scheme used in this filter couples the 1st, 4th and 7th resonators by two three quarter-wavelength bridging beams, as shown in Figure 7.5. This bridging technique results in the third-

order CC-beam filter as the feedforward path from the input to the output. There are two main reasons for adopting this bridging technique:

i) Since the main filter path comprises of 6 quarter-wavelength coupling beams, a single bridging between the 1st and 7th resonators would require bridging beam equivalent to $5\lambda/4$ or even $7\lambda/4$, due to geometrical restrictions. Such a long narrow beam would set unreasonable limitations on the maximum intrinsic stress in the structural layer to avoid buckling.

ii) The bridging path of this filter is a third-order CC-beam filter, and compared to the second-order feedforward path described in previous chapters, introduces two more transmission zeros and therefore, improves the roll-off further.

The synthesis of this filter follows the procedure presented in the Chapter 5. The 7th-order CC-beam filter, compromising all the CC-beam resonators and quarter-wavelength coupling beams, determines the filter passband and overall filter frequency response, while the 3rd-order filter of the parallel path, encompassing the 1st, 4th and 7th CC-beam resonators and two three quarter-wavelength bridging beams, governs the loss pole location.

Figure 7.6 displays the simplified mechanical model of the 7 CC-beam filter and its corresponding eigenmodes. Since there are seven resonating tanks in the system, there will be seven distinct eigenmodes, as shown in this figure, with in-phase (red), out-of-phase (blue) and stationary (black) resonators. All the resonators are in-phase with the input resonator at the first mode, while they are out-of-phase to their adjacent resonators in the highest mode. These seven mode shapes correspond to seven peaks in the frequency response, as shown in the Figure 7.8 (c), and will form the filter passband by proper termination.
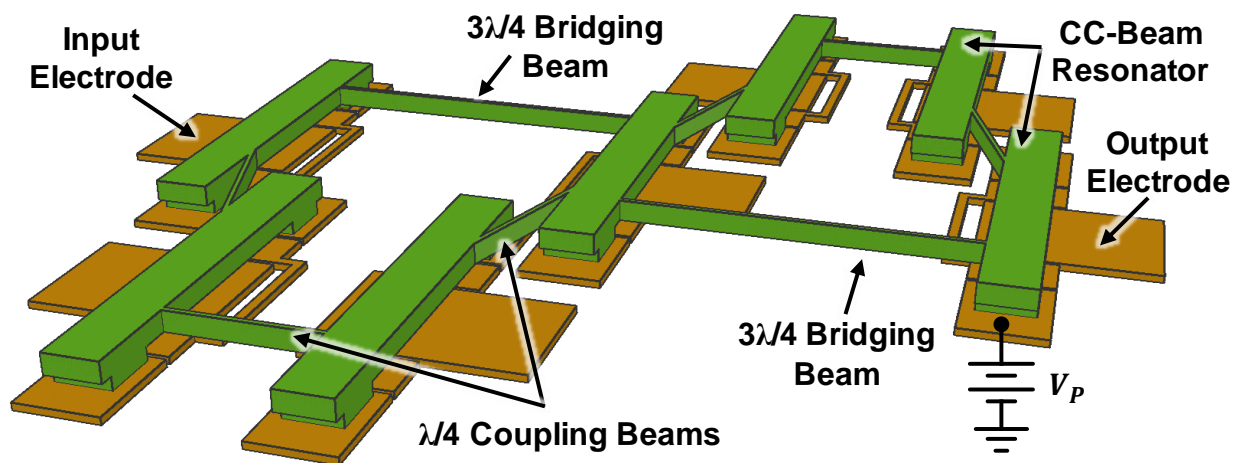

Figure 7.5: Perspective-view schematic for the 7th-order µmechanical filter with bridging between the 1st, 4th and 5th resonators. Tuning electrodes under each resonator allow precise placement of poles and zeros to achieve a sharp passband-to-stopband roll-off .

The 3 CC-beam filter of the feedforward path, shown in Figure 7.7, includes three identical resonators coupled by $3\lambda/4$ bridging beams. This third-order system has three distinct eigenmodes as shown in this figure. However, since the bridging beams are equivalent to three quarter-wavelength, the all in-phase eigenmode occurs at higher frequency compared to all out-of-phase one. Comparison of these eigenmodes with the main filter seven mode shapes shown in Figure 7.6,
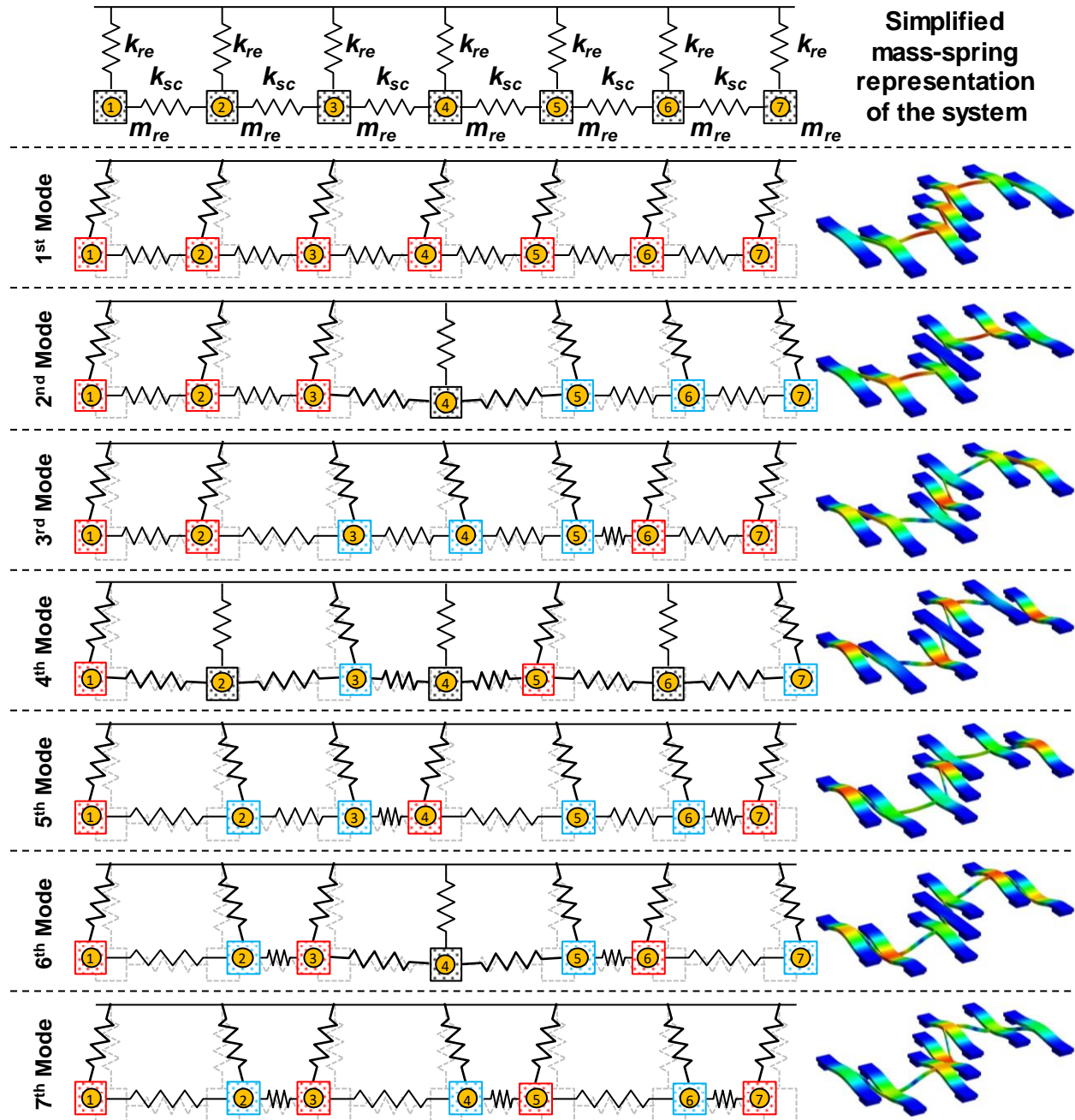

Figure 7.6: A simplified mass-spring model of the 7th-order filter shown in the figure 7.5. The high-order system has seven distinct mechanical mode shapes, as shown here. The resonators in red and blue are in-phase and out-of-phase with the input resonator, respectively. The ones in back are stationary.

confirms that the intermediate resonators have opposite displacement below and above the passband which is the basis of loss pole formation in the bridged filter.

Figure 7.8 expands on the investigation of the loss pole formation. As depicted in (c), the output resonator of the 7 CC-beam filter has equal displacement to the 3 CC-beam filter at two points on both side of the passband. Since the induced displacement from the two paths are out of phase, as shown in (d), the overall system transfer function will have loss poles on both side of the filter passband, as shown in (e). Further investigation of the bridged filter phase response shown in (f) reveals that there are 360° change in the phase at the loss pole frequencies, which corresponds to two overlaying transfer function zeros at the same frequency. The extra transmission zeros are due to the strategic bridging exploited in this filter that has higher order filter as the feedforward path and improves the filter roll-off furthermore.

The bridging technique described here provides a seven-order micromechanical filter with two transmission zeros on each side of the filter passband to achieve a filter frequency response with the fastest passband-to-stopband roll-off demonstrated in this frequency range.

7.4 TUNING VIA ELECTRICAL STIFFNESS

Achieving very sharp roll-off along with small insertion loss and small in-band ripple requires precise placement of poles and especially zeros. Although the matching tolerance of surface micromachining technology is reasonably good [7], it is not sufficient for filters with percent bandwidths below 0.5%. Fortunately, capacitive-gap transducers offer frequency tuning via voltage-controlled electrical stiffness, as governed by equation 7.9 borrowed from the Chapter 2. Here, $\alpha_e = W_e/L_r$ is the percentage of the beam length covered by the main electrode.

$$f_o(V_T) = f_o\sqrt{1 - \gamma V_T^2} \cong f_o\left(1 - \frac{\gamma}{2}V_T^2\right)$$

$$\gamma = \frac{\eta_{eT}^2}{k_{re}C_o} = \frac{1}{\omega_o^2}\cdot\frac{\varepsilon}{\rho}\cdot\frac{1}{d_o^3}\cdot\frac{1}{h\alpha_e}\cdot\frac{\left(2\int_0^{1-\frac{\alpha_e}{2}}\tilde{X}_{mode}(y)dy\right)\left(\int_{1-\frac{\alpha_e}{2}}^{1+\frac{\alpha_e}{2}}\tilde{X}_{mode}(y)dy\right)}{\int_0^1 \tilde{X}^2_{mode}(y)dy} \tag{7.9}$$

This equation predicts a large tuning range on the order of 200ppm for a 1V change in bias voltage for the CC-beam design used here. This tuning capability outright enables the high-order narrow-band capacitive-gap filter of this work, as without tuning, poles and zeros will miss their
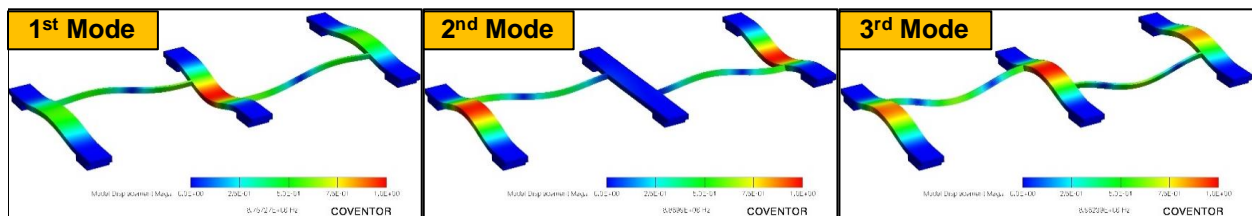

Figure 7.7: The mode shapes of the third-order CC-beam filter in the feedforward path.

marks for such a small filter bandwidth. As shown in Figure 7.5, tuning electrodes underlie all seven resonators to achieve maximum tuning ability. In order to maximize the overall tuning capability, the main electrodes of the intermediate constituent resonators were also used as extra tuning pads.

7.5 ELECTRICAL EQUIVALENT CIRCUIT

Figure 7.9 presents the complete electrical equivalent circuit of the 7th-order bridged micromechanical filter of Figure 7.5. A *RLC* resonating tank and a capacitor *T*-circuit represent each CC-beam resonator and flexural coupling beam. Transformers and negative capacitors at their input model the tuning via electrical stiffness. Velocity transformer ratios, η_{ci}s, are design parameter to achieve desired filter response. Equations 7.10 and 7.11 provide the expression for the transducer transformer ratio and static capacitance, used in the equivalent circuit of Figure 7.9.
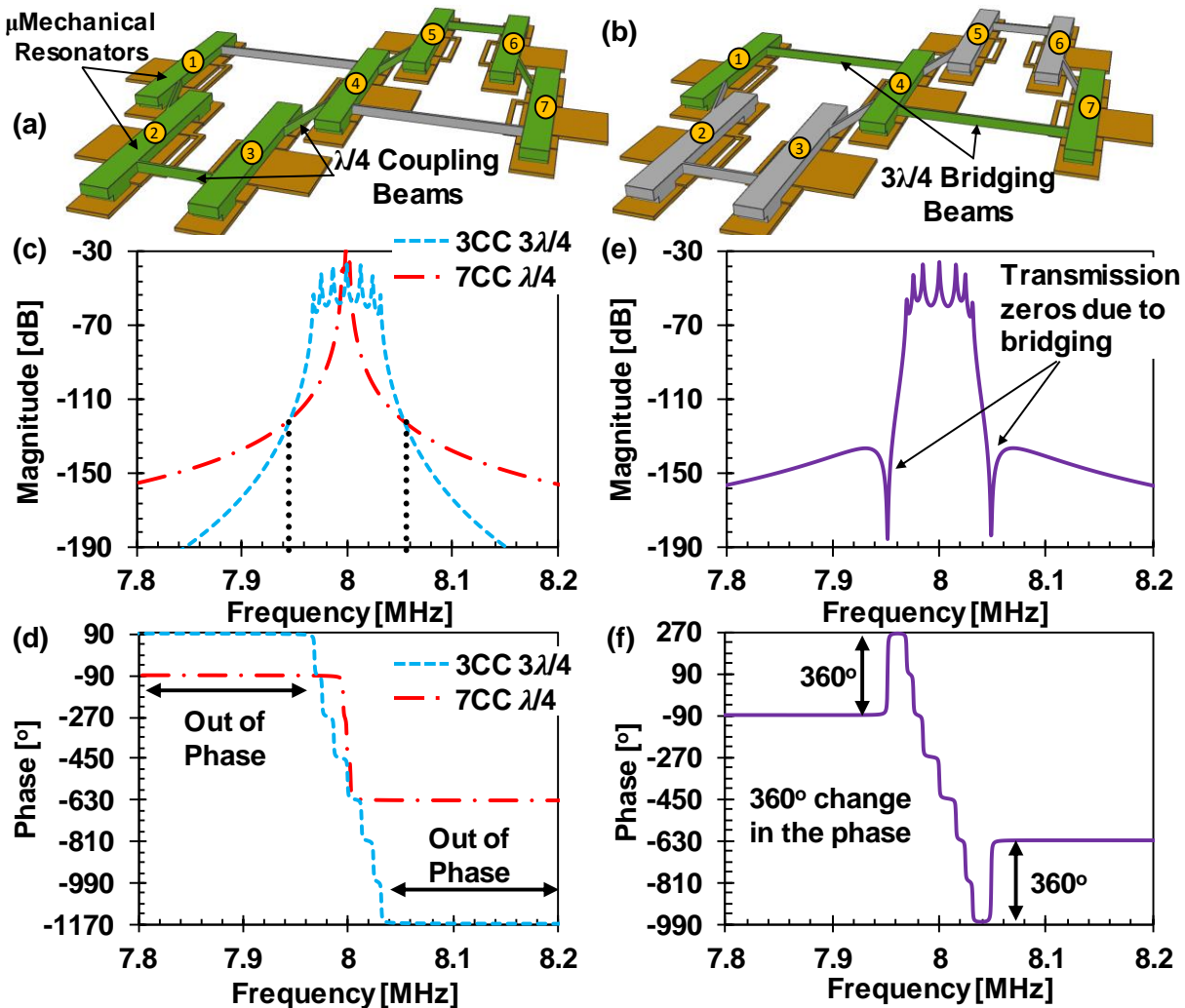
Figure 7.8: Unterminated 3rd-order, 7th-order, and bridged 7th-order filter magnitude and phase frequency responses, illustrating the formation of loss poles in the resonance frequency.

$$\eta_{ei} = \frac{|V_P - V_{Bi}|\varepsilon W_r L_r}{d_o^2} \int_{1-\frac{\alpha_e}{2}}^{1+\frac{\alpha_e}{2}} \left(\frac{\tilde{X}_{mode}(y)}{\tilde{X}_{mode}(1/2)} \right) dy \qquad (7.10)$$

Figure 7.9: The equivalent electrical circuit of the 7th-order bridged micromechanical filter, shown in figure 7.5. Beside the tuning electrodes underneath each resonator (highlighted in green), the main electrodes of the intermediate resonators (highlighted in purple) have been used as extra tuning pads to increase the overall tuning capability.

$$C_o = \alpha_e \frac{\varepsilon W_r L_r}{d_o}$$

$$\eta_{eTi} = \frac{|V_P - V_{Ti}|\varepsilon W_r L_r}{d_o^2} \sqrt{2 \int_0^{1-\frac{\alpha_e}{2}} \left(\frac{\tilde{X}_{mode}(y)}{\tild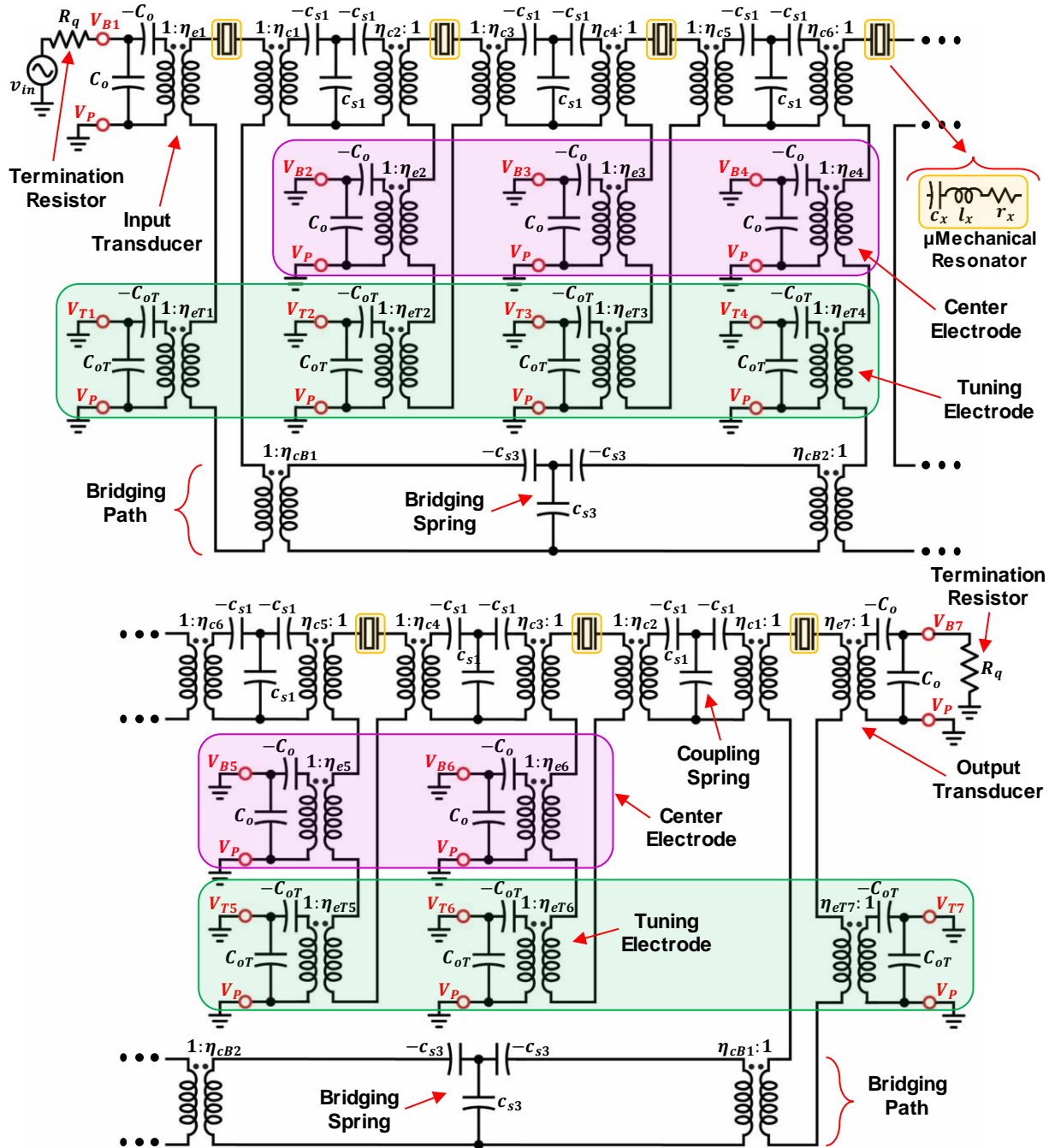e{X}_{mode}(1/2)}\right) dy \int_{1-\frac{\alpha_e}{2}}^{1+\frac{\alpha_e}{2}} \left(\frac{\tilde{X}_{mode}(y')}{\tilde{X}_{mode}(1/2)}\right) dy'}$$

(7.11)

$$C_{oT} = (1 - \alpha_e)\frac{\varepsilon W_r L_r}{d_o}$$

7.6 EXPERIMENTAL RESULTS

The 7th-order bridged filter was fabricated using a vertical gap surface-micromachining technology described in the previous chapters. Figure 7.10 (a) shows SEM graph of a released bridged micromechanical filters, clearly showing the coupling and bridging beams between the constituent resonators. As mentioned in Chapter 5, the proper termination and measurement of this filters require a buffer, trans-impedance or unity gain, shown in Figure 7.10 (b)

Figure 7.11 presents the frequency response of the 7th-order bridged Chebyshev filter of Figure 7.5 terminated by 20kΩ board-level resistors, frequency-tuned using dc-bias voltages under 3V, and measured under 1mTorr in a custom-built vacuum chamber. Without suitable tuning via electrical stiffness, the transmission poles and zeros fail to distribute as designed originally, due to the very tight requirement on the process variation. The required termination resistance R_q depends on the filter percent bandwidth and the motional resistance R_x of the constituent resonators, as derived in Chapter 4. Although use of wider resonators, or arrays of them, could reduce the needed Rq, this might not be advisable given the advantages of high-impedance in emerging low-power nano-scale wire-less communication systems.
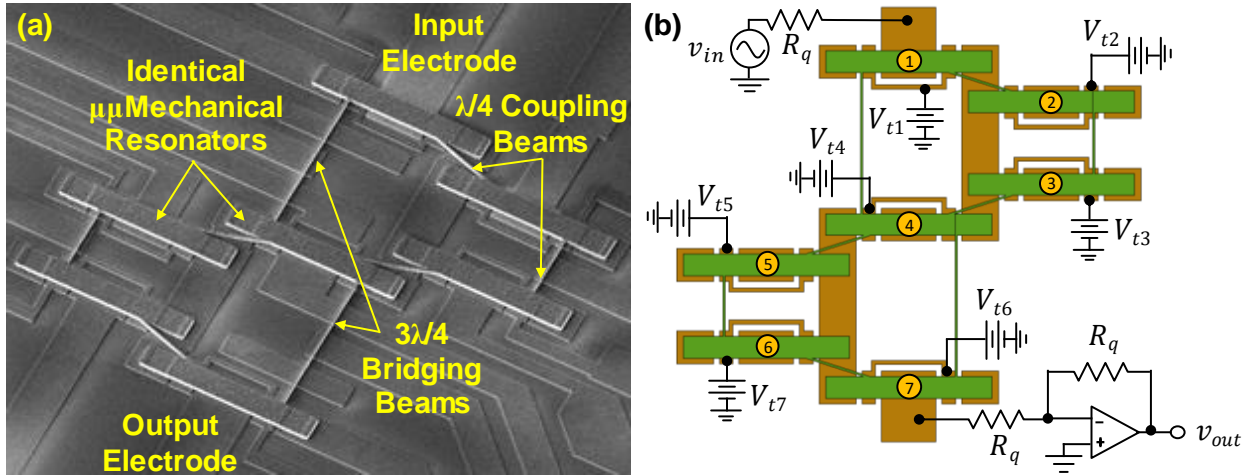

Figure 7.10: (a) SEM graph of a released 7th-order bridged filter and (b) the measurement circuitry used for proper termination and tuning of the filter response.

119

As shown, the filter achieves an impressive insertion loss of 1.6dB with less than 0.5dB of in-band ripple for a 0.3% bandwidth centered at 8.06MHz. Here, low-resistance interconnects helped to reduce the insertion loss of the properly-terminated filter. This filter response exhibits 40dB of out-of-band rejection and a 20dB shape factor of 1.45, which bests the previous mark of 1.86 for a similar frequency MEMS-based filter [35]. Such a sharp roll-off provides excellent rejection of adjacent channels, which could then pack with higher density. The tiny shape factor confirms both the utility of high filter or-der and the efficacy of non-adjacent resonator bridging.

Figure 7.12 presents the measured phase and group delay responses of the terminated filter, showing over 1260° of phase change consistent with the order of the filter and a group delay ripple of 0.5ms. This value is commensurate with the needs of narrowband communication receivers, which unlike wideband ones, can tolerate larger group delays without degradation in system characteristics, e.g., bit error rate.

To further demonstrate the remarkable performance of this filter, Figure 7.13 provides the two-tone measurement done on the terminated filter of Figure 7.5. This filter has third-order intercept point *IIP3* of 25dBm and 37.7dBm for tone spacing of 160kHz and 400kHz respectively.
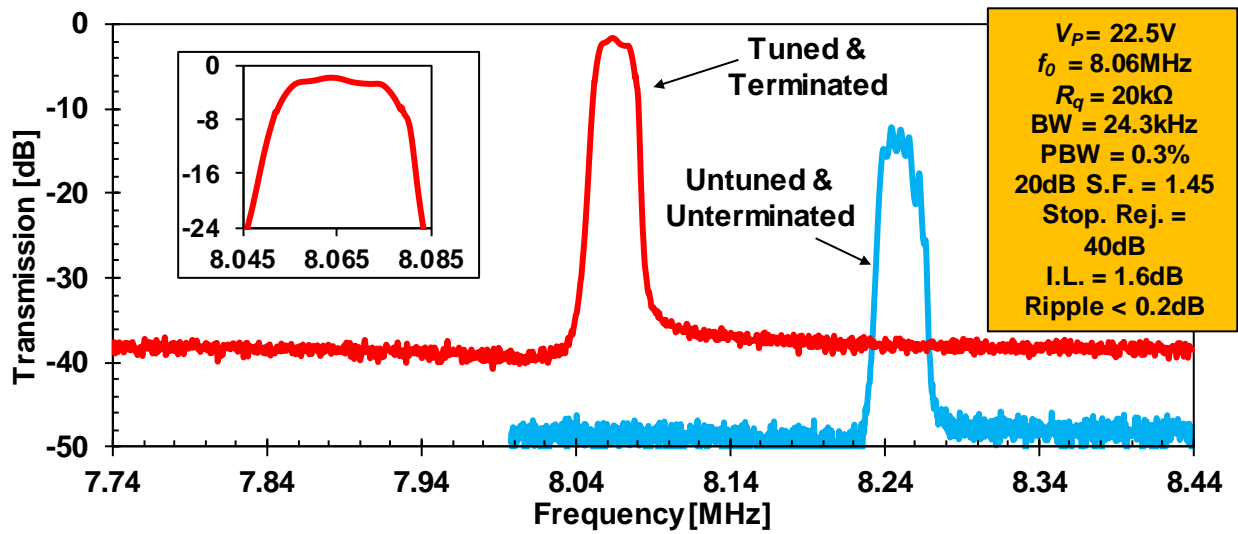
Figure 7.11: Measured frequency characteristic for the 7th -order bridged micromechanical filter of Fig. 7.5. The inset zooms in on the filter passband.
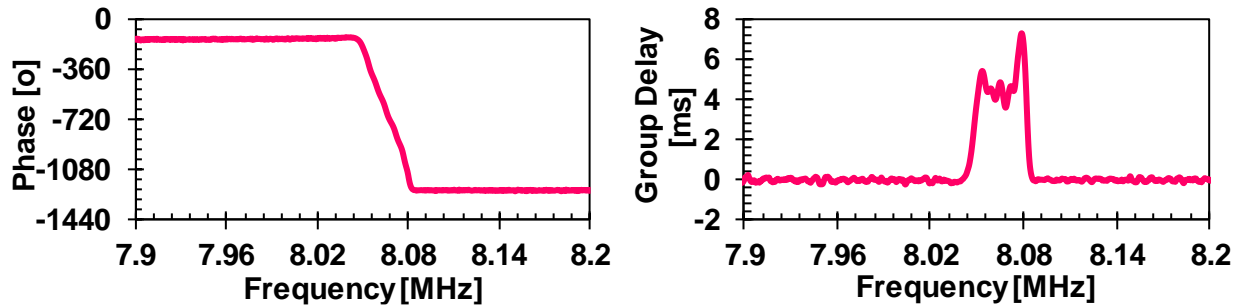
Figure 7.12: Measured phase response (left) and group delay response (right) for the terminated filter of Fig. 7.5.

120

This *IIP3* corresponds to the dynamic range of 92.36dB and 100.83dB, respectively, for a system with 10dB of minimum *SNR* requirement.

Figure 7.14 compares the frequency response of the filter presented in this chapter to a conventional microwave filter currently being used in Ham Radio applications. The filter of Figure 7.11 provides the frequency selection required for channel selection and power reduction, not to mention the distinguished size differences, as shown in the inset of this figure.

Table 5.2 summarizes the filter design parameters and measurement results.

Figure 7.13: Two-tone measurement of the filter nonlinearity (left) and the corresponding third-order intercept point IIP3 as a function of relative tone spacing (right).

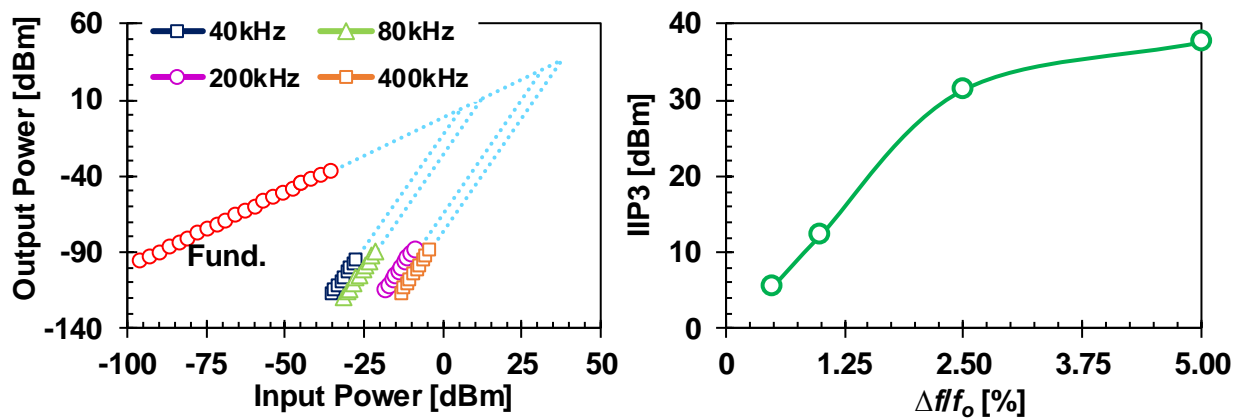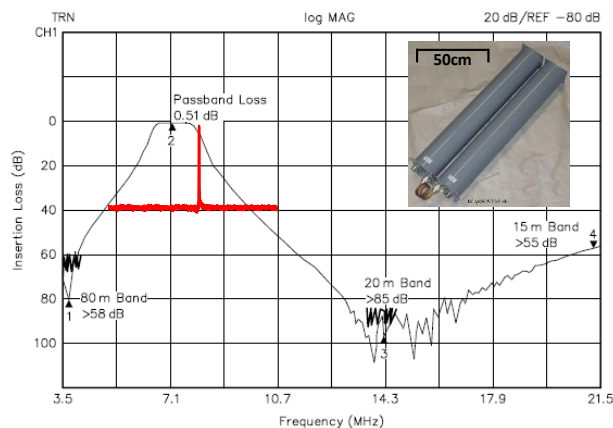Figure 7.14: Measured frequency characteristic for the 7th -order bridged micromechanical filter of Figure 7.5 compared to a conventional microwave filter. The inset shows the generic dimension of microwave filters at these frequencies.

121

Table 7.1: Bridged Filter Design Summary

Parameter	7CC 3λ/4 Design		Units
	Design/Sim.	Meas.	
Center Frequency, f_o	8.469	8.074	MHz
Resonator Q	10,000	15,100	—
Bandwidth, BW	27.3	24.3	kHz
Percent Bandwidth, (BW/f_o)	0.322	0.3	%
Filter DC-Bias, V_P	30	22.5	V
Loaded q_i^*	0.7654	--	—
Normalized Filter Coupling Coef., k_{12}^*, k_{67}	0.597	--	—
Normalized Filter Coupling Coef., k_{23}^*, k_{56}	0.431	--	—
Normalized Filter Coupling Coef., k_{34}^*, k_{45}	0.465	--	—
Filter Coupling Beam Length L_{s12}, L_{s23}, L_{s34}, L_{s45}, L_{s56}, L_{s67}	22.3	--	μm
Bridging Beam Length, L_{s14}, L_{s47}	51.8	--	μm
Filter Coupling Beam Width W_{s12}, W_{s23}, W_{s34}, W_{s45}, W_{s56}, W_{s67}	0.75	--	μm
Bridging Beam Width, W_{sB}	0.75	--	μm
Coupling/Bridging Beam Thickness, h	2	1.985	μm
Resonator Mass @ I/O, m_{re}	5.829x10^{-13}	5.902x10^{-13}	kg
Resonator Stiffness @ I/O, k_{re}	1.923x10^3	1.772x10^3	N/m
Resonator Damping @ I/O, c_{re}	3.036x10^{-9}	1.841x10^{-9}	Ns/m
Filter Coupling Location, l_{c1-3} $l_{c4}= l_{c3}$, $l_{c5}=l_{c2}$, $l_{c6}=l_{c1}$	5.1, 4.65, 4.75	5.5, 5.05, 5.15	μm
Bridging Location, l_{cB}	2.3	2.7	μm
Coupling Beam Stiffness k_{s12a}, k_{s23a}, k_{s34a}, k_{s45a}, k_{s56a}, k_{s67a}	-109.56	87.72	N/m
Coupling Beam Stiffness k_{s12c}, k_{s23c}, k_{s34c}, k_{s45c}, k_{s56c}, k_{s67c}	109.56	103.09	N/m
Bridging Beam Stiffness, k_{sB}	125.68	214.42	N/m
Bridging Beam Stiffness, k_{sB}	-125.68	-155.09	N/m
Filter Coupling Capacitance c_{s12a}, c_{s23a}, c_{s34a}, c_{s45a}, c_{s56a}, c_{s67a}	-0.0091	-0.0114	F
Filter Coupling Capacitance c_{s12c}, c_{s23c}, c_{s34c}, c_{s45c}, c_{s56c}, c_{s67c}	0.0091	0.0097	F
Bridging Capacitance, c_{sB}	0.008	0.0047	F
Bridging Capacitance, c_{sB}	-0.008	-0.0064	F
Mechanical Transformer Turn Ratio at l_{c1-3}, η_{c1-3} $\eta_{c4}=\eta_{c3}$, $\eta_{c5}=\eta_{c2}$, $\eta_{c6}=\eta_{c1}$	5.44, 6.40, 6.16	4.93, 5.73, 5.54	C/m
Mechanical Transformer Turn Ratio at l_{cB}, η_{cB}	23.57	18.06	C/m
Equivalent Inductance, l_x	5.829x10^{-13}	5.902x10^{-13}	H
Equivalent Capacitance, c_x	4.323x10^{-4}	5.644x10^{-4}	F
Equivalent Resistance, r_x	3.036x10^{-9}	1.841x10^{-9}	Ω
Electromechanical Coupling Coefficient, η_e	1.833x10^{-6}	1.532x10^{-6}	C/m
Calculated Equivalent Resistance, R_x	0.904	0.852	kΩ
Calculated Equivalent Inductance, L_x	0.173	0.25	H
Calculated Equivalent Capacitance, C_x	2.12	1.52	fF
Static Overlap Capacitance, C_o	9.44	10.12	fF
Electromechanical Coupling C_x/C_o	22.5	15.0	%
Termination Resistance, R_Q	22	20	kΩ
Insertion Loss, IL	0.3	1.6	dB
20 dB Shape Factor	1.42	1.45	—
Stopband Rejection, SR	90	40	dB

*From filter cookbooks.

Chapter 8 STRONG-COUPLING SUB-20NM-GAP CAPACITIVE RESONATORS

The sharp roll-off filters presented in the previous chapters were realized at high frequency (HF) spectrum, i.e. 3MHz to 30MHz, suitable for long-range low-data rate applications such as Ham radio and wireless sensor networks. Implementation of capacitive filters at higher frequencies and also in high-data rate applications requires demonstration of capacitive resonators with simultaneous strong electromechanical coupling and high quality factor at the frequencies of interest. This might seem a challenging task, since the capacitive resonator coupling (C_x/C_o) decreases by the resonance frequency square, as given in equation 2.22. This work attempts to correct the common misbelief that capacitive resonators lack the coupling strength required for high-frequency application.

Electrode-to-resonator gaps as small as 13.2nm achieved on a 59.5-MHz capacitive-gap transduced disk resonator of this work have now enabled a measured electromechanical coupling strength (C_x/C_o) greater than 1.62% at a bias volt-age of only 5.5V while retaining an unloaded Q of 29,640, for a $k_t^2 Q$ product of 576 that sets the record at VHF. Several key discoveries contribute to this successful demonstration, including a modified polysilicon etch recipe that enables considerably smoother etch sidewalls than previously achievable, allowing more uniform sidewall sacrificial layer deposition and preventing structure pull-in by removing asperities and their associated strong electric fields. This combination of high (C_x/C_o) and Q stands to reduce power consumption in low-noise oscillators, improve sensitivity for zero-quiescent all-mechanical receivers, and expand the range of filters accessible to capacitive-gap transduced resonators to more mainstream wireless communication applications with much improved insertion loss performance.

8.1 HIGH-FREQUENCY CAPACITIVE RESONATORS

Capacitive-gap transduced resonators are well known to provide high on-chip Q's, with values reaching 150,000 at VHF [79] and 40,000 at 3GHz [40]. Q's this high enable 0.1% bandwidth channel-select filters with low insertion loss and high rejection [3] for ultra-low power transceivers [24]; as well as low-power, low-noise oscillators with best-in-class figure of merits on the order of -225dB. Other characteristics that distinguish these resonators over alternatives

Table 8.1: Comparison between contour-mode AlN, quartz and capacitive technologies at VHF.

	f_o [MHz]	C_x/C_o [%]	R_x [Ω]	Q	$k_t^2 Q$	Area [μm]^2
Contour Mode AlN [45]	85	0.86	125	2,100	22	10,000
Quartz [83]	149	0.48	460	10,000	58	21,200
This Work	60	1.62	54	29,640	576	3,200

include designable spurious mode suppression [48] and a voltage-controlled on/off self-switching capability [23] that allows realization of switchable filter [80] or oscillator [81] banks without the performance hit from series switches. At HF (from 3-30 MHz), capacitive-gap transduced resonators also post strong electromechanical coupling, up to 30%, as demonstrated in the previous chapters.

Despite these advantages, capacitive-gap transduced micromechanical resonators still struggle to realize the needed (C_x/C_o) values applicable to wider bandwidth filters centered at VHF or higher frequency, such as the 3% band-width ones used in existing smartphones. Higher (C_x/C_o) than the 0.1% attained in [48] are desirable for higher order channel-select filters using more than two resonator array-composites. For example, a 3-resonator filter works best with $(C_x/C_o) \sim 0.25\%$; a 4-resonator with ~0.56%. To satisfy such (C_x/C_o) needs, recent efforts employ piezoelectric materials, but with significant reduction in Q and consequent increase in undesirable insertion loss to 8dB for 0.27% bandwidth, which is not acceptable right after the antenna in an RF front-end [29].

Alas, the path to higher (C_x/C_o) for higher Q capacitive-gap transduced devices is quite clear: Simply reduce the electrode-to-resonator capacitive gap [39]. As suggested by the simulation results of Fig. 2, a single wineglass disk resonator of Fig. 1 can achieve a (C_x/C_o) stronger than 1% and a motional impedance smaller than 100Ω by employing a 25nm gap spacing with a bias voltage V_P of 10V. Further reducing the gap to 10nm accompanied by 58V of V_P achieves a coupling strength of 6% at GHz frequency.

Although gap reduction via ALD partial-gap filling [44], [82] down to an effective 37nm confirmed the possibility of higher (C_x/C_o) ~0.58% for capacitive-gap transduced resonators, this
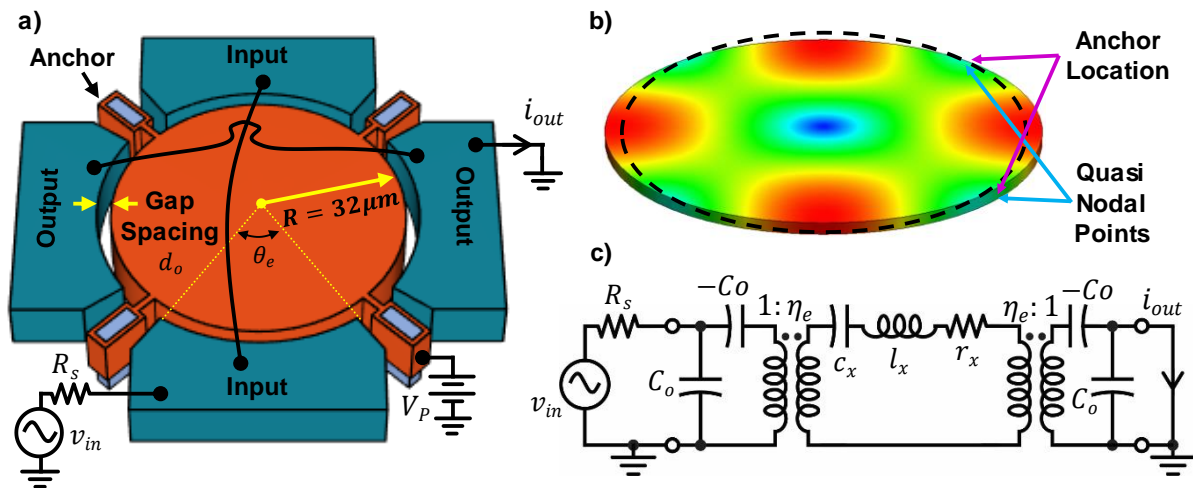

Figure 8.1: (a) Illustration of a wine-glass disk resonator in a typical two port operation scheme. (b) Mode shape and quasi nodal points where the supports attach. (c) Electrical equivalent LCR circuit.

is a far cry from what is possible. Indeed, one must ask the question, "What is the gap spacing limit?"

Pursuant to answering this question, this work demonstrates electrode-to-resonator gaps as small as 13.2nm achieved on a 59.5-MHz capacitive-gap transduced disk resonator that yield a measured electromechanical coupling strength (C_x/C_o) greater than 1.62% at a bias voltage of only 5.5V, which together with an unloaded Q of 29,640 achieves a $k_t^2 Q$ product of 576 that far exceeds that of competitors [83], as shown in Table 8.1. This combination of high (C_x/C_o) and Q not only cuts a path towards power reduction for low-noise oscillators and higher sensitivity for zero-quiescent all-mechanical receivers [45] [84], but also expands the range of filters accessible to capacitive-gap transduced resonators to more mainstream wireless communication applications.

8.2 ELECTROMECHANICAL COUPLING (C_X/C_O)

The electromechanical coupling factor (C_x/C_o) gauges the efficiency of energy transfer between electrical and mechanical domains. It sets the upper bound on the percent bandwidth of a micromechanical filter [49], the tuning range of a capacitive-gap transduced resonator's center frequency [62], the sensitivity of capacitive microphones, and the efficiency of CMUT devices [85]. The electromechanical coupling factor for the capacitive-gap transduced wine-glass resonator shown in Fig. 8.1, defined as the mechanical energy relative to the total energy, takes the form of equation 8.1, adopting the governing equations from [50] and following the procedure described in Chapter 2 for CC-beam resonator. Here, ε_o, V_P, d_o, ω_o, R, ρ, θ_e, $R_m(r)$ are vacuum permittivity, bias voltage, gap spacing, the disk radian resonance frequency, radius, density, electrode angle (cf. Fig. 1), and resonance mode shape function [19], respectively.

$$\frac{C_x}{C_o} = \varepsilon_o \cdot \frac{V_P^2}{d_o^3} \cdot \frac{R}{2\pi\rho\omega_o^2} \cdot \frac{\sin^2(\theta_e)}{\theta_e} \cdot \frac{R_m^2(R)}{\int_0^R R_m^2(r)r\,dr} \qquad (8.1)$$
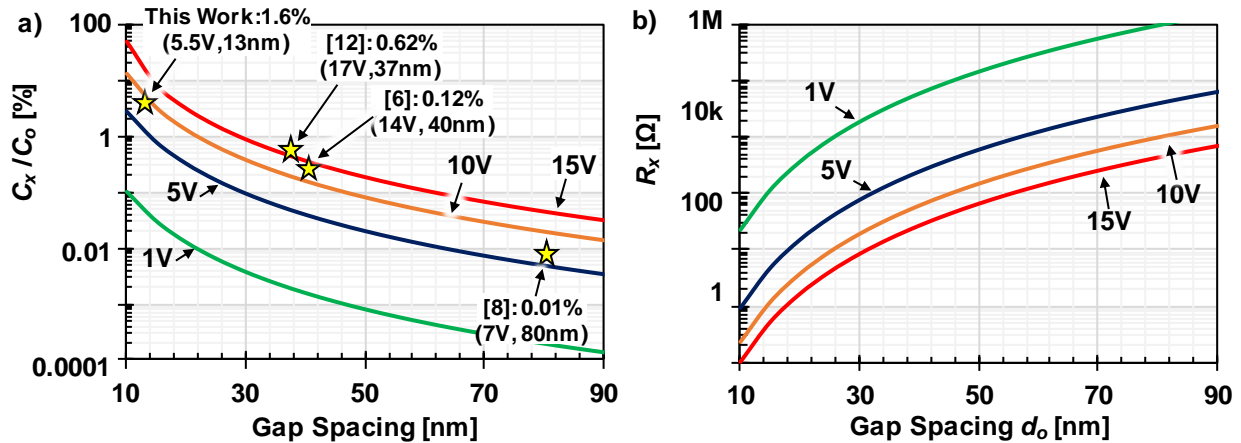

Figure 8.2: Simulated plots of (a) electromechanical coupling strength (C_x/C_o) and (b) motional resistance R_x versus electrode-to-resonator gap spacing d_o and bias voltage V_P for a 2μm-thick 60-MHz wineglass disk resonator with Q=70,000.

125

This expression makes very clear the importance of achieving a small electrode-to-resonator gap do for maxi-mum (C_x/C_o), where a third power dependence makes gap spacing the strongest control knob by far. Note that (8.1) correctly predicts that capacitive-gap transducers with gaps of 100nm already exhibit coupling strengths that outperform AlN piezoelectrics at HF (up to 30MHz), as presented in the previous chapters. To outperform AlN above VHF, smaller gaps are needed. For example, at GHz frequencies gaps below 20nm are desirable.

8.3 LIMITATIONS ON THE BIAS VOLTAGE

Shrinking the transducer gap spacing in order to provide stronger coupling arises questions on the maximum bias voltage that such a small gap can endure before any catastrophic breakdown. This concern amplifies for gaps smaller than 20nm, where a bias voltage of 20V results in the enormous electric field of 10MV/cm in the transducer. This electric field suffices to breakdown most of the insulator materials used in semiconductor industry. Since the capacitive transducer of this work employs vacuum in the gap, the dielectric breakdown will not limit the bias voltage applied to the transducer. Therefore, the bias voltage is constrained by (1) electrostatic pull-in and (2) quantum effects, i.e. tunneling currents.

8.3.1 ELECTROSTATIC PULL-IN

The electric field in the gap exerts electrostatic force on the electrodes and attracts the suspended electrode towards the stationary electrode, as described in Chapter 2. Due to the symmetry of the wineglass disk resonator of Figure 8.1, the electrostatic forces on the disk are balanced and cancel out each other. Therefore, the disk resonator does not have any gross displacement towards any electrodes. However, as the bias voltage increases and the electrostatic force grows, it makes the disk and the portions of the electrodes that are not anchored expand and move towards each other, and eventually collapse, as shown in Figure 8.3 (a).

Figure 8.3 (b) presents the pull-in voltage of the disk resonator of Figure 8.1 for different gap spacing. The decrease in the gap spacing between electrodes boosts the electric field and the electrostatic force on the resonator, hence, reducing the pull-in voltage. Identical gap spacing between the disk resonator and all the four electrodes is the underlying assumption of the pull-in voltage function shown in Figure 8.3 (b). Nonuniform gap spacing disturbs the balance between the four electrostatic forces on the disk and makes the resonator drift toward the closer electrodes, as shown in figure (c), and therefore, reducing the pull-in voltage. Figure 8.3 (d) presents the change in the pull-in voltage as the function of nonuniformity in the gap spacing. For example, if the gap spacing for the two electrodes on the left side is 10% smaller, the pull-in voltage drops 40% due to this nonuniformity.

The pull-in voltage presented in the Figure 8.3 are strongly design dependent and one can optimize the resonator and the electrodes geometry to improve the pull-in voltage. For example, investigation of the electrostatic pull-in for a resonator with 10nm gap spacing revealed the fact that the pull-in occurred at the electrode corners, as shown in Figure 8.4 (a). Modifications in the resonator (1) to remove the weak electrode corners and (2) to widen the anchors for stronger support, improved the pull-in voltage 3x to 30V, as shown in Figure 8.4 (b).
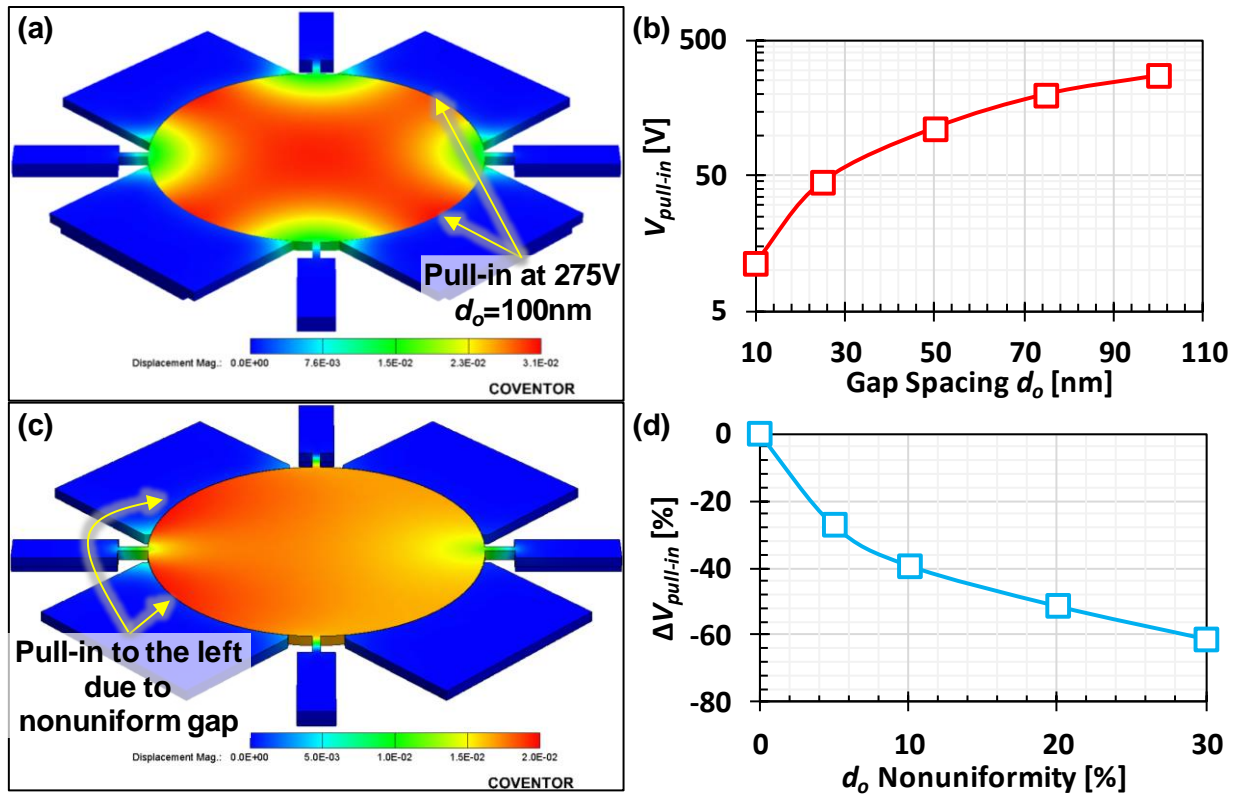

Figure 8.3: (a) The electrostatic simulation for the pull-in of the wineglass disk resonator of Figure 8.1, (b) the resonator pull-in voltage as the function of the gap spacing, (c) the electrostatic pull-in simulation for the nonuniform gap spacing, (d) the decrease in the pull-in voltage as the function of gap spacing nonuniformity.
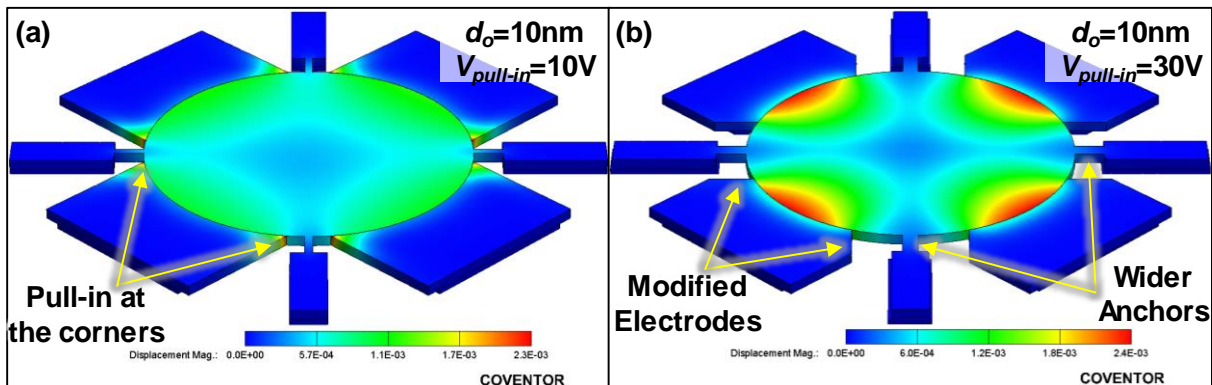

Figure 8.4: (a) Electrostatic pull-in of 10nm-gap resonator, and (b) improvement in the pull-in voltage by removing the electrode corners and making anchors wider for stronger support.

8.3.2 QUANTUM TUNNELING

Application of gap spacing on the order of 20nm and smaller brings up the prospect of encountering quantum effects, such as direct tunneling or Fowler-Nordheim tunneling. Extremely small gaps allow penetration of electron wave function and therefore, electron tunneling through a potential barrier, such as the vacuum gap between two electrodes of the resonator described here. Figure 8.5 (a) illustrates the direct tunneling mechanism for a simplified metal-dielectric-metal system and equation 8.2 provides the Schuegraf's approximation [86] for direct tunneling current density. Here, q, $\hbar$, m^* ϕ_b, and V_B are electron electric charge, reduce Plank's constant, effective electron mass, electrode's work function and applied voltages, respectively. F_e is the average electric field across the gap which can be approximated by V_B/d_o. This equation suggests direct tunneling is negligible for any gap spacing larger than 3nm.

$$
J_{DT} = \frac{q^3}{16\pi^2 \hbar \phi_b} \cdot \frac{1}{\left(1 - \sqrt{1 - \frac{qV_B}{\phi_b}}\right)^2} \cdot F_e^2
$$
$$
\cdot exp\left(-\frac{4}{3} \cdot \frac{\sqrt{2m^*}\phi_b^{1.5}}{\hbar q} \cdot \frac{1}{F_e} \cdot \left\{1 - \left(1 - \frac{qV_B}{\phi_b}\right)^{1.5}\right\}\right)
$$

(8.2)

As the applied bias voltage increases, the electric field across the gap intensifies and bends the energy bands, as shown in the simplified schematic of Figure 8.5 (b). This band bending effectively reduces the width of the potential barrier and increases the tunneling current, known as Fowler-Nordheim tunneling. Figure 8.5 (c) presents the Fowler-Nordheim tunneling current
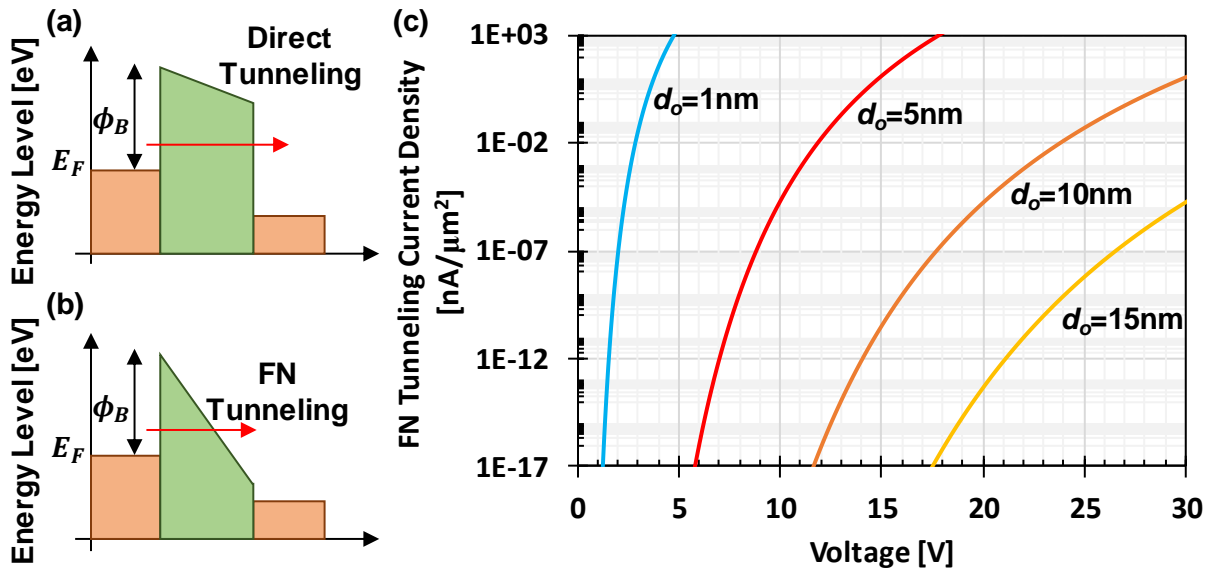

Figure 8.5: Simplified energy band configuration for (a) direct and (b) Fowler-Nordheim tunneling mechanisms. (c) The Fowler-Nordheim tunneling current density as a function of applied voltage for different gap spacing.

density as a function of bias voltage for different gap spacing, based on the equation of 8.3 [87]. This figure shows that bias voltage of 3.5V across 1nm gap introduces tunneling current density less than 1nA/μm2. This voltage corresponds to the electric field magnitude of 35V/cm, which is the electric field required to introduce this current in any given gap, as equation 8.3 is only a function of the electric field, not the gap and the bias voltage.

$$J_{FN} = \frac{q^3}{16\pi^2\hbar\phi_b} \cdot F_e^2 \cdot exp\left(-\frac{4}{3}\frac{\sqrt{2m^*}\phi_b^{1.5}}{\hbar q} \cdot \frac{1}{F_e}\right) \tag{8.3}$$

8.4 NANOSCALE GAP SPACING

Inevitably, benefits afforded by scaling generally come with consequences. In particular, a shrinking electrode-to-resonator gap invites numerous possible issues, including

i) Asperities in the gap sharp enough to concentrate electric fields to the point of breakdown (*c.f.* Figure 8.10).

ii) Asperities that reduce the effective gap distance, disturbing the force balance on opposite sides of the disk, and thereby lowering the pull-in voltage.

iii) Compressive film stress caused by slower shrinkage of the disk with decreasing temperature relative to the substrate that effectively stretches the disk edges into contact with the surrounding electrode (*c.f.* Figure 8.9).

iv) Obstructions in the gap, e.g., from condensation.

Each of the above, of course, are interrelated. In particular, compressive stress issues amplify if there are asperities, which arguably puts surface roughness among the most disruptive issues. Recognizing this, the fabrication process to achieve sub-20nm gaps puts particular importance on attaining as smooth and straight sidewalls as possible.
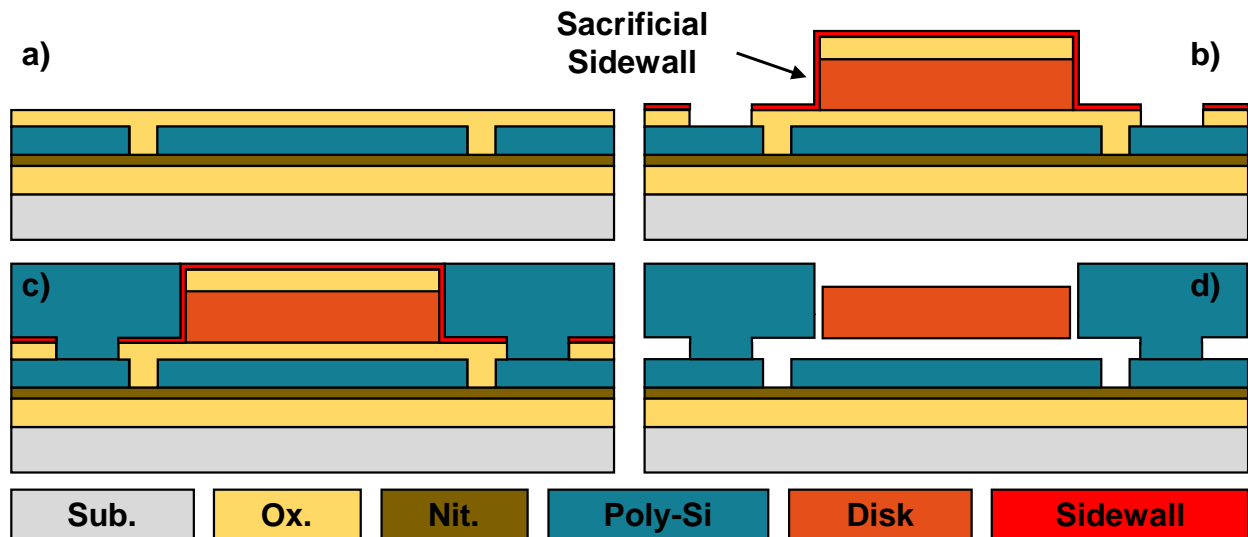

Figure 8.6: Fabrication process yielding tiny-gap resonators.

Figure 8.6 summarizes the fabrication process yielding the Figure 8.1 disk resonator. The process begins with blanket LPCVD depositions of oxide and nitride to form an isolation layer, followed by LPCVD oxide deposition and patterning to form a mold into which doped polysilicon is deposited then CMP'ed down to yield thick, low-resistance interconnect, as shown in (a). The resultant flat surface after CMP'ing facilitates subsequent blanket LPCVD of bottom sacrificial oxide, structural polysilicon, and top oxide hard mask, the last two of which are patterned and etched to delineate the disk. It is of utmost importance to minimize the residual stress in the deposited polysilicon layer. The 64µm-wide resonator will be suspended 20nm or less away from the electrodes and any residual stress or stress gradient in the structure make the structure shorten to the electrodes, as shown in Figure 8.7. To suppress this issue, this work studied the polysilicon residual stress for different deposition temperatures and annealing time and temperatures, as shown in Figure 8.8. The process of this work employs polySi deposited at 590ºC and annealed at 1000ºC for 30min to achieve very low residual stress (5MPa) and zero stress gradient, both much smaller than the critical values of 60MPa and 50MPa/µm, respectively, that could otherwise cause shorts.

It is here where the carefully designed etch recipe summarized in Figure 8.9 makes all the difference in the ability to achieve sub-20nm gaps. Specifically, the HBr-based polySi etch is anisotropic and yields a smoother sidewall than a Cl2-based etch, since the etch rate depends less on the silicon crystalline orientation and polySi grain boundaries.
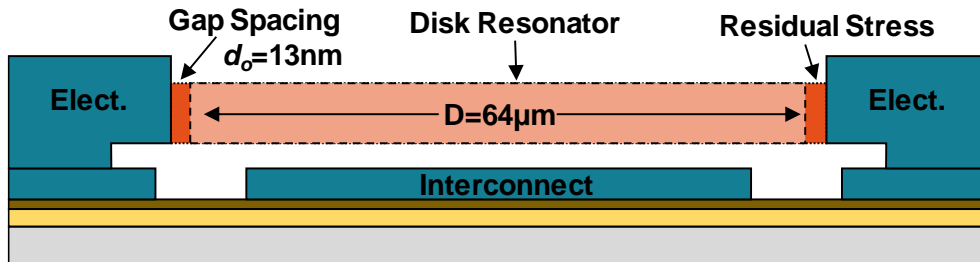

Figure 8.7: Illustration depicting how residual stress can cause shorts between disk and electrode when the gap becomes very small.
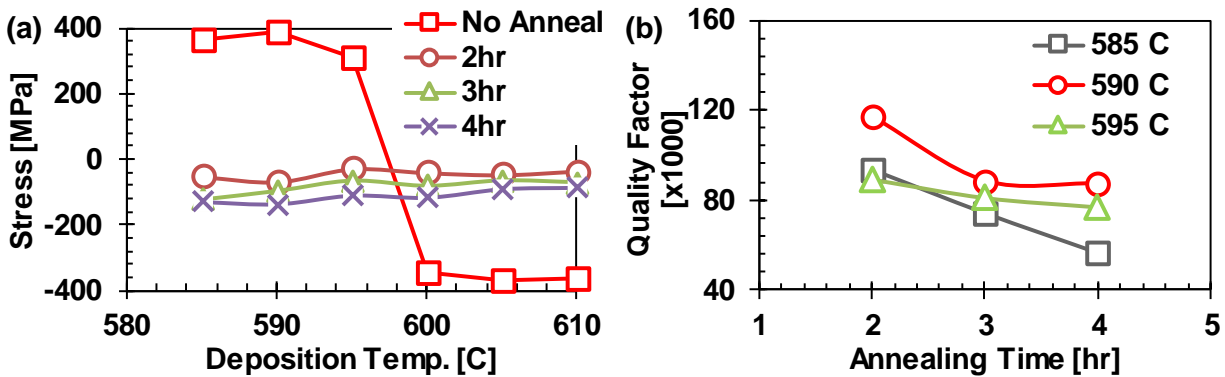

Figure 8.8: (a) The polysilicon residual stress as a function of deposition temperature, for different annealing time at 1000oC. (b) The resonator quality factor degradation with annealing time for different deposition temperature.

130

The smooth sidewalls devoid of asperities larger than 10nm high now facilitate deposition of the gap-setting side-wall sacrificial oxide down to 10nm via LPCVD at 930°C. Deposition of such a thin layer using LPCVD is a challenging task. The CVD process deposits scarce oxide patches across the wafer based on the local condition on the wafer and CVD nucleation requirement. As the deposition continues, this nonuniform layer grows into a uniform conformal layer, as shown in Figure 8.10. To achieve the uniform layer, this works modified the LPCVD oxide deposition recipe: (1) higher deposition temperature to increase the mobility of the oxide patches on the surface, and (2) lower deposition pressure and gas flows to slow down the deposition process and provide the time required by the CVD process to form the uniform layer. In the future attempts, utilization of atomic layer deposition (ALD) system which can precisely control the layer thickness down to atomic monolayers can alleviate the need for high-temperature oxide deposition and also provide much better dielectric layer uniformity across the wafer.

Patterning and etching of electrode anchors follows the oxide deposition to yield the cross-section of Figure 8.6 (b). Subsequent polySi deposition and doping, followed by CMP and

Step	TCP RF [W]	Bias RF [W]	Gap [cm]	HBr [sccm]	Cl$_2$ [sccm]	O$_2$ [sccm]	He [sccm]	CF$_4$ [sccm]
#1	200	40	6.03	0	0	0	0	100
#2	250	55	6.03	150	4	1	4	0
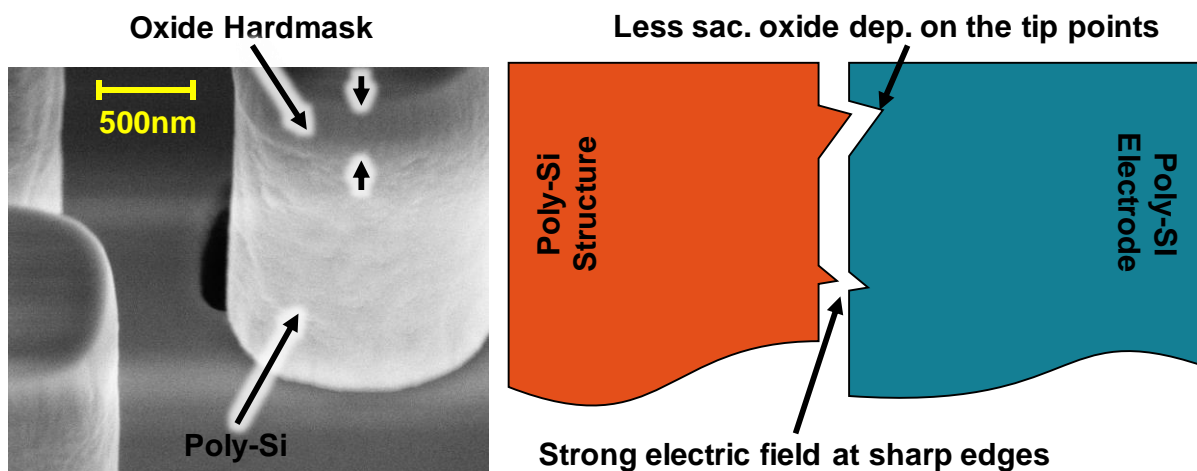
Figure 8.9: Practical considerations indicated at top right demand polySi sidewall smoothness on the same order or smaller than the sidewall sacrificial film thickness. The LAM TCP 9400SE etcher recipe summarized in the table achieves a very smooth surface, shown in the SEM above. Here, step #1 breaks through any native oxide, then successive cycles of processing/cooling of step #2 etch the polySi.

Figure 8.10: Two steps of a CVD process: (1) sparse nucleation at the beginning of the process, (2) which will develop to a uniform layer as the deposition continues.

131

electrode patterning and etching then yield the planarized cross-section of (c). Finally, wet-etching in 49% HF yields the released resonator of (d).
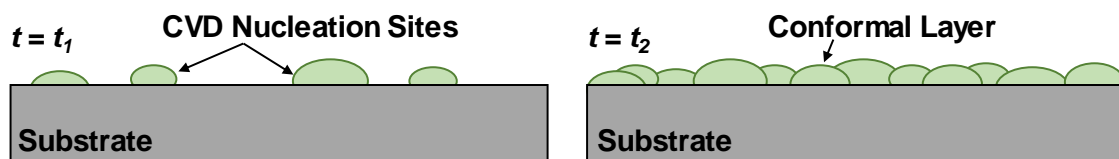
Fig. 8.11 presents the SEM micrograph of a released wine-glass disk resonator with zoom-in on the electrode-to-resonator overlap. Here, the smooth-sidewall structure achieved by the Fig. 8.9 etch recipe contrasts sharply with the much rougher electrode etch done via a conventional SF6-based chemistry aimed more at higher polysilicon-to-oxide selectivity.

8.5 EXPERIMENTAL RESULTS

Fig. 8.12 presents the vacuum-measured frequency response of the fabricated wineglass disk of Fig. 8.1 for various bias voltages V_P. The unloaded Q of this resonator is 29,640, measurable at 10µTorr and with small V_P. As V_P increases, R_x shrinks to only 54Ω at V_P=5.5V, which is considerably smaller than the 750Ω interconnect resistance (cf. Fig. 8.11 (b)), allowing the latter to load the overall Q down to 2,500, as predicted by the equivalent circuit of Figure 8.11 (c). Thus, preservation of the unloaded resonator Q of 29,640 in future devices calls for much lower interconnect resistance, perhaps provided by metals.

Replotting the data of Fig. 8.12 as frequency versus V_P yields Fig. 8.13 (a), from which curve-fitting [17] accurately extracts a remarkable 13.2nm electrode-to-resonator gap spacing. As evident from this figure, the 59.5MHz-wineglass resonator has more than 1MHz of tuning range for only 5.5V of biasing voltage, all consistent with the expected increase in electrical stiffness with decreasing gap spacing. The electrical stiffness at 5.5V is 23.4kN/m, which is 3.05% of the disk's 766.5kN/m mechanical stiffness.
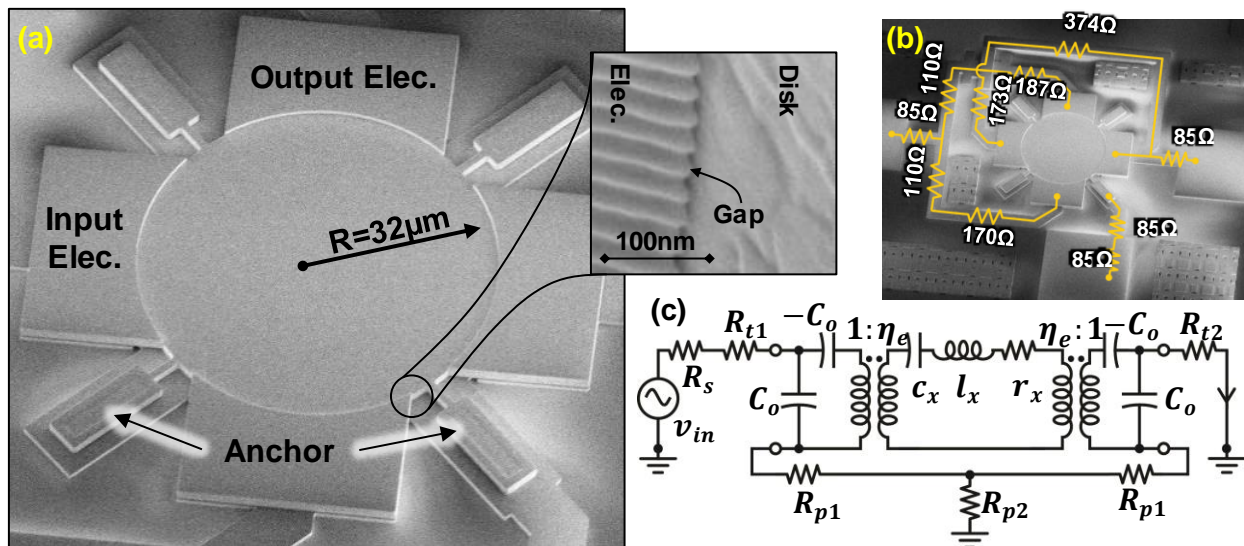

Figure 8.11: (a) SEM of a released wineglass disk resonator with zoom-in to highlight the smooth structure etch compared to the standard high-selectivity electrode etch. (b) Trace resistance on the input/output path as well as the bias path can load the resonator and degrade its quality factor Q.

The electromechanical coupling factor (C_x/C_o) was extracted from measured frequency response curves using the expression given in equation 8.4, derived from the electrical circuit of Fig. 8.1 (c). Here, f_s and f_p are the series and parallel resonance frequencies, respectively, of the one-port measurement. Fig. 8.13 (b) plots (C_x/C_o) versus bias voltage, showing an impressive (C_x/C_o) of 1.6% at 5.5V bias, which matches the prediction of (8.1) using the measured gap spacing.

$$\frac{C_x}{C_o} = \frac{f_p^2 - f_s^2}{f_s^2} \times 100 \tag{8.4}$$

Figure 8.13 (c) puts the achieved electromechanical coupling strength in perspective by comparing the small gap device to a resonator with 85nm gap spacings. The large gap device biased at even 30V cannot provide the coupling strength of the small gap device at 2.5V. At equal electric field across the gap, the 13nm-gap device offers 5.6 times stronger coupling, compared to the 85nm-gap device, as expected form equation 8.1. Figure 8.13 (d) shows electromechanical coupling strength for devices with different gap spacing, confirming the predictions of the equation 8.1 and advertising the controllability of the process for a desired coupling strength.

To address concerns about the linearity of a capacitive-gap transducer with such a tiny gap, the two-tone nonlinearity measurement summarized in Fig. 8.13 (e) and (f) reveals third-order intercept points (IIP3's) of +23dBm and +29dBm for tone spacings of 580kHz and 3MHz, respectively, both already adequate for today's cellular handsets, and if even needed, with room for improvement via mechanical coupled arraying.

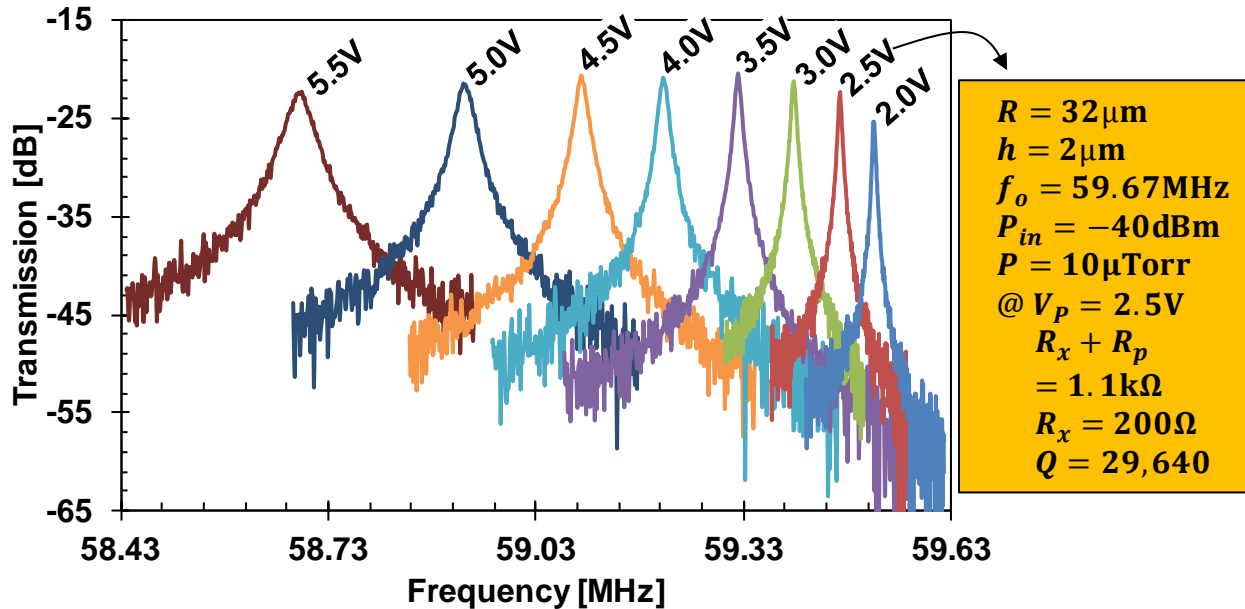
Figure 8.12: Measured frequency response of the WG disk resonator for various VP's. With 3.0V bias, the unloaded Q is 29,640 with a motional resistance of 200Ω. The Q decreases at higher voltages when the motional resistance of the device becomes significantly smaller than that of the polySi interconnect, suggesting that metal interconnect be used in future devices to prevent this Q reduction.

The histogram of the gap spacing distribution across a die is given in Figure 8.14 (a). The process described in this chapter has average thickness of 15nm and standard deviation of 2nm. The application of ALD system to deliver the gap spacing can potentially reduce the deviation to
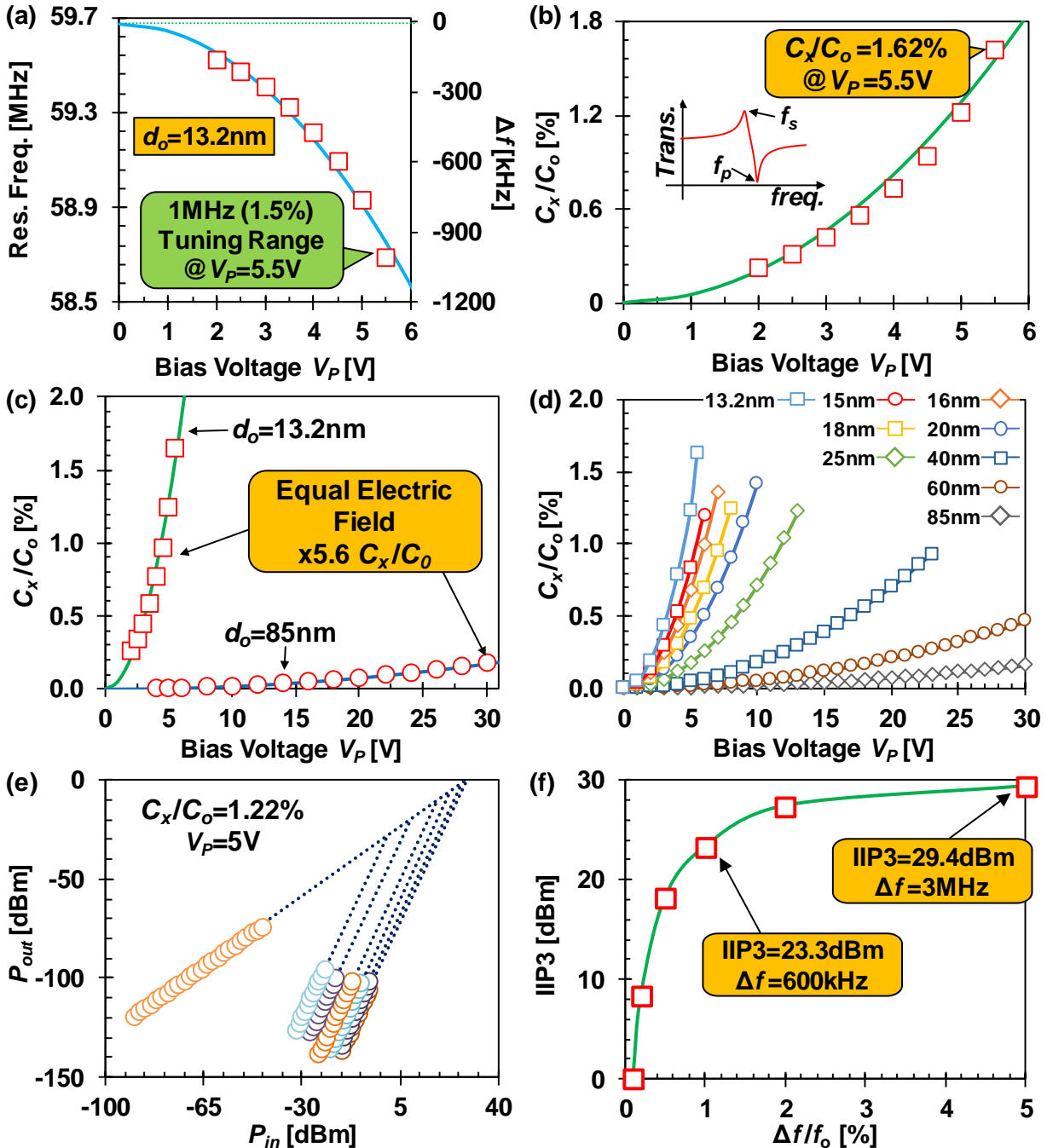
Figure 8.13: 10µTorr-vacuum-measured (a) resonance frequency and (b) electromechanical coupling (C_x/C_o) for a 13.2nm-gap WG disk determined using series f_s and parallel f_p resonance frequencies, both plotted against bias voltage V_P. (c) and (d) show the coupling strength of wineglass disk resonators with different gap spacing. (e) Two-tone nonlinearity measurement of the 13.2nm-gap WG disk and (f) plot of IIP3 versus tone offset from the center frequency.

sub-Angstrom due to the immense controllability of the process. The change in the ambient temperature shifts the resonance frequency by modification of material properties and the resonator's dimensions, as shown in Figure 8.14 (b). However, the temperature fluctuation does not change the transducer performance and electromechanical coupling strength, as shown in Figure 8.14 (c). The robust transducer performance against temperature fluctuations is due to the similarity between the material properties of the deposited polysilicon layers and the silicon substrate. Adaptation of this work for non-homogenous structures, e.g. diamond disk resonators on the silicon substrate, requires careful investigation and optimization of the process.

The ambient pressure is one of the main factors limiting the quality factor of the capacitive resonators, as shown in Figure 8.14 (d). As the pressure increases, the total energy leaked to the gas molecules soars and consequently, the resonator quality factor decreases. However, the small-gap device shows less degradation in the quality factor Q for a given ambient pressure, compared to a 50nm-gap resonator, as shown in figure (e). Therefore, the 13nm-gap resonator does not require high-vacuum hermetic packaging which will simplify the packaging process and reduces the overall cost.

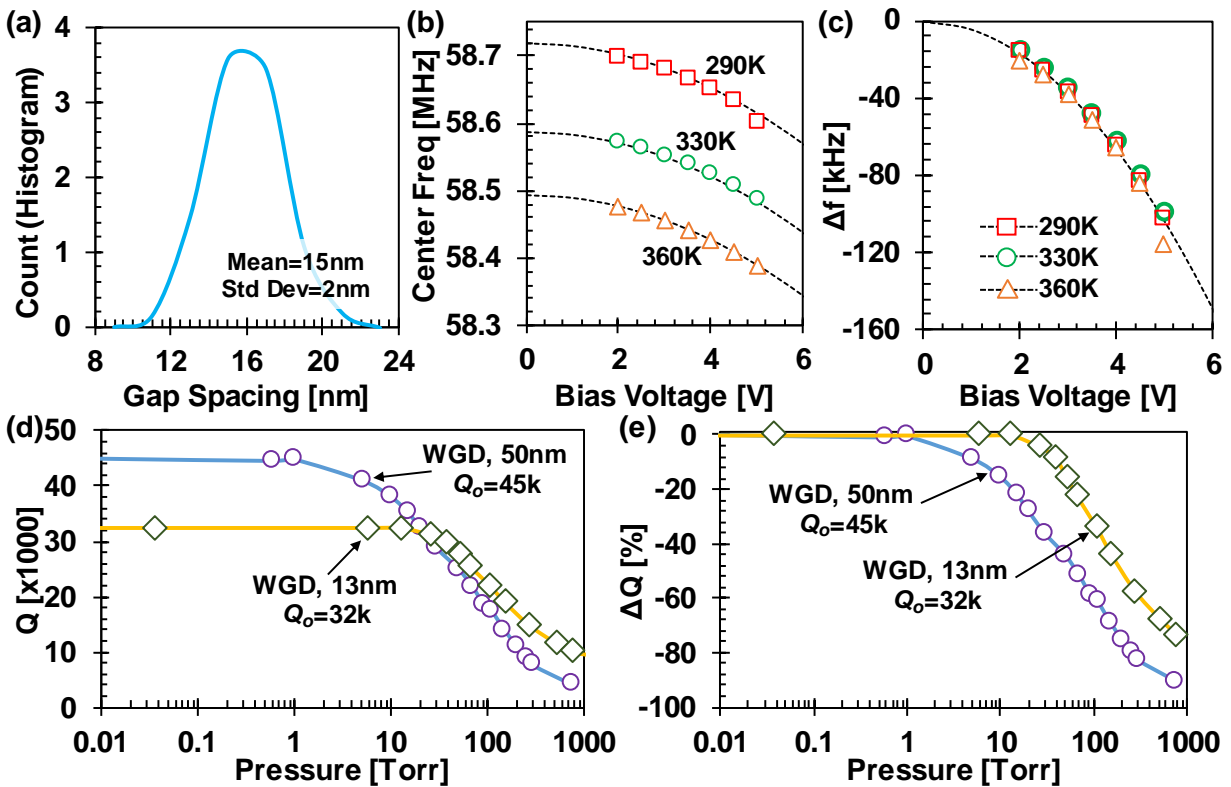

Figure 8.14: (a) The histogram of gap spacing distribution across a die. (b) Resonance frequency and (c) relative change in the resonance frequency of the wineglass disk as a function of bias voltage measured at different temperature. (d) The resonator quality factor and (e) the relative change in the Q as a function of ambient pressure for the 13nm-gap device and a 50nm-gap resonator.

135

Chapter 9 CONCLUSION

This dissertation explored the advantages of the application of capacitive-gap micromechanical resonators and filters in the wireless communication systems. This thesis focused on the novel methods to improve the performance of capacitive channel-select filters and pave the way for high frequency realization. The theory and the models developed in this thesis accurately predicted the small-signal and also nonlinear performances of capacitive transducers and offered a coherent system for implementation in any circuit analysis tools.

9.1 ACHIEVEMENTS

The transcendental expressions developed in Chapter 2 to describe the parallel-plate capacitive transducer of a clamped-clamped beam resonator predicted the strong electromechanical coupling of this resonators at HF. Combination of strong coupling and high quality factor makes CC-beam resonators an excellent choice to achieve channel selection required to decrease the receiver power consumption. Investigation of fabricated CC-beam resonators confirmed the theoretical predictions and RF measurements showed strong electromechanical coupling (C_x/C_o) of more than 10% and quality factor of 15,100. This CC-beam resonator exceeds the performance of any competing technologies and forms the framework for the successful demonstration of channel select filters. The simplification assumptions of this chapter provide excellent approximations to the transcendental expressions to be used in any circuit simulator and optimizer.

The filter design procedure of Chapter 3 provides powerful insight into the filter design, and the various tradeoffs between filter specifications and resonator characteristics. The mechanical and electrical equivalent circuits of this chapter demonstrated the formation of system poles around the filter center frequency by mechanical coupling of identical resonators and highlighted the importance of the mechanical design of narrow coupling beams. Consequently, Chapter 4 explored the narrow coupling beam design and offered new formulation and further understandings of extensional- and flexural-mode coupling beams.

Armed by the findings of previous chapters on resonator, filter and coupling beam design, Chapter 5 attempted to achieve channel-select filters and offer a new method to improve the performance of the existing filters. This chapter presented a non-conventional strategic bridging between non-adjacent resonators of 3rd- and 4th-order filters to insert and manipulate transmission loss poles in the filter transfer function. Precise placement of these generated loss poles improved the passband-to-stopband roll-off of the aforementioned filters, characterized by 20dB shape factor as small as 1.84 for channel-select filters with 0.1% to 0.3% fractional bandwidth and small insertion loss of only 1dB.

Chapter 6 investigated the nonlinearity sources of a capacitive transducer and the developed expressions predicted acceptable nonlinearity performance for capacitive resonators and filters. The proposed channel-select receiver of this work relieves the dynamic range requirements on the integrated circuit stages by eliminating all interfering signal. Therefore, the nonlinear characteristics of the channel-select filters are of utmost important. Two-tone measurements on the fabricated bridged filters confirmed the theoretical predictions and showed nonlinear performances sufficient for today's wireless applications. These filters demonstrated third-order intercept point IIP3 of up to 36dBm, equivalent to dynamic range of 90.5dB.

To further take advantage of the strong electromechanical coupling high quality factor the CC-beam resonators offer, Chapter 7 presented a seventh-order bridged micromechanical filter with remarkable roll-off, characterized by 20dB shape factor of 1.45. This channel-select filter with 0.3% fractional bandwidth had only 1.6dB of insertion loss, necessary for realization of receiver with very small noise figure. Two-tone measurement on this filter showed 31.4dBm of IIP3. The presented high-order filter of this chapter with such an excellent performance forms the essential framework for the application of capacitive channel-select filters in the receiver front-ends.

To pave the way for further research on channel-select filters at higher frequencies, Chapter 8 attempted to address the erroneous common belief that capacitive transducers fall short of the provision of strong electromechanical coupling at higher frequencies. The specially-designed fabrication processes of this chapter to (1) deposit low-stress polysilicon layers, (2) etch the polysilicon structure with smooth sidewall, and (3) deposit a conformal and uniform thin oxide layer, empowered the realization of sub-20nm gap transducers. The presented wineglass disk resonator with gap spacing of only 13.2nm delivered strong electromechanical coupling of 1.6%, the strongest coupling recorded so far for capacitive resonators at VHF.

9.2 FUTURE RESEARCH DIRECTIONS

The findings of this dissertation showed the advantages of channel selection and further enhanced the performances of capacitive resonators and filters.

The bridged micromechanical filter design procedure developed in this dissertation for CC-beam resonators can also be implemented for other types of micromechanical resonators at higher frequencies to boost the passband-to-stopband roll-off and provide extra rejection at the adjacent channels. The bridging technique is also capable of reducing the system footprint: sharper roll-off and higher stopband rejection mean a filter with lower order and smaller number of resonators can satisfy the desired performances.

The presented sub-20nm gap capacitive transducer cultivates more correct expectations for the efficacy of small gaps. The combination of high (C_x/C_o) and Q, which has long been a primary driver for RF MEMS research, stands to not only cut VHF low noise oscillator power consumption

to sub-µW levels and improve sensitivity for zero-quiescent all-mechanical receivers, but creates opportunities to apply MEMS resonator technology to the highly profitable and lucrative RF filter market for smartphones, where gaps of 10nm with higher bias voltage should allow the 6% (C_x/C_o)'s at GHz frequencies needed for such filters.

BIBLIOGRAPHY

[1] A. Goldsmith, Wireless Communications, Cambridge University Press, 2005.

[2] E. Lee, J. Kubiatowicz, J. Rabaey and A. Sangiovanni-Vincentelli, "The TerraSwarm Research Center (TSRC) (A White Paper)," Technical Report UCB/EECS-2012-207, EECS Department, University of California, Berkeley, 2012.

[3] E. Latronico, E. A. Lee, M. Lohstroh, C. Shaver, A. Wasicek and M. Weber, "A Vision of Swarmlets," *IEEE Internet Computing,* vol. 19, no. 2, pp. 20-28, 2015.

[4] D. Cabric, I. D. O'Donnell, M. S. W. Chen and R. W. Brodersen, "Spectrum sharing radios," *IEEE Circuits and Systems Magazine,* vol. 6, no. 2, pp. 30-45, 2006.

[5] I. M. J. R. P. A. J. V. J. L. W. a. C. E. W. I. K. S. Gilhousen, "On the capacity of a cellular CDMA system," *Veh. Technol. IEEE Trans. On,* vol. 40, no. 2, pp. 303-312, 1991.

[6] J. Mitola, "The software radio architecture," *Commun. Mag. IEEE,* vol. 33, no. 5, pp. 26-38, 1995.

[7] G. Yuan, X. Zhang, W. Wang and Y. Yang, "Carrier aggregation for LTE-advanced mobile communication systems," *IEEE Communications Magazine,* vol. 48, no. 2, pp. 88-93, 2010.

[8] P. Mercier and A. Chandrakasan, Ultra-Low-Power Short-Range Radios, Cham, Switzerland: Springer, 2015.

[9] X. W. C. W. Md. Arafat Rahman, "A review of high energy density lithium–air battery technology," *Journal of Applied Electrochemistry,* vol. 44, no. 1, pp. 5-22, 2014.

[10] H.-K. C. W.-T. P. Le-Giang Tran, "RF power harvesting: a review on designing methodologies and applications," *Micro and Nano Syst Lett,* vol. 12, pp. 5-14, 2017.

[11] A. Rowe, R. Mangharam and R. Rajkumar, "FireFly: A Time Synchronized Real-Time Sensor Networking Platform," in *Wireless Ad Hoc Networking: Personal-Area, Local-Area, and the Sensory-Area Networks*, CRC Press Book, 2006.

[12] B. A. Warneke and K. S. J. Pister, "An ultra-low energy microcontroller for Smart Dust wireless sensor networks," in *IEEE International Solid-State Circuits Conference*, 2004.

[13] K.-L. Du and M. N. S. Swamy, Wireless Communication Systems, Cambridge University Press, 2010.

[14] R. Ruby, P. Bradley, D. Clark, D. Feld, T. Jamneala and K. Wang, "Acoustic FBAR for filters, duplexers and front end modules," in *IEEE MTT-S International Microwave Symposium Digest*, 2004.

[15] "User Equipment (UE) conformance specification; Part 1: Protocol conformance specification (3GPP TS 34.123-1 version 10.3.1 Release 10)," European Telecommunications Standards Institute (ETSI),, 2013.

[16] E. H. Armstrong, "The super-heterodyne-its origin, development, and some recent improvements," *Radio Eng. Proc. Inst. Of,* vol. 12, no. 5, pp. 539-552, 1924.

[17] B. Razavi, RF Microelectronics, 2nd ed., New York: Prentice Hall, 2011.

[18] R. C. Ruby, P. Bradley, Y. Oshmyansky, A. Chien and J. D. Larson, "Thin film bulk wave acoustic resonators (FBAR) for wireless applications," in *2001 IEEE Ultrasonics Symposium. Proceedings*, 2001.

[19] M. Hikita, H. Kojima, T. Tabuchi and Y. Kinoshita, "800-MHz high-performance SAW filter using new resonant configuration," *Microw. Theory Tech. IEEE Trans. On,* vol. 33, no. 6, pp. 510-518, 1985.

[20] T. L. Naing, T. O. Rocheleau, ZeyingRen, S.-S. Li and C. T.-C. Nguyen, "High-Q UHF Spoke-Supported Ring Resonators," *Journal of Microelectromechanical Systems,* vol. 25, no. 1, pp. 11-29, 2016.

[21] A. A. Abidi, "Direct-conversion radio transceivers for digital communications," *IEEE J. Solid-State Circuits,* vol. 30, no. 12, pp. 1399-1410, Dec. 1995.

[22] A. A. Abidi, "The Path to the Software-Defined Radio Receiver," *IEEE J. Solid-State Circuits,* vol. 42, no. 5, pp. 954-966, 2007.

[23] C. T.-C. Nguyen, "MEMS-based RF channel selection for true software-defined cognitive radio and lowpower sensor communications," *IEEE Communications Magazine,* vol. 51, no. 4, pp. 110-119, 2013.

[24] T. L. Naing, "A 78-microwatt GSM phase noise-compliant pierce oscillator referenced to a 61-MHz wineglass disk resonator," *IFCS,* 2013.

[25] C. T.-C. Nguyen, "MEMS Technology for Timing and Frequency Control," *IEEE Transactions on Ultrasonics, Ferroelectrics, and Frequency Control,* vol. 54, no. 2, pp. 251-270, 2007.

[26] A. S. Sedra and P. O.Brackett, Filter Theory and Design: Active and Passive, Beaverton, OR: Matrix, 1978.

[27] A. I. Zverev, Handbook of Filter Synthesis, New York: Wiley, 1967.

[28] K. Wang and C. T.-C. Nguyen, "High-order medium frequency micromechanical electronic filters," *Journal of Microelectromechanical Systems,* vol. 8, no. 4, pp. 534-556, 1999.

[29] G. Piazza, "Single-Chip Multiple-Frequency ALN MEMS Filters Based on Contour-Mode Piezoelectric Resonators," *JMEMS,* vol. 16, no. 2, pp. 319 - 328, 2007.

[30] R. Abdolvand, B. Bahreyni, J. E. -Y. Lee and F. Nabki, "Microw. Theory Tech. IEEE Trans. On," *Micromachines ,* vol. 7, no. 9, p. 160, 2016.

[31] S.-S. Li, Y.-W. Lin, Z. Ren and C.-C. Nguyen, "An MSI micromechanical differential diskarray filter," in *Solid-State Sensors, Actuators and Microsystems Conference, TRANSDUCERS*, 2007.

[32] S.-S. Li, Y.-W. Lin, Z. Ren and C.-C. Nguyen, "A micromechanical parallel-class diskarray filter," in *IEEE International Frequency Control Symposium*, 2007.

[33] T.-T. Yen, C.-M. Lin, Y.-J. Lai, D. Wittwer, M. A. Hopcroft and A. P. Pisano, "Fine frequency selection techniques for aluminum nitride Lamb wave resonators," in *IEEE International Frequency Control Symposium (FCS)*, 2010.

[34] C. Zuo, N. Sinha, M. B. Pisani, C. R. Perez, R. Mahameed and G. Piazza, "Channel-Select RF MEMS Filters Based On Self- Coupled A1N Contour-Mode Piezoelectric Resonators," in *IEEE Ultrasonics Symposium Proceedings*, 2007.

[35] B. Kim, R. H. Olsson and K. E. Wojciechowski, ""AlN Microresonator-Based Filters With Multiple Bandwidths at Low Intermediate Frequencies," *J. Microelectromechanical Syst.,* vol. 22, no. 4, pp. 949-961, 2013.

[36] R. H. Olsson, C. M. Washburn, J. E. Stevens, M. R. Tuck and C. D. Nordquist, "VHF and UHF mechanically coupled aluminum nitride MEMS filters," in *IEEE International Frequency Control Symposium*, 2008.

[37] D. Weinstein, H. Chandrahalim, L. F. Cheow and S. A. Bhave, "Dielectrically transduced single-ended to differential MEMS filter," in *IEEE InternationalSolid-State Circuits Conference ISSCC*, 2006.

[38] H. Chandrahalim, D. Weinstein, L. F. Cheow and S. A. Bhave, "High-κ dielectrically transduced MEMS thickness shear mode resonators and tunable channel-select RF filters," *Sens. Actuators Phys.,* vol. 136, no. 2, pp. 527-539, 2007.

[39] C. T.-C. Nguyen, "RF MEMS for Channelizing Low-Power Radios," in *International Conference on Solid-State Sensors, Actuators and Microsystems (TRANSDUCERS)*, Barcelona, 2013.

[40] T. L. Naing, "2.97-GHz CVD diamond ring resonator with Q >40,000," in *IFCS*, 2012.

[41] M. Akgul, R. Schneider, Z. Ren, G. Chandler, V. Yeh and C. T. C. Nguyen, "Hot filament CVD conductive microcrystalline diamond for high Q, high acoustic velocity micromechanical resonators," in *IEEE International Frequency Control Symposium*, 2011.

[42] Y. W. Lin, L. W. Hung, S. S. Li, Z. Ren and C. T. C. Nguyen, "Quality Factor Boosting via Mechanically-Coupled Arraying," in *International Solid-State Sensors, Actuators and Microsystems Conference, TRANSDUCERS* , 2007.

[43] L.-W. Hung, Z. A. Jacobson, Z. Ren, A. Javey and C. T.-C. Nguyen, "Capacitive transducer strengthening via ALD-enabled partial-gap filling," in *Hilton Head,*, 2008.

[44] M. Akgul, "Capacitively transduced micromechanical resonators w/ simultaneous low motional resistance and Q>70,000," *Hilton-Head,* 2010.

[45] G. Piazza, "Piezoelectric Aluminum Nitride Vibrating Contour-Mode MEMS Resonators," *JMEMS,* pp. 1406-1418, 2006.

[46] R. Ruby, P. Bradley, J. L. III, Y. Oshmyansky and D. Figueredo, "Ultra-miniature high-Q filters and duplexers using FBAR technology," in *Digest of Technical Papers, 2001 IEEE International Solid-State Circuits Conference*, San Francisco, California, 2001.

[47] S.-S. Li, M. U. Demirci, Y.-W. Lin, Z. Ren and C. T.-C. Nguyen, "Bridged micromechanical filters," in *IEEE International Frequency Control Symposium*, Montreal, Canada, 2004.

[48] M. Akgul, "A passband-corrected high rejection channel-select micromechanical disk filter," in *IFCS*, Taipei, 2014.

[49] J. Naghsh Nilchi, R. Liu and C.-C. Nguyen, "7th order sharp-roll-off bridged micromechanical filter," *Transducers,* 2015.

[50] Y.-W. Lin, S. Lee, S.-S. Li, Y. Xie, Z. Ren and C. T.-C. Nguyen, "Series-Resonant VHF Micromechanical Resonator," *IEEE Journal of Solid-State Circuits,* vol. 39, no. 12, pp. 2477-2491, 2004.

[51] S. L. Jang, Y. K. Wu, C. C. Liu and J. F. Huang, "A Dual-Band CMOS Voltage-Controlled Oscillator Implemented With Dual-Resonance LC Tank," *Microwave and Wireless Components Letters,* vol. 19, no. 12, pp. 816-818, 2009.

[52] R. C. Ruby, P. Bradley, Y. Oshmyansky, A. Chien and J. D. L. III, "Thin Film bulk wave acoustic resonators (FBAR) for wireless applications," in *IEEE Ultrasonics Symposium*, 2001.

[53] C. C. Ruppel, R. Dill, A. Fischerauer, G. Fischerauer and A. Gawlik, "SAW devices for consumer communication," *IEEE Transactions on Ultrasonics, Ferroelectrics, and Frequency Control,* vol. 40, no. 5, pp. 438-452, 1993.

[54] S. S. Rao, Vibration of Continuous Systems, John Wiley & Sons, 2007.

[55] F. D. Bannon, J. R. Clark and C. T.-C. Nguyen, "High-Q HF mi-cromechanical filters," *IEEE J. Solid-State Circuits,* vol. 35, no. 4, pp. 512-526, 2000.

[56] J. Wang, J. E. Butler, T. Feygelson and C. T.-C. Nguyen, "1.51-GHz polydiamond µmechanical disk resonator with impedancemismatched," in *IEEE International Conference on Micro Electro Mechanical Systems*, 2004.

[57] S. D. Senturia, Microsystem Design, springer, 2001.

[58] C. T.-C. Nguyen, "Frequency-selective MEMS for miniaturized communication devices," *IEEE Transaction on Microwave Theory and Technology,* vol. 47, pp. 1486-1503, 1999.

[59] S. Tadigadapa and K. Mateti, "Piezoelectric MEMS sensors: state-of-the-art and," *Measurement Science and Technology,* vol. 20, p. 092001, 2009.

[60] B. A. J, B. S. J, P. J, O. A, R. D and B. H, "Micromachined III–V cantilevers for AFM-tracking scanning Hall probe microscopy," *Journal of Micromechanics and Microengineering,* vol. 13, no. 1, p. 124, 2002.

[61] H. Sehr, I. S. Tomlin, B. Huang, S. P. Beeby, A. G. R. Evans, A. Brunnschweiler, G. J. Ensell, C. G. J. Schabmueller and T. E. G. Niblock, "Time constant and lateral resonances of thermal vertical bimorph actuators," *Journal of Micromechanics and Microengineering,* vol. 12, no. 4, p. 410, 2002.

[62] M. Akgul, L. Wu, Z. Ren and C. T. C. Nguyen, "A negative-capacitance equivalent circuit model for parallel-plate capacitive-gap-transduced micromechanical resonators," *IEEE Transactions on Ultrasonics, Ferroelectrics, and Frequency Control,* vol. 61, no. 5, pp. 849-869, 2014.

[63] R. L. Kubena, "MEMS-based quartz oscillators and filters for on-chip integration," in *IFCS*, 2005.

[64] R. Ruby, "Method of Extracting Unloaded Q Applied Across Different Resonator Technologies," in *IUS*, 2008.

[65] W.-T. Hsu and C. T.-C. Nguyen, "Stiffness-compensated temperature-insensitive micromechanical resonators," in *IEEE Int. Conference on Micro-Electro-Mechanical Systems*, 2002.

[66] X. L. Feng, C. J. White, A. Hajimiri and M. L. Roukes, "A self-sustaining ultrahigh-frequency nanoelectromechanical oscillator," *Nature Nanotechnology,* vol. 3, pp. 342-346, 2008.

[67] C. T. C. Nguyen and R. T. Howe, "CMOS micromechanical resonator oscillator," in *IEEE International Electron Devices Meeting*, 1993.

[68] Y. Lin, W. C. Li, B. Kim, Y. W. Lin, Z. Ren and C. T. C. Nguyen, "Enhancement of micromechanical resonator manufacturing precision via mechanically-coupled arraying," in *IEEE International Frequency Control Symposium*, 2009.

[69] M. A. Abdelmoneum, M. M. Demirci, S.-S. Li and C. T. C. Nguyen, "Post-fabrication laser trimming of micromechanical filters," in *IEEE International Electron Devices Meeting*, 2004.

[70] T. M. Bloomstein and D. J. Ehrlich, "Laser deposition and etching of three-dimensional microstructures," in *International Conference on Solid-State Sensors and Actuators, TRANSDUCERS*, 1991.

[71] D. Joachim and L. Lin, "Characterization of selective polysilicon deposition for MEMS resonator tuning," *Journal of Microelectromechanical Systems,* vol. 12, no. 2, pp. 193-200, 2003.

[72] R. A. Johnson, Mechanical Filters in Electronics, New York, NY: Wiley, 1983.

[73] J. Naghsh Nilchi, R. Liu, S. Li, M. Akgul, T. O. Rocheleau and C. T.-C. Nguyen, "Third order intermodulation distortion in capacitive-gap transduced micromechanical filters," in *IEEE International Frequency Control Symposium*, Denver, 2015.

[74] Keysight Advanced Design System (ADS) [computer software], Release 2016.01.

[75] F. Lin and M. Rais-Zadeh, "Tunable RF MEMS Filters: A Review," in *Encyclopedia of Nanotechnology*, Dordrecht, Springer Netherlands, 2016, pp. 4233-4243.

[76] A. Shooshtari and M. Rafiee, "Nonlinear forced vibration analysis of clamped functionally graded beams," *Acta Mechanica,* vol. 23, p. 221, 2011.

[77] R. Navid, J. R. Clark, M. Demirci and C. T. C. Nguyen, "Third-order intermodulation distortion in capacitively-driven CC-beam micromechanical resonators," in *IEEE International Conference on Micro Electro Mechanical Systems*, 2001.

[78] K. Wang, J. Koo, R. Ruby and B. Otis, "21.7 A 1.8mW PLL-free channelized 2.4GHz ZigBee receiver utilizing fixed-LO temperature-compensated FBAR resonator," in *IEEE International Solid-State Circuits Conference*, 2014.

[79] M. A. Abdelmoneum, "Stemless wine-glass-mode disk micromechanical resonators," in *MEMS*, 2003.

[80] S.-S. Li, Y.-W. Lin, Z. Ren and C. T.-C. Nguyen, "Self-switching vibrating micromechanical filter bank," in *IEEE International Frequency Control Symposium*, 2005.

[81] T. L. Naing, "Simultaneous multi-frequency switchable oscillator and FSK modulator based on a capacitive-gap MEMS disk array," in *MEMS*, 2015.

[82] T. J. Cheng, "High-Q, low impedance polysilicon resonators with 10 nm air gaps," *MEMS,* 2010.

[83] D. T. Chang, F. P. Stratton and D. J. Kirby, "A New MEMS-Based Quartz Resonator Technology," in *Hilton Head*, 2004.

[84] R. Liu, "Zero quiescent power VLF mechanical communication receiver," *Transducers,* 2015.

[85] G. G. Yaralioglu, "Calculation and measurement of electromechanical coupling coefficient of capacitive micromachined ultrasonic transducers," *IEEE Transactions on UFFC,* vol. 50, no. 4, pp. 449-456, 2003.

[86] J. C. Ranuarez, M. Deen and C.-H. Chen, "A review of gate tunneling current in MOS devices," *Microelectronics Reliability,* vol. 46, pp. 1939-1956, 2006.

[87] L. M and S. EH, "Fowler–Nordheim tunneling into thermally grown SiO2," *Journal of Applied Physics,* vol. 40, no. 1, pp. 278-283, 1969.